Università
degli
Studi di Padova

Scuola Di Scienze
CORSO DI LAUREA IN SCIENZA DEI MATERIALI

TESI DI LAUREA MAGISTRALE

STUDY OF NIOBIUM SPUTTERED COPPER ACCELERATING CAVITIES AS A POSSIBLE ALTERNATIVE TO THE BULK TECHNOLOGY

Relatore: **Prof. Vincenzo Palmieri**

Candidata: **Martina Martinello**

Correlatore: **Dr. Sergey Stark**

A.A 2013/2014

ACKNOWLEDGMENTS

Vorrei ringraziare prima di tutto il Prof. Enzo Palmieri, il quale oltre ad avermi dato la possibilità di realizzare il seguente lavoro di tesi al meglio, mi ha consentito di partecipare ad esperienze internazionali, le quali sono state particolarmente utili per aver arricchito le mie conoscenze in materia di tesi, e mi hanno permesso di vivere nuove ed intense emozioni. Colgo inoltre l'occasione per ringraziare il Dott. Walter Venturini e la Dott.ssa Irene Mondino in quanto mi hanno permesso di lavorare con loro durante il periodo di Summer Student Program che ho svolto presso il CERN. Grazie a loro ho potuto comprendere in modo più approfondito come avviene il funzionamento di una misura RF e quali informazioni possono essere tratte da questa.

Un sentito ringraziamento lo dedico al Dott. Sergey Stark che mi è stato particolarmente vicino durante la stesura della tesi, e che grazie al suo lavoro ci permette di usufruire di un sistema RF per la caratterizzazione delle cavità molto avanzato. Ringrazio inoltre tutti i colleghi del laboratorio di superconduttività per i consigli preziosi datami in questi mesi. Un particolare ringraziamento ad Antonio il cui aiuto costante in laboratorio è stato molto utile per lo svolgimento della tesi. Grazie anche a Stefano, per essere un grande amico, e con cui sono felice di aver condiviso questi anni di università.

Ringrazio con il più sentito affetto mia mamma che mi è stata sempre vicino fornendomi l'aiuto economico e morale durante questi anni di Università, perché ha sempre creduto in me dandomi il coraggio e la voglia di andare sempre avanti. Un grazie anche a mia sorella Nuna, a Cesare, e a Massimo, perché so che qualsiasi cosa accada posso sempre contare su di loro.

Un grazie di cuore va a Mattia, per aver condiviso questi anni insieme, per essermi stato vicino nei momenti belli e in quelli difficili. Grazie per starmi accanto giorno dopo giorno con così tanto affetto. Grazie perché insieme abbiamo raggiunto un'altro importante traguardo, che non sarà altro che un nuovo inizio, insieme.

"[...] Così tra questa
immensità s'annega il pensier mio:
e il naufragar m'è dolce in questo mare."

G. Leopardi

ESTRATTO

Nel seguente lavoro di tesi verranno presentati differenti studi riguardo le proprietà superconduttive in radiofrequenza (RF) di cavità a film sottile di Niobio su Rame. Sono state studiate due tipologie di cavità differenti: risuonatori a quarto d'onda (QWRs) e cavità ellittiche 6GHz, in entrambe le tipologie di cavità studiate, un film superconduttore di Niobio è stato depositato via sputtering sul substrato in Rame.

Le cavità a quarto d'onda sono state caratterizzate durante lo svolgimento di un Summer Student Program presso il centro di ricerca CERN. Tali cavità sono attualmente studiate per il progetto HIE-ISOLDE che prevede un upgrading della facility ISOLDE presente al CERN. Tale upgrading è volto all'implementazione di cavità superconduttive QWRs nello stadio di accelerazione lineare della facility stessa. Queste vengono caratterizzate tramite misure RF allo scopo di comprendere quali risonatori raggiungono le specifiche richieste dal progetto HIE-ISOLDE. Inoltre, allo scopo di investigare le proprietà superficiali delle cavità, una stima del valore di RRR del film depositato è stata effettuata studiando la variazione della frequenza di risonanza della cavità nei pressi della temperatura critica.

Presso i Laboratori Nazionali di Legnaro (LNL) sono state invece studiate cavità ellittiche 6GHz, a film sottile di Niobio su Rame. La ricerca è stata in questo caso volta allo studio dello sputtering di film superconduttori di Niobio su cavità 6GHz in Rame, agendo sui parametri di deposizione, allo scopo di ottenere buone performance superconduttive in RF di tali risonatori. L'obiettivo è stato raggiunto effettuando una deposizione di Niobio ad alta temperatura in cui il substrato viene riscaldato a 400°C. Tale cavità presenta il più alto valore di Q-factor tra le cavità 6GHz analizzate.

Dato che il maggior problema della cavità a film sottile di Niobio su Rame è il Q-slope, che ne limita notevolmente l'utilizzo in acceleratori in cui vengono richiesti elevati gradienti, viene proposto un nuovo modello come possibile spiegazione di tale problema. In questo modello la perdita di performance della cavità viene analizzata dal punto di vista termico, ricavando che la causa principale di ciò potrebbe essere proprio la presenza dall'interfaccia Niobio/Rame. Questa sarebbe causa di un innalzamento importante di temperatura che logora le proprietà superconduttive del film di Niobio.

Sono stati inoltre riscontrati elevati valori di temperatura del bagno di Elio, nei pressi della superficie esterna della cavità, che portano a pensare che la cavità durante la misura a $1.8K$ non è, in realtà , circondata da Elio superfluido. Questa potrebbe invece essere circondata da uno strato di Elio in forma vapore, e dunque, lo scambio termico con il bagno potrebbe essere ora governato dal regime di film boiling anziché dalla conducibilità di Kapitza.

ABSTRACT

Several studies regarding the radiofrequency (RF) superconducting proprieties of thin film Niobium on Copper cavities are presented. Two types of Niobium on Copper cavities are analyzed: Quarter Wave Resonators (QWRs) and elliptical 6GHz cavities, in both cases a superconducting Niobium film is deposited via sputtering on the Copper substrate.

The QWRs were characterized at CERN, in the framework of a Summer Student Program. Such cavities are nowadays under study at CERN for the project HIE-ISOLDE. The purpose of this project is the upgrading of ISOLDE facility by the implementation of superconducting accelerating cavities in its linear acceleration section. The RF characterization of QWRs is performed in order to evaluate if the resonator reaches the HIE-ISOLDE specification. In addition, for a more complete understanding of the cavity surface properties, the RRR was evaluated by analyzing the resonance frequency shift near the critical temperature.

The 6GHz Niobium on Copper cavities were instead studied at LNL, INFN. The research was carried out in order to obtain a Niobium thin film with good RF superconducting performances, working on the sputtering parameters. The goal was reached with a high temperature Niobium deposition in which the substrate was heated at $400°C$. This cavity has the highest Q-factor values found for the analyzed 6GHz cavities.

Furthermore, since the Q-slope is the main problem of the Niobium on Copper cavities, which limits the possibility of the implementation in very high gradient accelerators, a new model is proposed as a possible explanation of this issue. This model analyses the Q-slope as a thermal problem and highlights that the lowering of the performances is due to the Niobium/Copper interface. Because of this interface, a pronounced temperature rinsing occurs, which makes worse the superconducting properties.

Moreover, elevated values of temperature were found in the Helium bath near the external cavity surface, during the measurement of the Cu1_3 cavity. Hence, it may be not surrounded by super-fluid Helium but by a vapor Helium layer instead, and the heat exchange may take place, therefore, following the film boiling regime.

INDEX

INTRODUCTION

Particle accelerators are a fundamental instrument for research in physics. They allow to study the building blocks of the matter and the force acts to keep them together. Accelerators can be seen as the largest microscopes that can be implemented. The finer detail in the structure of fundamental particles can be revealed only by using wavelengths below $\lambda < 10^{-15} m$. Such wavelengths, necessary for understanding the sub-nuclear matter, are obtained only with high energy particles, in accordance with the De Broglie wavelength definition. This fact is a consequence of the quantum mechanics particles behavior, in which for looking at a very short range a higher momentum is required. In addition to the discovery of smaller structures, the accelerators can be used to produce new particles and more massive are them, higher energy is requested, according to the Einstein equation $E = mc^2$.

Usually the accelerated particles are: electrons or positrons, protons or antiprotons, monatomic ions and, sometimes, heavy ions.

Accelerating cavities allows the particles acceleration thanks to their electric field distribution. In such radiofrequency resonators, in order to obtained the acceleration, particles must be in phase with the field itself. At each passage through the cavity, particles gain a finite energy, and if many cavities are present, particle beam increases its energy progressively, gaining energy from each member of the chain. The efficiency of such devices is enhanced by using superconducting materials which have low surface resistance and then they involve low dissipated power, at the same accelerating field. The implementation of superconductor materials permits to reach higher particles accelerating gradients, with lower power consumption. As it will be explained in Chapter 1, normal conducting materials have no chance to reach low surface resistance and for such application the employment of superconducting materials become essential. Superconducting accelerating cavities are indeed used nowadays in many laboratories around the world.

By the way the challenge is now to find an alternative technology to bulk Niobium cavities. The most superconducting cavities employed in the accelerators are made in bulk Niobium, this metal has the highest critical temperature among the others superconducting elements of the periodic table. On the contrary, it has low values of thermal conductivity, hence, the presence of

defects causes easily the increasing of the temperature which can brings to the thermal breakdown of the superconducting state. Furthermore the Niobium bulk technology is particularly expensive because of the higher cost of the entire Niobium cavity production. Indeed the material itself is quite expensive, but the so high costs are especially due to: the cavity fabrication, in particular for the electro-beam welding, the post-purification treatments, the chemical treatments, and so on. The Niobium thin film on Copper technology is a great alternative, because of the many advantages offered by the Copper substrate, as the higher thermal conductivity and the minor cost. On the other hand, the Niobium thin film technology has not achieved yet its maximum potentiality. The Q-slope problem, i.e. the decreasing of the Q-factor as the accelerating field increases, represents the main limitation. Solving of the Q-slope will be the real step ahead, making the accelerator technology less expensive.

Because of the advantage offered, the thin film technology was already employed in accelerators. Examples are heavy ion facilities, like ALPI at LNL, and hadrons colliders, like LHC at CERN. The superconducting Niobium sputtered cavities will be placed also in the accelerator stage of the ISOLDE facility at CERN. This upgrading allows to increase the energy gain of the facility.

In Chapter 2, after an explanation about how an accelerating cavity works and the different geometries of such devices, the state-of-the-art of thin film technology is reported. The main characterization method of such resonators is the RF measurement of the cavity Q-factor as a function of the accelerating field. The RF measurements were done for two different cavities geometry. The Quarter Wave Resonators were measured at the European Center for Nuclear Research (CERN), and 6GHz cavities where measured at the Legnaro National Laboratories (LNL, INFN). In chapter 3 it is explained how in either cases the measurements are done, analyzing also the main differences between the two RF systems.

Also the Niobium thin film sputtering research was carried out in order to understand how a Niobium thin film with a good RF superconducting proprieties could be deposited on 6GHz Copper cavities. In Chapter 4 the experimental work on the magnetron sputtering deposition is explained.

The results of the RF measurements of the QWRs and 6GHz cavities, are reported in Chapter 5. The data analysis about the QWRs measurements consists of: the errors analysis made with propagation of uncertainly and a Monte Carlo like method, the indirect calculation of both the thickness and the RRR of the Niobium sputtered film. In order to compare the surface proprieties between the 6GHz sputtered cavities, an estimation of the residual resistance was performed by using the BCS theory. In addition two different possible explanation about the Q-slope problem were performed.

Chapter 1

INTRODUCTION TO SUPERCONDUCTIVITY

Normal conducting materials cannot reach very low values of resistivity even at low temperature, indeed they are limited in DC by their residual resistivity and in AC by the anomalous skin effect. Superconducting materials show instead zero resistivity in DC and very low resistivity value in AC depending on the material properties. These different behaviors will be here explained putting particular attention to superconducting state explanation. Several theories were proposed until now, in order to understand the superconducting state, unfortunately there is no one really able to explain it completely. The first theories about superconductivity will be reported arriving at the BCS microscopical theory, which is one of the more reliable for low temperature superconductors.

1.1 NORMAL CONDUCTOR

The Ohm's law explain that a metal, which is exposed to a constant electric field $\bar{E}$, produces an electric current density $\bar{J}$ directly proportional to the field, and with the same direction and verse:

$$\bar{J} = nq\bar{v} = \sigma\bar{E} \tag{1.1}$$

the proportionality constant σ is the conductivity of the material and it is defined by the Drude's model as :

$$\sigma = \frac{1}{\rho} = \frac{ne^2}{m}\tau \tag{1.2}$$

where ρ is the resistivity of the material, n is the free electron density, e is the elementary charge, m is the electron mass and τ is the collision time.

Usually the electrical resistivity is dominated at room temperature by the collisions between the conduction electrons and the lattice thermal phonons, ρ_{ph}, whereas at liquid Helium temperature by collisions with impurities and imperfections in the lattice, ρ_i. The resistivity can be therefore expressed by the Matthiessen's rule as sum of these two contributions:

$$\rho(T) = \rho_{ph}(T) + \rho_i \tag{1.3}$$

If the defect concentration is small, $\rho_{ph}(T)$ is independent of the number of defects, and ρ_i is often independent of the temperature. The phonons contribution $\rho_{ph}(T)$ vanishes for $T \to 0$ because of the freezing of the phonons, so, for a normal conductor, the resistivity at low temperature is equal to ρ_i and it is called residual resistivity. The ratio between the resistivity at room temperature and the residual resistivity defines the Residual Resistivity Ratio (RRR) :

$$RRR = \frac{\rho(300K)}{\rho_i} = \frac{\rho_{ph}(300K)}{\rho_i} + 1 \tag{1.4}$$

This ratio is an indication of the sample purity, a bulk material has high level of purity with $\mathrm{RRR} > 250$, whereas a good thin film has $\mathrm{RRR} \sim 100$ because the surfaces of the film acts as defects of the lattice [1].

1.1.1 The Normal Skin Effect

Considering a metal piece which occupies the half-space $x > 0$ and that is exposed to an electromagnetic wave normally incident on its surface, as is shown in Figure 1.1 :

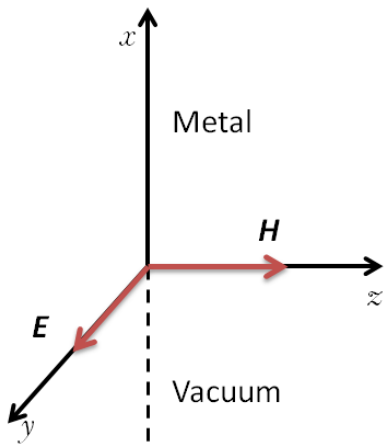

Figure 1.1 - Scheme of the space arrangement of the metals and the vacuum.

the Maxwell equations are:

$$\bar{\nabla} \times \bar{\mathrm{B}} = \mu_0 \bar{\mathrm{J}} + \varepsilon_0 \mu_0 \frac{\partial \bar{E}}{\partial t} = \mu_0 \sigma \bar{E} \tag{1.5}$$

$$\overline{\nabla} \times \overline{\mathrm{E}} = -\frac{\partial \overline{\mathrm{B}}}{\partial \mathrm{t}}$$

where μ is the magnetic permittivity. The displacement term $\partial \bar{E}/\partial t$ can be neglected because at RF field it is much smaller compare to the conduction current in metal. Taking into account an electromagnetic field of the type $\overline{\mathrm{E}}(\mathrm{x},\mathrm{t}) = \overline{\mathrm{E}}_0 \mathrm{e}^{\mathrm{i}(\mathrm{kx}-\omega \mathrm{t})}$, $\overline{\mathrm{B}}(\mathrm{x},\mathrm{t}) = \overline{\mathrm{B}}_0 \mathrm{e}^{\mathrm{i}(\mathrm{kx}-\omega \mathrm{t})}$, even the current density has the shape $\bar{\mathrm{J}}(\mathrm{x},\mathrm{t}) = \bar{\mathrm{J}}_0 \mathrm{e}^{\mathrm{i}(\mathrm{kx}-\omega \mathrm{t})}$, and the solutions of the Maxwell's equations are:

$$\begin{aligned} ik\mathrm{B}_0 &= \mu \mathrm{J}_0 = \mu\sigma E_0 \\ ikE_0 &= i\omega \mathrm{B}_0 \end{aligned} \tag{1.6}$$

Resolving this system one finds the dispersion law between the wave vector k and the angular frequency ω:

$$k = \pm(1-i)\sqrt{\frac{\mu\omega\sigma}{2}} = \pm(k_1 - ik_2) \tag{1.7}$$

So that the wave vector cannot diverge going deep in the material, only the solution with the minus sign can be used in this model. Indeed using the solution $k = -(k_1 - ik_2)$ one finds the following result:

$$\overline{\mathrm{E}}(\mathrm{x},\mathrm{t}) = \mathrm{E}_0 \mathrm{e}^{-\mathrm{i}(\mathrm{k}_1\mathrm{x}-\omega \mathrm{t})} \mathrm{e}^{-\mathrm{k}_2\mathrm{x}} \tag{1.8}$$

So the imaginary part of the wave vector gives an exponential decreasing of the field into the metal: $\mathrm{e}^{-\mathrm{k}_2\mathrm{x}} = \mathrm{e}^{-\mathrm{x}/\delta}$, i.e. the field penetrates into a thin surface layer of the metal called *skin penetration depth* δ:

$$\delta = \frac{1}{k_2} = \sqrt{\frac{2}{\mu\omega\sigma}} \tag{1.9}$$

The penetration depth results inversely proportional to both the angular frequency and the conductivity.

In order to analyze the AC properties of a metal it is necessary to take into account the surface impedance Z_S, which is the ratio between the electric field on the metal surface $E_y(0)$ and the current density $J_y(x)$ integrated over the thickness of the metal [2]. Since the impedance is a complex quantity, it can be defined as:

$$Z_S = \frac{E_y(0)}{\int_0^\infty J_y(x)dx} = R_S - iX_S \tag{1.10}$$

where R_S is the surface resistance which determines the energy loss of the electromagnetic wave into the material, and it is related to the change in amplitude of the wave. X_S is the surface reactance which is related to the change in phase of the wave reflected from the metal surface.

Looking at the Equation 1.10, and using the relation $J = \sigma E$, one obtains the following equation for the surface impedance:

$$Z = (1 - i)\sqrt{\frac{\mu\omega}{2\sigma}} \tag{1.11}$$

Therefore one finds:

$$R_S = X_S = \sqrt{\frac{\mu\omega}{2\sigma}} = \frac{1}{\sigma\delta} \tag{1.12}$$

Then the energy losses are equal to the phase shift between the waves outside and inside the metal. The surface resistance is inversely proportional to the skin depth and it increases with the field frequency and decreases with the conductivity. This behavior is called *normal skin effect.*

1.1.2 THE ANOMALOUS SKIN EFFECT

The result found above is related to the Ohm's law $J = \sigma E$, however if the skin depth δ becomes smaller than the electronic mean free path l, this equation will be not valid anymore as the normal skin effect behavior. When this condition take place the electric field is not uniform inside the mean free path and a local treatment is now necessary in order to analyze the problem.

Increasing the frequency the skin depth decreases prominently and approaching low temperature the mean free path increases, so at very high frequency and/or at very low temperature could happen that $\delta \ll l$. In this case the electrons do not spend all their time between collisions in the field penetrated region, as a consequence they shield less efficiently the electric field leading to an higher RF surface resistance than the one expected from the Equation 1.12.

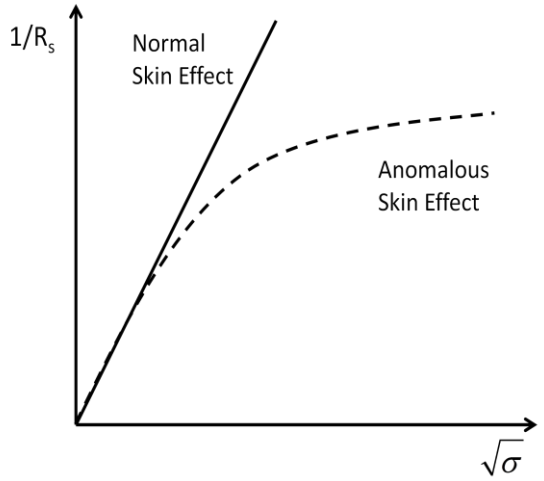

FIGURE 1.2 - NORMAL AND ANOMALOUS SKIN EFFECT ON THE GRAPH R_S^{-1} VERSUS $\sigma^{1/2}$.

Since the electrons that are moving at large angle spend little time in the electric field region, their interaction with the RF field is negligible and it is possible to consider that only the electrons that are moving parallel to the surface take part to the conduction. So it is necessary to define an effective electron density n_{eff} and an effective conductivity σ_{eff}:

$$n_{eff} = \frac{n_e \delta}{l} \qquad \sigma_{eff} = \frac{ia\sigma}{kl} \tag{1.13}$$

where i is the imaginary number, a is real coefficient, k is the wave vector. The surface impedance in the anomalous limit is found to be:

$$Z = (1 - i\sqrt{3}) \left[\sqrt{3}\pi \left(\frac{\mu_0}{4\pi}\right)^2\right]^{1/3} \omega^{2/3} \left(\frac{l}{\sigma}\right)^{1/3} \tag{1.14}$$

This result shows that $X_S = \sqrt{3} R_S$, the phase shift is now slightly bigger than the energy losses. In addition the surface impedance is proportional to $\omega^{2/3}$ so the frequency contribution is heavier than in a normal regime. When the anomalous regime is reached, the resistivity cannot decrease anymore by increasing the conductivity, as it is shown in Figure 1.2.

Therefore, when one works with high frequency and low temperature the anomalous skin effect appears and it is not possible to reach low value of surface resistivity. So the normal conducting metals, even at low temperature, exposed to radiofrequency will have always a rather high surface resistance. For the application in which low surface resistance is mandatory, it is necessary to resort to another material class: the superconductors.

1.2 THE SUPERCONDUCTING STATE

In 1911 Kamerlingh Onnes observed for the first time that the electrical resistance of Mercury drops to zero when it is cooled at $4.2K$. This phenomenon in which the material shows zero resistivity if cooled under its critical temperature was called superconductivity, and the corresponding material was called superconductor. A superconductor material shows another important property, it is also a perfect diamagnetic material. When a superconductor is exposed to an external magnetic field, the field is completely throws out from the interior, and the magnetic induction is equal to zero inside the superconductor. In the surface layer of the material a current appears and the magnetic field produced by this current acts as a perfect screen for the external field. This is the so-called Meissner-Ochsenfeld effect.

It is possible to define three critical parameters that determine the superconducting phase transition: the critical temperature T_C, the critical magnetic field H_C, and the critical current density J_C. These parameters define the critical surface in a three-dimensional space, Figure 1.3, that is the boundary between the superconductivity and the normal state.

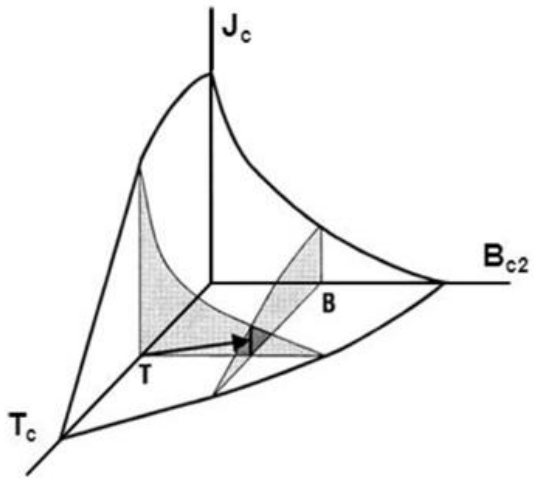

FIGURE 1.3 - CRITICAL SURFACE: BELOW THIS SURFACE THE SUPERCONDUCTOR STATE APPEARS, WHEREAS ABOVE IT THE NORMAL STATE APPEARS.

A material can show superconducting properties only below the critical surface ($T < T_C$, $H < H_C$, $J < J_C$), so the superconducting state can be destroyed not only by increasing the temperature but also increasing the magnetic field or the current density (the critical current density creates a magnetic field equal to H_C). The critical magnetic field decreases by increasing the temperature, so $H_C(T)$ can be expressed empirically by the Equation 1.15:

$$H_C(T) = H_C(0)\left[1 - \left(\frac{T}{T_C}\right)^2\right] \tag{1.15}$$

The trend is shown in Figure 1.4, so the superconducting transition appears at $T = T_C$ only if the external magnetic field is equal to zero, $H = 0$. Such transition is a second-order phase transition, it shows a discontinuity in the second derivatives of the free energy. It means that no latent heat absorption occurs during the transition.

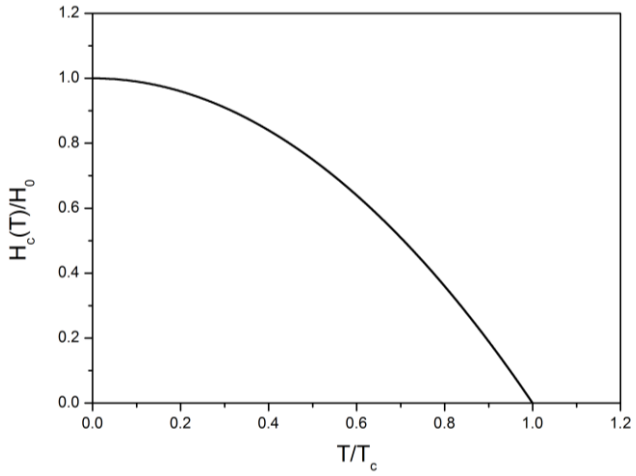

FIGURE 1.4 - TREND OF THE CRITICAL MAGNETIC FIELD AS A FUNCTION OF TEMPERATURE.

A first-order phase transition appears when $H \neq 0$, in this case critical temperature has lower values than in the previous case. The first derivatives of free energy are discontinuous and this leads to an absorption of the latent heat during the transition.

The heat capacity behavior is another fundamental property of the superconducting state. Unlike the normal-conductor, under the critical temperature the heat capacity has an exponential dependence on temperature:

$$C_V = \gamma T + BT^3 \qquad \gamma = \frac{\pi^2}{3} {k_B}^2 N(E_F) \qquad T > T_C$$
$$C_V = e^{-\Delta/k_B T} \qquad T < T_C \tag{1.16}$$

For $T > T_C$ there are both the electronic contribution, γT, where k_B is the Boltzman's constant and $N(E_F)$ is the density of states at the Fermi energy, and the phonons contribution, BT^3. For $T < T_C$ the exponential behavior implies the presence of an energy gap 2Δ between the excited states and the ground state of the electronic system. In according to the second-order phase transition the energy gap has to vanish at the critical temperature, so the electronic spectrum depends on the temperature even for superconductors [2].

1.2.1 TWO FLUID MODEL

In 1934 Gorter and Casimir proposed the *two fluid model* as a macroscopic explanation of superconductivity. According to this theory the charge carriers can be divided in two different components called fluids. One is the super-electrons fluid, this component does not carry entropy, so for $T = 0K$ all the electrons are super-fluid. The other one is the normal component which is responsible of the energy losses via Joule effect, in fact for $T \geq T_C$ all the electrons belong to this fluid. The density of charge carriers is then defined as:

$$n = n_s + n_n \qquad \frac{n_s}{n} = 1 - \frac{n_n}{n} \tag{1.17}$$

where n_n is the density of the normal-electrons and n_s is the density of the super-electrons. The dependence of the temperature of super-electrons density is given by:

$$n_s(T) = n_s(0)\left(1 - \left(\frac{T}{T_C}\right)^4\right) \tag{1.18}$$

So the trend of the two fluid as a function of temperature is shown in Figure 1.5.

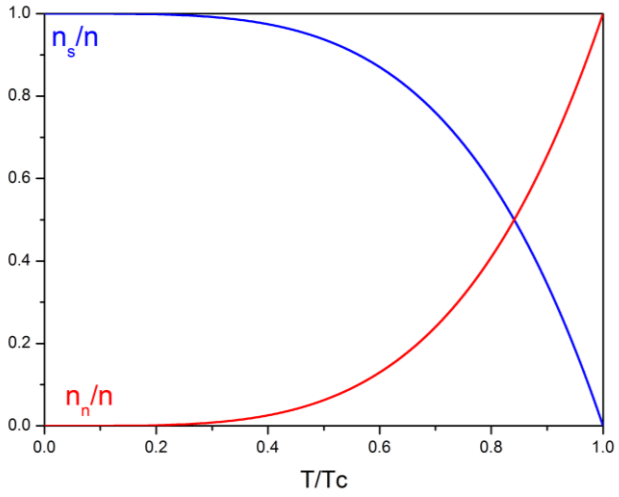

FIGURE 1.5 - NORMAL AND SUPER-FLUID AS A FUNCTION OF TEMPERATURE IN ACCORDING TO TWO FLUID MODEL.

The total current J_{tot} also is given by the sum of the superconducting current J_s and the normal-conducting current J_n:

$$J = J_n + J_s \tag{1.19}$$

The two currents flow in parallel.

The brothers Heinz and Fritz London proposed another macroscopic theory in order to understand the experimental results about superconductor materials, as the perfect conductibility and the Meissner effect.

The normal-conducting fluid under an external electric field can be described as a damped forced harmonic oscillator:

$$m\frac{d\bar{v}_n}{dt} + m\frac{\bar{v}_n}{\tau} = -e\bar{E} \tag{1.20}$$

Whereas the superconducting fluid is accelerated without friction, so there is no scattering term ($\tau_s \to \infty$):

$$m\frac{d\bar{v}_s}{dt} = -e\bar{E} \tag{1.21}$$

and the super-electrons current density can be defined as: $\bar{J}_s = -n_s e\bar{v}_s$.

Substituting the super-electrons velocity $\bar{v}_s$ into the Equation 1.21,one finds:

$$\frac{\partial \bar{J}_S}{\partial t} = \mu_0 \lambda_L^2 \bar{E} \tag{1.22}$$

which is the *first London* equation, where λ_L is the *London penetration depth*:

$$\lambda_L^2 = \sqrt{\frac{m}{\mu_0 e^2 n_s}} \tag{1.23}$$

The first London equation shows that in the stationary state, where $\partial \bar{J}_S/\partial t = 0$ there is no electric field inside the superconductor, so in direct current (DC) the conduction takes place without losses, but in alternating current (AC) the variation of a super-electron current density inside the material involves the formation of an electric field and so the resistance becomes non zero.

Using the first London equation and the Faraday-Lenz equation $\overline{\nabla} \times \bar{E} = -\frac{\partial \bar{H}}{\partial t}$ one obtains:

$$\frac{\partial}{\partial \mathrm{t}}(\mu_0 \lambda^2 \overline{\nabla} \times \bar{\mathrm{J}} + \bar{\mathrm{H}}) = 0 \tag{1.24}$$

so:

$$\overline{\nabla} \times \bar{\mathrm{J}} = -\frac{\bar{\mathrm{H}}}{\mu_0 \lambda^2} \tag{1.25}$$

this is the *second London equation* which can be written also as:

$$\bar{\mathrm{J}} = -\frac{\bar{\mathrm{A}}}{\mu_0 \lambda^2} \tag{1.26}$$

where $\bar{\mathrm{A}}$ is the vector potential which is defined as $\bar{\nabla} \times \bar{A} = \bar{H}$. Using again the London equations and the Maxwell's equation for static field one finds the following results:

$$\nabla^2 \bar{\mathrm{H}} = \frac{1}{\lambda_L^2} \bar{\mathrm{H}} \qquad \nabla^2 \bar{\mathrm{J}}_{\mathrm{s}} = \frac{1}{\lambda_L^2} \bar{J}_s \tag{1.27}$$

Now, supposing that the superconductor extends in the half-space $x > 0$ and the field is applied parallel to its surface in the direction z, one finds the solution:

$$H_z = H_0 e^{-x/\lambda_L} \qquad J_y = -\frac{1}{\lambda_L} e^{-x/\lambda_L} \tag{1.28}$$

This means that the magnetic field decays exponentially increasing the distance from the surface, so it is present in the superconductor within a thin layer of thickness about λ_L. The London penetration depth λ_L is the decay constant, so it defines the distance at which the magnetic field reaches $1/e$ of its value at $x = 0$. The magnetic field is allowed to penetrate in the surface region because the super-currents are not able to screen it completely. Indeed both the magnetic field and the super-currents exist into the material for a length defined by the London penetration depth [2,3].

From the equation 1.23 it is possible to notice that λ_L depends on super-electron density n_s, which introduces a temperature dependence that can be defined ,with a good approximation, as:

$$\lambda(T) = \frac{\lambda(0)}{\left[1 - \left(\frac{T}{T_C}\right)^4\right]^{1/2}} \tag{1.29}$$

1.2.2 Surface Impedance In Two Fluid Model

Taking into account the first London equation, Equation 1.22, and solving for the case of RF currents $J_s = J_{s,0} e^{i\omega t}$, the superconducting current density can be defined as:

$$\bar{\mathrm{J}}_{\mathrm{s}} = -\frac{i}{\omega \mu_0 \lambda_L^2} \bar{E} = -\mathrm{i}\sigma_{\mathrm{s}} \bar{E} \tag{1.30}$$

and the two fluid currents become:

$$J = J_n + J_s = (\sigma_1 - i\sigma_2) E \tag{1.31}$$

where the real and the imaginary part of the conductivity are defined as:

$$\sigma_1 = \frac{n_n e^2 \tau}{m(1+\omega^2\tau^2)} \qquad \sigma_2 = \frac{n_s e^2}{m\omega} + \frac{n_n e^2 (\omega\tau)^2}{m\omega(1+\omega^2\tau^2)} \tag{1.32}$$

it means that σ_1 is related to the normal fluid and σ_2 is related to both the super fluid and the normal fluid. A schematic representation of the superconductor admittance is shown in Figure 1.6 in which the normal fluid is represented as an inductance and a resistance put in parallel, whereas the super-fluid is represented as an inductance. The two fluid components are also put in parallel and it is possible to notice that for $\omega = 0$ the normal electrons resistance is short-cut by the inductance of both the normal and super currents. Under this condition the current can flow freely without resistance. On the other hand for $\omega \neq 0$ both the inductive and the resistive contributions generate current losses.

So that for normal conductors the relaxation time τ is much smaller than the RF period, it is possible to use the approximation $\omega\tau \ll 1$, finding:

$$\sigma_n = \frac{n_n e^2 \tau}{m} \qquad \sigma_s = \frac{n_s e^2}{m\omega} \tag{1.33}$$

Now using the Maxwell equation as in the previous section, it is possible to define:

$$\nabla^2 \mathrm{E} = \mu_0 \omega \mathrm{i}(\sigma_n - i\sigma_s)\mathrm{E} = \tau_{\mathrm{tot}}^2 \mathrm{E} \tag{1.34}$$

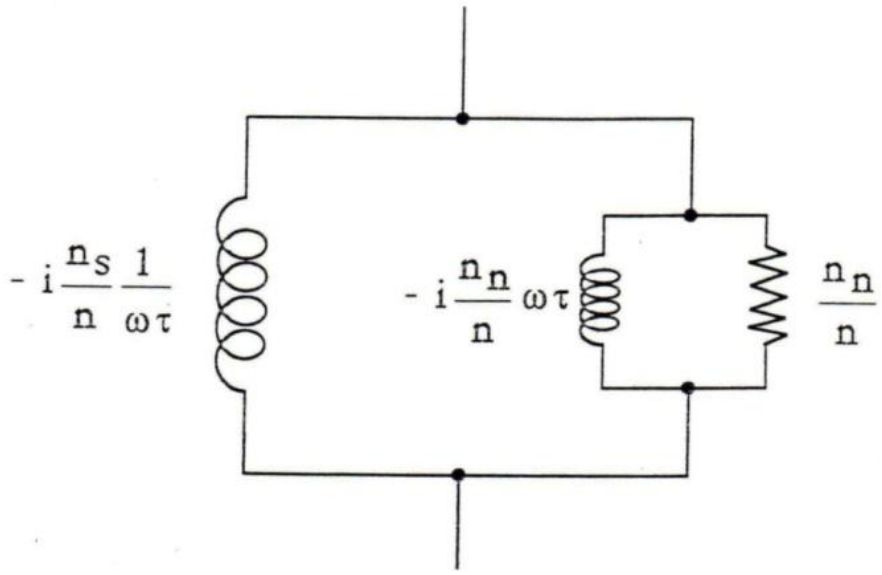

FIGURE 1.6 - SUPERCONDUCTOR ADMITTANCE CIRCUIT.

which allows to obtain the superconductor surface impedance in two fluid model approximation:

$$Z_S = \frac{E_0}{J_0/\tau_{tot}} = \frac{\tau_{tot}}{\sigma} = \sqrt{\frac{i\omega\mu_0}{\sigma_n - i\sigma_s}} \tag{1.35}$$

Making the approximation $\sigma_n \ll \sigma_s$, i.e. the conductivity of the normal fluid is much smaller than the conductivity of super-fluid, the real and the imaginary part of the impedance becomes:

$$R_s = \frac{1}{2}\sigma_n \omega^2 \mu_0^2 \lambda_L^3 \qquad X_s = \omega\mu_0\lambda_L \tag{1.36}$$

the superconductor surface resistance depends on the frequency, the normal fluid conductivity and the London penetration depth in which the temperature dependence is contained. The surface resistance depends on the normal conducting properties, in particular it shows a proportionality with the relaxation time τ which is directly proportional to the mean free path. So the surface resistance increases with the mean free path.

1.2.3 London and Pippard Superconductors

The London's equations came from a local model in which the super-current density $\bar{J}_s$ is related to the vector potential $\bar{A}$ at the same point.

A general non-local relation between the super-current density $\bar{J}_s$ and the vector potential $\bar{A}$ can be find using the Chamber's integral:

$$\bar{J}_s(\bar{r}) = \int_{\xi} \hat{Q}(\bar{r} - \bar{r}')\bar{A}(\bar{r}') \cdot d\bar{r} \tag{1.37}$$

where $\hat{Q}$ is an operator which converts the vector potential $\bar{A}$ into $\hat{Q}\bar{A}$ and it is nonzero only for $|\bar{r} - \bar{r}'| \leq \xi_0$, ξ_0 is the coherence length, i.e. the length in which the charge carriers operate coherently.

It is easy to note that only if $\bar{A}(\bar{r}')$ is constant within ξ this integral approaches to London result. So it means that when the characteristic length over which the vector potential changes is lower than the coherence length the London model is not valid anymore. In other worlds when the coherence length ξ_0 is much smaller than the penetration depth a λ non-local model becomes necessary.

Pippard proposed a non-local model based on the Chamber's integral shown in the Equation 1.28, he found that the penetration depth increases by decreasing the electronic mean free path, Figure 1.7, as it happens for example increasing the impurities concentration in the material.

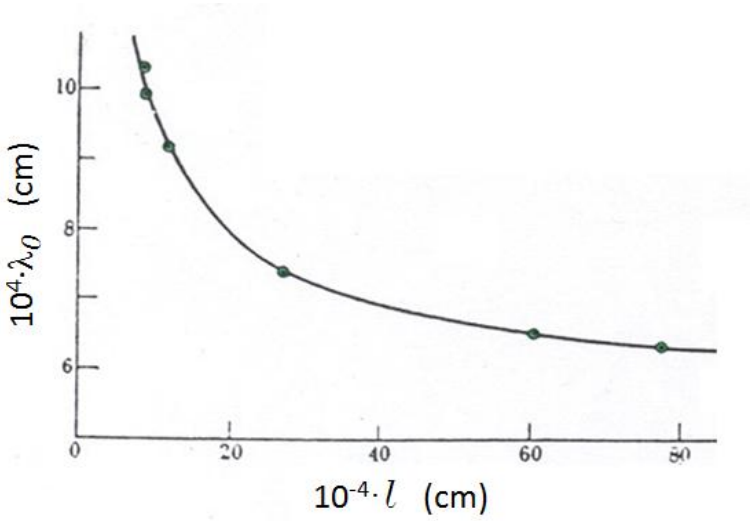

FIGURE 1.7 - PENETRATION DEPTH AS A FUNCTION OF MEAN FREE PATH.

Unlike for the London's model in which the penetration depth depends only on the applied field, for the Pippard's non-local model the penetration depth can depend on the mean free path in accordance with experimental results. In order to introduce this dependence the effective length of coherence ξ is defined by the empirical equation:

$$\frac{1}{\xi} = \frac{1}{\xi_0} + \frac{1}{l} \tag{1.38}$$

where ξ_0 is the coherence length of the pure metal, and l is the electronic mean free path; the equation shows that the coherence length increases with a large density of defects. The effective penetration depth is also defined:

$$\lambda_{eff} = \lambda_L \left(\frac{\xi_0}{\xi}\right)^{1/2} = \lambda_L \left(1 + \frac{\xi_0}{l}\right)^{1/2} \tag{1.39}$$

Superconductors with $\lambda \ll \xi$ are called Pippard's superconductors, or first type superconductors, whereas superconductors with $\lambda > \xi$ are called London's superconductors or second type superconductors. The schematic rapresentation of thedifference between these two categories is dispayed in Figure 1.8.

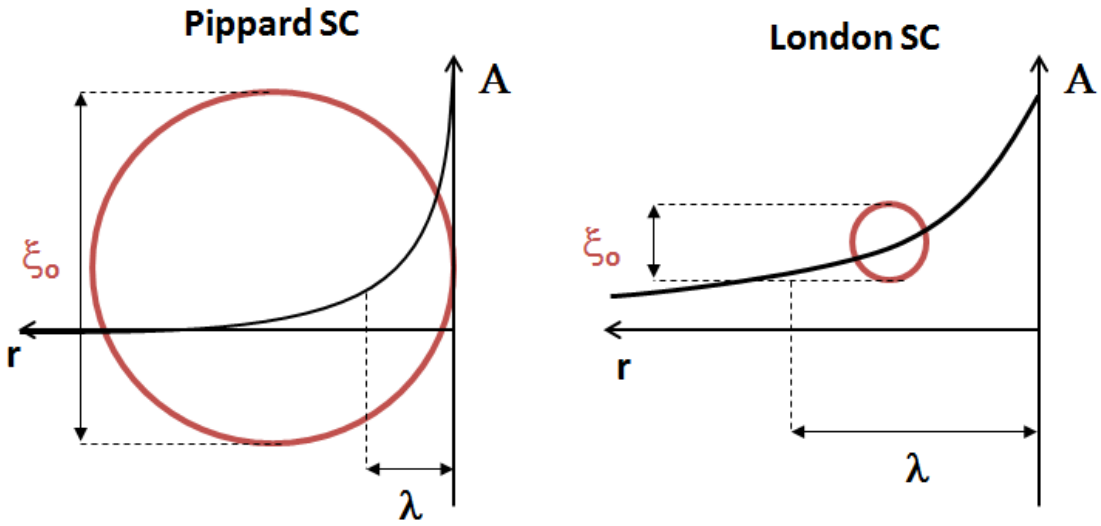

FIGURE 1.8 - SCHEME OF PIPPARD AND LONDON SUPERCONDUCTOR.

The limit between first type and second type superconductors is easily found using the *Ginzburg-Landau parameter*, defined as: $K_{GL} = \lambda/\xi$. Indeed it is possible to use the following assumption:

$$\begin{aligned} K_{GL} &< \frac{1}{\sqrt{2}} \quad \rightarrow \quad I\ type\ SC \\ K_{GL} &> \frac{1}{\sqrt{2}} \quad \rightarrow \quad II\ type\ SC \end{aligned} \tag{1.40}$$

Observing the Ginzburg-Landau parameter one notices that first type superconductor can become more and more of second type by adding even more impurities.

The first and the second type superconductors show different behaviur even regarding the phase transition. Indeed the I type superconductors have an abrupt transition in which the material passes from the normal state to Meissner state when it reaches $T < T_C$; on the other hand the II type superconductors have two different critical magnetic fields, the lower critical field H_{C1} and the upper critical field H_{C2}. For $H < H_{C1}$ the material is completely in its superconductor state and for $H > H_{C2}$ it is completely in its normal-conductor state. When the external magnetic field is in between these critical parameters an intermediate state called *mixed state* appears and the material presents both normal- conducting and superconducting zones.

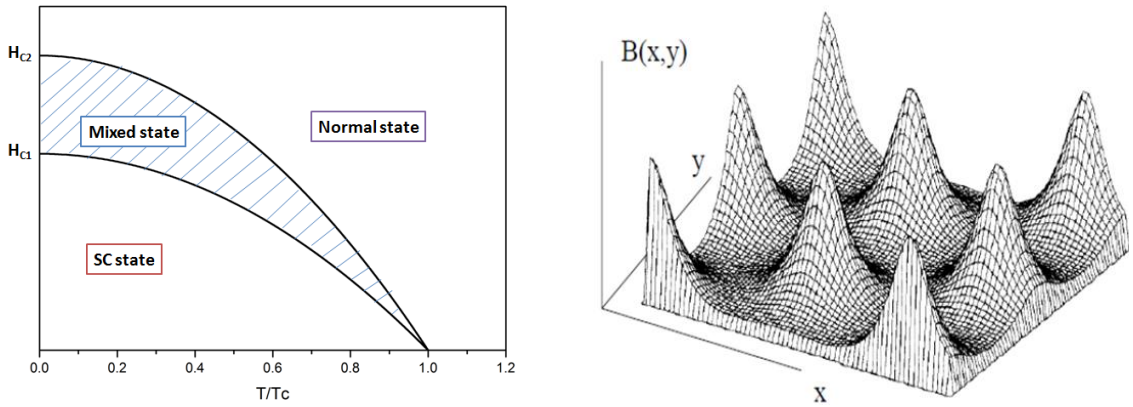

(A) (B)

FIGURE 1.9 - II TYPE SUPERCONDUCTOR: (A) MAGNETIC FIELD VERSUS TEMPERATURE, (B) VORTEX FLUX.

As one can see from Figure 1.9 (A) the mixed state needs a presence of an external magnetic field H, and whether there is this field, two different critical temperatures can be also defined. The mixed state is characterized by the penetration of the magnetic field inside microscopic normal-conducting filament futures surrounded by superconductive zone. Such filaments are called vortexes or fluxons, Figure 1.9 (B), and they are disposed according to an exagonal lattice. Because of this partial penetration of the magnetic field the mixed state does not show a perfect diamagnetic properties.

The normal-conductive core of the vortex contains one quantum of magnetic flux ϕ_0 supported by the supercurrents that flow around the vortex itself. The currents are much stronger close to the vortex axis, that is always parallel to the external magnetic flux. Increasing the distance the current intensity decreases as long as it become lower than the critical value. Indeed beyond this distance one arrives at the superconducting region. The magnetic flux is quantized in an integer numbers of a unitary quantity ϕ_0:

$$\phi_0 = \frac{hc}{2e} \cong 2 \cdot 10^{-7} Gauss \cdot cm^2 \tag{1.41}$$

the presence of a factor 2 suggests that the superconducting currents are carried by electron pairs intead by a single electron.

If a superconductor is driven by a current $\bar{J} > \bar{J}_C$, the vortexes will move perpendicular to $\bar{J}$ because of the Lorentz force:

$$\bar{F}_L = \bar{J} \times \bar{\phi}_0 \tag{1.42}$$

this motion is called *vortexes flux flow* and it causes energy losses. This situation can be controlled by the presence of the defects in the material, indeed these can link the vortexes,

putting them into a minimum of the Gibbs free energy. This linking of the vortexes is called *pinning* and thanks to this phenomenon the current can run without dissipation, if the pinning force is higher than the Lorentz one [4].

1.3 MICROSCOPIC THEORY OF SUPERCONDUCTIVITY

The microscopic theory of superconductivity was developed by Bardeen, Cooper and Schrieffer in 1957 and it was called BCS theory.

In 1950 it was found that the critical temperature is different considering a superconducting metal composed by different isotopes:

$$T_C \propto M^{\alpha} \tag{1.43}$$

where M is the mass of the isotope and α for the majority of superconducting elements is close to 0.5. This dependence is called *isotopic effect* and so if the ions mass change only the characteristics of the lattice vibrations, it suggests that superconductivity is not only an electronic phenomenon but it depends also on phonons. Later studies have demonstrated that electros and phonons can interact generating an additional interaction between electrons.

Let us taking into account the interactions between electrons and phonons, Figure 1.10. Considering a free electron that is moving in a crystal within a wave vector $\bar{k}_1$, this electron at some point can excite a lattice vibration, i.e. it can decay in a phonon with wave vector $\bar{q}$ and in an electron with wave vector $\bar{k}_1{}'$:

$$\bar{k}_1 = \bar{k}_1' + \bar{q} \tag{1.44}$$

The phonon $\bar{q}$ can immediately interact with another electron $\bar{k}_2$ causing their annihilation with a production of an electron with a wave vector $\bar{k}_2{}'$:

$$\bar{k}_2 + \bar{q} = \bar{k}_2' \tag{1.45}$$

So the entire process can be summarized as:

$$\bar{k}_1 + \bar{k}_2 = \bar{k}_1' + \bar{k}_2{}' \tag{1.46}$$

From this equation it is clear that the process is actually an electron-electron interaction in which two electrons from their states $\bar{k}_1$ and $\bar{k}_2$ ends up to the states $\bar{k}_1'$ and $\bar{k}_2{}'$. It is important to underline that such a situation can happened also at $T = OK$, indeed it does not presuppose a initial presence of a phonon.

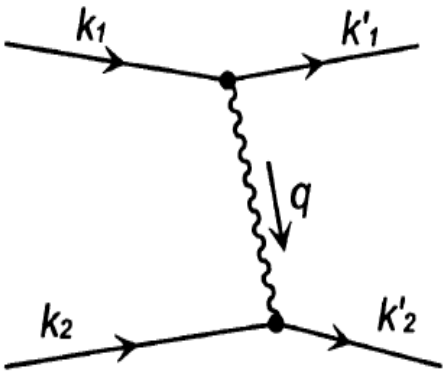

FIGURE 1.10 - DIAGRAMS OF ELECTRON-ELECTRON INTERACTION MEDIATED BY A PHONON.

When the electron wave vector changes from $\bar{k}_1$ to $\bar{k}_1{}'$ the local electron density increases so the surrounding ions are attracted and they start to move toward it. Because of their large mass the movement of the ions will continue also after that the charge compensation arises, creating a local positive charge excess and attracting, as a consequence, the second electron $\bar{k}_2$. So an electron-electron attraction arises but such attraction can happen only whether the frequency of the electron density oscillations is less than the Debye frequency ω_D:

$$\omega = \frac{\varepsilon(\bar{k}_1) - \varepsilon(\bar{k}_1{}')}{\hbar} < \omega_D \tag{1.47}$$

Indeed the Debye frequency is the maximum possible frequency for lattice vibration in a crystal.

The BCS theory asserts that: *Electrons with energies that differ from the Fermi energy by no more than* $\hbar\omega_D$ *are attracted to each other*. The rest of the electrons do not interact. So the electron interaction can be written as:

$$\left|\bar{\varepsilon}(\bar{k}) - \varepsilon_F\right| \leq \hbar\omega_D \qquad \left|\bar{\varepsilon}(\bar{k}') - \varepsilon_F\right| \leq \hbar\omega_D \tag{1.48}$$

where ε_F is the Fermi energy. Thus only the electrons that occupy the states within a narrow spherical layer of thickness $2\Delta k$ near the Fermi surface can experience mutual attraction and the thickness $2\Delta k$ depends on the Debye energy.

Note that the electrons are allowed to scatter from the state $\bar{k}$ to the state $\bar{k}'$ only if before the scattering event the state $\bar{k}$ is full while the state $\bar{k}'$ is empty. Such interaction can occur also at $T = 0K$ because for a superconductor the minimum of energy at $T = 0K$ corresponds to a situation in which the Fermi surface is outspread: some states below the Fermi energy are occupied whereas some states above it are empty. This spread covers an energy interval about

$2\Delta_0$. Then the states are filled up in pairs: the state $\bar{k}$ becomes occupied only if also the state $-\bar{k}$ becomes occupied, and vice versa for the empty states. The electrons that interact with each other must have opposite momentum [5].

Analyzing the electron-electron interaction using the quantum-mechanics perturbation theory it was found that this interaction is independent of $\bar{k}$, thus it follows a spherical symmetry which can occur only in a state with orbital momentum equal to zero: $l = 0$. It means that the interacting electrons have the same spatial wave function, so since electrons are Fermi particles their total wave function has to be antisymmetric, so they must have different spin. Such electron bond pair, where the electrons have opposed spin and momentum, is called Cooper pair [2].

The Cooper pairs are bosons and so they condense into a common ground state. This stable ground state E_{GS} is below the Fermi energy E_F and the energy difference between these quantities defines Δ: $\Delta = E_F - E_{GS}$. The energy gap $2\Delta(T)$ appears between the bosonic ground state and the normal conducting energy level. At $T = 0K$ all electrons are coupled in Cooper pairs and by increasing the temperature the pairs are gradually broken and the electrons start to fill the energy levels above the gap Figure 1.11. Once T_C is reached all pairs are broken into normal electrons and Δ disappears [4].

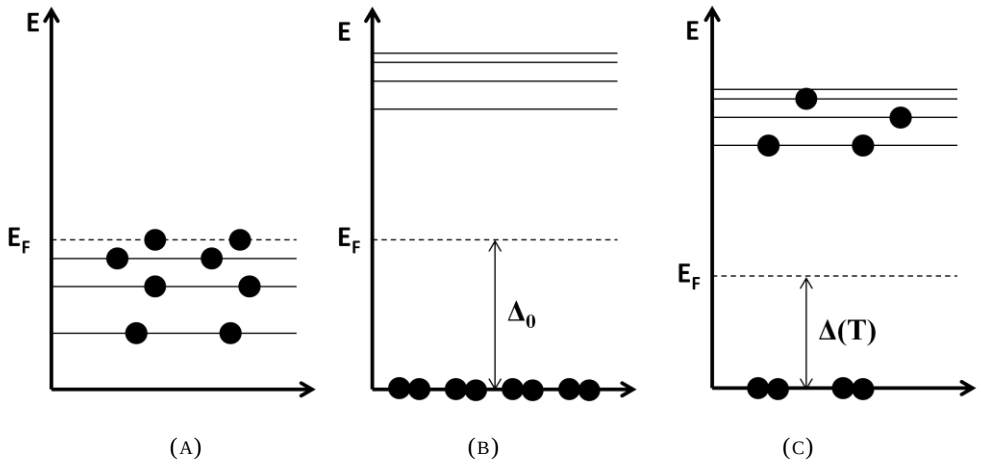

FIGURE 1.11 - ENERGY SPECTRUM FOR A NORMAL CONDUCTOR (A) AND FOR A SUPERCONDUCTOR FOR $T = 0K$ (B) AND FOR $T < T_C$ (C).

So in order to break a Cooper pair one needs at least an energy equal to the energy gap $2\Delta_0$.

Let us consider the one-electron excitation spectrum [5,6], shown in Figure 1.12 (a). It displays the energy of an elementary excitation, E_k, that is how much the energy increases after one electron with momentum $\bar{k}$ is added to a superconductor:

$$E_k = \sqrt{\frac{\hbar^2}{2m}(k^2 - k_F^2) + \Delta_0^2} \tag{1.49}$$

where k_F is the Fermi wave vector. From the graph is easy to recognize that the energy levels of the elementary excitations become denser at $E_k \to \Delta_0$. The density of states of the superconductor can be defined as:

$$\rho(E) = N(0)\frac{E}{\sqrt{E^2 - \Delta_0^2}} \tag{1.50}$$

where $N(0)$ is the density of states at the Fermi level. The equation shows a singularity at the gap edge, in which $\rho(E) \to \infty$, as is shown in Figure 1.12 (b).

As it was seen before, the electrons involved in the Cooper pairs are those within an energy range $2\Delta k \sim k_B T_C$ of the Fermi energy. This energy can be written as:

$$k_B T_C = \delta\left(\frac{p^2}{2m}\right) = \frac{p}{m}\delta p = v_F \delta p \tag{1.51}$$

Then the momentum spread of electron that is attending the pairing interaction can be defined as:

$$\delta p = \frac{k_B T_C}{v_F} \tag{1.52}$$

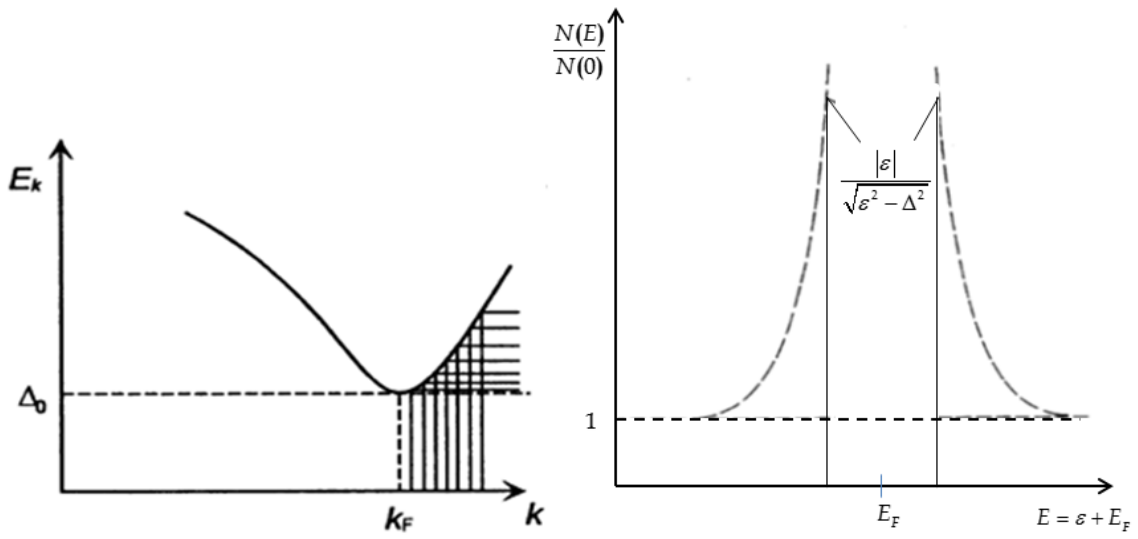

(A) (B)

FIGURE 1.12 - (A) ONE ELECTRON EXCITATION SPECTRUM, (B) BCS DENSITY OF STATE AS A FUNCTION OF ENERGY, NEAR THE FERMI ENERGY.

Resorting now the Heisenberg's uncertainty principle, it is possible to find out the spatial extend of the Cooper pair, that is the coherence length ξ_0:

$$(\xi_0)(\delta p) \approx \hbar \qquad \xi_0 \sim \frac{\hbar v_F}{k_B T_C} \tag{1.53}$$

For Niobium the coherence length is $\xi_0 \sim 39nm$, this length is quite large compared to inter-atomic distances and it means that the superconducting electrons own a long-range order. So ξ_0 is a macroscopic distance, as a proof that the Cooper pairs show a Bose statistics in which the interacting electrons form a unique macroscopic state [3].

The BCS theory predicts also that the pairing energy Δ_0 has to be in the order of magnitude of the critical temperature T_C. These two quantities are indeed defined as:

$$\Delta_0 \approx 2\hbar\omega_D e^{-1/N(0)V} \qquad k_B T_C \approx 1.13\hbar\omega_D e^{-1/N(0)V} \tag{1.54}$$

where V is the potential of the actractive interaction [7]. Comparing these equations one obtains:

$$\Delta_0 \approx 1.76 \cdot k_B T_C = \frac{\mathrm{s}}{2} k_B T_C \tag{1.55}$$

where and the coherence length can be also written in terms of Δ_0 as:

$$\xi_0 \approx 1.76 \frac{\hbar v_F}{\Delta_0} \tag{1.56}$$

As discussed before, the energy gap Δ_0 is temperature dependent, for temperature close to $0K$, i.e. for $T \ll T_C$, the BCS theory finds:

$$\Delta(T) \sim \Delta_0 - (2\pi\Delta_0 k_B T)^{1/2} e^{-\Delta_0/k_B T} \tag{1.57}$$

the exponential variation is very small since $e^{-\Delta_0/k_B T} \approx 0$; so Δ remains nearly constant until a significant number of electrons are excited . On the other hand for temperatures close to T_C $\Delta(T)$ decreases quickly to zero and the dependence for $T \approx T_C$ can be approximated as:

$$\frac{\Delta(T)}{\Delta_0} \sim 1.74 \cdot \left(1 - \frac{T}{T_C}\right)^{1/2} \tag{1.58}$$

In regard of these two formulas the entire dependence is sketched in Figure 1.13. By the way, a useful approximation to the theoretical behavior for $\Delta(T)$ from $0K$ to T_C is given by:

$$\frac{\Delta(T)}{\Delta_0} = \left[cos\left(\frac{\pi t^2}{2}\right)\right]^{1/2} \tag{1.59}$$

where $t = T/T_C$ is the reduced temperature.

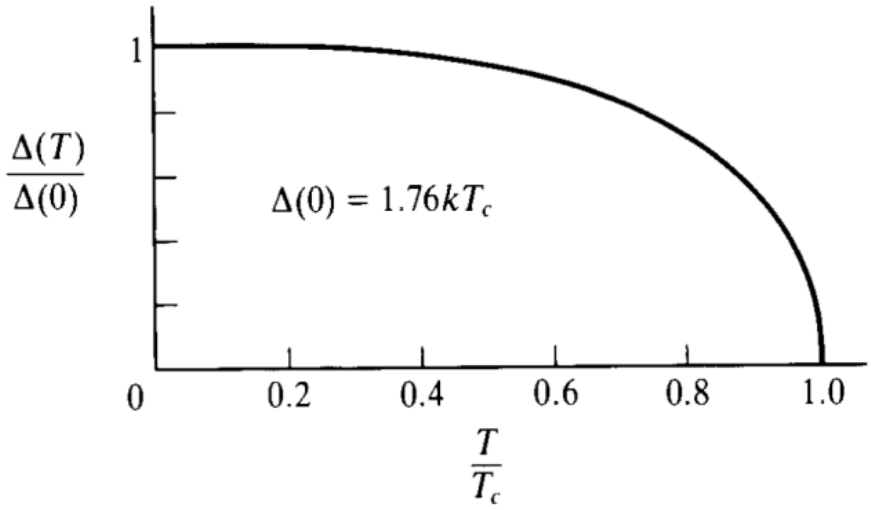

FIGURE 1.13 - TEMPERATURE DEPENDENCE OF THE ENERGY GAP.

1.3.1 BCS ELECTRODYNAMICS OF SUPERCONDUCTORS

Let us recall the surface impedance found for a normal metal, Equation 1.11:

$$Z = R - iX = (1 - i)\sqrt{\frac{\mu\omega}{2\sigma_n}} \tag{1.60}$$

it was found by [8] that this result can be easily extended to the superconductor case replacing the normal conductivity σ_n with a complex conductivity $\sigma = \sigma_1 - i\sigma_2$.

The real part of the conductivity, in the normal skin effect regime $(\hbar\omega \ll 2\Delta)$ can be defined as:

$$\frac{\sigma_1}{\sigma_n} = \frac{2\Delta}{k_B T}\frac{e^{-\Delta/k_B T}}{(1 + e^{-\Delta/k_B T})} ln\left(\frac{\Delta}{\hbar\omega}\right) \tag{1.61}$$

$$\frac{\sigma_2}{\sigma_n} = \frac{\pi\Delta}{\hbar\omega} tanh\left(\frac{\Delta}{2k_B T}\right) \tag{1.62}$$

Where σ_1/σ_n is due to the quasi-particles that are thermically excited or exited by photons interaction, i.e. the Cooper pair broken after the exchange of the energy $\hbar\omega$. On the other hand the term σ_2/σ_n considers only the Cooper pair generation

The temperature dependence of σ_1/σ_n and σ_2/σ_n is shown in Figure 1.14. As expected the contribution of the normal-electrons σ_1/σ_n is equal to 1 at $T = T_C$ and it decreases by decreasing the temperature zeroing itself for $T = 0K$.

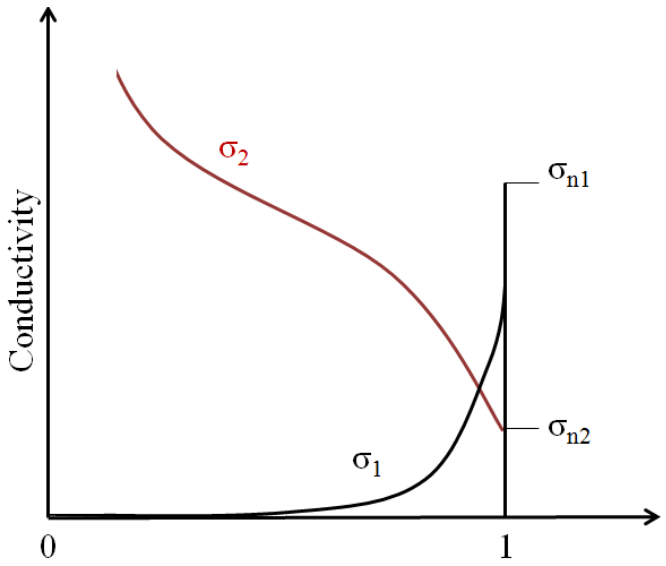

FIGURE 1.14 - TEMPERATURE DEPENDENCE OF THE REAL AND THE IMAGINARY PART OF THE CONDUCTIVITY.

The inductive contribution of both the normal and the super-electrons is defined into σ_2/σ_n which increases by decreasing the temperature, reaching the maximum value for $T = 0K$, whereas it defines only the normal electrons inductive contribution for $T = T_C$.

Studying the superconductor surface impedance by using these results, it is possible to define the BCS resistance as:

$$R_{BCS}(\omega, T) = A{\rho_n}^{1/2}\omega^2 ln\left(\frac{\Delta}{\hbar\omega}\right)\frac{e^{-\Delta/k_BT}}{T\sqrt{sT_c}(1+e^{-\Delta/k_BT})^2} \cong \frac{A'\omega^2}{T}e^{-\Delta/k_BT} \qquad (1.63)$$

where A is a constant value which depends on the material parameters (Fermi velocity, London penetration depth, coherence length, electrons mean free path), for Niobium $A \approx 6 \cdot 10^{-21}(\Omega K^3/ms^4)^{1/2}$. The BCS result shows that a good superconductor, with small R_{BCS}, must have good electrical properties in the normal-conducting state, i.e. small ρ_n. The exponential temperature dependence suggests that by decreasing the temperature also the superconductor BCS resistance decreases. Moreover taking into account the direct proportionality between Δ and T_c one finds that the ratio T_c/T must be maximized in order to minimize R_{BCS}. In addition is

important to underline that R_{BCS} increases by increasing the angular frequency ω of the external field, so the losses are higher whether the material is exposed to higher frequency field.

Comparing this result with the experimental one, Figure 1.15, one can see that up to a certain temperature the BCS resistance fits the observed surface resistance data, whereas below certain temperature the surface resistance approaches a constant value. This means that the surface resistance R_S is actually given by the sum of the BCS resistance $R_{BCS}(T)$ and the so-called residual resistance R_0 which is temperature independent:

$$R_S = R_{BCS}(T) + R_0 \tag{1.64}$$

There are many different causes of the residual resistance. Examples of the main causes are: the non ideality of the surface, the presence of an oxidized layer on the surface or within the grain boundary, the presence of defects in the superconductor penetration depth region, the trapped magnetic flux inside the superconductor, the presence of the interstitial hydrides , and so on.

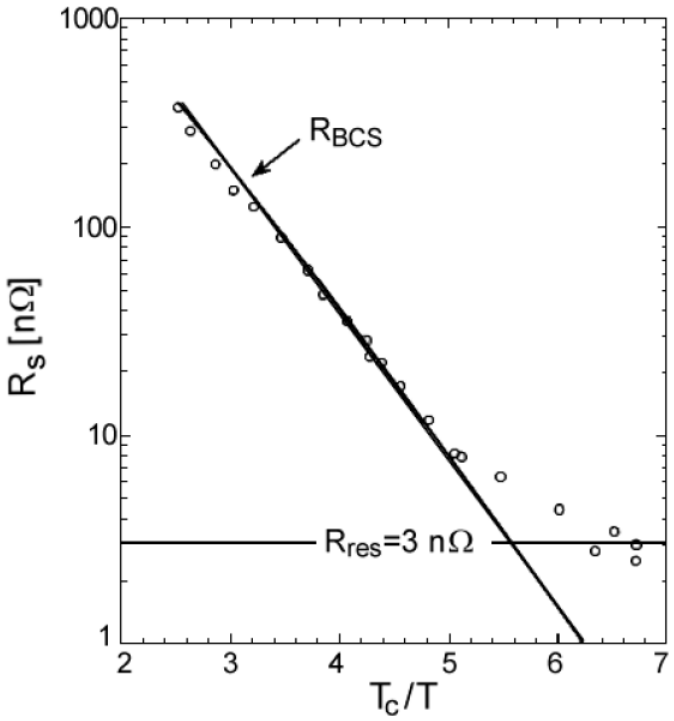

FIGURE 1.15 - SURFACE RESISTANCE VERSUS TEMPERATURE.

The BCS theory calculates also the penetration depth behavior in the local limit, where the electromagnetic field has no large variation in space, so the coherence length is much smaller than the penetration depth: $\xi_0 \ll \lambda$. In the presence of a vector potential $\bar{A}$ the velocity of the charge carriers is given by the two terms:

$$\bar{v} = \frac{\bar{p}}{m} - \frac{e\bar{A}}{mc} \tag{1.65}$$

so the current induced in the superconductor can be also divided in two terms, $\bar{J}_1$ and $\bar{J}_2$. $\bar{J}_1 \propto \bar{p}/m$ is the paramagnetic current part and it reduces the diamagnetic current $\bar{J}_2 = ne^2\bar{A}/mc$ which is responsible to the electromagnetic shielding. One can easily notice that $\bar{J}_2$ corresponds to the London equation.

The penetration depth behavior as a function of temperature is given by the thermal excitation of the Cooper pairs and only near the critical temperature T_C the effects of the electromagnetic field excitation become relevant. Thus $\lambda(\omega, T) \cong \lambda(T)$ can be evaluated by studying the behavior of the two current terms $\bar{J}_1$ and $\bar{J}_2$ under this approximation, leading to:

$$\frac{1}{\lambda^2(T)} = \frac{1}{\lambda^2(0)}\left(1 - 2\int_{\Delta}^{\infty} -\frac{\partial f(E)}{\partial E} g^{\pm}(E)dE\right) \tag{1.66}$$

where $f(E)$ is the Fermi-Dirac distribution:

$$f(E) = \frac{1}{1 + e^{E/k_B T}} \tag{1.67}$$

and $g(E)$ is the density of states:

$$g^{\pm}(E) = \frac{(E^2 + \Delta^2 + \hbar\omega)}{[\pm(E^2 - \Delta^2)^{1/2}] \cdot [(E + \hbar\omega)^2 - \Delta^2]^{1/2}} \tag{1.68}$$

in the normal state for $\Delta = 0$, the integral reduces to $f(0) = 1/2$, so the paramagnetic currents compensate completely the diamagnetic ones and the Meissner effect does not appear. For superconducting state $\Delta \neq 0$ and the two terms do not balance completely each other leading to a finite value of penetration depth [7]. Increasing the temperature the integral becomes smaller and smaller, so for $T \to 0$ one finds the value $\lambda(0)$.

For $T/T_C > 0.8$ this equation can be approximated with the results found by the two fluid model:

$$\frac{1}{\lambda^2(T)} = \frac{1}{{\lambda_0}^2}\left[1 - \left(\frac{T}{T_C}\right)^4\right] \tag{1.69}$$

where in general λ_0 is not equal to the penetration depth at zero temperature $\lambda(0)$. Whereas for $T/T_C < 0.5$ the equation reduces to:

$$\lambda(T) = \lambda(0)\left(1 + \sqrt{\frac{\pi\Delta}{2k_BT}}\, e^{-\Delta/k_BT}\right) \tag{1.70}$$

where the exponential behavior is the signature of the energy gap Δ.

Chapter 2

ACCELERATING CAVITIES

Resonant cavities play an essential role in accelerators, allowing particles being accelerated. The efficiency of such devices is increased by using superconducting materials which implies low surface resistance values. In the optics to reach high gradient with low power consumption the implementation of superconducting materials is mandatory. The RF behavior of a cavity is similar to a resonance RLC circuit and, depends on the geometrical properties of the cavity, certain kind of mode useful for the acceleration can be excited. Nowadays the challenge is to find an alternative technology to bulk Niobium able to give at least the same performance. For this reason the chapter ends up showing the state of the art of Niobium thin film on Copper cavities technology.

2.1 RADIOFREQUENCY CAVITIES

2.1.1 RESONANT CAVITIES AS ACCELERATING STRUCTURE

A resonant cavity is a device capable to store energy in the form of microwave electromagnetic energy. The RF frequency range of such device is between $50MHz$ and $6GHz$.

Radiofrequency accelerating cavities are the key component of the modern particle accelerators. The RF field stored into the resonators allows to accelerate charged particles, these can reach small fraction of speed of light (as heavy-ions) or velocity near the speed of light (as electrons, positrons, protons, and so on). Indeed at each passage through one cavity the particle gain a finite energy. If many cavities are present, particle beam gains energy progressively due to each member of the chain.

A resonant cavity is equivalent to a classical RLC resonant circuit where the resonant frequency ω_0 is defined as:

$$\omega_0 = \frac{1}{\sqrt{LC}} \tag{2.1}$$

and in order to understand well the properties of this resonator, the '*pill-box cavity*' is analyzed.

The pill-box cavity is the simplest resonator, such cavity is simplified as a hollow cylinder, as is shown in Figure 2.1, and when the beam holes are neglected the spatial distribution of the electromagnetic field can be calculated analytically.

Considering a perfect conductor, the electromagnetic field, near the surface of the conductor, has to satisfy the boundary conditions:

$$\hat{n} \times \bar{E} = 0 \qquad \hat{n} \cdot \bar{H} = 0 \tag{2.2}$$

the electric field must be perpendicular to the surface whereas the magnetic field must be parallel to it.

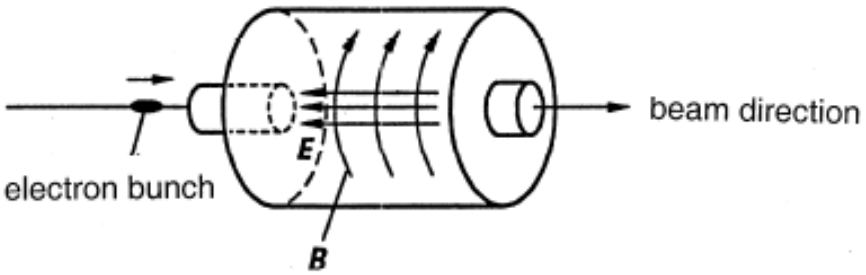

FIGURE 2.1 - ELECTROMAGNETIC FIELD IN A PILL-BOX CAVITY FOR A TM010 MODE.

Assuming an electric field with a temporal dependence: $E(t) = E_0 e^{i\omega t}$, it generates a concatenated magnetic field in according with Maxwell's equation:

$$\oint_{\Gamma_1} \bar{B} \cdot d\bar{s} = \frac{1}{c^2} \frac{\partial}{\partial t} \int_{S_1} \bar{E} \cdot \hat{n}\, dS_1 \quad , \quad B(t) = \frac{i\omega r}{2c^2} E_0 e^{i\omega t} \tag{2.3}$$

the intensity of this magnetic field increases with the distance r from the center of the pill-box. According to the Faraday-Lentz's law, a time-dependent magnetic field generates in turn an electric field which opposes itself from the generating field:

$$\oint_{\Gamma_2} \bar{E} \cdot d\bar{s} = -\frac{\partial}{\partial t} \int_{S_2} \bar{B} \cdot \hat{n}\, dS_2 \qquad -E_1(r)h = -h \frac{\partial}{\partial t} \int_{S_2} B(r)\, dr \tag{2.4}$$

Also this electric field has a temporal variation and it is able to generate a concatenated magnetic field and so on. The fields distribution are sketched in Figure 2.2.

Therefore, the field can be described as a series where the field contributions decrease gradually, and the real field inside the cavity is the value of convergence of the series:

$$E_z(r,t) = E_0 e^{i\omega t} J_0\left(\frac{\omega r}{c}\right) \tag{2.5}$$

$$J_0(x) = \left[1 - \frac{1}{(1!)^2}(x)^2 + \frac{1}{(2!)^2}(x)^4 + \frac{1}{(3!)^2}(x)^6 + \cdots\right] \quad , \quad x = \left(\frac{\omega r}{c}\right) \tag{2.6}$$

where $J_0(x)$ is the zero-order Bessel function; the shape of the electric field $E(r)$ is showed in Figure 2.3.

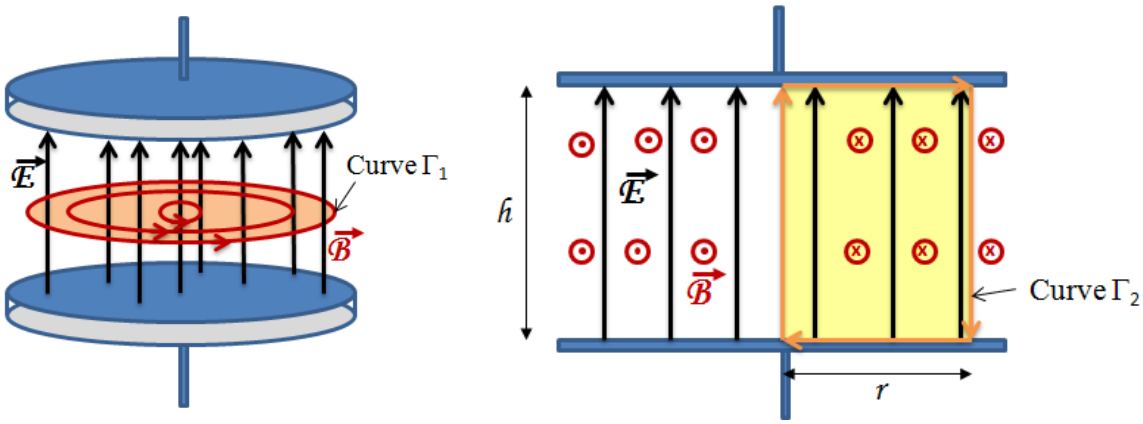

(A) (B)

FIGURE 2.2 - SKETCH OF THE ELECTRIC AND MAGNETIC FIELD DISTRIBUTION IN A PILL-BOX CAVITY EXCITED IN A TM_{010} MODE. IN (A) IT IS UNDERLINED THE SURFACE S_1 IN WHICH THE ELECTRIC FIELD PASSES THROUGH AND IN (B) THE PLANE S_2 IN WHICH THE MAGNETIC FIELD FLUX IS DEFINED.

In order to do not have any electric field on the resonator walls, the walls must be fixed in correspondence to one node of the Bessel function. From the 2.7 it is evident that the resonance frequency depends on which node n_i is chosen, but it is independent of the cavity length. Fixing the walls to the first node the trend of the electric and magnetic field is shown in Figure 2.3 (b,c) , and the resonance frequency is equal to:

$$\omega_{0,i} = \frac{n_i c}{a} \qquad \omega_{0,1} = 2.405\frac{c}{a} \tag{2.7}$$

where a is the pill-box radius. This particular configuration is called *transverse magnetic 010 mode* (TM_{010}). The TM mode is usually chosen for the acceleration because along the beam axis the electric field reaches its maximum value whereas the magnetic field has its minimum value. The TM_{010} mode is also usually preferred because has the lowest *eigenfrequency*. On the other hand the *transverse electric modes* (TE) cannot be used in particle acceleration because they have no longitudinal electric field.

Let us now define the accelerating field E_{acc}, that is the field used to accelerate the particles in the accelerator. Considering an electron which is travelling closed to the speed of light c and that enters into the cavity at time $t = 0$, and lives at time $t = d/c$, the condition of maximum acceleration of such electron is the following:

$$t = \frac{d}{c} = \frac{1}{2}T_{RF} = \frac{\pi}{\omega_0} \tag{2.8}$$

namely the time in which the electron passes through the cavity is equal to half an RF period T_{RF}. Since the electric field that is seen by the electron, E_{el}, points always in the same direction, the accelerating voltage is given by:

$$V_{acc} = \left| \int_0^d E_{el}\, dz \right| \tag{2.9}$$

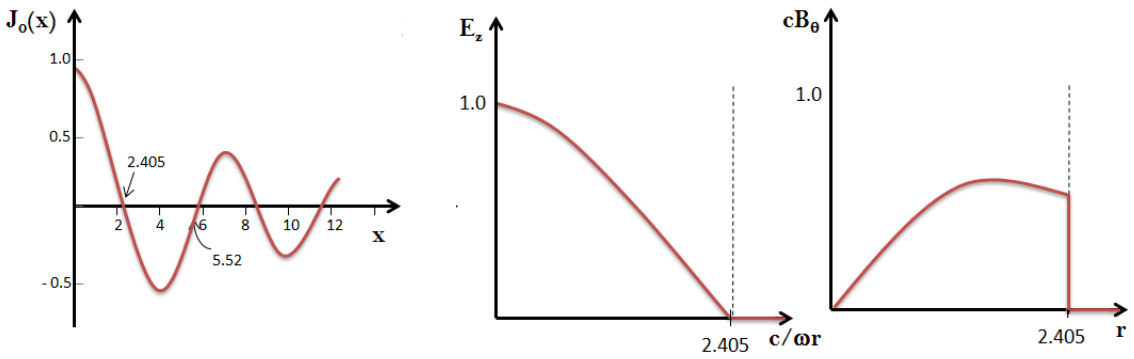

(A) (B)

FIGURE 2.3 - (A) FIRST ORDER BESSEL FUNCTION OF THE CURRENT DENSITY VERSUS CAVITY LENGTH. (B) ELECTRIC AND MAGNETIC FIELD TREND IN A TM_{010} PILL-BOX CAVITY.

Using $t(z) = z/c$ the electric field seen by electron can be defined as: $E_{el} = E_z(z)e^{i\omega z/c}$, so:

$$V_{acc} = \left| E_0 \int_0^d e^{i\omega z/c}\, dz \right| = dE_0 \frac{sin\left(\frac{\omega_0 d}{2c}\right)}{\frac{\omega_0 d}{2c}} = dE_0 T \tag{2.10}$$

where the quantity T is called *transit-time factor*. The transit-time factor is a measure of the reduction in the energy gain caused by the sinusoidal time variation of the field in the accelerating gap. The average accelerating electric field E_{acc} that the electron sees during the transit is then:

$$E_{acc} = \frac{V_{acc}}{d} = E_0 T \tag{2.11}$$

Considering a pill-box excited in TM_{010} mode if the Equation 2.8 is satisfy, the transit-time factor will be $T = 2/\pi$, and the accelerating field will be $E_{acc} = 2E_0/\pi$.

2.1.2 FIGURES OF MERIT

The figures of merit of accelerating structure are very important in order to understand whether the specification and the performance of the cavity satisfies the requests.

In order to understand how large the accelerating field can be, two figures of merit are defined: E_{pk}/E_{acc} and H_{pk}/E_{acc}. E_{pk} is the peak surface electric field and H_{pk} is the peak surface magnetic field which cannot exceed the RF critical magnetic field H_C^{RF}. So the accelerating field is maximized when the ratio E_{pk}/E_{acc} is minimized.

For the TM_{010} mode:

$$E_{pk} = E_0 \qquad H_{pk} = \sqrt{\frac{\varepsilon_0}{\mu_0}} E_0 J_1(1.84) = \frac{E_0}{647\Omega} \tag{2.12}$$

So, the figures of merit becomes:

$$\frac{E_{pk}}{E_{acc}} = \frac{\pi}{2} \qquad \frac{H_{pk}}{E_{acc}} = 2430 \frac{A/m}{MV/m} \tag{2.13}$$

Until now the cavity was considered as having a perfect conducting walls, but the energy losses are present in a RF resonator also using a superconducting cavity, as it was explained in the previous section.

The current flows into a surface layer of the cavity walls, in order to sustain the RF field, so the dissipated power P_C is equal to the negative change in time of the stored energy U:

$$P_C = -\frac{dU}{dt} \tag{2.14}$$

Hence, the stored energy U does not remain constant inside the cavity but it has an exponential time decay:

$$U(t) = U_0 e^{-\frac{\omega_0 t}{Q}} \tag{2.15}$$

this decay depends on the resonator characteristics, indeed the time constant of the decay depends on the *quality factor* Q, i.e. the most important figure of merit. The quality factor is then defined as:

$$Q = \frac{\omega_0 U}{P_C} = \frac{\omega_0}{\Delta\omega} \tag{2.16}$$

and it indicates the number of RF periods are needed for dissipating the entire energy stored in the cavity. It also specifies the frequency selectivity of the resonator, indeed $\Delta\omega$ is the bandwidth of the resonant curve. The total energy stored in the cavity is given by:

$$U = \frac{1}{2}\mu_0 \int_V |\bar{H}|^2 \, dv = \frac{1}{2}\varepsilon_0 \int_V |\bar{E}|^2 \, dv \tag{2.17}$$

where V is the volume of the cavity. The power dissipated on the cavity walls depends on the surface resistance R_S and the magnetic field $\bar{H}$:

$$P_C = \frac{1}{2} R_S \int_S |\bar{H}|^2 \, ds \tag{2.18}$$

where S is the interior cavity surface, these equation is found out approximating that the surface resistance does not change over the cavity surface. Thus the quality factor becomes:

$$Q = \frac{\omega_0 \mu_0 \int_V |\bar{H}|^2 \, dv}{R_S \int_S |\bar{H}|^2 \, ds} = \frac{G}{R_S} \tag{2.19}$$

where G is the *geometrical factor*, this is a constant value which contain whole information about the geometry of the resonator and it is independent of the cavity's size.

Another important figure of merit is the shunt impedance R_a, this quantity is defined in three different ways:

$$R_a = \frac{{V_C}^2}{P_C} \ [\Omega/cell] \qquad R_a^C = \frac{{V_C}^2}{2P_C} \ [\Omega/cell] \qquad r_a = \frac{{V_C}^2}{{P_C}'} \ [\Omega/m] \tag{2.20}$$

the first one derives from the accelerator definition, the second one circuit theory and the third one from LINAC, where ${P_C}'$ is the power dissipated per unit length. Then as the shunt impedance is larger as the power dissipation is minimized, and this is the desired situation for a cavity employed in accelerator.

2.1.3 NORMAL-CONDUCTOR VERSUS SUPERCONDUCTOR CAVITIES

The quality factor Q describes the power losses, and it is inversely proportional to the surface resistance. It means that high quality factor allows to spare some power especially when one cares with high accelerating field in continuous wave (CW) or in long-pulse operation. Indeed the dissipated power increases with the square of the operating field, then, seen the high cost of

the RF power, the most economical way for accelerating particles is to use resonator cavity with as higher Q-factor as possible.

Copper cavities are limited to accelerating field of a few megavolt per meter because the cost of the RF power becomes prohibitive, for example several megawatts per meter of RF power are required to operate with a Copper cavity at $5MV/m$.

In order to maximize the cavity Q-factor, a superconductor material must be used, indeed only superconductor materials can reach very low surface resistance at low temperature and under a RF field. The RF surface resistance of a superconductor is typically five orders of magnitude lower than that for Copper and so the Q-factor is five order of magnitude higher.

In addition, it is important to underline that the wall losses heat the liquid Helium which surrounds the cavities, causing Helium evaporation; this liquid Helium must be refilled and so the cryogenic cost are also very important. The *efficiency* η is a quantity which indicates the AC power required to operate the refrigerator, this is given by the product of the *Carnot efficiency* η_C and the *technical efficiency* η_T. Typical value of these efficiency at $2K$ are: $\eta_C = 0.007$ and $\eta_{CT} = 0.2$, leading to a total refrigerator efficiency $\eta = 0.0014 = 1/700$. This means that the AC power reduction from a Copper cavity at $300K$ to a superconducting cavity at $2K$ is about 10^3.

The employment of superconducting cavities produces another important advantage, it allows to make the beam hole much larger than using the normal conducting ones and this entails more beam stability by reducing the impedance of *higher-order modes*. This beam stabilization is very important for example for *high-current storage rings* and for *linear colliders* (LINAC) [3,9].

2.2 Circuit Model for Cavity Resonator

The resonant mode has to be excited in the cavity by using a RF source. The power from the source is carried using an input probe, called *input coupler*, whereas the transmitted power probe, called *pick-up*, picks up the power transmitted through the cavity. The configuration is shown in Figure 2.4. Usually the input coupler is movable and the transmitted power is instead fixed.

The input coupler is a conductor which penetrates the cavity arranging a coaxial cable in which the cavity is the external conductor and the input probe is the inner one. The overlap between the cavity field and the field which propagates into the cut-off region from the input coupler is called coupling strength. Since the cavity field decreases exponentially with distance in the cut-off regions, the input coupling strength can be easily adjusted by changing the penetration of the inner conductor, in particular the strength increase exponentially by inserting the coupler into the cavity.

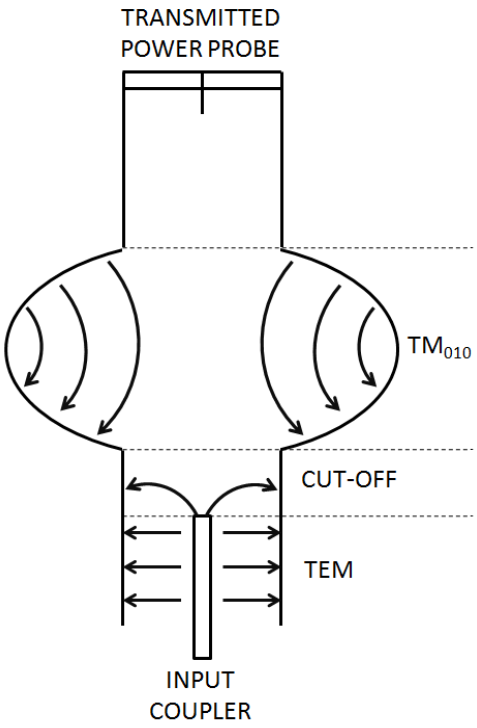

FIGURE 2.4 - CAVITY SCHEME WITH THE RF PROBES AND THE ELECTRIC FIELD LINES TREND.

Actually there are different methods for coupling the field into or out of the cavity, the most common methods are: the electric-coupling probe or antenna, a magnetic-coupling loop at the end of a coaxial transmission line, a hole in a cavity wall with a waveguide connected.

In order to understand the cavity behavior, let us analyze what happens after that the RF source, which drives the cavity at its fundamental resonant frequency , is switched off. Some power will be dissipated in the cavity walls and some power will leak out through both the input and the output coupler. The total power dissipated is given by the sum of these three contributions:

$$P_{tot} = P_C + P_e + P_t \tag{2.21}$$

where P_e is the power leaking back to the input coupler and P_t is the power leaking forward to the pick-up probe.

So the system cavity-input coupler-transmitted coupler is characterized by this total power dissipated, and the quality factor of this system is called *loaded quality factor* Q_L:

$$Q_L = \frac{\omega_0 U}{P_{tot}} \tag{2.22}$$

and the intrinsic quality factor of a cavity in now indicated with Q_0. The loaded quality factor also plays a central role in the exponential decay of the stored energy:

$$U = U_0 e^{-\frac{\omega_0 t}{Q_L}} \quad , \quad \frac{dU}{dt} = -P_{tot} = -\frac{\omega_0 U}{Q_L} \tag{2.23}$$

where U_0 is the stored energy at $t = 0$. Thus the constant decay of the stored energy is:

$$\tau_L = \frac{Q_L}{\omega_0} \tag{2.24}$$

It is evident that by measuring the time decay and knowing the resonance frequency the loaded Q-factor is determined.

Since P_{tot} contains the contribution of both the cavity and the couplers losses, also the loaded Q-factor is given by these contributions and defining a quality factor for each of them, Q_L can be written as:

$$\frac{P_{tot}}{\omega_0 U} = \frac{P_C + P_e + P_t}{\omega_0 U} \quad , \quad \frac{1}{Q_L} = \frac{1}{Q_0} + \frac{1}{Q_e} + \frac{1}{Q_t} \tag{2.25}$$

where Q_e and Q_t are the external quality factors, defined as:

$$Q_e = \frac{\omega_0 U}{P_e} \quad , \quad Q_t = \frac{\omega_0 U}{P_t} \tag{2.26}$$

As it was explained before, each coupler has a certain *coupling strength* which specifies how strongly the couplers interact with the cavity. The coupling strength can be quantified as:

$$\beta_e = \frac{Q_0}{Q_e} = \frac{P_e}{P_C} \quad , \quad \beta_t = \frac{Q_0}{Q_t} = \frac{P_t}{P_C} \tag{2.27}$$

From the previous equation one notes that whether the coupling strength is large, the power losses into the coupler will be larger than the power dissipated by the cavity walls.

Knowing the coupling strengths and the loaded Q-factor, the intrinsic quality factor Q_0 can be easily found, indeed:

$$\frac{1}{Q_L} = \frac{1}{Q_0}(1 + \beta_e + \beta_t) \tag{2.28}$$

An interesting point to underline is that the loaded Q-factor depends on the cavity and on the coupler geometry, and also the coupling strength of the coupler depends on the cavity Q-factor, Q_0.

Let us consider the most common situation, where coupling strength for the transmitted coupler β_t is very weak, in this way one can evaluate the cavity performance without considering the transmitted coupler [10]. The system will be now described as an equivalent AC circuit for developing the steady-state and the transient behavior of the cavity. The AC circuit model is made using the quasi-static approximation: the time constant of the cavity is long compared to the RF period.

The cavity is modeled as a circuit with an inductance L, a capacitance C, and circuit shunt resistance R; for the external circuit there are: the RF generator, an isolator and an input coupler. The isolator, that is a circulator connected to a load, is necessary so as the signals coming back from the cavity terminates in a matched load. The system and the equivalent circuit are shown in Figure 2.5.

The RF generator and the isolator are modeled in the equivalent circuit as an ideal current source and a shunt admittance G_0. The RF generator and the coupler are connected with a lossless transmission line with a characteristic admittance $G_0$and the coupling between the transmitted coupler and the cavity is modeled as a transformer, in this way the transmission line and the cavity are matched with an arbitrary impedance. The quantity in the external circuit will be denoted with a primer symbol and the ones in the resonator circuit with no primes.

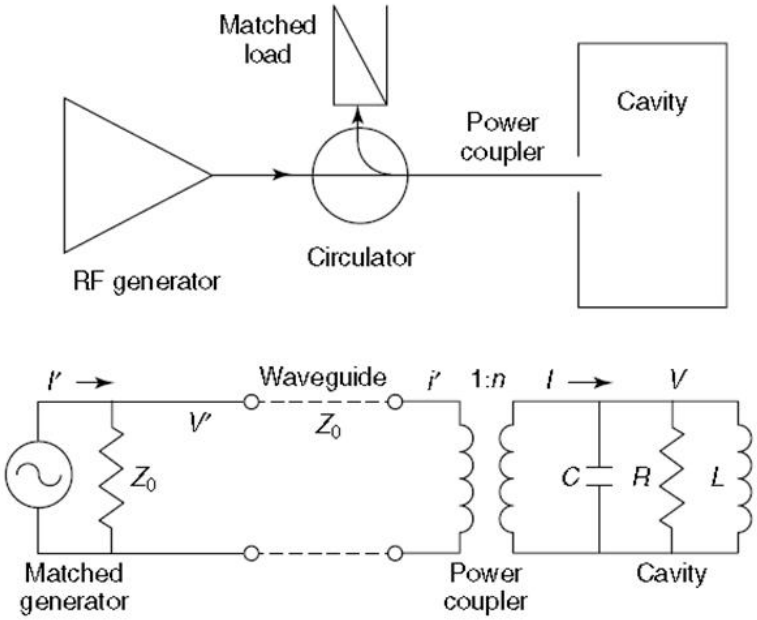

FIGURE 2.5 - BLOCK DIAGRAMS OF RF SYSTEM COMPONENT (UPPER) AND EQUIVALENT CIRCUIT FOR A CAVITY SYSTEM DRIVEN WITH ONE COUPLER.

2.2.1 THE STEADY STATE BEHAVIOR

The resonator voltage is given by $V_C = Z_C i$, where Z_C is the impedance of the shunt resonant circuit and i is the driving current. Considering the transformer coupling, the voltage and the driven current become:

$$V_C = nV' \quad , \quad i = i'/n \tag{2.29}$$

and so the impedance becomes:

$$Z_C = \frac{V_C}{i} = n^2 \frac{V'}{i'} = n^2 Z_C' \tag{2.30}$$

where Z_C' is the resonator impedance transformed into the generator circuit. Then the circuit can be transformed into the primary circuit with:

$$Z_C' = \frac{1}{j\omega C' + \frac{j\omega}{L'} + R'} \tag{2.31}$$

where: $C' = n^2 C$, $L' = L/n^2$, $R' = R/n^2$. The stored energy in the circuit resonator is:

$$U = \frac{1}{2} C V_C^2 \tag{2.32}$$

and the average power dissipated in the resonator is:

$$P_C = \frac{G_C V_C^2}{2} = \frac{V_C^2}{2R_a} \tag{2.33}$$

The unloaded quality factor can be now written as:

$$Q_0 = \frac{\omega_0 U}{P_C} = \omega_0 R_a C \tag{2.34}$$

Whereas the power dissipated in the external load is:

$$P_e = \frac{V'^2}{2Z_0} \tag{2.35}$$

and so the external quality factor can be written as:

$$Q_e = \frac{\omega_0 U}{P_e} = \omega_0 n^2 Z_0 C \tag{2.36}$$

this quality factor is independent from the cavity losses. Using the equations 2.34 and 2.36, one finds the relationship between n and the coupling strength β:

$$\beta = \frac{R_a}{n^2 Z_0} \tag{2.37}$$

this means that larger n implies smaller coupling strength β. Using this relation it is possible to express the circuit model formula as a function of β instead of n:

$$R' = \beta Z_0 \quad , \quad C' = \frac{R_a C}{\beta Z_0} \quad , \quad L' = \frac{\beta Z_0 L}{R_a} \tag{2.38}$$

Considering a cavity driven on resonance frequency, the load impedance for the guide is $Z_L = R' = \beta Z_0$, and considering the wave emitted from the generator into the guide, the *reflection coefficient* Γ produced by the load impedance becomes:

$$\Gamma = \frac{Z_L - Z_0}{Z_L + Z_0} = \frac{\beta - 1}{\beta + 1} \tag{2.39}$$

and the *standing wave ratio S* is:

$$S = \frac{1 + |\Gamma|}{1 - |\Gamma|} \tag{2.40}$$

Depending on the value of the coupling strength β three different situations take place:

- $\beta < 1 \rightarrow$ the coupler and the cavity are *undercoupled* and:

$$|\Gamma| = \frac{1 - \beta}{1 + \beta} \quad , \quad S = \frac{1}{\beta} \tag{2.41}$$

- $\beta > 1 \rightarrow$ the coupler and the cavity are *overcoupled* and:

$$|\Gamma| = \frac{\beta - 1}{\beta + 1} \quad , \quad S = \beta \tag{2.42}$$

- $\beta = 1 \rightarrow$ the coupler and the cavity are *critically coupled* and:

$$|\Gamma| = 0 \quad , \quad S = 1 \tag{2.43}$$

The critically coupled case is defined as the condition in which the coupler and the cavity are perfectly matched, the system results in a matched cavity load, whereas as $\beta \rightarrow 0$ the system results in a short-circuit load ($\Gamma \rightarrow -1$) and as $\beta \rightarrow \infty$ in an open-circuit load ($\Gamma \rightarrow +1$). Then the reflected power is:

$$P_r = P_f|\Gamma|^2 = P_f\left(\frac{\beta-1}{\beta+1}\right)^2 \tag{2.44}$$

where P_f is the incident power from the RF generator. From energy conservation, one finds that the power flowing into the cavity P_C is given by:

$$P_C = P_f(1-|\Gamma|^2) = P_f\frac{4\beta}{(1+\beta)^2} \tag{2.45}$$

it is easy to note that P_C reaches its maximum value for $\beta = 1$, in which $P_C = P_f$. Now it is possible to use this result for finding the value for the stored energy in the steady-state. In this situation the stored energy is constant, so $dU/dt = 0$ and $U = U_0$. Using the Equation 2.45 it is possible to explicit U_0 in terms of β:

$$U_0 = \frac{P_C Q_0}{\omega_0} = \frac{4\beta P_f}{(1+\beta)^2}\frac{Q_0}{\omega_0} \tag{2.46}$$

and even from this equation it is clear that the stored energy is maximum for =1 when the cavity is perfectly matched with input coupler. Moreover solving for β the Equation 2.44 gives the following result:

$$\beta = \frac{1 \pm \sqrt{P_r/P_f}}{1 \mp \sqrt{P_r/P_f}} \tag{2.47}$$

where the upper sign is used for the *overcoupled* case and the lower sign is used for the *undercoupled* case. Thanks to this equation one can find experimentally the coupling strengths value by knowing both the forward P_f and the reflected P_r power. By the way, a strong approximation was made making the equivalent circuit model for a cavity coupled with one coupler, indeed a more realistic situation is described making the equivalent circuit for a cavity coupled with two coupler. Such a circuit is sketched in Figure 2.6.

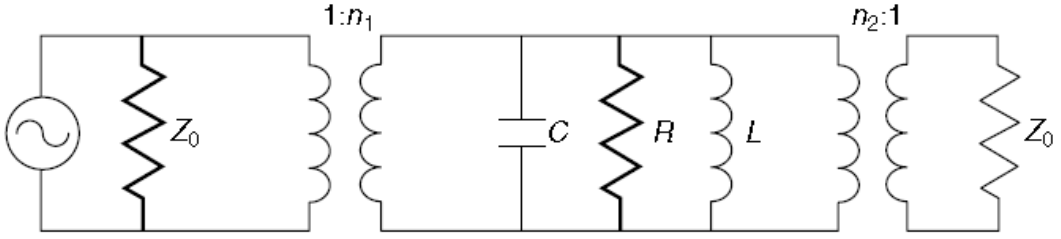

FIGURE 2.6 - EQUIVALENT CIRCUIT OF A CAVITY COUPLED WITH TWO COUPLERS.

Taking into account, as before, the reflection coefficient for the input guide, it is defined as:

$$\Gamma_1 = \frac{\beta_1 - \beta_2 - 1}{1 + \beta_1 + \beta_2} \tag{2.48}$$

So in the perfect matched between input coupler and cavity case the reflection coefficient must be: $\Gamma_1 = 0$, and the Equation 2.48 give the following solution:

$$\beta_1 = 1 + \beta_2 \tag{2.49}$$

Analyzing this results one finds that because $\beta_2 \geq 0$, the matched condition of the input guide implies that $\beta_1 \geq 1$, so only in the weakly coupled limit for the transmitted guide, so for $\beta_2 \cong 0$, one can finds $\beta_1 \cong 1$ for the matched case.

2.2.2 THE TRANSIENT BEHAVIOR

Considering the Equation 2.47, from an incident wave that comes out from the generator with amplitude V_f, the effective reflected wave in a steady-state has an amplitude V_r given by:

$$V_r = \frac{\beta - 1}{\beta + 1} V_f \tag{2.50}$$

and the total steady-state voltage across the resonator impedance at the coupler is:

$$V = n(V_f + V_r) = \frac{2\beta n}{1 + \beta} V_f \tag{2.51}$$

Let us now take into account what happens if at time $t = 0$ the generator is switched on. A wave with amplitude V_f leaves the generator, this wave will be partially reflected at the coupler and partially transmitted to the resonator. The time dependence is found from the stored energy behavior:

$$U(t) = U_0 \left(1 - e^{\frac{-t}{2\tau_L}}\right)^2 \tag{2.52}$$

So, combining the time dependence $1 - e^{-t/\tau}$ with the steady state result, one finds that the time-dependent resonator voltage is:

$$V_0(t) = V_f\left(1 - e^{-t/\tau}\right)\frac{2\beta n}{1+\beta} \tag{2.53}$$

So that the forward voltage is constant after $t = 0$, it is easy to find also the reflected wave time-dependent voltage:

$$V_r(t) = V_f\left[\left(1 - e^{-\frac{t}{\tau}}\right)\frac{2\beta n}{1+\beta} - 1\right] = V_f|\Gamma(t)| \tag{2.54}$$

From which the time-dependent reflection coefficient results:

$$\Gamma(t) = \left(1 - e^{-\frac{t}{\tau}}\right)\frac{2\beta n}{1+\beta} - 1 \tag{2.55}$$

In terms of travelling-wave power, the average reflected power can be defined as:

$$P_r(t) = P_f|\Gamma(t)|^2 = P_f\left[\left(1 - e^{-\frac{t}{\tau}}\right)\frac{2\beta n}{1+\beta} - 1\right]^2 \tag{2.56}$$

and the power flowing into the cavity is:

$$P_C(t) = P_f(1 - |\Gamma(t)|^2) = P_f\left\{1 - \left[\left(1 - e^{-\frac{t}{\tau}}\right)\frac{2\beta n}{1+\beta} - 1\right]^2\right\} \tag{2.57}$$

Let us analyze the results obtained. As expected at $t = \infty$ the results approach to the ones found for the steady-state case. At $t = 0$ the wave generated from the RF generator reaches the coupler and: $V_r(0) = -V_f$, $P_r(0) = P_f$ and $P_C(0) = 0$, so the incident power is completely reflected. The transient behavior depends on the coupling strength β, as is shown in Figure 2.7.

For $\beta < 1$ the reflected power $P_r(t)$ decreases monotonically from its initial value P_f to its steady state value; For $\beta > 1$ the reflected power $P_r(t)$ decreases until it reaches zero and after it increases reaching its steady-state value.

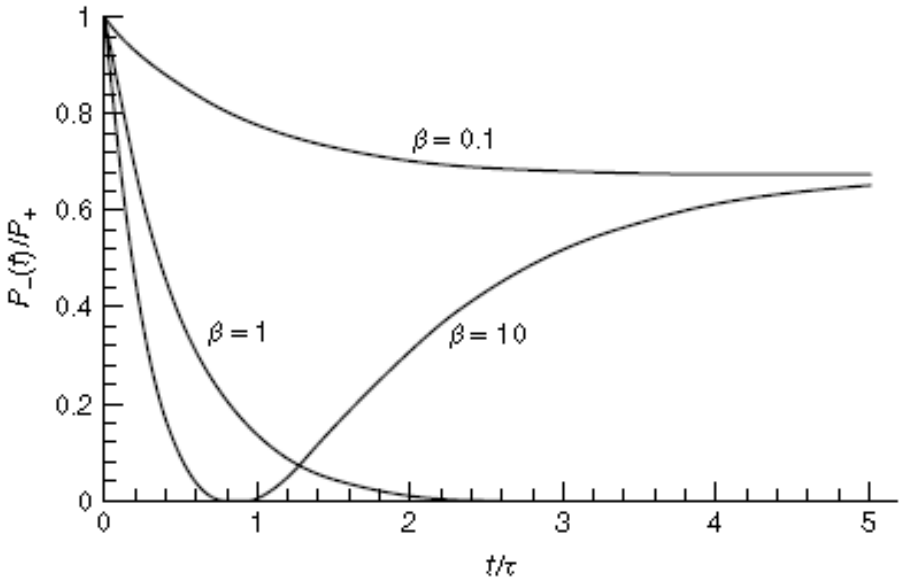

FIGURE 2.7 - BACKWARD POWER AS A FUNCTION OF TIME FOR THE THREE DIFFERENT COUPLING REGIMES.

Now it is important to underline that when the cavity is fed with a input wave from the generator, it radiates a wave back through the coupler. The reflected power, or voltage, in the input coupler is so given by two travelling waves, the direct reflection of the incident power P_f and the emitted wave from the cavity P_e:

$$P_r = \left(\sqrt{P_e} - \sqrt{P_f}\right)^2 \tag{2.58}$$

These two waves are out of phase and the relative amplitude of these waves determines whether the coupling regime is over-coupled, under-coupled or critically coupled. Then the effective reflected wave shows a time-dependence because of the presence of a radiated wave from the cavity. Let us take into account what happens if at time $t = 0$ the generator is switched off. As already seen in the previous section, the stored energy shows an exponential decay:

$$U(t) = U(0)e^{-t/\tau} \tag{2.59}$$

The reflected power consist only of the emitted power and combining the time dependence $e^{-t/\tau}$ with the Equation 2.46, this power results:

$$P_r = P_e = \frac{4\beta^2 P_f}{(1+\beta)^2} e^{-t/\tau_L} \tag{2.60}$$

where P_f is the forward power just before it was turned off. The emitted power depends on the coupling strength β, for $\beta \to 0$ one finds $P_e = 0$, for $\beta = 1$ one finds $P_e = P_f$ and for $\beta \to \infty$ one finds $P_e = 4P_f$. Solving for β the Equation 2.39 at time $t = 0$, one can define the coupling strength when the RF is switched off:

$$\beta = \frac{1}{2\sqrt{P_f/P_e} - 1} \tag{2.61}$$

this expression is very useful because it permits to find experimentally the value of β without knowing whether the cavity is over- or under-coupled, unlike the steady-state Equation 2.47.

2.3 Cavity Geometries

The cavities can be divided in different classes depends on the ratio $\beta = v/c$ where v is the speed of the accelerated particle and c is the speed of light. High-β cavity, accelerates electrons, positrons, or high energy protons with $\beta \cong 1$, and they are based on the resonant mode TM_{010}. Structures with β between 0.2 and 0.7 are medium β cavity which accelerates protons and ions, in this range there are both cavity based on TEM mode and cavity based on a TM mode. Low β cavities accelerates particles at small fraction of the speed of light as heavy ions, clusters. Such cavities operates usually at low frequency and in a TEM-like mode. The main cavity types with their resonance frequency and the particles velocity range covered, are shown in Figure 2.8

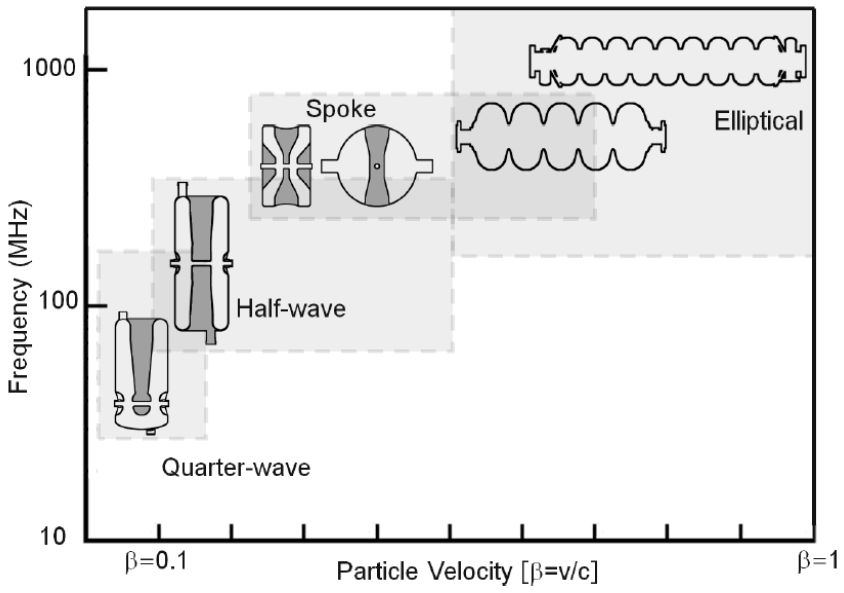

Figure 2.8 - Range of frequency versus particle velocity covered by the main cavities types.

High-β accelerating structures are usually a single-cell cavity operating in the TM_{010} mode or a chain of coupled cells operating as well in the TM_{010} mode. In order to obtain particle acceleration for each gap, the electric field is shifted of π in adjacent cell ($\pi - mode$), so that the charged particles pass through each cell in half an RF period. The cell-to-cell coupling is guaranteed thanks to the electric field at the beam holes.

Usually such structures are elliptical cavity half-cell (the half-cell length is a quarter of the wavelength) as it is shown in Figure 2.9, this shape was discovered in order to eliminate the problem of multipacting, indeed the elliptical shape allows to avoid one-point multipacting. The maximum value of the peak electric field occurs near the iris and the maximum peak magnetic field occurs close to the equator. A the iris the elliptical arc reduces the peak electric field, making the lower the probability to incur in field emission. Whereas large equatorial radius reduces the peak magnetic field by increasing the surface, exposed to the field, decreasing in this way the current density.

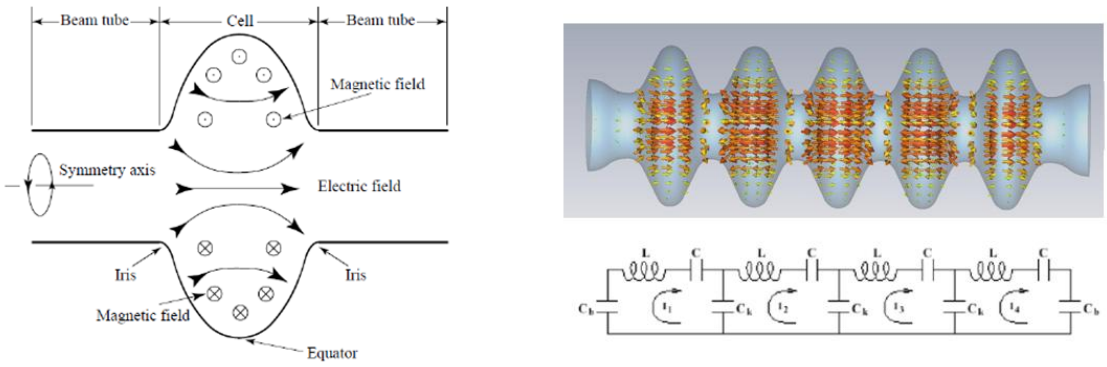

FIGURE 2.9 - (A) SKETCH OF THE FIELD INSIDE AN ELLIPTICAL CAVITY. (B) 3-D REPRESENTATION OF THE ELECTRIC FIELD INSIDE A CHAIN OF ELLIPTICAL CAVITIES CAPACITIVE COUPLED.

The medium-β elliptical cavities are obtained by an axial compressions of the standard elliptical cavity dimension maintaining constant the resonance frequency. The range of acceleration is about $0.5 < \beta < 0.8$, under 0.5 it becomes mechanically unstable. The electric peak field remains at the iris region whereas the peak magnetic field increases near the equator region. Also the medium-β spoke resonator is largely used with $\beta \sim 0.5$. The spoke cavity derives from an half-wavelength resonant transmission line operating in a TEM mode. Such $\lambda/2$ transmission line has a short at both ends and the maximum voltage is reached in the middle, it is called single-spoke resonators. For a multi-spoke resonators the electric field has a difference of phase of π for adjacent gaps ($\pi - mode$), and the coupling takes place via magnetic field linking

through the large opening (Figure 2.10). The advantage of the spoke cavity use near $\beta \sim 0.5$ is that the spoke cavities are smaller at the same frequency compared to elliptical structures, so the spoke resonator can be made at half frequency but with the same dimensions as the elliptical one, allowing to save refrigeration.

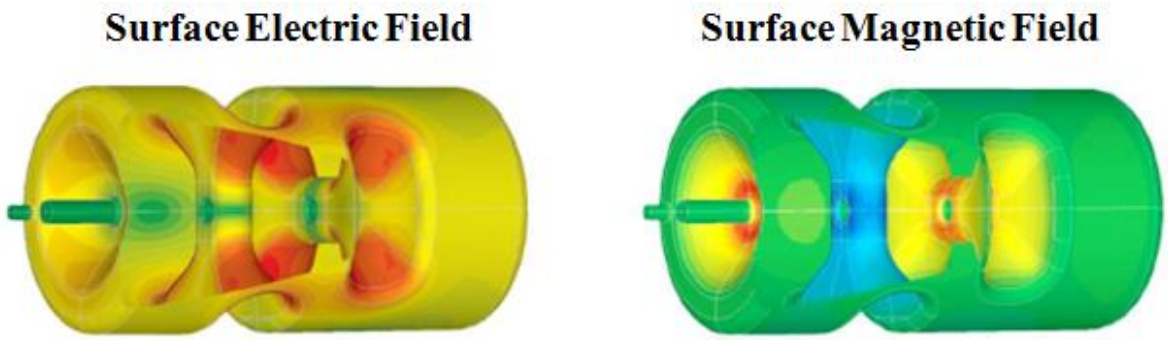

FIGURE 2.10 - 3-D REPRESENTATION OF THE ELECTRIC FIELD (LEFT) AND MAGNETIC FIELD (RIGHT) FOR A DOUBLE SPOKE RESONATOR.

A typical low-β resonator ($0.01 < \beta < 0.2$) is the Quarter-Wave Resonator which derives from a quarter-wavelength transmission-line. The QWR is indeed a coaxial line, with length $l = \lambda/4$, shorted at one end in which the maximum electric field is where the gap is located. Such resonators work usually at low frequency, about $100 - 200MHz$, because the accelerating gap is proportional to $\beta\lambda$, so they are also rather large. The structure is provided which an inner conductor which is hollow and filled with liquid Helium. A representation of QWR is shown in Figure 2.11, the maximum electric field is at the gap, and the maximum magnetic field is instead at the short end. In addition this cavity is characterize to have high peak field over accelerating field ratio and also the value of surface electric and magnetic fields result rather high, compared to the elliptical cavities. Increasing the number of gaps in a QWR, the energy gain increases but the beam stability becomes also more technically difficult. These cavities, because of the large size, are particularly sensible to mechanical vibrations so they need a mechanical damper or an electronic fast tuner.

Another medium β resonator is the half wave resonator (HWR) and it is like two quarter wave resonator facing each other, they provide the same accelerating voltage with about twice power dissipation.

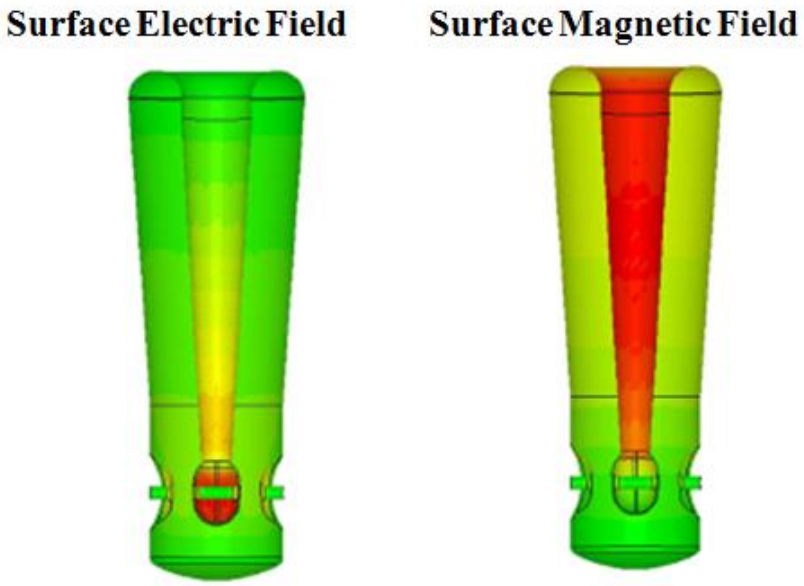

FIGURE 2.11 - 3-D REPRESENTATION OF THE ELECTRIC FIELD (LEFT) AND MAGNETIC FIELD (RIGHT) FOR A QUARTER WAVE RESONATOR.

The very-low β resonators $(0.01 < \beta < 0.04)$ are 4-gap QWR structures and superconducting Radiofrequency Quadrupole (RFQ). The RFQ is used for the acceleration of very low velocity ions $\beta < 0.01$. In these structures a strong electric focusing is provided by the quadrupoles, and the acceleration is provided by a longitudinal field component synchronous with ion bunches. They are typically normal conducting with a resonance frequency between 50 and 400 MHz.

2.4 NIOBIUM THIN FILM ACCELERATOR CAVITIES: THE STATE OF THE ART

The Niobium film technology offers different advantages. The high thermal conductivity of Copper increases the cavity thermal stability against thermal breakdown of superconductivity. Indeed the thermal conductivity of Copper at $4.2K$ is between 300 and 2000 $Wm^{-1}K^{-1}$ depending on the purity, against the low Niobium thermal conductivity of about 75 $Wm^{-1}K^{-1}$ at $4.2K$ of Niobium with $RRR = 100$. Another advantage is the cost saving of Niobium material, which becomes particularly important in the case of large size cavities.

In addition the residual resistance of Niobium thin film on Copper is less sensitive to DC magnetic field, thanks to the higher value of upper critical field, H_{c2}, compared to Niobium bulk. Indeed the contribution to the residual resistance due to an external magnetic field is defined as:

$$R_{mag} = \frac{H_{ext}}{2H_{c2}} R_n \tag{2.62}$$

where R_n is the normal state resistance, H_{ext} is the external magnetic field. Thanks to that the degree of magnetic shielding used in the cryostat is reduced. [3]

Thanks to these benefits 300 four-cell Niobium thin film Copper cavities ($350MHz$) have been produced for LEP2. In the early coatings one of the main problem encountered was the poor film adhesion, such fact was attributed to the presence of contaminant particles on the Copper substrate. Then the preliminary treatments for the Copper substrates were optimized, in particular the electro polishing and chemical polishing techniques, so that the substrate got a more smooth and clean surface. Also the Niobium deposition was deeply studied in order to obtain the better cavity performances, the film quality was monitored by the evaluation of the RRR which should be more than 10 for considering the deposited film as having good purity level. The best films were obtained by cylindrical magnetron sputtering. After this success also in LHC sixteen $400MHz$ Niobium on Copper cavities were applied [11]. In Figure 2.12 the best performances of LHC cavity at $4.5K$ and $2.5K$ are shown.

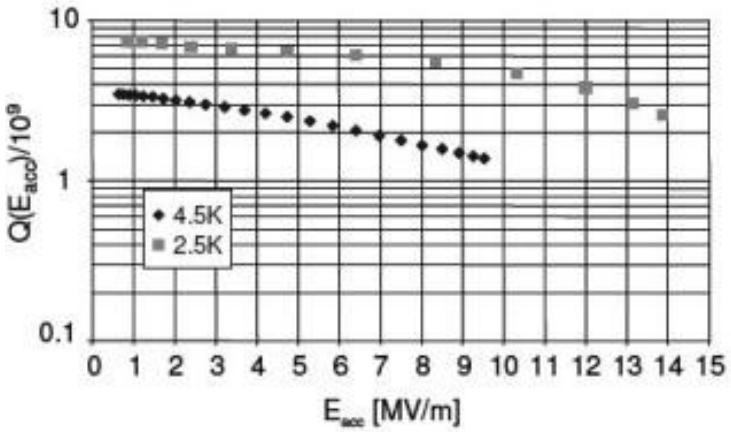

FIGURE 2.12 - TYPICAL PERFORMANCE OF INDUSTRY-PRODUCED LHC $400MHz$ CAVITIES.

The Q-factor decreases considerably with the accelerating field, such Niobium on Copper cavity behavior is called Q-slope and it is responsible to the lower performance of sputtered cavities. The Niobium film technology is indeed not yet competitive for high frequency applications compared to bulk one.

Regarding the low-β cavities, 58 QWR have been produced by deposition of a superconducting layer on a Copper substrate. Most of such substrates were initially Lead plated and with a later upgrading the Pb layer was substituted with a sputtered Niobium film, now only 2

Pb/Cu QWRs are still installed [12]. Because of the complex QWR shape, a DC bias diode sputtering was chosen instead of magnetron sputtering. Thanks to the applied bias, which promotes the impurity release during the film growth, a high quality Niobium film was obtained. The performances are shown in Figure 2.13.

Also for the ISOLDE facility upgrading the Niobium sputtering on Copper QWRs are under study, the measurement and the development will be described in the following chapter, part of this thesis work indeed concern the RF measurement and characterization of such QWR.

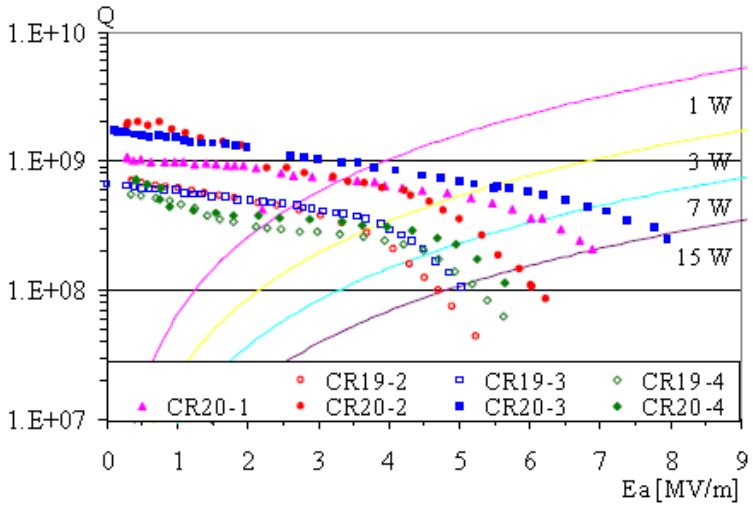

FIGURE 2.13 - Q-FACTOR VERSUS ACCELERATING FIELD OF HIGH β QUARTER WAVE RESONATOR AS MEASURED ON LINE IN FALL 2006.

The Q-slope problem was initially attributed at the fine grain size of the Niobium sputtered films, but probably this is not the dominant problem, indeed even cavities sputtered with large grain films show Q-slope. Also film with high value of RRR about 44 and large grain were obtained, using Kripton instead of Argon as inert gas during the deposition, nevertheless the Q-slope was still present. The interface between Copper and Niobium was also studied, in particular the results by using a oxide-free Copper substrate were compared with the one found using a standard Copper substrate (in which an oxide layer naturally appears at the surface). The critical temperature values were found to be lower in the case of oxide free Copper. As the critical temperature results suggest, in according with the XRD spectra, larger stress appears in the case film grown on oxidized copper substrate. Moreover the effects of hydrogen were studied, i.e. the formation of hydrides which have a well-known disastrous effect in case of bulk technology. Even in this case the effect of hydrides is more pronounced in the case of oxide-free substrate [13]. Another approach was to use a gettering underlayer, namely Titanium, but also this attempt does not show particular benefits [14].

The effects of deposition angle on film morphology and superconducting properties were studied in order to understand the role of this parameter. The highest values of RRR were found for normal deposition angle whereas the lowest values were found for grazing angles, where the film becomes amorphous. An evolution of the magnetron sputtering, the HPPMS (High Power Pulsed Magnetron Sputtering) technique, is under development at CERN. A high pulsed voltage is applied on the target ($1kV$), allowing to obtain a highly dense plasma in which Niobium atoms are partially ionized. Whether a suitable bias is applied to the substrate this technique allows to obtain a deposition with a normal angle of incidence everywhere.

Another solution, a cathodic arc coating, was tried at INFN in order to improve the Nb/Cu cavity performance. In this way the film deposited is thicker than with the usual sputtering techniques, and the Niobium behavior is expected to be bulk-like. Results obtained with sample Niobium films are promising, their RRR values and grain sizes are larger, as compared to Niobium magnetron sputtered films deposited at the same temperature. A filtered UHV arc system was also used to produce quasi micro-droplet-free samples. It has been shown also that by means of the linear arc it is possible to coat an inner surface of the 1.3-GHz copper cavity.

The more interesting examples of the deposition system used until now for elliptical cavities coating, are shown in Figure 2.14. At CERN a cylindrical magnetron sputtering configuration was used, in which the internal magnet moves along the cavity length in order to deposit the whole inner cavity surface, Figure 2.14 (a). At INFN-LNL the same idea about the cylindrical magnetron sputtering configuration was performed [15], but using a ring shaped cathode in order to obtain the magnetic field as parallel as possible to the cathode surface and to maximize the deposition rate Figure 2.14 (b). The same cathode shape was used also in a post-magnetron configuration using two external coils around the cavity, as it is shown in Figure 2.14 (c).

Several research activities about Niobium film superconducting cavities were carried out in the last decades. However such technology does not yet achieved its ultimate performance, contrary to what has been obtained with niobium sheet cavities. Anyway, the different advantages offered by the thin film technology establish a valid reason for continuing the research for the better thin film cavity performance and understanding, and overcoming, the Q-slope problem.

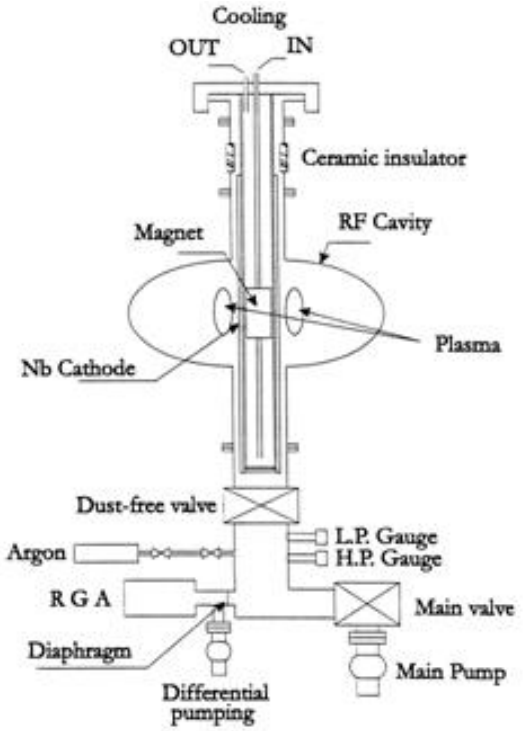

(A)

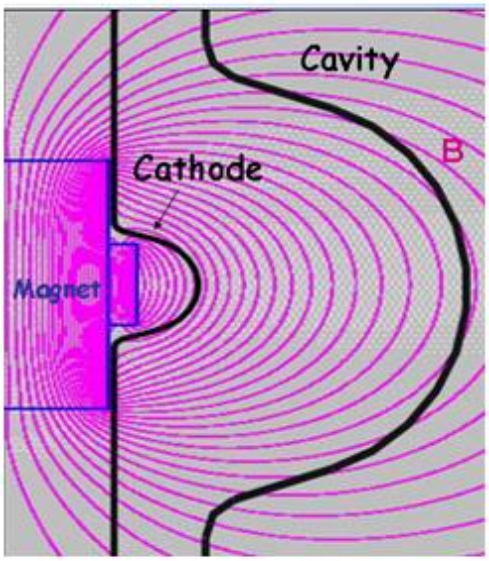

(B)

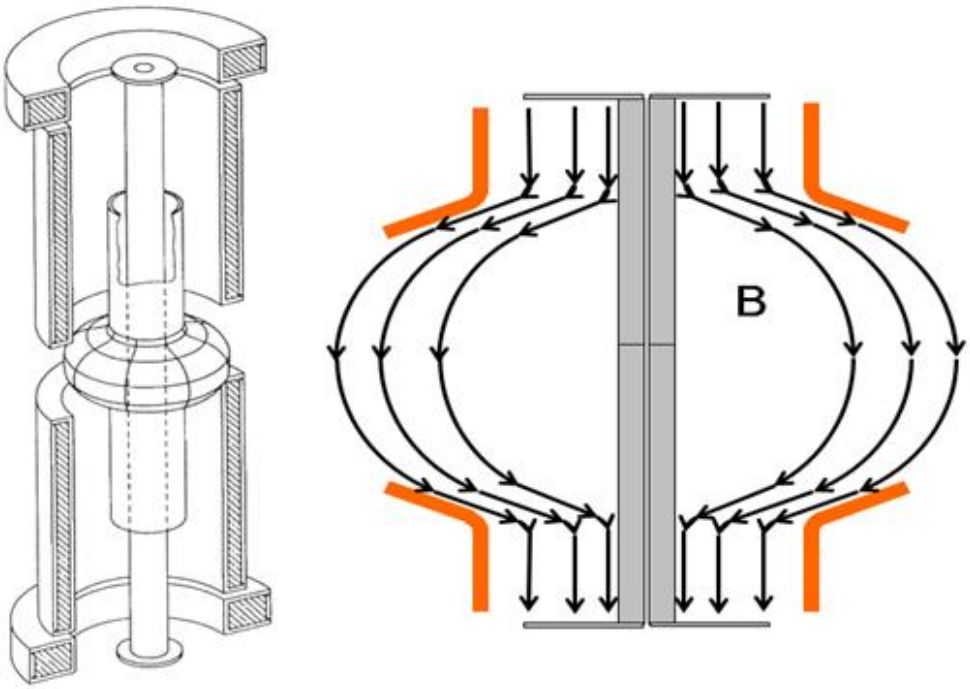

(C)

FIGURE 2.14 -MAGNETRON SPUTTERING SYSTEM FOR 1.5GHZ ELLIPTICAL CAVITIES COATING. (A) CERN CYLINDRICAL MAGNETRON CONFIGURATION, (B) RING CATHODE SHAPE APPLIED ON THE CERN CONFIGURATION (INFN-LNL), (C) POST-MAGNETRON CONFIGURATION WITH A RING CATHODE SHAPE (INFN-LNL).

Chapter 3

NIOBIUM SPUTTERING ON 6GHZ CAVITIES

In this Chapter the experimental work with elliptical 6GHz cavities is explained. A short introduction about the magnetron sputtering techniques is followed by the description of the system used for the Niobium on Copper deposition and its further upgrading. After one deposition in a dummy cavity, where sputtered quartz samples were studied, four deposition were made directly on 6GHz cavities. It is here explained how the Copper substrate is prepared before the deposition, how each sputtering process was done and why, and what one can expect as a results.

3.1 6GHZ CAVITIES

The 6GHz cavities are used in order to study the radiofrequency properties of different materials; indeed this small scale resonators are not usable in a real accelerator but they offer different advantage as a test RF cavity. For studying new superconducting materials it is more convenient to deal with these scaled resonators instead of planar samples. They allow to measure directly the RF properties of the superconductor material with which such cavities are made from, and, in addition, the technological problems due to the particular shape of the cavity can be encountered and studied for overcoming them.

The small dimension of the 6GHz cavity involves smaller costs and time regarding not only the fabrication, but also the post-treatments, as mechanical and chemical treatments, compared to real cavities. The RF measurements become less expensive since a liquid Helium Dewar can be used at this purpose instead of a real cryostat and, also in this case, the advantages are again the smaller cost and time reduction.

Thanks to these advantages it is possible to perform a large number of RF test and to obtain as a consequence a large statistics about the cavity performance.

However it is also true that the RF test results depend on cavity frequency and so the 6GHz results cannot be directly compared with the ones found for real elliptical accelerating cavities. They have to be rescaled taking into account the difference between the resonance frequencies.

The 6GHz cavities are produced by spinning techniques. The major advantage of this method of fabrication is that such cavities do not need any electro-beam welding and the fabrication cost is considerably reduced. On the other hand a seamless cavity presents some damage in the inner surface so a mechanical polishing in essential for refining the surface.

6GHz cavity is constituted by the cell, that is the zone in which the electric and magnetic fields are defined (see Chapter 2), it is the most important part of the cavity, and by two cut-offs that end with a seamless flange which allows to fix the cavity in the stand for the RF test. The region where the cut-off ends and the cell starts is called iris.

The geometrical characteristics of the 6GHz cavity are (Figure 3.1):

- Cavity length: $96.65mm$,
- Cut-off length: $35.1mm$
- Cell length: $26.45mm$
- External cut-off diameter: $24mm$
- Cavity thickness: $2mm$

In the case of thin film cavities technology, the 6GHz cavity becomes the substrate for the Niobium deposition. Such substrate is suitable for optimizing the sputtering process for Niobium on Copper accelerating cavities. Once the sputtering process is developed and optimized for 6Ghz cavities, this can be easily rescaled for being applied with the real accelerating cavities.

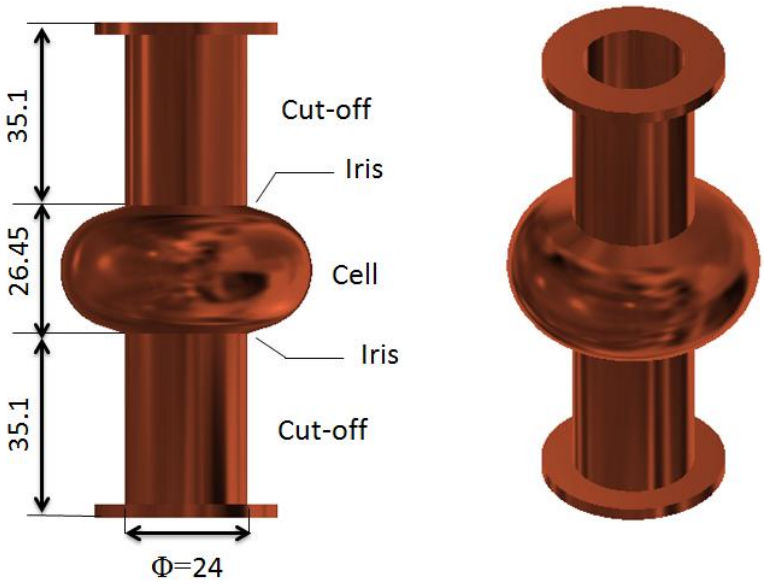

FIGURE 3.1 - SCHEMATIC REPRESENTATION OF A 6GHZ CAVITY.

3.2 INTRODUCTION TO MAGNETRON SPUTTERING TECHNIQUE

Sputtering is a Physical Vapor Deposition (PVD) technique widely used for the surface erosion and for the film deposition. It exploits the plasma generation given by a glow discharge.

When a voltage is applied between two electrodes inside a chamber containing gas at low pressure, a continuous discharge appears. The electrons that are moving from the cathode to the anode collide with the gas atoms causing its ionization and secondary electrons emission. The ions formed strike the cathode producing other second electrons emission. When this secondary electrons are enough to counterbalance the ions lost, the discharge is self-sustained and such regime is called *glow discharge*. The glow discharge is characterized by a *plasma* region, this zone is globally neutral, even though positive and negative charged particles are present in large number.

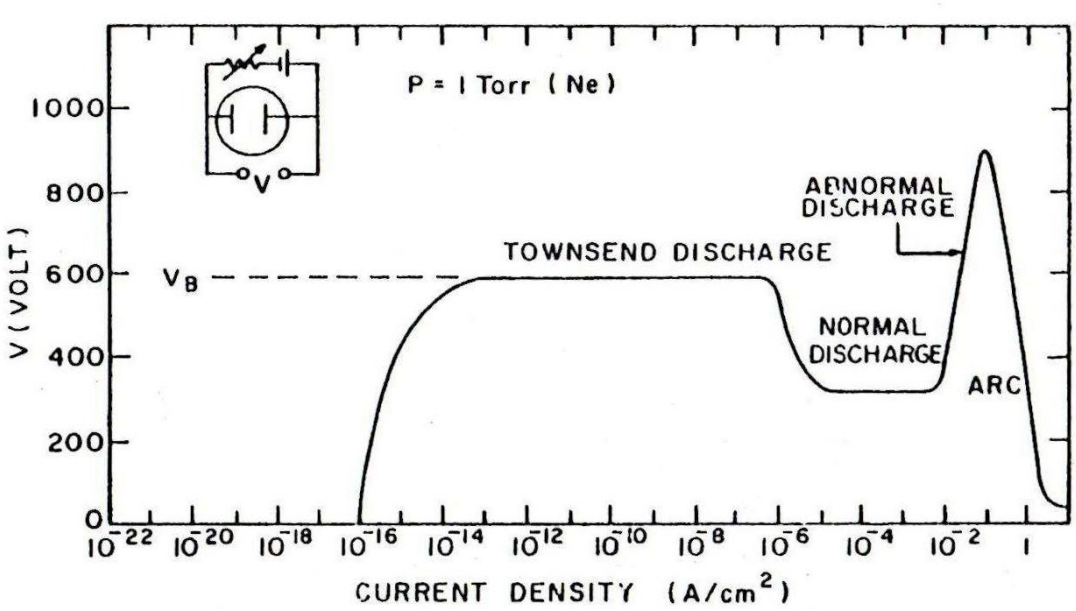

FIGURE 3.2 -VOLTAGE VERSUS CURRENT DENSITY CHARACTERISTIC CURVE FOR A DISCHARGE IN VACUUM WHIT CONSTANT DISTANCE BETWEEN THE ELECTRODES AND AT LOW PRESSURE.

A discharge in vacuum, with a constant distance between the cathode and the anode, and at low pressure, shows a characteristic current-voltage curve, as displayed in Figure 3.2. The glow discharge region can be divided in the normal and abnormal discharge; sputtering process is done in the abnormal discharge region, so, it is characterized by the increasing of the voltage as the cathode current increases.

The easiest sputtering configuration is called *Diode Sputtering*, the cathode is composed by the *target material*, i.e. the material which must be deposited on the substrate. The anode is instead usually composed by the substrate and the vacuum chamber. A negative high voltage is

applied to the cathode, usually about $-500V$, while the chamber and the substrate are grounded. For obtaining a high purity film, a preliminary pressure of about $10^{-8}mbar$ is essential. Once this pressure is reached, a inert gas, usually Argon, is injected into the chamber reaching pressure about $10^{-1}mbar$. With this configuration the ions are formed far away from the cathode and the secondary electrons have large probability to be lost in the chamber walls. Because of that the ionization efficiency is rather small and so pressure lower than $10^{-1}mbar$ can not be used, otherwise the glow discharge does not occur.

This sputtering configuration can be modified by adding a supplementary electrode between anode and cathode, the process is now called *Biased Diode Sputtering*. Whether this electrode is grounded, and the substrate is put a negative voltage, then the ions will be attracted also by the substrate, bombarding the film during its growth. This effect promotes the impurity released and a reduction of the film defects.

A more efficient sputtering configuration is called *Magnetron Sputtering* where a magnetic field is applied near the cathode surface. The electrons responsible for the ionization starts to move helicoidally around the magnetic field lines, and because also the electric field is present, the global motion is described by the Lorentz's force, $\bar{F}_L$:

$$\bar{F}_L = q(\bar{E} + \bar{v} \times \bar{B}) \tag{3.1}$$

The direction of the electrons is perpendicular to both the electric and the magnetic field as the *drift velocity* $\bar{v}_D$ shows:

$$\bar{v}_D = \frac{\bar{E} \times \bar{B}}{B^2} \tag{3.2}$$

The drift velocity reaches its maximum value when the electric and magnetic fields are perpendicular to each other. Since ions are heavier than electrons, and the magnetic field used is rather small, in the order of $200Gauss$, they are not subjected to this helical motion.

A magnetic confinement of the electrons is established because of their helical motion around the magnetic field. Hence the electrons are not lost on the chamber wall anymore, and the ionization efficiency is maximized. The higher ionization efficiency allows to deal with lower Argon pressure than in a diode configuration, with the advantage of less impurity deposited during the film growth. The sputtering efficiency is therefore maximized using a magnetron sputtering configuration.

3.3 MAGNETRON SPUTTERING SYSTEM

The system used for performing the Niobium sputtering on 6GHz Copper cavity is schematically shown in Figure 3.3. The system consists in: a Niobium cathode, a vacuum chamber, an external coil. The Niobium cathode during the sputtering process is put at high negative voltage, whereas the vacuum chamber is grounded. The vacuum chamber is connected with a pumping system and an Argon line, in this way it is possible to reach a good primary pressure before the process (in the range of Ultra High Vacuum). During the sputtering instead the Argon gas is allowed to flow into the chamber in order to reach a pressure in the range of Medium-Low Vacuum. The pumping system is composed by two pumps, a turbo-molecular ($60l/s$) and a rotary pump ($20m^3/h$), and by one full-range gauge (with a Pirani and a Bayard-Alpert gauge) which reads the pressure inside the system.

During the sputtering process the external coil is fed using a power supply and it produces a magnetic field whose field lines are, approximately, parallel to the cathode, at the center of the coil.

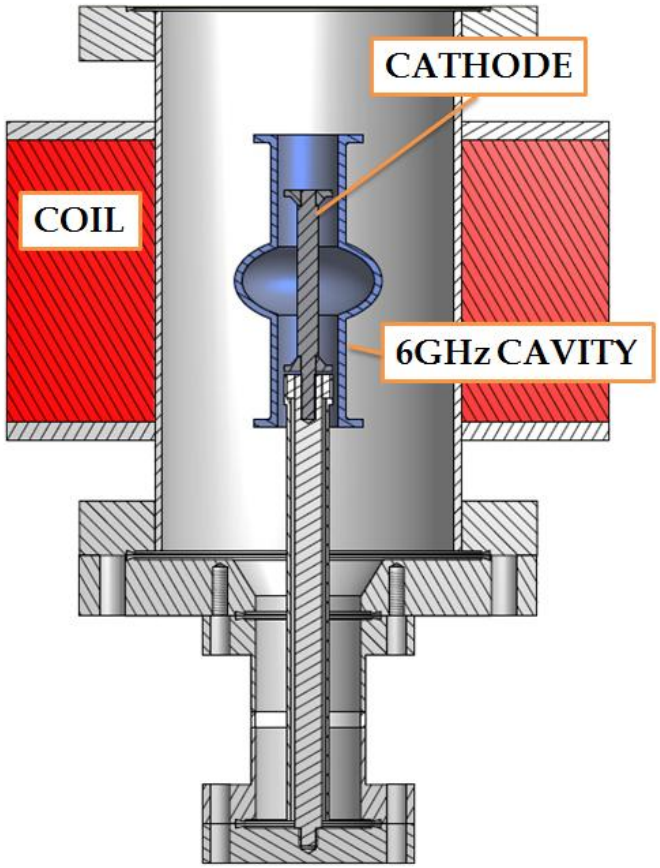

FIGURE 3.3 - SCHEMATIC VIEW OF THE SYSTEM USED FOR NIOBIUM SPUTTERING.

During the process the electric field is radial respect to the cavity axis and the magnetic field is orthogonal to the electric one. When the glow discharge occurs Argon ions, Ar^+, are produced close to the cathode surface so the most part of them will impact on the target.

The cathode has a cylindrical shape and it ends with two Niobium wings, that are necessary in order to minimize the electrons lost during the process. Indeed the wings act as an electrostatic mirror because they have the same negative voltage as the cathode. Thus ,the electrons move with a spiral motion up and down around the cathode, allowing to create a plasma sheet around the cathode itself. The overall electrons motion is sketched in Figure 3.4.

Where the electric and magnetic fields are orthogonal to each other the cathode erosion reaches its maximum value. Using an external coil around the cathode, the magnetic field is quite perpendicular to the electric one and sputtering yield is then maximized. Such a system is called *Post Magnetron*, and its employment has different advantage since it does not use any internal magnets. The magnets implementation would need a cooling system inasmuch their demagnetization occurs whether its Curie temperature is reached.

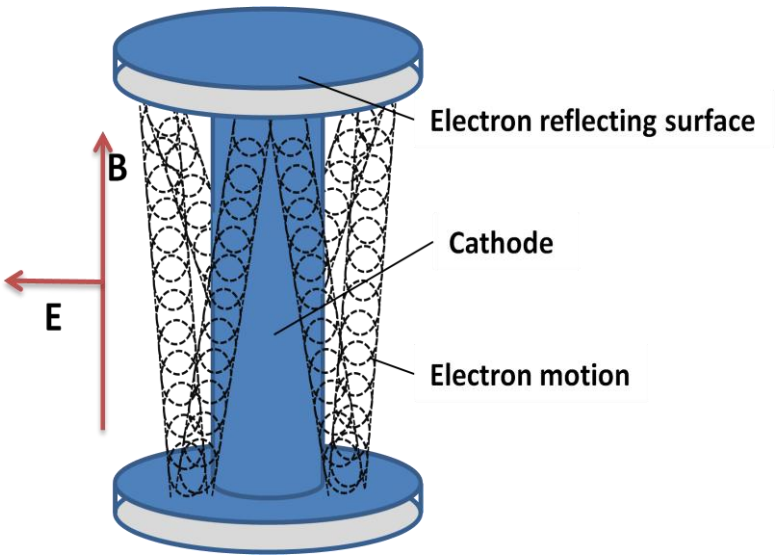

FIGURE 3.4 - SCHEME OF THE CATHODE AND THE WINGS THAT ACT AS A ELECTRON MIRRORS.

The 6GHz cavities have a very small cut-off diameter and the insertion of the magnets and the cooling system is not of easy implementation inside the cathode profile. For this reason the Post Magnetron System is the most suitable configuration to implement the Niobium sputtering on 6GHz cavities.

In the previous section it was shown that sputtering configuration with the cathode longer than the cavity was already studied, using both a post-magnetron configuration and a conformal configuration in which the magnets were inserted into the cathode.

For this thesis research the cathode is a Niobium cylinder $7mm$ wide and $60mm$ length, it ends with two wings that have $12mm$ as diameter. The cathode is therefore smaller than the cavity and it is possible to define three key cathode-cavity positions (Figure 3.5):

- Low position: the cathode fill completely the upper cut-off and the cell of the cavity.
- Central position: the cathode fill the cell and half upper cut-off and half lower cut-off of the cavity.
- High position: the cathode fill completely the lower cut-off and the cell of the cavity.

It is clear that in order to sputter the whole inner surface of the cavity, a linear movement, which allows the cavity to reach these three position, is required.

A linear movement of the cavity is realized in order to maintain the magnetic field as parallel as possible to the cathode surface. The cathode position must be at the center of the external coils which generates the magnetic field.

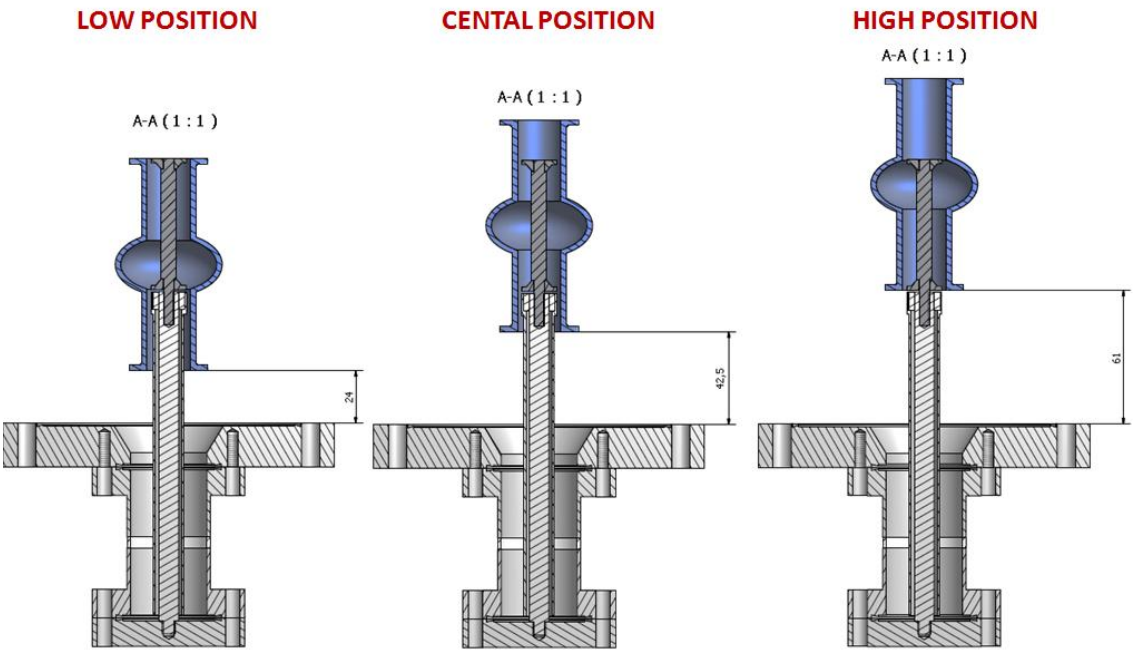

FIGURE 3.5 - REPRESENTATION OF THE KEY POSITIONS OF THE CATHODE INTO THE CAVITY.

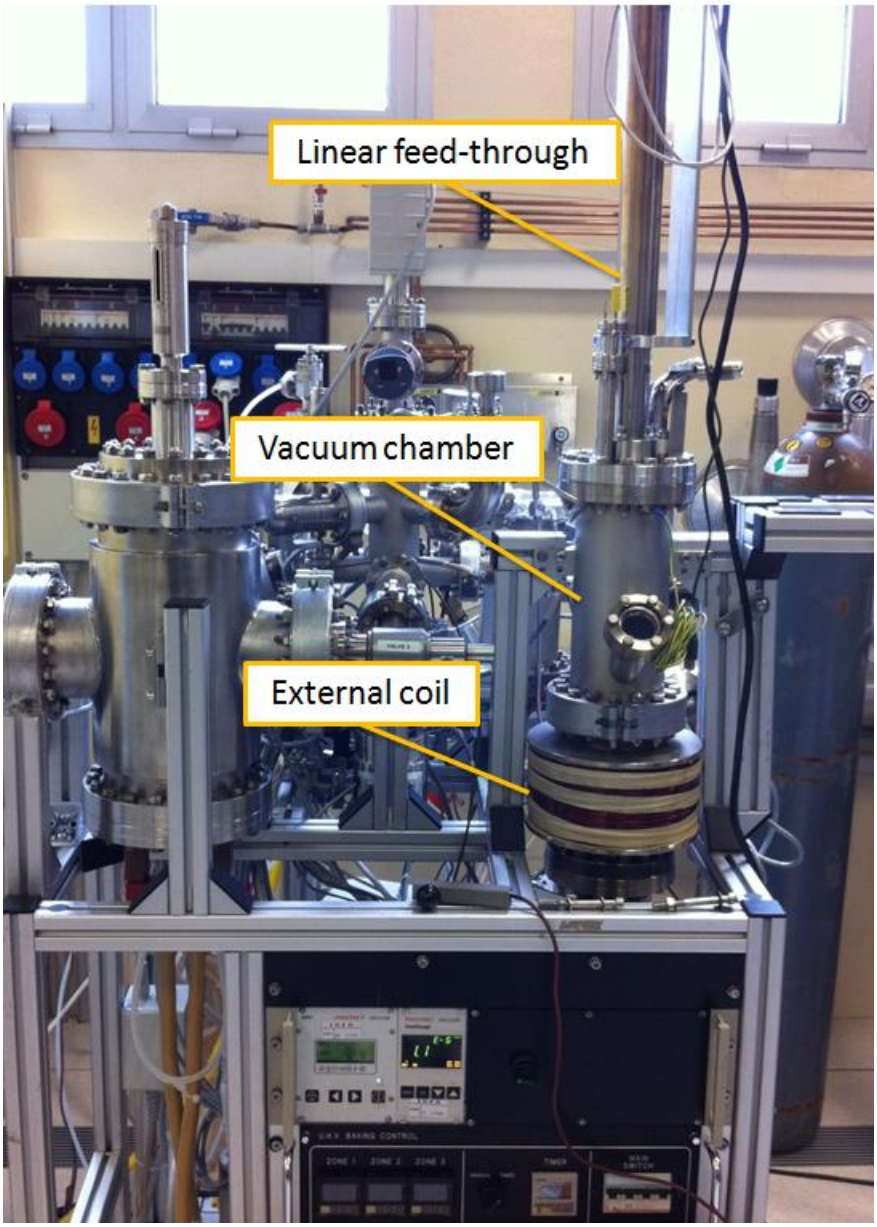

FIGURE 3.6 - PHOTO OF THE SYSTEM USED FOR THE NIOBIUM SPUTTERING DEPOSITION.

The system is therefore provided with a vacuum linear feed-through in which the cavity is mounted, as it is shown in Figure 3.6. The linear feed-through is supplied by a stepper motor which allows to choose the speed and the coordinates of the cavity motion. The stepper motor is interfaced with a Lab View program where these parameter can be fixed as desired.

3.4 SET UP FOR NIOBIUM DEPOSITION

3.4.1 CHOICE OF THE SPUTTERING PARAMETER

Different parameter can be changed during a magnetron sputtering process, as: the current, the voltage, and the power set at the cathode, the Argon working pressure and the magnetic field.

The cathode can be fed in current, in voltage or in power by using a power supply, the mode depends on what parameter one prefers to govern. A discharge in vacuum, with a constant distance between the cathode and the anode at low pressure, follows a characteristic voltage-current curve, that is shown in Figure 3.2. Therefore, monitoring the trend between current, voltage and power is it possible to check whether the process is really given by a sputtering deposition, i.e. if it follows the abnormal glow discharge characteristic curve..

Moreover, the parameters have to be chosen taking into account that the cathode is not cooled and it can increase its temperature prominently during the Argon ion bombardment, specially by using high cathode current. Thus it is important not to achieve temperatures near the Niobium melting point. Actually the Niobium cathode is screwed on a stainless steel support and, because it has a lower melting temperature than Niobium, one has to be careful to do not reach such temperature.

The parameters were tested without inserting into the chamber any substrate, in this way it was possible to see directly the cathode inside the vacuum chamber and to monitor its color during the process. When the cathode reaches high temperature it becomes incandescent, and one can see the emission of light associated with a color change. In Figure 3.7 it is shown the system used at this purpose.

The parameters that were modified during the test are: the working pressure (that is the pressure due to the Argon gas), the cathode current and the coil current (which determines the magnetic field). The cathode voltage and power were instead monitored during the time. The preliminary pressure, the pressure reached before the introduction of the Argon gas, was: $p = 4.5 \cdot 10^{-8} mbar$. The results found with this test are displayed in Table 3.1.

FIGURE 3.7 - PHOTO OF THE SYSTEM USED FOR TESTING THE NIOBIUM SPUTTERING PARAMETERS.

Looking at the first attempt, both the cathode voltage and power were not very stable, and higher than those found by using higher magnetic field or higher working pressure. It means that the cathode surface was dirty, probably covered with an oxide surface layer which during this run was sputtered away. Regarding the others tests, the parameters were quite constant and it can be note that the cathode voltage and the power decreasing by increasing the working pressure or by increasing the magnetic field, with the same cathode current set. Indeed in both cases the Argon ionization becomes higher, and the plasma resistance decreases.

The cathode current is a measurement of the ions that strike the cathode, so whether the plasma density increases, also the cathode current grows. For sputtering process higher plasma density is usually required. From this test one can declare that the best parameters are: $I = 0.1A$ as cathode current, $H = 275Gauss$ as magnetic field and $p = 2 \cdot 10^{-2}mbar$ as working pressure. At the end of this run the cathode becomes incandescent, so it is important to keep in mind that the sputtering cannot be done for long period of time by using this setting. The value of the magnetic field is found out by using the *characteristic curve* of the coil which correlates the current with the magnetic field.

TABLE 3.1- PARAMETERS MONITORED DURING THE SPUTTERING TEST.

Working Pressure $p = 8 \cdot 10^{-3} mbar$						
N. Attempt	**I^{Coil}[A]**	**V^{Coil} [V]**	**B^{Coil} [Gauss]**	**I [A]**	**V [V]**	**P [W]**
1	4	6.26	225	0.05	820÷764	43÷38
2	4.5	7.14	250	0.05	616÷550	30÷25
3	5	7.88	275	0.05	584÷520	24÷19
Working Pressure $p = 1 \cdot 10^{-2} mbar$						
N. Attempt	**I^{Coil}[A]**	**V^{Coil} [V]**	**B^{Coil} [Gauss]**	**I [A]**	**V [V]**	**P [W]**
4	4	6.39	225	0.05	606÷597	29
5	4.5	7.16	250	0.05	535÷463	27÷23
6	5	8	275	0.05	440÷420	21
Working Pressure $p = 2 \cdot 10^{-2} mbar$						
N. Attempt	**I^{Coil}[A]**	**V^{Coil} [V]**	**B^{Coil} [Gauss]**	**I [A]**	**V [V]**	**P [W]**
7	4	6.39	225	0.05	395÷407	20
8	4	6.39	225	0.1	410÷419	43÷40

3.4.2 SPUTTERING ON QUARTZ SAMPLES

The first sputtering was made by using a dummy cavity in which some Quartz samples were fixed. The dummy cavity was mounted on the linear feed-through and then inserted into the vacuum chamber.

It is necessary to do a *baking* of the entire vacuum system before to do the sputtering process. During the baking process the system is heated at $T = 150°C$. Thanks to the high temperature, the molecules adsorbed by the vacuum chamber have enough energy to leave the surface. The molecules desorbed are then pumping away thanks to the pumping system.

The baking of the system was done at $T = 150°C$ for hundred hours.

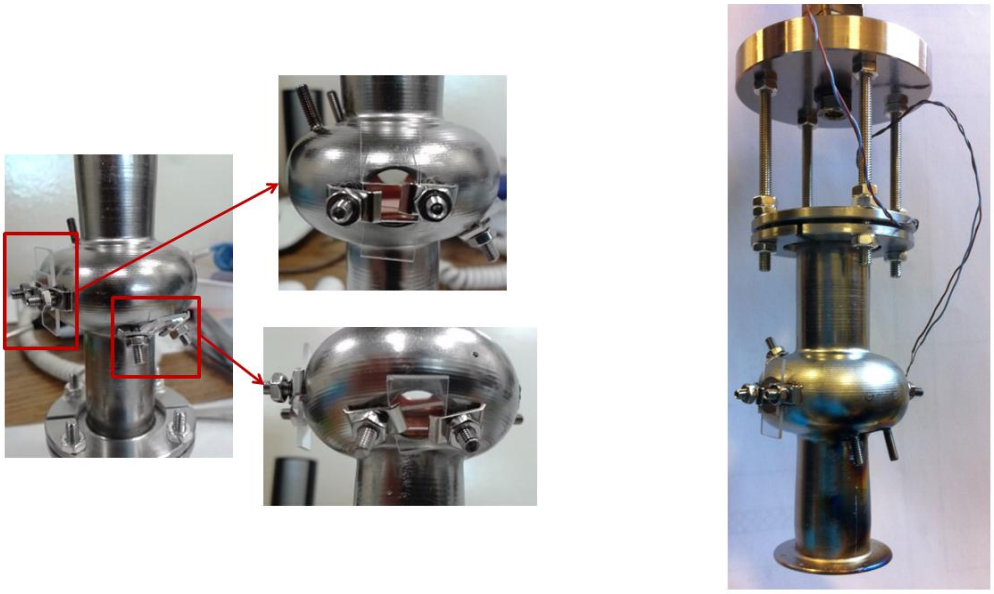

(A) (B)

FIGURE 3.8 - PHOTOS OF THE QUARTZ SUBSTRATES FIXED AT THE DUMMY CAVITY(A) AND OF THE DUMMY CAVITY MOUNTED ON THE LINEAR FEED-THROUGH.

The sputtering into the dummy cavity was made as follows: one sputtering run with the cavity in high position, one with the cavity in lower position and five run with the cavity in central position. Each sputtering run goes on for two minutes, the preliminary pressure was $p = 2{,}2 \cdot 10^{-9} mbar$ and the working pressure $p = 2 \cdot 10^{-2} mbar$. The other sputtering parameters are summarized in Table 3.2.

Initially the parameters found with cathode test were set, but the glow discharge appears only by increasing the working pressure. Then for the next runs the magnetic field was increased so that the Argon ionization is maximized and the plasma can appear at lower pressure.

TABLE 3.2 - PARAMETERS USED FOR DUMMY CAVITY SPUTTERING. THE VALUES INDICATED FOR THE RUNS 3-9 ARE MEANS VALUE.

Cavity Position	N Run	P_{work} [mbar]	T_{cavity} [°C]	I[A]	V[V]	P[W]	I^{Coil} [A]	B^{Coil} [Gauss]
High	1	$6 \cdot 10^{-2}$	80	0.09	1100	70	4	225
Low	1	$2 \cdot 10^{-2}$	75	0.11	400	38	5.5	325
Center	5	$2 \cdot 10^{-2}$	50	0.11	400	40	6	350

After the Niobium deposition the thickness of the two film were measured by using a profilometer, the thicknesses found were about $s = 500nm$. The duration of the sputtering process, considering only the runs done in the center position, was about *10 minutes*. Therefore it is possible to calculate the *deposition rate*:

$$Deposition\ Rate = \frac{Film\ Thickness\ [nm]}{Deposition\ Time\ [min]} = 50nm/min \tag{3.3}$$

The Niobium films deposited were characterized with the *critical temperature* and the *RRR* measurements.

For doing such measurements the sample has to be fixed into a holder whit four metallic contacts that are pressed on the Niobium film. The current flows between the two external contacts whereas the voltage drop is collected by the internal ones allowing to obtain the resistance of the film. Such measurement is called *four-contact* and the great advantage is that it is not affected by the wire resistance. Furthermore the sign of the current injected into the surface is continuously inverted. The mean value of the voltage drop obtained is due only to the real resistance of the sample and it is not affected by a contact resistance. Photos of the system are shown in Figure 3.9.

The sample holder is fixed at one end of a probe, which can be inserted into a Dewar filled with *liquid Helium*. The probe has to be inserted gradually so that the sample can decrease slowly its temperature from $300K$ to $4.2K$. In this way the resistance of the sample is monitored as a function of temperature. The *RRR* of a Niobium thin-film sample is calculated as a ratio of the film resistance at $300K$ and the one just before the critical temperature T_C:

$$RRR = \frac{\rho(300K)}{\rho_{res}} = \frac{R(300K)}{R(10K)} \tag{3.4}$$

The resistivity just before the critical temperature, at $10K$ is the residual resistivity and the ratio between the resistivity is equal to the ratio between the resistance measured with the same geometrical condition. Indeed the resistivity is defined as: $\rho = R\Sigma/l$, where Σ is the surface and l is the sample length, but Σ and l remain the same during the measurements at $300K$ and $10K$.

When the critical temperature of the Niobium film is reached the resistance drops to value so small that become impossible to measure, i.e. the superconducting transition takes place. The critical temperature is then calculated by using the transition curve:

$$T_C = \frac{T_{90\%} - T_{10\%}}{2} \tag{3.5}$$

where $T_{90\%}$ is the temperature at 90% of the transition and $T_{10\%}$ is the temperature at 10% of the transition.

The results show bad characteristics of the film: the critical temperature is smaller than the value found in literature for Niobium bulk, that is $T_C = 9.2\ K$, and the RRR values are very small [3]. This means that the Niobium films do not have either high purity level and good crystallographic properties. The critical temperature is related with the crystallographic properties by the following equation:

$$T_C \approx 1.13\hbar\theta_D e^{-1/(N(0)V-\mu)} \tag{3.6}$$

where $N(0)$ is the density of states at the Fermi level, V is the electron-phonon coupling constant, θ_D is the Debye temperature, and μ is the electron-electron interaction.

FIGURE 3.9 - PHOTOS OF THE HOLD SAMPLE AND THE PROBE FOR THE RRR AND T_C MEASUREMENTS.

TABLE 3.3 - CRITICAL TEMPERATURE AND RRR OF NIOBIUM ON QUARTZ SAMPLES.

Sample Position	**RRR**	**T_C (K)**	**ΔT_C (K)**
Equator	2.87	8.7	$2.4 \cdot 10^{-2}$
Upper cell zone	2.45	8.57	0.23

The electron-phonon interaction V decreases whether the lattice constant increases, causing also the decreasing of the critical temperature. So the low T_C value found means that the Niobium film is grown with large compressive stress.

3.5 COPPER SUBSTRATE TREATMENTS

The treatments of the Copper substrate are very important in order to obtain a good film quality. It was found that whether the film is grown on a smooth surface, the film deposited has less defects and better superconducting properties [14,15].

As was already mentioned the 6GHz Copper cavities, used as a sputtering substrate, are made by spinning [16]. The cavities made by this technique present some damage and scratches in the inner surface. For obtaining a smooth inner surface, the cavity needs both mechanical and chemical treatments.

Therefore, after the fabrication, the following treatments are made:

- **Mechanical polishing**: The cavity is filled with an abrasive media and then it is fixed to a vibrator system. This method, used at LNL to polish the inner surface of the cavity, is called *vibro-tumbling*.

- **Picking**: A mixture of Phosphoric and Nitric acids is used as a primary chemical etching that removes fast the surface impurities as the residuals from the fabrication, tumbling and so on.

- **Electro Polishing** (EP): In this electrochemical process a Copper cathode is inserted into the cavity, which is instead the anode. The inner surface of the cavity is treated with a chemical solution of Phosphoric acid and Buthanol in ratio 3:2. This treatment remove materials from the surface, taking away also the contaminants and the surface oxide layer. This process is usually used to remove hundreds *microns*.

- **Chemical Polishing** (CP): A specific chemical polishing for Copper is a mixture called SUBU which contains Sulfamic acid, Hydrogen peroxide, n-Buthanol and Ammonium citrate. This solution is used at 70°C and it produces a smoother Copper surface by removing only a few *microns.* After the SUBU the cavity is passivated using a diluted solution of Sulfamic acid.

- **Niobium Sputtering**

- **High Pressure Rinsing** (HPR): High purity water at high pressure, of about $100bar$, is directed into the cavity by a nozzle which is fixed just before the cavity as it is shown in Figure 3.12. This process removes the dust particles from the inner cavity surface in order to avoid field emission during the RF measurements.

- **Film Stripping**: The film stripping is done with a solution containing surfactants, Fluoridric and Fluoboric acids.

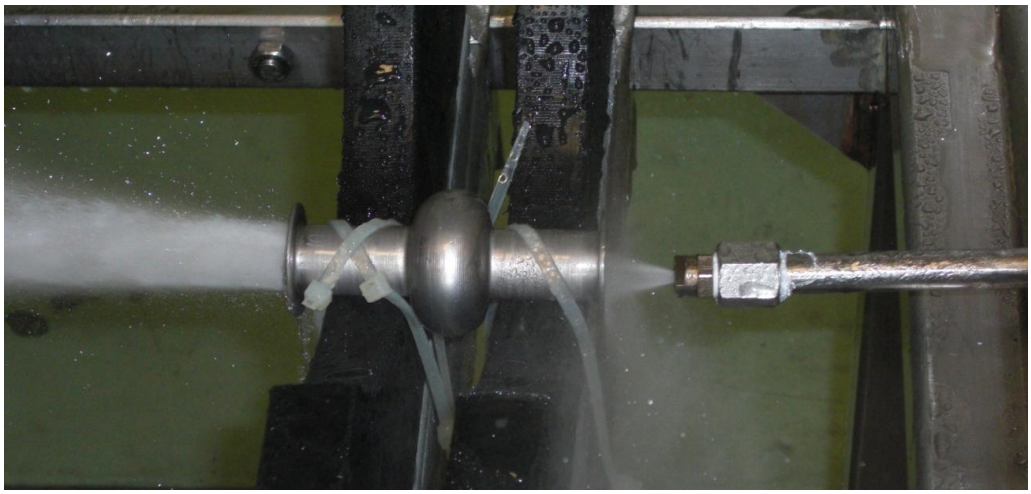

FIGURE 3.10 - HIGH PRESSURE RINSING MADE IN A BULK NIOBIUM 6GHZ CAVITY.

3.6 ROOM TEMPERATURE NIOBIUM SPUTTERING ON 6GHZ CAVITY

3.6.1 FIRST 6GHZ SPUTTERING: CU1_1

The first Niobium deposition was made on the Cu1 Copper substrate, using the same parameters found during the sputtering on the Quartz samples.

A thickness of about $2\,microns$ is required for Niobium thin film accelerating cavities. Since a deposition rate of about $50\,nm/minutes$ it was found by using these parameters, the total deposition time has to be $40\,minutes$.

One run of deposition was done in the high position, one in the lower position and twenty runs were done in the central position. Each run was made for 2 minutes, the preliminary pressure was $p_{preliminary} = 1.7 \cdot 10^{-9} mbar$ and the working pressure was $p_{working} = 2 \cdot$

$10^{-2}mbar$. The current at the external coil was fixed at $I^{Coil} = 6A$ which corresponds a magnetic field of $B = 333Gauss$. The cathode current was fixed at $I^{Cathode} = 0.1A$ and the voltage and the power measured was about $V^{Cathode} = 380V$ and $P^{Cathode} = 30W$. The time of delay between one run and the next depended on the temperature reached by the cavity, it was established that the cavity temperature had not to exceed $T = 100°C$.

The cavity temperature is monitored by using a *K-type thermocouple*. Such thermocouple is made by a *Chromel* ($NiCr$) and *Allumel* ($NiAl$) wire that are welded together in one point, this point is called warm junction and it is at the temperature which has to be monitored. A Copper strip is used for fixing the warm junction at the external cavity surface, Figure 3.11.

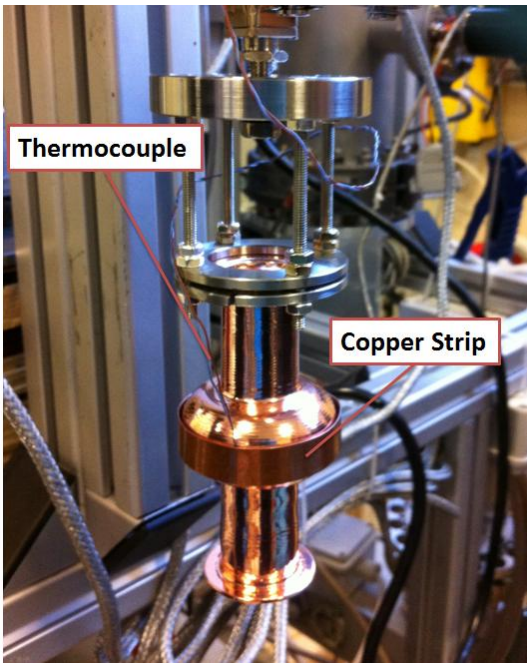

FIGURE 3.11 - PHOTOS OF THE THERMOCOUPLE FIXED BY A COPPER STRIP ON THE EXTERNAL CAVITY SURFACE.

After the deposition the cavity was submitted to High Pressure Rinsing. The HPR caused a partial removal of the film. Fortunately this went away from the cut-off region, and, because the electromagnetic field are presents in the cell region, the RF test was made anyway.

In Figure 3.12 some photos of the film removed by HPR are displayed. In some zones in the cut-off the Niobium film seems to be composed by two different layers. This can be due to the fact that the cut-off region was completely sputtered only for one deposition run, so a discontinuity along the cut-off appears and probably this can also the cause of the film poor adhesion.

3.6.2 SECOND 6GHZ SPUTTERING: CU1_2

After the first sputtering the conclusion was that the poor adhesion is probably due to the non continuous deposition along the entire cavity. The second deposition attempted to optimize the process in order to obtain a good adhesion of the film.

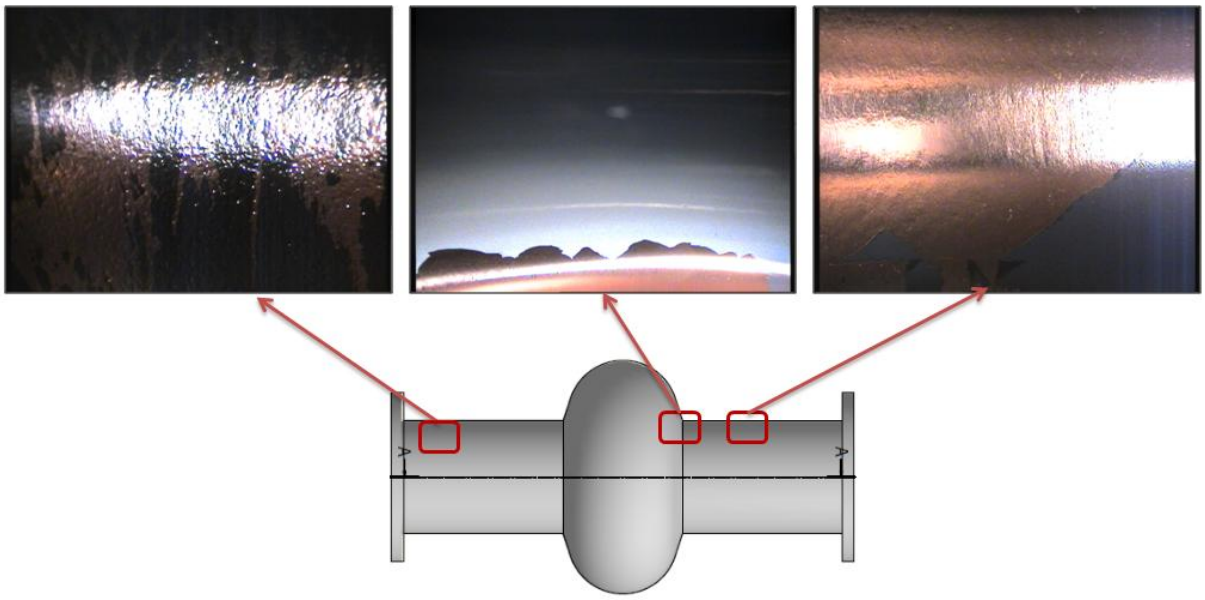

FIGURE 3.12 - PHOTOS OF THE NIOBIUM FILM REMOVED BY HIGH PRESSURE RINSING.

This deposition was done with a continuous movement of the cavity which starts from the high position, reaches the low position and comes back to the started position. The cavity movement is also set with different speed. Let us analyze the forward path of the cavity:

- Low speed: when the cavity starts from the high position
- Slow speed: when the cavity is close to the center position
- Low speed: when the cavity is close the low position

Similarly, the backward path of the cavity has a lower speed near the central position. A scheme of the movement is sketched in Figure 3.13.

The deposition was done by making 20 sputtering runs for two minutes each with the cavity that moved up and down along the cathode length.

The sputtering parameters were the following. Preliminary pressure: $p_{preliminary} = 4.5 \cdot 10^{-9} mbar$, obtained after 36 hours of baking of the system, working pressure: $p_{working} = 2 \cdot 10^{-2} mbar$. The current at the external coil was fixed at $I^{Coil} = 6A$ which corresponds a magnetic field of $B = 333 Gauss$. The cathode current was fixed at $I^{Cathode} = 0.1A$ and the

voltage and the power measured was about $V^{Cathode} = 340V$ and $P^{Cathode} = 28W$. As it was done for the first deposition, the time delay between one run and the next depended on the temperature reached by the cavity, it was established that the cavity temperature had not to exceed $T = 100°C$.

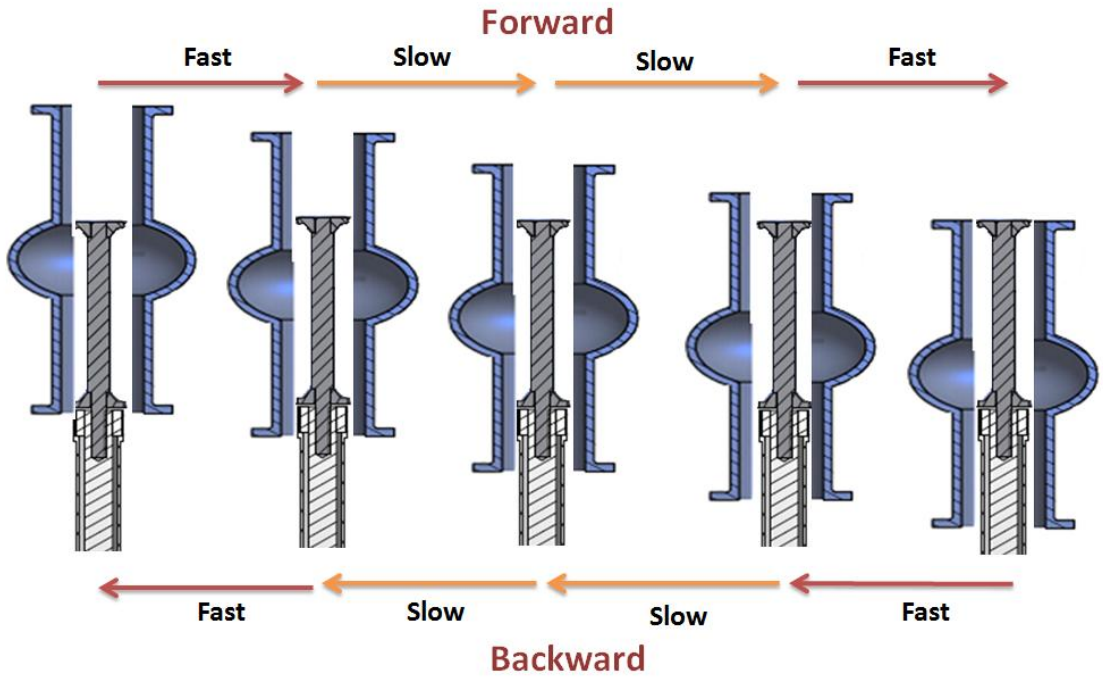

FIGURE 3.13 - SCHEME OF THE CAVITY MOVEMENT DURING THE DEPOSITION.

The RF measurements were made before and after the High Pressure Rinsing, by the way the HPR in this case did not remove the Niobium film.

3.6.3 THIRD 6GHZ SPUTTERING: CU2_1

The third Niobium sputtering was made in the same way that the second one. Indeed it is important to understand whether the poor film adhesion is really solved by doing a deposition with a continuous movement of the cavity.

Unfortunately the HPR caused again the removal of the deposited Niobium film. In this case the film survive practically only in the equator region. At this point it is important to understand whether the film adhesion is better in the equator region or whether the high pressure rinsing is much stronger in the cut-off region. Let us analyze these two hypothesis.

The sputtered atoms are usually emitted with a cosine distribution, so that the cavity equator represents the only region in which the sputtered atoms arrive with zero angle from the cathode surface. Previous studies [17] showed that the arrival angle of Niobium depositing atoms

on the inner surface of the cavity could influence the superconducting film properties. Indeed, atoms arriving at the substrate with oblique incidence are subject to shadowing effects. In the shadowed area there is a lower atom flux and furthermore the diffusion in this zone is limited by the low surface mobility of niobium atoms. It was already demonstrated that the incident angle does not influence too much the roughness of the film [18], but maybe this could cause a worst adhesion at the substrate. This last hypothesis could also explain the bad performance of the Niobium sputtered cavities, indeed the inner cavity surface has a complex shape compared to the usual substrate for sputtering deposition and it is very difficult to have a normal incidence for sputtered atoms.

The nozzle where the water comes out during the HPR is slightly sloping thus the high pressure water strikes first the cut-off and later the whole inner cavity surface. The cut-off is then stricken with higher force than the other cavity surface, and at this point the not well bounded Niobium film comes away from the substrate.

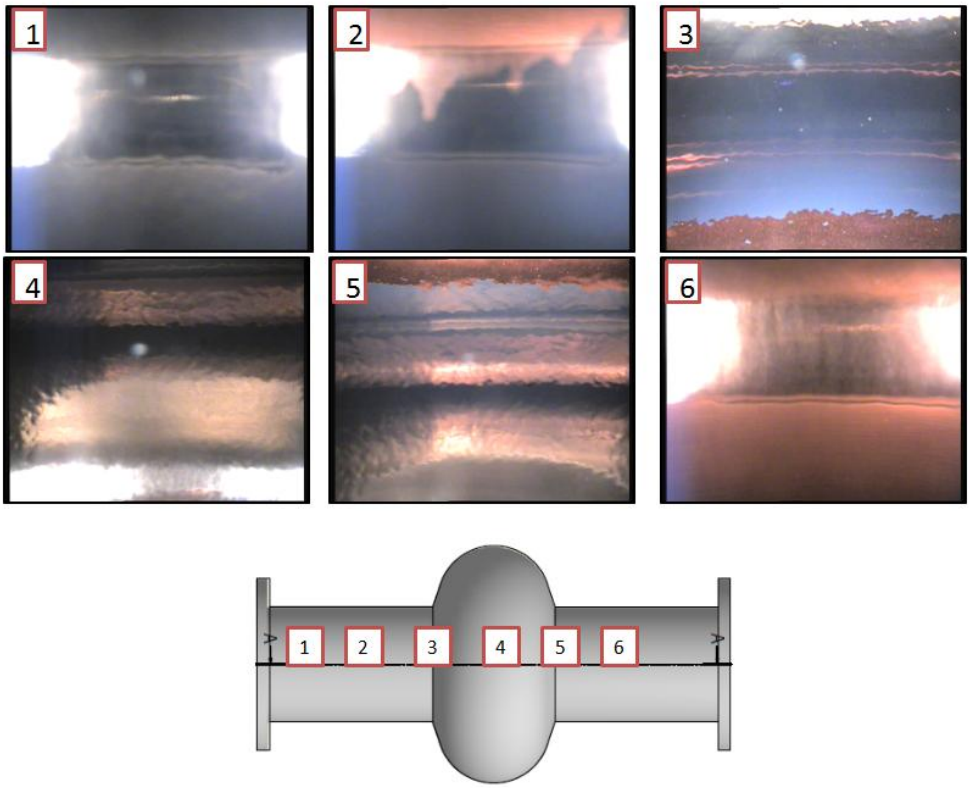

FIGURE 3.14 - SCHEME OF THE CAVITY MOVEMENT DURING THE DEPOSITION.

If the film removal is due to the HPR process, because the high pressure water is too much localized in one point, it will mean that the problem is not the non-normal incidence of the deposited atoms. In the opposite case a new cathode shape should be considered.

3.7 HIGH TEMPERATURE NIOBIUM SPUTTERING ON 6GHZ CAVITY

Sputtering is a physical vapor deposition (PVD), where the species from the gas phase condensate directly on the substrate, growing the films. Depending on its energy, once the atom reaches the surface it can be: adsorbed, re-evaporated from the surface, chemisorbed, physisorbed, diffuse over the surface and interact with other surface species until a low energy site is reached.

The growth depends on different parameters, as: diffusion rate over the surface and into the bulk, desorption, shadowing, and so on. Important parameters for the film growth are also the substrate temperature and the deposition rate. When the atoms have low mobility the film has usually low density and high porosity, and a fibrous structure appears. The grain size of a polycrystalline film is affected by a variety of parameters. Large crystallite sizes are favored by high substrate temperature, high adatom diffusivity during deposition, and high annealing, low deposition flux, and low impurity content, high film thickness, high energy of bombarding ions/atoms [19].

High substrate temperature promotes high atoms surface mobility. The surface temperature supplies energy to the condensed atoms allowing them to move easily over the surface. The higher atoms mobility promotes the decrease of the lattice defect and to improve the crystallinity of the film.

The important parameter for the high temperature deposition is the homologous temperature θ:

$$\theta = \frac{T_{substrate}}{T_{melting\ of\ target}} \tag{3.7}$$

The Figure 3.17 shows the microstructure of the film growth as a function of pressure and homologous temperature. Let us analyze the homologous temperature dependence.

The zone-1 has a low homologous temperature, and the film structure is columnar giving a fibrous texture. Indeed the atoms mobility is low and they tend to remain where they arrived. The porosity is therefore very high and each columns is usually composed by very small grains.

At higher substrate temperatures , zone-T, the small island with large surface and small volume starts to coalesces and the grains become larger. In this range of homologous temperature a local epitaxial growth takes place on individual grains, so the structure is still columnar but now the columns are actually elongated grains.

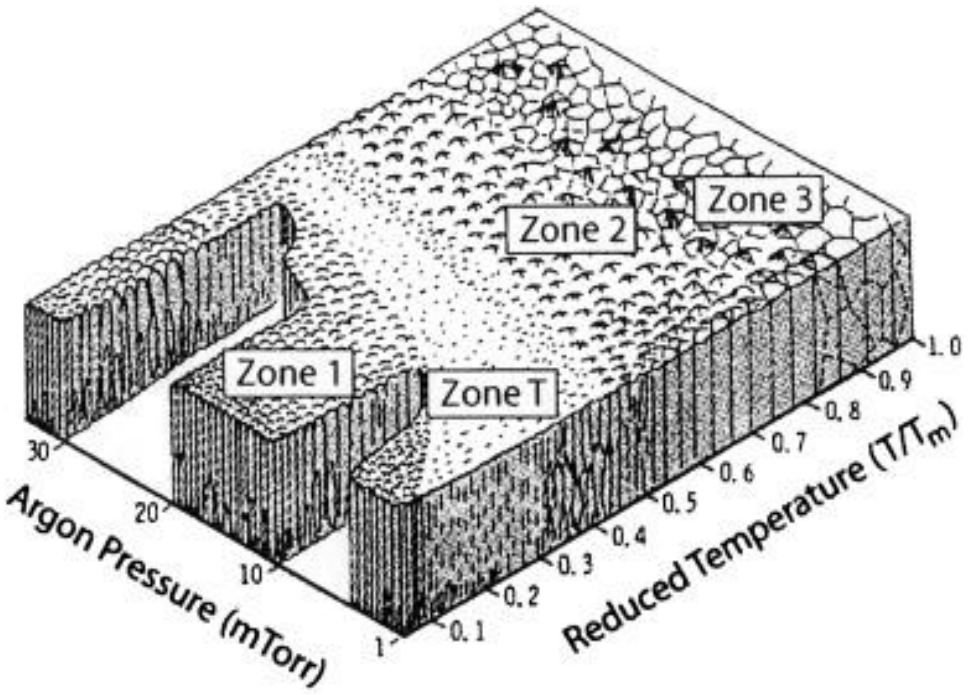

FIGURE 3.15 - REPRESENTATION OF THE DIFFERENT FILM GROWTH ZONE AS A FUNCTION OF PRESSURE AND HOMOLOGOUS TEMPERATURE .

At higher temperatures, zone-2, bulk diffusion becomes significant. During the film thickening process large grains grow at the expense of smaller or unfavorably oriented grains. The zone-3 is instead characterized by a secondary recrystallization, also called abnormal grain growth, after that the film structure is homogenous in the growth direction and composed of columnar crystals [20].

3.7.1 SPUTTERING SYSTEM UPGRADE

The magnetron sputtering system explained in Section 3.3 was used to perform the room temperature depositions. However this system had serious technical limitation and the upgrading becomes essential for realizing the high temperature sputtering.

Often the cavity-cathode alignment was a serious problem. Indeed between the cathode wings and the inner cavity surface there is about two millimeters, this means that whether the cavity is not perfectly centered on its support, it can be scratched by the cathode during the movement. This problem can cause also short-circuit if it happens during the sputtering process.

To avoid this problem, a flexible bellow with three external and adjustable screws is added just on the coil, as it is shown in Figure 3.16. Adjusting the screws, that are arranged in one plain, the coil follows the angular changes and, since the cathode is flanged to the coil also the cathode is moved with the screws adjusting.

3.7.2 FOURTH 6GHZ SPUTTERING: CU1_3

The high temperature sputtering on 6GHz cavity was done in order to obtain good crystallographic film properties.

For heating the substrate it is necessary to insert a heating element inside the vacuum chamber. This is technologically difficult, indeed the vacuum chamber is rather small and the cavity is mounted on a linear feed-through and it moves during the deposition.

As first attempt a heating wire was wrapped up around the cavity as is shown in Figure 3.17. The cavity thus prepared was put into the system but it was not possible to give a stable voltage at the cable, probably the arcs was formed from the inner to the external conductor of the heating wire. This solution seemed not working well and it was so rejected.

The second attempt was made by using a circular heating lamp. The lamp was centered and fixed around the cavity's equator by using a Niobium wire that was fixed at the cavity support. The Niobium wire was covered with a ceramic beads thus the metal wire was not in direct contact with the Quartz's lamp body.

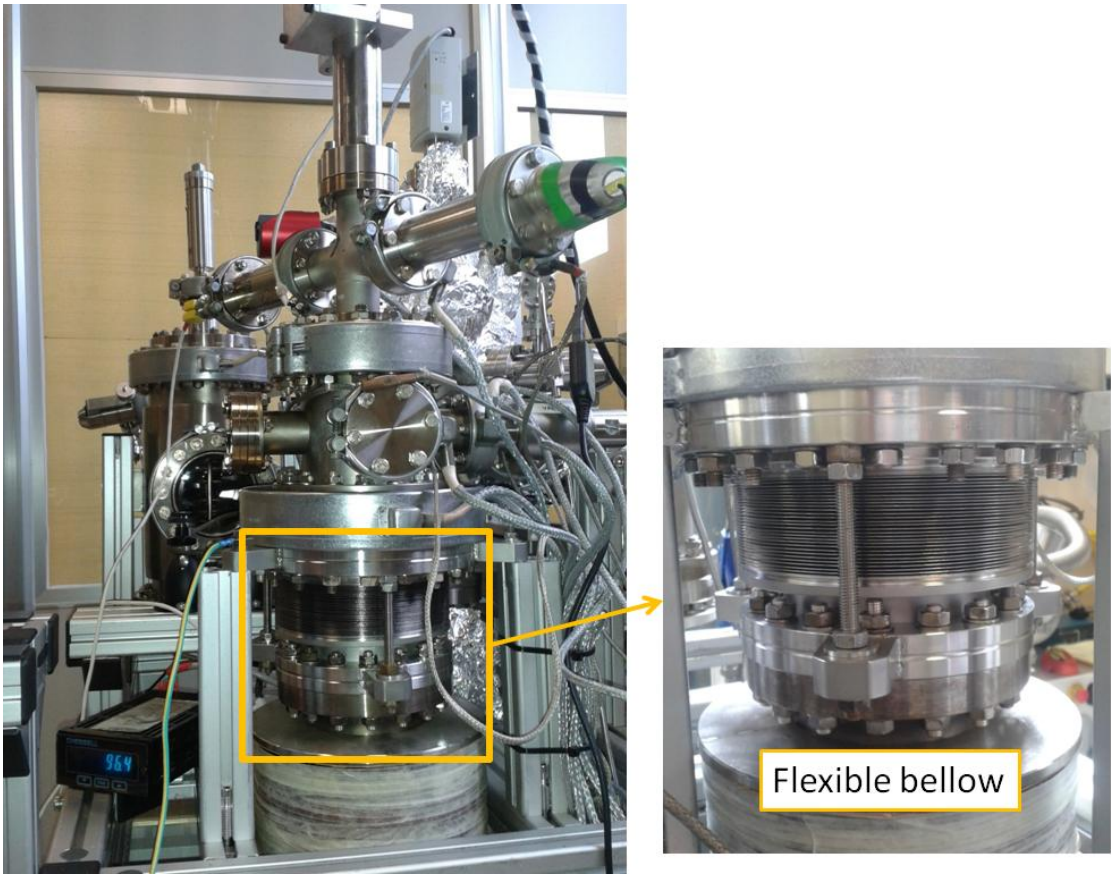

FIGURE 3.16 - PHOTO OF THE NEW SYSTEM USED FOR HIGH TEMPERATURE SPUTTERING, THE FLEXIBLE BELLOW USED FOR CAVITY-CATHODE ALIGNMENT IS HIGHLIGHTED.

Using the lamp, the cavity heating transfer takes place by radiation, so the heat flow from the heater elements to the Copper substrate is given by:

$$Q = \varepsilon_{cavity}\sigma\left({T_{heater}}^4 - {T_{cavity}}^4\right) \tag{3.8}$$

where σ is the Stefan-Boltzmann constant and ε_{cavity} is the emissivity of Copper substrate. The electro-polished Copper has a very low emissivity: $\varepsilon_{Cu\ electro-polished}$~0.03, so the heat transfer is not efficient and it is very difficult to heat the cavity. Furthermore the vacuum chamber is made in Stainless Steel which has higher emissivity than Copper: $\varepsilon_{Stainless\ Steel}$~0.6 so the vacuum chamber may be heated more than the Copper substrate [21].

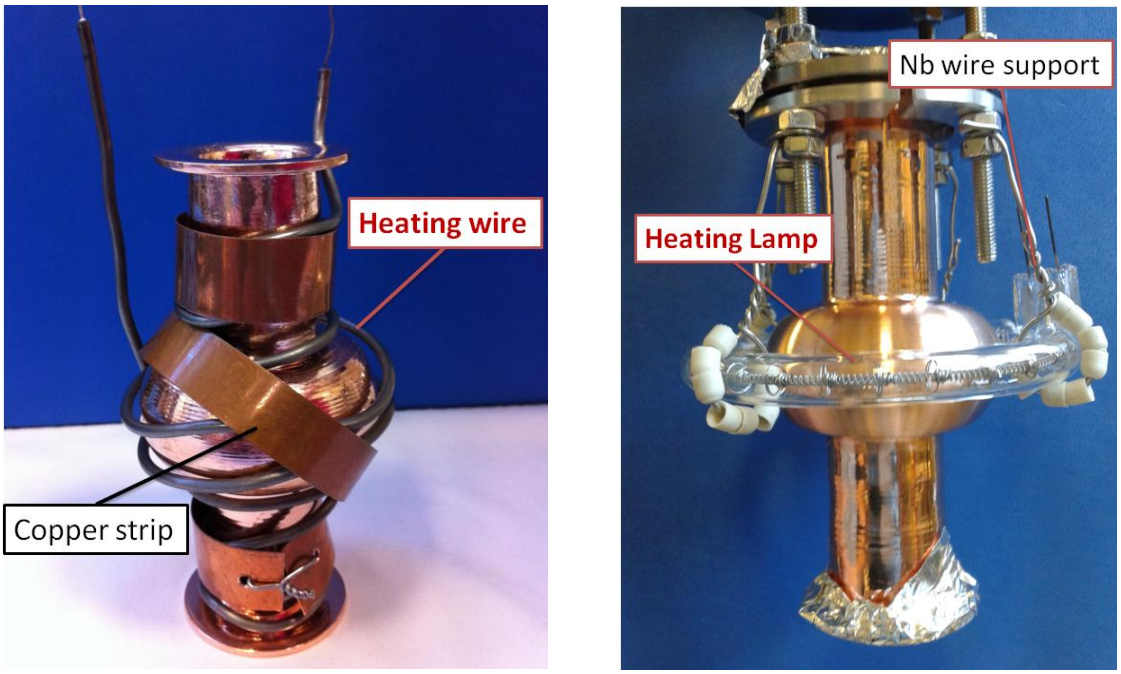

(A) (B)

FIGURE 3.17 - (A) PHOTO OF THE CAVITY SURROUNDED BY A HEATING WIRE, (B) PHOTO OF THE HEATING LAMP FIXED AROUND THE CAVITY'S EQUATOR.

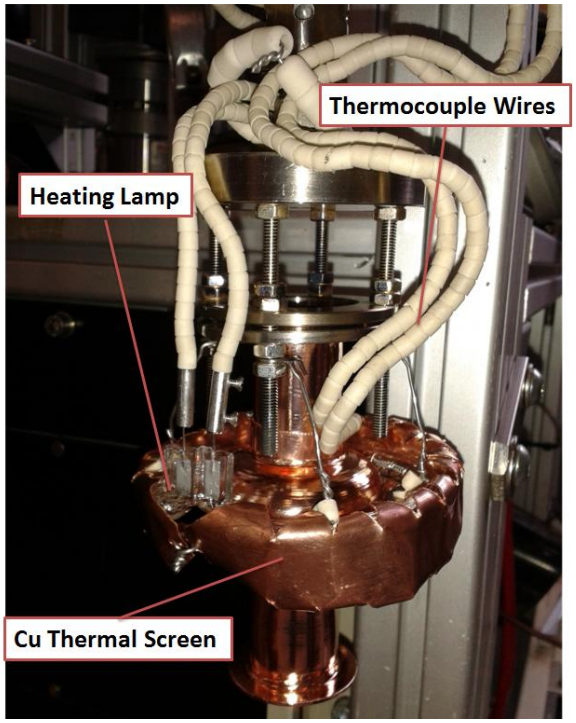

FIGURE 3.18 - PHOTO OF THE CAVITY MOUNTED ON THE LINEAR FEED-THROUGH WITH THE HEATING LAMP AND THE COPPER THERMAL SCREEN.

To avoid this problem it is necessary to use a Copper thermal screen between the substrate and the vacuum chamber. A structure in Copper was made and fixed around the lamp as it is shown in Figure 3.18.

The sputtering process was made by making 25 sputtering run of two minutes, with the cavity heated at $400°C$. As the previous deposition a continuous movement of the cavity was used.

Let us calculating the homologous temperature θ:

$$\theta = \frac{T_{substrate}}{T_{melting\ of\ target}} = \frac{400°\text{C}}{2477°\text{C}} = 0.16 \tag{3.9}$$

unfortunately it is not very high, however the film growth is close to the zone-T mentioned in the previous section, and the grain should be larger than the room temperature deposition case. Using Copper as a substrate it is not possible to reach very high temperature because its melting point is rather low: $T_{melting}^{Cu} = 1084°C$ [22].

The sputtering parameters were the following. A preliminary pressure of $p_{preliminary} = 2 \cdot 10^{-9} mbar$ was obtained after about 36 $hours$ of the baking of the system. During the heating of the substrate the pressure increased because of the higher temperature reached also by the vacuum chamber inner surface. The real pressure before the sputtering runs was about $p_{preliminary}^{after\ heating} = 2 \cdot 10^{-7} mbar$.

The working pressure was, as usual, $p_{working} = 2 \cdot 10^{-2} mbar$. The current at the external coil was fixed at $I^{Coil} = 6A$ which corresponds to a magnetic field of $B = 333 Gauss$. Because of the heating of the entire system the voltage of the coil was not stable and the values oscillated from about $10.4V$ to $12.3\,V$. The cathode current was fixed at $I^{Cathode} = 0.1A$ and the voltage and the power measured were about $V^{Cathode} = 370V$ and $P^{Cathode} = 35W$.

The voltage and the power of the cathode were slightly higher than in the case of room temperature depositions. This change can be appear because at the pressure at $p_{working} = 2 \cdot 10^{-2} mbar$, the number of Argon molecules is less at high temperature than at room temperature, in according with the ideal gas law: $pV = nRT$. Also the number of ionized molecules inside the plasma is smaller and the resistance of the plasma is higher.

In this case the temperature, reached by the coil, was the crucial parameter. Indeed in order to be sure to not damage the coil, in particular the insulating layer around the Copper wire, the heating was turned off when the coil voltage reached value around $12V$.

In addition, because of the increasing of the pressure during the heating, the cleaning of the cathode was made for about 20 $seconds$ before each deposition, maintaining the cavity far from the cathode.

(A) (B)

FIGURE 3.19 - PHOTO OF THE SUBSTRATE SURFACE'S ROUGHNESS. (A) THE CUT-OFF IS FOCUSED, (B) THE CELL IS FOCUSED.

The RF test was made after the High Pressure Rinsing which did not remove the Niobium film deposited. The better film adhesion can be due to the high temperature deposition or to the higher roughness of the Copper substrate, Figure 3.19. In this case the substrate is rough because of the several chemical treatment: stripping, etching, electro polishing. By the way, as disadvantage, the roughness creates shadow zones for the sputtered atoms, compromising the uniformity of the deposition. Because of that, such substrate is usually undesired.

Chapter 4

RF MEASUREMENTS

In this chapter the methods used for characterizing the accelerating cavities are analyzed: the Q-factor measurement at room temperature, the frequency shift measurements done for the QWRs, and the Q-factor versus accelerating field measurements done for both the QWRs and 6GHz cavities. The systems used for the RF measurement done at LNL for 6GHz cavities and at CERN for QWRs are here depicted, it is also explained how such tests are performed in the two cases. The errors in the final graph Q-factor versus accelerating field, for the QWRs measurements, are calculated with two different methods, these are here examined and compared.

4.1 QUARTER WAVE RESONATOR RF TEST

The Quarter Wave Resonator (QWR) RF measurements were made at CERN for the HIE-ISOLDE project. The purpose of this project is to increase the energy gain of the REX-ISOLDE facility by means of a superconducting LINAC. In this way it will be possible to reach higher accelerating gradients, and so higher particle energies (up to $10 MeV/u$). At this purpose the Niobium thin film technology was preferred to the Niobium bulk technology because of the technical advantages like the higher thermal conductivity of Copper and the higher stiffness of the cavities which are less sensitive to mechanical vibrations. The Niobium coating is being optimized on test prototypes which are qualified by RF measurements at $4.5 K$, the working temperature of the HIE-ISOLDE's LINAC. The main method used to characterize such cavity consists of measuring the values of Q-factor, in continuous wave (CW) mode, for different accelerating fields.

The QWRs RF measurement is a vertical test which is done within the V5 cryostat at SM18 at CERN, in Figure 3.2 is shown a scheme of the cryostat. The cavity is maintained in a common vacuum with the cryostat, the pressure is about $p = 10^{-8} mbar$; the Helium liquid is filled into the inner conductor of the QWR and the Helium level is kept constant thanks to a reservoir that is refilled when the Helium level decreases.

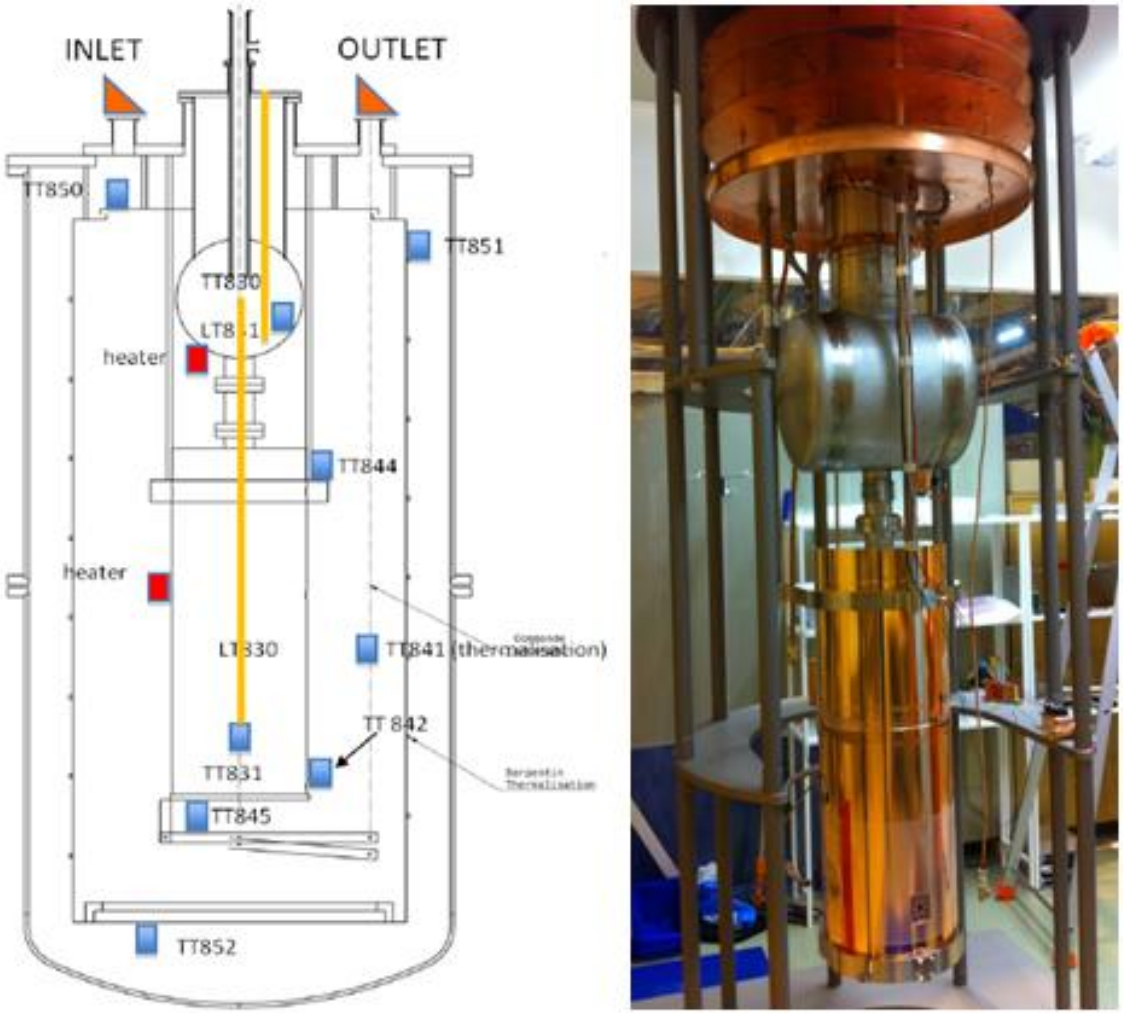

FIGURE 4.1 - SCHEME AND PHOTO OF THE CRYOSTAT USED FOR QWRS RF TEST [23].

The upper part of the cryostat is at $300K$, so four passive radiation screens help to decrease the thermal load from the upper cryostat flange to the Helium bath. The cavity is also surrounded by a thermal shield cooled at $50K$ by Helium gas. Several thermometers are used to monitor both the cavity and the cryostat temperature [23].

The RF system is shown in Figure 4.2 and it is schematized in Figure 4.3. The *RF generator* provides the signal which is split in three different parts: one is send to a PLL system, one to a *frequency meter* and one is send to the *power amplifier* by using a PIN attenuator.

The *Phase-Locked Loop* (PLL) system kept the RF signal at the peak of the cavity resonance, this system is provided of a mixer that is fed with both the generated (forward) and the transmitted signal. The *mixer* compares the two input frequency and gives as output a voltage signal proportional to the phase difference between them. Then the output of the RF box is a DC voltage proportional to the phase error. This signal is used as input for the main RF generator.

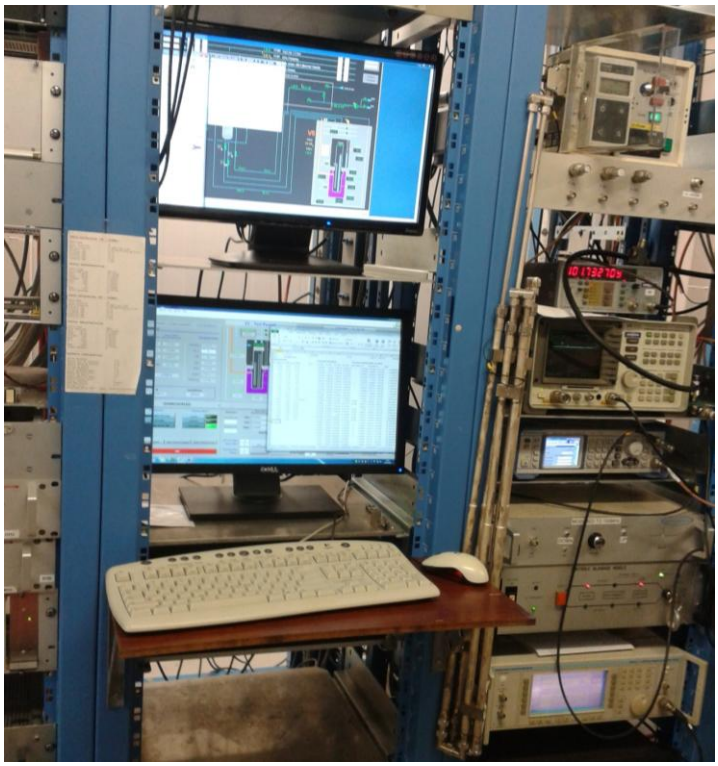

FIGURE 4.2 - PHOTO OF THE RF SYSTEM USED FOR QWRS MEASUREMENTS.

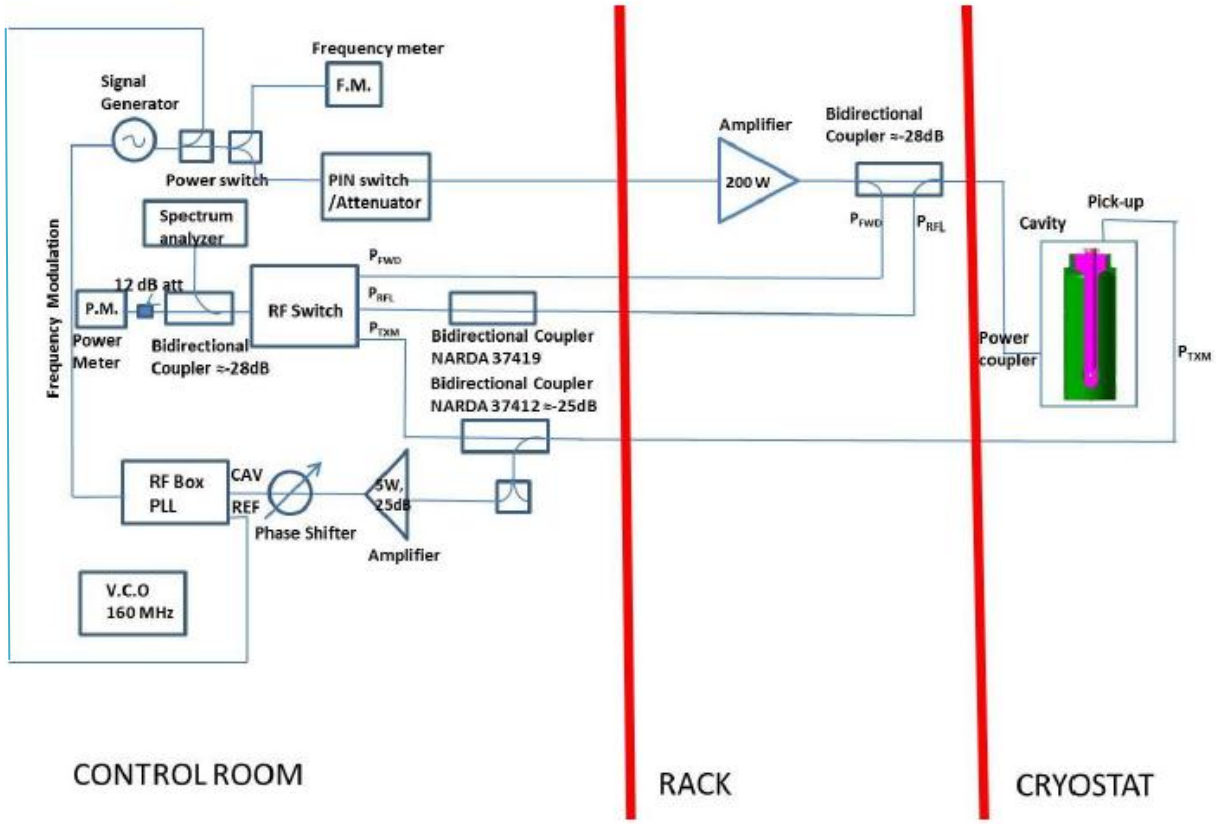

FIGURE 4.3 - SCHEME OF THE RF SYSTEM USED FOR QWRS MEASUREMENTS [24]. COURTESY OF I. MONDINO.

The amplified signal is instead used to drive the *input coupler* of the cavity. The cavity reflects back to the forward line part of the incident power, another part of the power is dissipated inside the cavity and the remaining part of the power is transmitted to the output coupler antenna, *pick-up*. As already mentioned part of the transmitted power is send to the PLL system. The forward, the reflected and the transmitted power are measured by using a power meter.

Before to proceed with the RF measurement, it is important to **calibrate the RF line**. During this calibration the power attenuations of the entire RF line are measured. A scheme of the RF line is shown in Figure 3.2.

The attenuation of the forward, reflected and transmitted powers are obtained as:

$$P_{FWD}^{attenuation} = P_{A\rightarrow FWD} - P_{A\rightarrow C} - COLD\ PART\ (coupler) \tag{4.1}$$

$$P_{RFL}^{attenuation} = P_{B\rightarrow RFL} + P_{B\rightarrow C} + COLD\ PART\ (coupler) \tag{4.2}$$

$$P_{TXM}^{attenuation} = P_{D\rightarrow TXM} + COLD\ PART\ (pick-up) \tag{4.3}$$

It follows that the real forward, reflected and transmitted powers are calculated as:

$$P_f = P_{FWD}^{measured} + P_{FWD}^{attenuation} \tag{4.4}$$

$$P_r = P_{RFL}^{measured} + P_{RFL}^{attenuation} \tag{4.5}$$

$$P_t = P_{TXM}^{measured} + P_{TXM}^{attenuation} \tag{4.6}$$

Once the cables calibration is done, the following step is measuring the **calibration point**.

As it was explained in the theoretical section, the calibration point is done by feeding the cavity with very low field and measuring the forward, reflected and transmitted power, the decay time and the coupling strength.

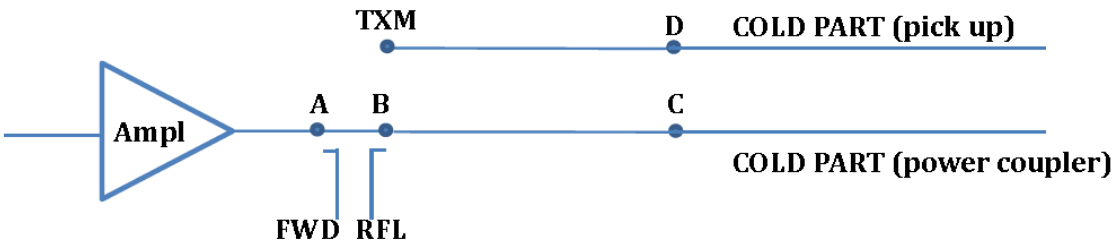

FIGURE 4.4 - RF CABLE LINE SCHEME [24]. CURTESY OF I. MONDINO.

FIGURE 4.5 - VOLTAGE DECAY SIGNAL SEEN BY THE SPECTRUM ANALYZER [24].

The decay time is found out by looking the transmitted voltage from a spectrum analyzer after that the RF is switched off, Figure 4.5. The transmitted voltage is proportional to the square root of the stored energy, so the transmitted voltage decay is given by:

$$V(t) = V_0 e^{-2t/\tau_L} \tag{4.7}$$

From the spectrum analyzer it is possible to measure the time at half of the voltage decay $t/2$ which is related to the decay time with the following relations:

$$ln\frac{V_0}{V(t)} = ln2 = \frac{t}{2\tau_L} \quad , \quad \tau_L = \frac{t}{2ln2} \tag{4.8}$$

With the RF on and low field applied the forward, reflected and transmitted powers are measured, these data are useful to the coupling strength calculation:

$$\beta_C = \frac{1 \pm \sqrt{P_{RFL}/P_{FWR}}}{1 \mp \sqrt{P_{RFL}/P_{FWR}}} \quad , \quad \beta_t = \frac{P_{TXM}}{P_c} \tag{4.9}$$

where P_c is given by: $P_c = P_{FWR} - P_{RFL} - P_{TXM}$. The sign of the β_C equation depends on the coupling regime of the coupler-cavity system, the upper sign is for over-coupling regime and the lower sign is for the under-coupling regime. In order to understand which is the coupling strength regime, the cavity is driven in pulse mode and the reflected signal is observed from the spectrum analyzer. The shape of the reflected signal gives uniquely the coupling regime as is shown in Figure 4.6.

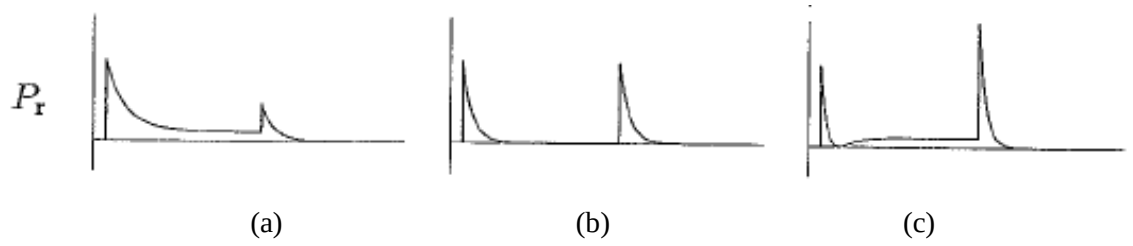

FIGURE 4.6 - REFLECTED POWER IN PULSED MODE. THE SHAPE DEPENDS ON THE COUPLING REGIME: (A) UNDER-COUPLING, (B) CRITICAL COUPLING, (C) OVER-COUPLING.

Now the unloaded quality factor can be calculated as:

$$Q_0 = \omega_0 \tau_L (1 + \beta_C + \beta_t) \tag{4.10}$$

The accelerating field can be also calculated with the measured data:

$$E_{acc} = \sqrt{\frac{U}{k_1}} \quad , \quad U = \frac{Q_0 P_c}{\omega_0} \tag{4.11}$$

where k_1 is a constant which depends on the cavity geometry and in the case of ISOLDE Quarter Wave Resonators it is equal to: $k_1 = 0.207 J/(MV/m)^2$. At this stage the first point of the graph Q versus E_{acc} is obtained.

However the benefit of the calibration point is to find the correlation between the stored energy and the transmitted power, indeed this value is constant during the entire curve measurement. This constant value is the decay time of the pick-up:

$$\tau_t = \frac{Q_t}{\omega_0} = \frac{U}{P_{TXM}} \tag{4.12}$$

and thanks to the calculation of τ_t, the other point of the graph $Q(E_{Acc})$ are more easily calculated.

The graph Q versus E_{acc} is performed in continuous wave mode (CW) by increasing the forward power thus the field inside the cavity is also increased as well as the accelerating field. Then P_{FWR} , P_{RFL} and P_{TXM} are measured at each point and the Q-factor and the accelerating field are calculated using the following equations:

$$E_{acc} = \sqrt{\frac{U}{k_1}} = \sqrt{\frac{\tau_t P_{TXM}}{k_1}} \qquad Q_0 = \frac{\omega_0 U}{P_c} = \frac{\omega_0 \tau_t P_{TXM}}{P_c} \tag{4.13}$$

The QWR's coupler is movable and it can be adjusted before to proceed with the CW measurement. As it was already explained during the calibration point measurement the coupling

strength is calculated. If the value obtained is close to 1, the regime is close to the critical coupling where the matching is perfect. Whether the value of β_C is far from 1, the matching condition is rather poor. This situation can be improved by moving the coupler. This must be moved more inside the cavity whether the regime is under-coupled, and it must be moved outside the cavity whether the regime is over-coupled. Indeed, as it is written in Chapter 2, the cavity field fall off exponentially with distance in the cut-off region, and so, the coupling strength increases with the coupler penetration inside the cavity.

Usually the QWR measurements of Q-factor versus accelerating field done at CERN are performed with different coupling regime, tempting to get closer to the critical condition.

4.1.1 CAVITY CONDITIONING

The cavity conditioning is a procedure necessary in order to avoid multipacting.

Multipacting is a resonant process which takes place once one electron is emitted from the cavity inner surface. This emitted electron is accelerated by the electric field perpendicular to the surface, while the surface magnetic field bends the electron trajectory along quasi circular orbits. Thus, it returns to its point of origin and impacts on the cavity walls producing secondary electrons emission (one-point multipacting). This secondary electrons can be, as before, accelerated and bended by the RF field and , upon impact, they can produce other electrons. If the number of secondary emitted electrons is larger than the number of impacting ones and whether the electrons trajectories satisfy specific resonance conditions, the electron currents will increase exponentially. This condition arises when the *secondary emission coefficient* (SEC) is larger than one, this coefficient is material dependent. It was found that for Niobium at energies between 150 and $1050eV$ the SEC is larger than one, however, this value is actually very sensitive to adsorbates at the surface and it can change considerably with surface treatments.

Actually the most common scenario in the elliptical cavities is the two-point multipacting in which the electrons trajectories include two impact sites. In the QWRs both the one-point and the two-point multipacting take place.

When multipacting occurs the transmitted power from the cavity remains constant even though the forward power is increased. Indeed the supplied energy is not stored in the cavity anymore but it is converted by the involved electrons in kinetic energy. This implies that by increasing the power the Q factor decreases remaining at a constant value of accelerating field.

The cavity conditioning consists of feeding the cavity with RF power pulsed in amplitude. Usually the pulse time is short, about $100\,ms$ while the repetition rate is long, about $1s$. The power is set at high level and the conditioning is left for several minutes, sometimes hours, until

both the transmitted power and the Q value improve revealing the conclusion of multipacting. This procedure is always done before the CW measurement, when the cavity is still at room temperature and when the cavity is at cryogenic temperature.

4.1.2 HELIUM PROCESSING

The Helium processing is a procedure done in order to avoid field emission.

Field emission is a process in which the electrons escape from the surface as a consequence of applied surface electric field. Indeed this field increases the probability that an electron can tunnel through the work function barrier of the metal. Since field emission is observed to occur from localized sites, it seems that these sites of the surface, such a whiskers or sharp projections, enhance the surface electric field. A temperature map is often used to localize the emitter sites.

The electron ejected from the surface are accelerated by the electric field and when they hit the cavity walls a x-rays Bremsstrahlung radiation is emitted. When field emission occurs the Q value decreases, because the electron current emerging from the surface increases, stealing more and more energy. In this case by increasing the RF power, the accelerating field increases slowly, whereas the Q value falls down until the quench of the cavity is reached.

Once field emission is observed, Helium processing is performed as attempt to destroy the field emitters. The gaseous Helium is injected inside the cavity, until a pressure of about $10^{-5} mbar$ is reached, and then the cavity is fed, in CW mode or in pulsed mode, with high level of forward power. The forward power is chosen near the power level where field emission appeared. This process is then maintained for several minutes and the power is gradually increased.

4.1.3 THERMAL CYCLING

The thermal cycling is usually done to improve the cavity performance. The liquid Helium is removed from the QWR inner conductor and the cavity increases gradually its temperature until the thermal equilibrium is reached, thanks to the external shield, at $50\ K$. Once the Helium is refilled into the inner conductor, the cooling down of the cavity produces a small temperature gradient.

On the other hand, when the QWR is cooling down for the first time, its temperature changes from $300K$ to $4.2K$ and only the inner conductor of the QWR is directly in contact with the liquid Helium so the most part of the cavity is contact cooled. It means that a thermal gradient

is established from the upper part of the cavity to the bottom. This thermal inhomogeneity causes a voltage gradient and, according to the *Seebeck effect*, it induces currents to flow along the cavity surface. The thermoelectric currents generate an additional magnetic flux which can be trapped in the cavity walls. Therefore, whether a normal conducting zones exist on the surface, in a presence of magnetic field, an incomplete Meissner effect occurs before the superconducting transition. The presence of trapped flux influences the residual resistivity, making worse the cavity performances.

Reducing the temperature gradient, i.e. doing the thermal cycling, reduces the probability to incur again in incomplete Meissner effect due to the thermoelectric currents, and, also, the trapped magnetic flux is minimized [25].

By the way, the thermal cycling has not always the same effects and it is not yet clear how exactly it works.

4.1.4 Q-FACTOR VERSUS ACCELERATING FIELD CURVES ERROR ANALYSES

ERROR ANALYSIS VIA PROPAGATION OF UNCERTAINTIES

The first method used for calculating the error bars in the graph Q_0 versus E_{acc} is the **propagation of uncertainty**. It calculates the error propagation for a function of k variables: $y = f(x_1, x_2, \ldots, x_k)$, these variables are directly measured and affects by random errors of size $\sigma_1, \sigma_2, \ldots, \sigma_k$.

Considering to realize n measurements of each variables, and defining x_{ji} as the i-th measurements of the j-th variable it is possible to approximate the function y using a first-order Teylor's series expansion:

$$f(x_{1i}, x_{2i}, \ldots, x_{ki}) = f(\bar{x}_1, \bar{x}_2, \ldots, \bar{x}_k) + \sum_{j=1}^{n} \left(\frac{\partial f}{\partial x_i}\right)_{x_j=\bar{x}_j} (x_{ji} - \bar{x}_j) \tag{4.14}$$

where $\bar{x}_k$ are mean observed values. And the mean value of the function can be written as:

$$\bar{y} = \frac{\sum_{i=1}^{n} f(\bar{x}_1, \bar{x}_2, \ldots, \bar{x}_k)}{n} = \frac{nf(\bar{x}_1, \bar{x}_2, \ldots, \bar{x}_N) + \sum_{i=1}^{n}\sum_{j=1}^{n} \left(\frac{\partial f}{\partial x_i}\right)_{x=\bar{x}} (x_{ji} - \bar{x}_j)}{n} \tag{4.15}$$

The last term in the equation is equal to zero because all the values x_{ji} are closed to $\bar{x}_j$, so:

$$\bar{y} = f(\bar{x}_1, \bar{x}_2, \ldots, \bar{x}_N) \tag{4.16}$$

Expanding now the i-th determination of y_i, around its mean value, by using the first-order Teylor series, one obtains:

$$y_i = f(\bar{x}_1, \bar{x}_2, \ldots, \bar{x}_k) + \sum_{j=1}^{n} \left(\frac{\partial f}{\partial x_j}\right)_{x_j=\bar{x}_j} (x_{ji} - \bar{x}_j) \tag{4.17}$$

The deviation respect to the mean value is:

$$y_i - \bar{y} = \sum_{j=1}^{n} \left(\frac{\partial f}{\partial x_j}\right)_{x_j=\bar{x}_j} (x_{ji} - \bar{x}_j) \tag{4.18}$$

So the variance results:

$$\sigma^2(y) = \frac{\sum_{i=1}^{n}(y_i - \bar{y})^2}{n-1} = \frac{\sum_{i=1}^{n}\left[\sum_{j=1}^{n}\left(\frac{\partial f}{\partial x_j}\right)_{x_j=\bar{x}_j}(x_{ji} - \bar{x}_j)\right]^2}{n-1}$$
$$= \frac{\sum_{i=1}^{n}\left[\sum_{j=1}^{n}\left(\frac{\partial f}{\partial x_j}\right)^2_{x_j=\bar{x}_j}(x_{ji} - \bar{x}_j)^2 + \sum_{l=1}^{k-1}\sum_{m=l+1}^{k}\left(\frac{\partial f}{\partial x_l}\right)\left(\frac{\partial f}{\partial x_m}\right)(x_{li} - \bar{x}_l)(x_{mi} - \bar{x}_m)\right]}{n-1} \tag{4.19}$$

The first term of the equation can be written as:

$$\sum_{j=1}^{k}\left(\frac{\partial f}{\partial x_j}\right)^2 \sum_{i=1}^{n}\frac{(x_{ji} - \bar{x}_j)^2}{n-1} \tag{4.20}$$

Thus:

$$\sigma^2(y) = \sum_{j=1}^{k}\left(\frac{\partial f}{\partial x_j}\right)^2 \sigma^2(x_j) \tag{4.21}$$

at this equation the covariance terms have to be added:

$$\left(\frac{\partial f}{\partial x_l}\right)\left(\frac{\partial f}{\partial x_m}\right)(x_{li} - \bar{x}_l)(x_{mi} - \bar{x}_m) \tag{4.22}$$

If the variables are independent to each other the covariance terms are small and they can be neglected.

In this thesis work the propagation on uncertainty was made considering only the first term, so the variance was calculated using the formula:

$$\sigma^2(y) = \sum_{j=1}^{k}\left(\frac{\partial f}{\partial x_j}\right)^2 \sum_{i=1}^{n}\frac{(x_{ji} - \bar{x}_j)^2}{n-1} \tag{4.23}$$

In the Appendix I all the formula used for this analysis are shown.

ERROR ANALYSIS VIA MONTE CARLO LIKE METHOD

The error bars in the graph Q_0 versus E_{acc} were evaluated numerically with a *Monte Carlo-like method*. When the Monte Carlo method is applied to uncertainty estimation, random numbers are used to randomly sample parameters' uncertainty instead of point calculation make by conventional method. During a measurement a certain state of a system is then described as a small region, characterized by a certain distribution, whose size depends on the accuracy of the measurement itself [26]. This method of uncertainty estimation offers different advantages. Indeed, often the functions are analytically intractable, i.e. the propagation of uncertainly is not feasible. A Monte Carlo method permits instead a direct computation of uncertainly, independently of how much complicated is the function.

The Monte Carlo-like method used as uncertainty estimation was carried out as follows. Several random numbers are generated, 5000 in this case, with a Gaussian distribution around a real measured value, and with a suitable standard deviation. This random number generation is performed for all observables of the experiment, i.e. the attenuation values for reflected, forward and transmitted power, the reflected, forward and transmitted power measured for both the calibration point and each point of the curve, the decay time $(t/2)$ and the resonance frequency.

The quantities Q_0 and E_{acc} are calculated with the same formulas used to generate a real graph, but starting from the generated value instead of from the real ones. In this way 5000 values of the final quantities Q_0 and E_{acc} are calculated and the standard deviations which characterize these populations are interpreted as standard uncertainties of these values.

The standard deviations set for each observable for both the propagation of uncertainty and the Monte Carlo-like methods, are shown in Table 4.1. The standard deviation for the powers depends on the range of the measured value, as indicated in the data sheet of the power meters used (*Rohde & Schwarz NRP-Z11*). The uncertainties of the power measurements, considering that the room temperature fluctuates from $15°C$ to $35°C$, are: $0.81dB$ (from $-67dBm$ to -$19dBm$ and from $+1dBm$ to $23dBm$), and $0.77dB$ (from $-19dBm$ to $1dBm$).

TABLE 4.1- STANDARD DEVIATION OF THE OBSERVABLES OF THE GRAPH $\boldsymbol{Q_0}$ VERSUS $\boldsymbol{E_{acc}}$.

Quantity	***Standard Deviation***
$P_{FWD}^{attenuation}$	$0.1\ [dBm]$
$P_{TXM}^{attenuation}$	$0.1\ [dBm]$
$P_{RFL}^{attenuation}$	$0.1\ [dBm]$
$P_{FWD}^{Cal.Point}$	$0.077\ or\ 0.081\ [dB]$
$P_{TXM}^{Cal.Point}$	$0.077\ or\ 0.081\ [dB]$
$P_{RFL}^{Cal.Point}$	$0.077\ or\ 0.081\ [dB]$
$P_{FWD}^{Cal.Point}$	$0.077\ or\ 0.081\ [dB]$
$P_{TXM}^{Cal.Point}$	$0.077\ or\ 0.081\ [dB]$
$P_{RFL}^{Cal.Point}$	$0.077\ or\ 0.081\ [dB]$
$t/2$	15%
f_0	$1\ [Hz]$

4.1.5 RESONANCE FREQUENCY SHIFT MEASUREMENTS NEAR CRITICAL TEMPERATURE

As it will be largely explained in the data analyzing section, the resonance frequency changes with temperature as a consequence of penetration depth change, in accordance with the *Slater's theorem*.

This theorem asserts that whether a small perturbation is made on the cavity walls, this will produce an unbalance of the electric and magnetic stored energies and the resonance frequency will shift to restore the balance. Considering the finite conductivity of the cavity wall as a perturbation, the resonance frequency shift results proportional to the penetration depth which in turn depends on the temperature [27, 28].

The resonance frequency shift is monitored during the warm-up of the cavity, starting from temperature about $5K$ and overcoming the transition temperature of the cavity. The resonance frequency curve as a function of temperature gives important information about the transition and the cavity surface properties. Indeed fitting this data, the *critical temperature* and the *mean free path* are estimated, allowing to calculate also the RRR and the R_{BCS} of the Niobium film analyzed.

The temperature is acquired using the thermometers: $TT842$, $TT844$, $TT831$ these are fixed at different position as one can notice from Figure 4.1.

4.1.6 ROOM TEMPERATURE RF TEST

At room temperature, about $300K$, the Niobium film of the cavity has normal conductor properties, and the loaded Q-factor, Q_L, can be easily obtained with a network analyzer, from the width of the resonance curve in the frequency domain: $Q_L = \Delta\omega/\omega_0$.

In addition the *standing wave ratio* (SWR) of the coupler can be measured with S_{11} mode and gives directly the value of β_C. As it was described in Chapter 2 the standing wave ratio is defined as:

$$\begin{aligned} \text{SWR} &= \frac{1}{\beta} \rightarrow \text{if undercoupled} \\ \text{SWR} &= \beta \rightarrow \text{if overcoupled} \\ \text{SWR} &= 1 \rightarrow \text{if critically coupled} \end{aligned} \tag{4.24}$$

From the network analyzer it is possible to understand the coupling regime by watching the Smith's charts. These charts are polar plots of the reflection coefficient; the radius of the plot is the magnitude of the ratio of the reflected power to the driven power, the angle is the phase difference between these two signals. In Figure 4.7 the Smith's chart are displayed in the three different regime.

The point of the origin of the graph represents the zero reflection, so: if the loop plotted passes through the origin, then the cavity will be critically coupled, if it contains this point the cavity will be over-coupling and if it is not the cavity will be under-coupling.

Then it is possible to calculate the unloaded Q-factor: $Q_0 = Q_L(1 + \beta_C)$. The contribution of β_t is neglected because it is too much smaller than β_C.

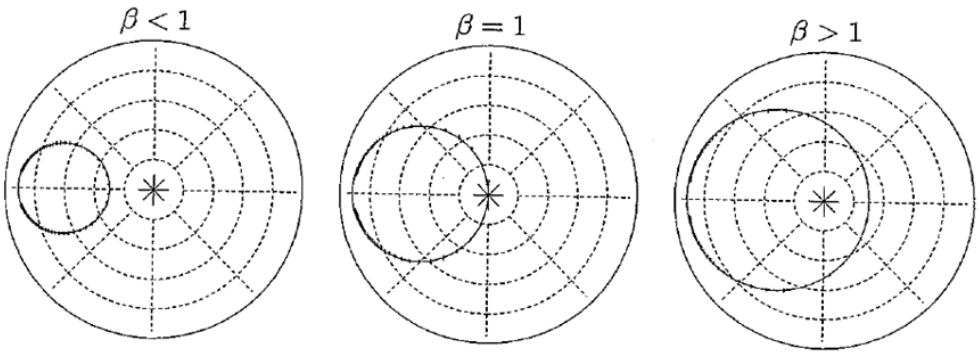

FIGURE 4.7 - THE SMITH'S CHART IN THE THREE DIFFERENT COUPLING REGIME.

A Copper QWR and a thin film Niobium on Copper QWR were measured at room temperature. As it will be explained in the data analyzing section, the Q-warm measurements could be useful in order to characterize the normal conducting properties of the Niobium thin film and, by making a model based on the AC properties of a metal, it is possible to obtain an estimation of the film thickness.

4.2 6GHz Cavities RF Test

The 6GHz cavities RF measurements were made at *National Laboratories of Legnaro* (LNL) with the purpose of study the surface material characteristic of such cavities.

The main method of characterization of 6GHz cavities consists, as before, of measuring the values of Q-factor, in continuous wave (CW) mode, for different accelerating fields.

After the Niobium sputtering and the HPR the 6GHz cavity is mounted on a RF stand; in order to preserve the cleanliness of the inner cavity surface, the assembly of the cavity has to be done in a clean-room. In Figure 4.8 two photos of the cavity mounted in the RF stand are shown. The RF stand is then inserted into the cryostat.

The cryostat used at LNL allows to insert three RF stand for measuring three cavity simultaneously. The cryostat owns two passive radiation screens that help to decrease the thermal load from the upper cryostat flange to the Helium bath; in order to isolate thermally the cryostat from the external environment it is also surrounded by three interspaces, the inner and the external ones are put in vacuum, whereas the one in the middle is filled with liquid Nitrogen.

In the down part of the cryostat, the liquid Helium surrounds completely the cavities, this liquid is in equilibrium with its gaseous phase, which is left to flowing out into a recovery line. The cryostat is also connected to a pumping system which allows to decrease the bath temperature by decreasing the Helium pressure, as it is shown in Figure 4.9. This cooling system allows to perform the RF test from $4.2K$ to $1.8K$. It is important to remember that liquid Helium makes a super-fluid transition when it is cooled before the so-called λ-point: $T_\lambda = 2.168K$. The cavity is then cooled by the normal fluid, He-I, from $4.2K$ to $2.17K$ and by the super-fluid Helium, He-II, from $2.17K$ to $1.8K$.

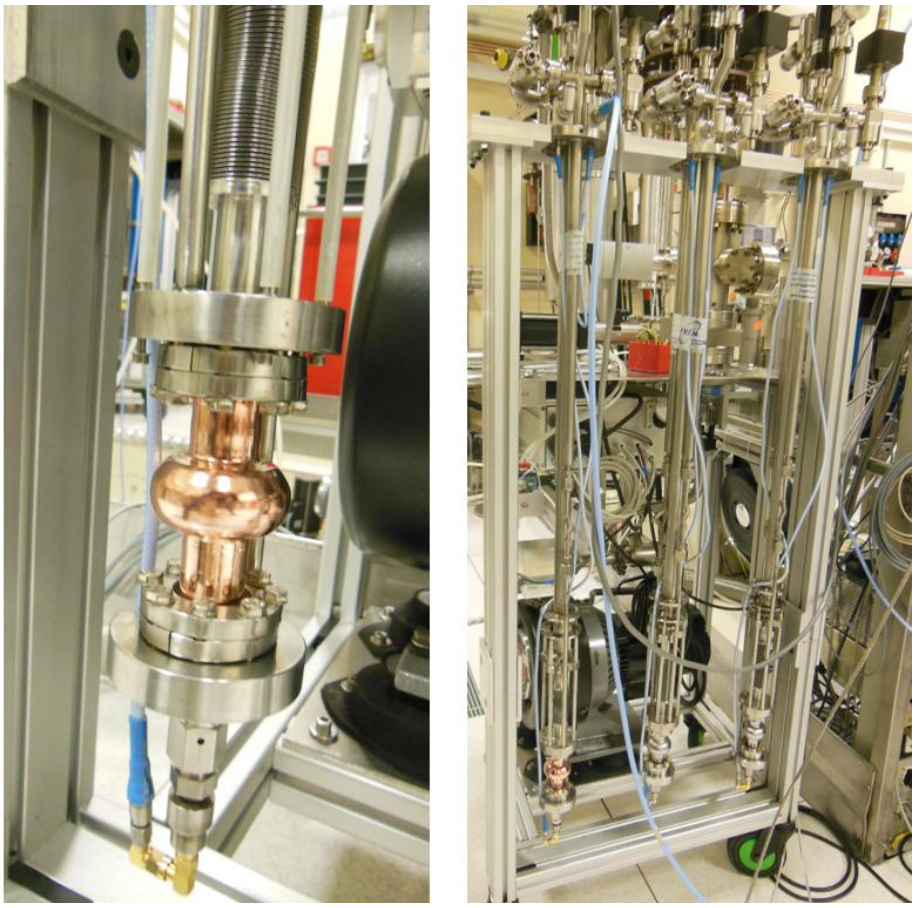

FIGURE 4.8 - PHOTOS OF THE CAVITY MOUNTED IN THE RF DESCENDENT.

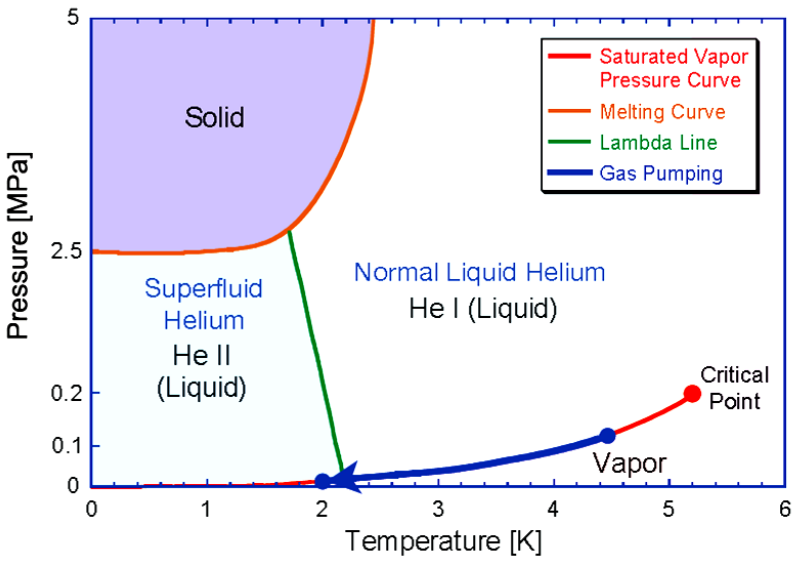

FIGURE 4.9 - PHASE DIAGRAM OF HELIUM.

The RF system is shown in Figure 4.10 and it is schematized in Figure 4.11. The *RF generator* provides the RF signal, as for the QWRs measurements this signal is split in three ones: one is sent to a PLL system, one to a *frequency counter* and one is sent to the RF *power amplifier* by using a PIN diodo attenuator.

The amplified signal is used to feed the cavity at its resonance frequency. A bidirectional coupler allows to measure the forward and the reflected signal, whereas parts of the transmitted signal are sent to the PLL system and to the power meter.

The system is also provided with a linear feed-through connected to a stepper motor which permits the coupler movement and so to choose its insertion level in the cavity. The motor allows to move smoothly the coupler, so its position can be chosen in order to minimize the reflected signal point by point, i.e. the cavity is measure in critical coupler regime.

Before to start the measurements the **RF line calibration** has to be done, in this way the power measured are corrected taking into account the internal dissipation.

The measured power is then multiplied by a calibration coefficient $K^{Correction}$ which takes into account the internal power attenuation of the RF line, as it shown in the following equations:

$$\begin{aligned} P_f^{Cavity} &= P_f^{Measured} \cdot K_f^{Correction} \\ P_r^{Cavity} &= P_r^{Measured} \cdot K_r^{Correction} \\ P_{pk}^{Cavity}(LS) &= P_{pk}^{Measured} \cdot K_{pk}^{Correction}(LS) \\ P_{pk}^{Cavity}(HS) &= P_{pk}^{Measured} \cdot K_{pk}^{Correction}(HS) \end{aligned} \tag{4.25}$$

The calibration coefficients are calculate as:

$$K_{fwr}^{Correction} = 10^{\left(P_{fwr}^{attenuator} + P_{A\to C} - P_{C\to D}\right)/10} \tag{4.26}$$

$$K_{rfl}^{Correction} = 10^{\left(P_{rfl}^{attenuator} + P_{B\to C} + P_{C\to D}\right)/10} \tag{4.27}$$

$$K_{pk}^{Correction}(LS) = 10^{\left(P_{pk}^{attenuator} + P_{F\to G}^{LS} + P_{E\to F}\right)/10} \tag{4.28}$$

$$K_{pk}^{Correction}(HS) = 10^{\left(P_{pk}^{attenuator} + P_{F\to G}^{HS} + P_{E\to F}\right)/10} \tag{4.29}$$

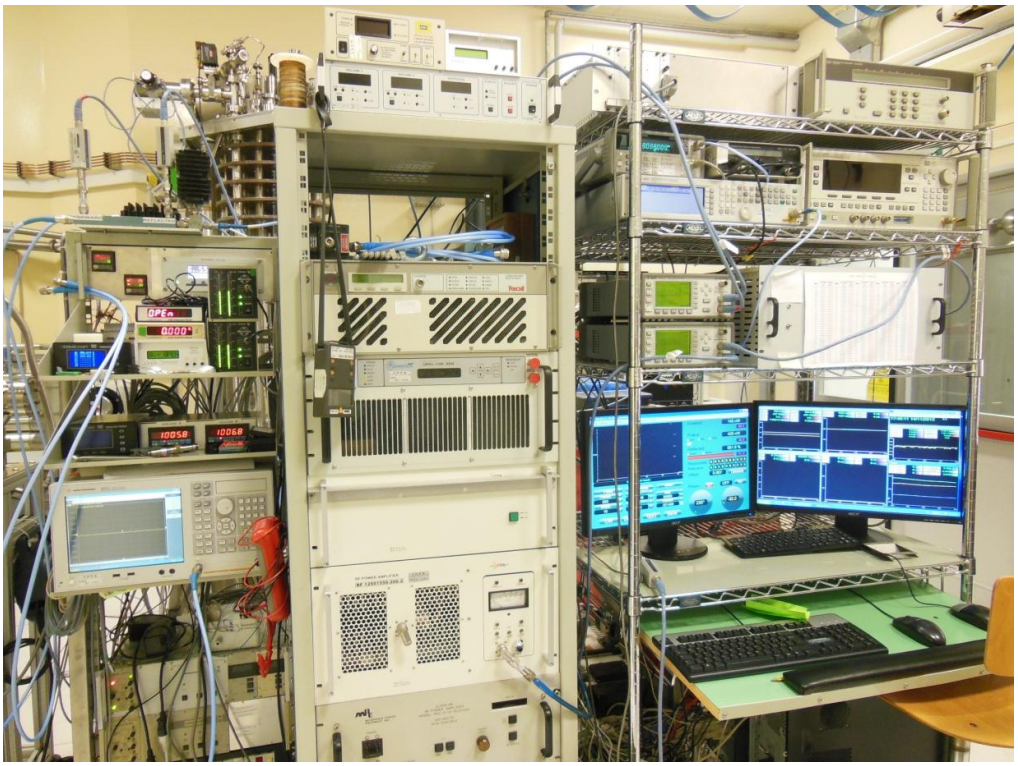

FIGURE 4.10 -PHOTO OF THE RF SYSTEM USED FOR 6GHZ CAVITIES MEASUREMENTS.

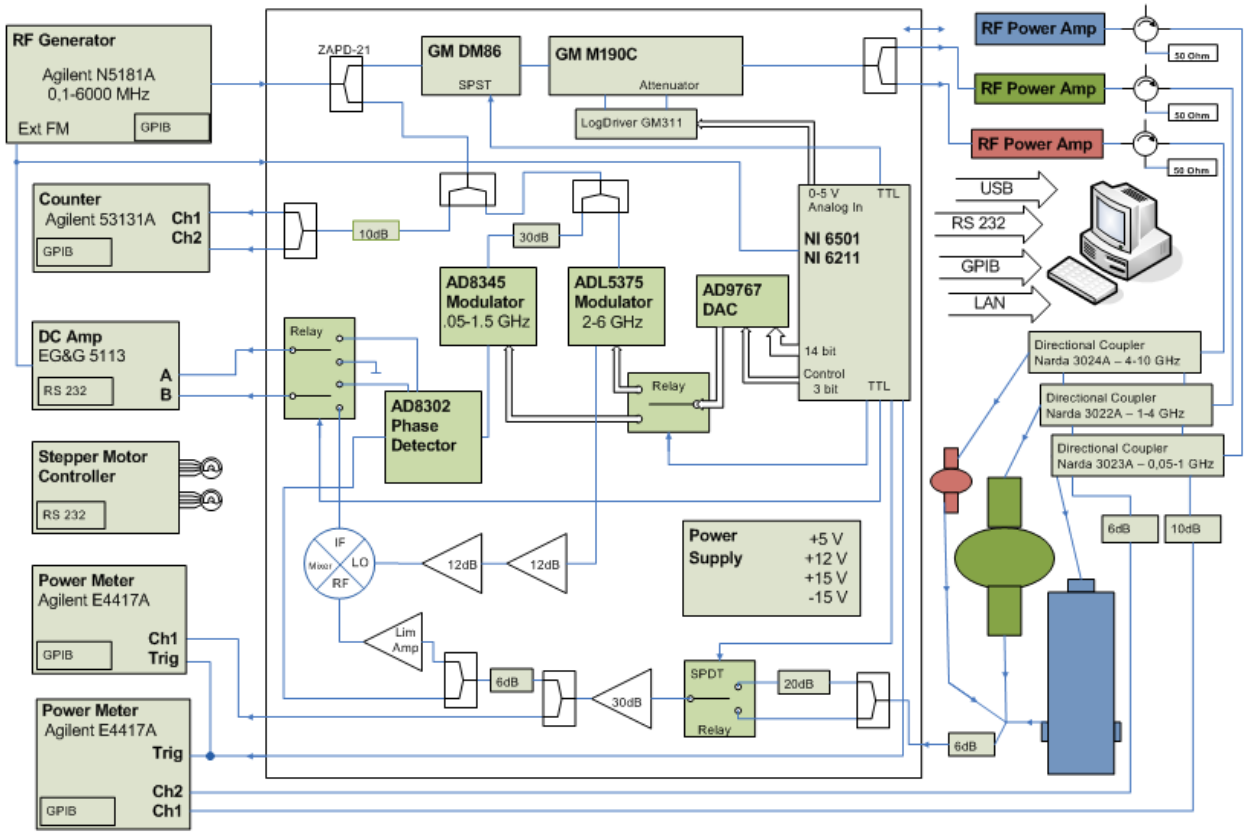

FIGURE 4.11 - SCHEME OF A RF SYSTEM USED FOR 6GHZ CAVITIES MEASUREMENTS. COURTESY OF S. STARK.

Where: $P_{A\to C}$ is the power attenuation given by the forward attenuator and the bidirectional coupler of the forward line, $P_{B\to C}$ is the analogous for the reflected line, $P_{C\to D}$ and $P_{E\to F}$ are respectively the power attenuation of the cables from the cryostat flange to the coupler antenna and to the pick-up antenna. The transmitted line attenuation $P_{F\to G}$ is given by the pick-up attenuator and the pick-up circuit. Whether additional attenuators are connected to the system their attenuations can be considered using the term $P^{attenuator}$.

For the pick-up line, two different correction factors are used, one for the low sensitivity, $K_{pk}^{Correction}(LS)$, and one for the high sensitivity, $K_{pk}^{Correction}(HS)$. The high sensitivity considers an additional attenuation of $20dB$, which is used to expand the dynamic range of the pick-up line.

The calibration coefficient $K^{Correction}$ is a dimensionless value, indeed the power attenuation are measured in dB.

The resonance frequency of the system is as first measured by a spectrum analyzer and then is set to the RF signal generator using a Visual Basics graphic interface. The critical coupling regime is obtained by adjusting not only the coupler position but also changing the phase of the forward RF signal.

The **calibration point** measurement is the first step of the RF test, during this step the cavity has to be fed using low power. So, the decay time of the transmitted power after that the RF signal is switched off is analyzed, Figure 4.13. The data are plotted as a linear function:

$$ln\frac{P_{pk}(0)}{P_{pk}(t)} = \frac{t}{\tau_L} \tag{4.30}$$

Then the decay time is the reciprocal of the slope of the straight line which fits the data. The Q-loaded is now easily obtained: $Q_L = \omega\tau_L$.

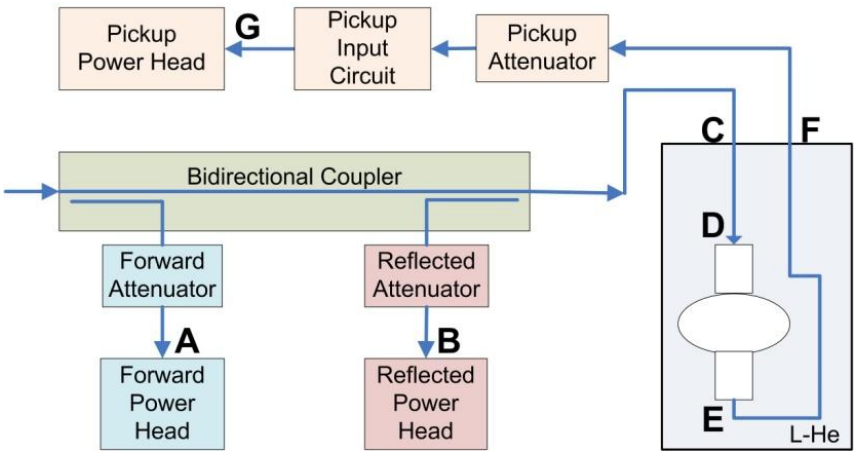

FIGURE 4.12 - SCHEME OF THE RF LINE AT LNL. COURTESY OF S. STARK.

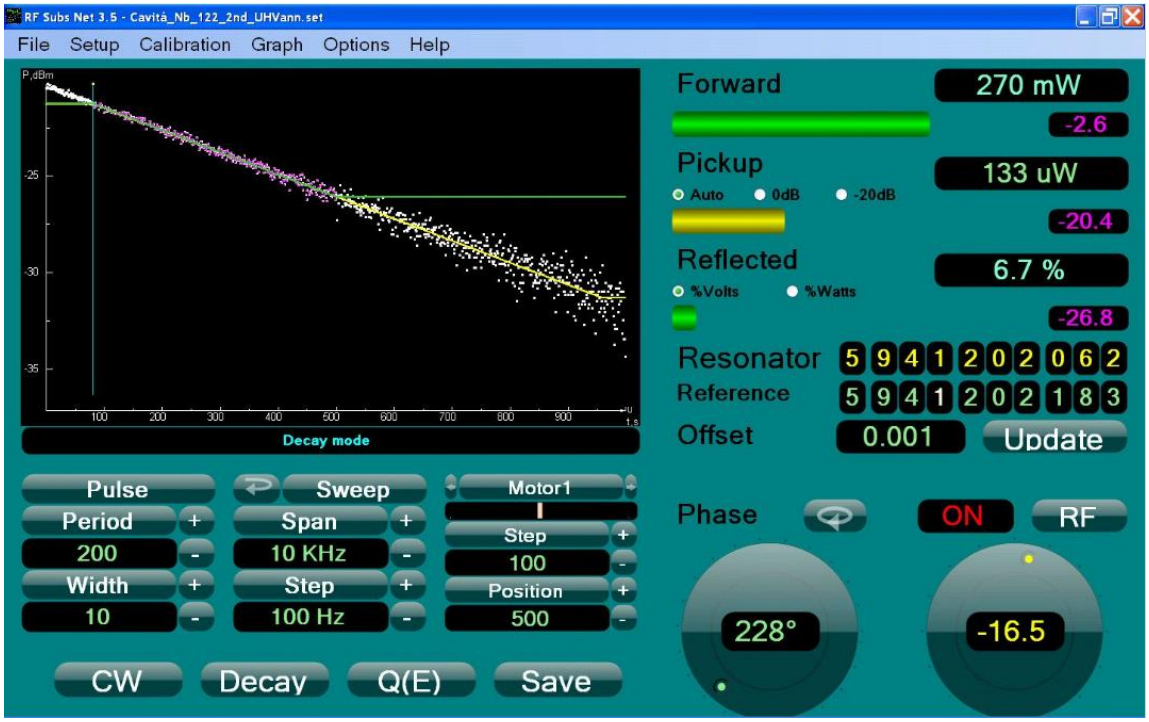

FIGURE 4.13 - GRAPHICAL INTERFACE OF THE PROGRAM USED FOR DOING THE RF MEASUREMENT. THE GRAPH OF THE POWER DECAY USED FOR THE DECAY TIME CALCULATION IS SHOWN.

The program measures the reflected, forward and transmitted power when the RF is on. From these values the power dissipated by the cavity is calculated as:

$$P_{diss} = P_f^{Cavity} - P_r^{Cavity} - P_{pk}^{Cavity} \tag{4.31}$$

Therefore also the cavity stored energy is obtained:

$$U_{st} = \frac{Q_L(1 + \beta_{cp} + \beta_{pk})P_{diss}}{\omega} \tag{4.32}$$

where the coupler coupling strength is $\beta_{cp} = 1$ because of the critical coupling, and $\beta_{pk} = P_{pk}^{Cavity}/P_{diss}$.

Let us define the *capacitance* C and the *active length* L, which is the gap length within the particles are accelerated, of a 6GHz cavity: $C = 0{,}321 \cdot 10^{-12}F$ and $L = 0{,}025m$. By using these geometrical constants the accelerating field and the Q-factor are calculated as:

$$E_{Acc} = \frac{\sqrt{U_{st}/C}}{L} \quad , \quad Q_{point} = \frac{\omega U_{st}}{P_{diss}} = \omega(E_{Acc}L)^2 \frac{C}{P_{diss}} \tag{4.33}$$

Now it is possible to calculate the constant value K_e which correlates the accelerating field and the power transmitted from the cavity during the curve measurement:

$$K_e = \frac{E_{Acc}}{V_{pk}^{Cavity}} = \frac{E_{Acc}}{\sqrt{P_{pk}^{Cavity} \cdot 400}} \tag{4.34}$$

This value is then used to calculate the value of the accelerating field and the Q-factor during the CW measurement of the curve:

$$E_{Acc} = K_e \sqrt{P_{pk}^{Cavity} \cdot 400} \quad , \quad Q_{point} = \omega (E_{Acc} L)^2 \frac{C}{P_{diss}} \tag{4.35}$$

4.3 Comparison Between The Two RF Systems

The two systems used for doing the RF measurements show clearly some dissimilarity. The main differences are now discussed.

The decay constant measurement during the calibration point acquisition is done at CERN by measuring the voltage value at half of the decay curve of the transmitted power. Whereas at LNL the power decay is linearized as a function of time, and the decay constant measurement is done by the slope extraction of the straight line which interpolates the data.

Furthermore, the value obtained from the calibration point and then utilized for the Q-factor and accelerating field calculation, is also a little bit different. In one case the pick-up time decay is measured, i.e. the ratio between the stored energy and the transmitted power, in the other case the ratio between the accelerating field and the transmitted voltage is instead measured:

$$\tau_t = \frac{U}{P_{TXM}} \quad \rightarrow \ at\ CERN \quad , \quad K_e = \frac{E_{Acc}}{V_{pk}^{Cavity}} \quad \rightarrow \ at\ LNL \tag{4.36}$$

As a consequence also the points during the CW measurement are calculated in a different way:

$$E_{acc} = \sqrt{\frac{\tau_t P_{TXM}}{k_1}} \quad , \quad Q_0 = \frac{\omega_0 \tau_t P_{TXM}}{P_c} \quad \rightarrow \ at\ CERN \tag{4.37}$$

$$E_{acc} = K_e V_{pk}^{Cavity} \quad , \quad Q_{point} = \omega (E_{Acc} L)^2 \frac{C}{P_{diss}} \quad \rightarrow \ at\ LNL \tag{4.38}$$

It is also possible to notice that the geometrical coefficient $k_1$used at CERN can be expressed with the geometrical constant used at LNL as:

$$k_1 = \frac{\mathrm{C}}{\mathrm{L}^2} = \frac{[\mathrm{F}]}{[\mathrm{m}]^2} = \frac{[\mathrm{J}]}{[\mathrm{V}\cdot\mathrm{m}]^2} \tag{4.39}$$

Another important difference between these systems is the coupling regime. Indeed at CERN the coupler can be moved only before the calibration point, while at LNL the coupler can be moved point by point during the curve acquisition. At LNL is then possible to maintain the critical coupled regime during the entire measurement allowing to minimize the power lost by reflection.

In addition, the Quarter Wave Resonators are measured with the purpose to insert them into the REX-LINAC accelerator of HIE-ISOLDE project; such accelerator works at $4.5K$ and the measurements are then made only at this temperature. The 6GHz cavities are instead measured for studying the materials properties and for comparing the results with the elliptical cavities that work in the accelerator usually at $1.8K$. Therefore for these cavities the curve $Q(E_{Acc})$ is acquired both at $4.2K$ and at $1.8K$.

Chapter 5

DATA ANALYSIS

The results of the RF measurements of the QWRs and 6GHz cavities, are here reported. The data analysis about QWRs measurements consists of: the errors analysis made with propagation of uncertainly and a Monte Carlo like method, and the indirect calculations of both the thickness and the RRR of the Niobium sputtered films. The 6GHz elliptical cavities data were at first analyzed using the BCS theory, in this way the residual resistances were extrapolated, allowing to compare quantitatively the 6GHz sputtered cavities.
The Q-slope at 1.8K was analyzed as a thermal problem, in which the dissipated power causes a thermal feedback loop which in turn reduces the cavity superconducting properties. Moreover from experimental evidences one can deduce that the thermal increment could also lead to a vapor Helium layer formation around the cavity surface.

5.1 RF MEASUREMENTS ON ACCELERATING CAVITIES

The RF measurement is the main method of characterization of accelerating cavities. How such measurements are performed is explained in Chapter 3. Niobium thin film cavities with two different geometries were characterized: Quarter Wave Resonators and elliptical cavities.

The QWRs were measured at the European Centre for Nuclear Research (CERN), for the HIE-ISOLDE project. Such resonators are low-β cavities which are usually implemented in LINAC for the heavy ions acceleration, as in the case of ISOLDE facility. Because the particles velocity is rather low, also the resonance frequency has to be low. The resonance frequency of the QWRs measured at CERN is $f = 101MHz$. Three QWRs were measured:

- **Q3_4**: Niobium thin film deposited by Biased Diode Sputtering
- **Q5_1**: Niobium thin film deposited by Magnetron Sputtering
- **QP1_4**: Niobium thin film deposited by Biased Diode Sputtering

The names Q3, Q5 and QP are referred to the identification of the Copper substrate, whereas the number, which follows it, indicates the Niobium film deposition. Indeed, whether the RF performance of a film is lower than expected, it is possible to utilize again the same Copper substrate, after that the Niobium film is stripped away.

The measurement of a QWR requires particular care since such cavities are easily subjected to multipacting and field emission. Therefore, RF conditioning is done at room temperature and at 4.5K for avoiding multipacting, and Helium processing is done during the measurements when field emission occurs.

In Figure 5.1 are reported the final Q-factor versus accelerating field curves found for these cavities. In the next section each cavity will be individually analyzed.

On the other hand, the elliptical cavities were measured at the Legnaro National Laboratories (LNL, INFN). Such cavities have high-β values, indeed they are usually used in storage ring, or collider, for accelerating particles close to the speed of light. The resonance frequency of the elliptical cavities is therefore rather high, typical values are between $400MHz$ and $1.5GHz$. However, the elliptical cavities tested at LNL are scaled resonators useful for new material research, as it is explained in Chapter 4, with resonance frequency $f = 6GHz$.

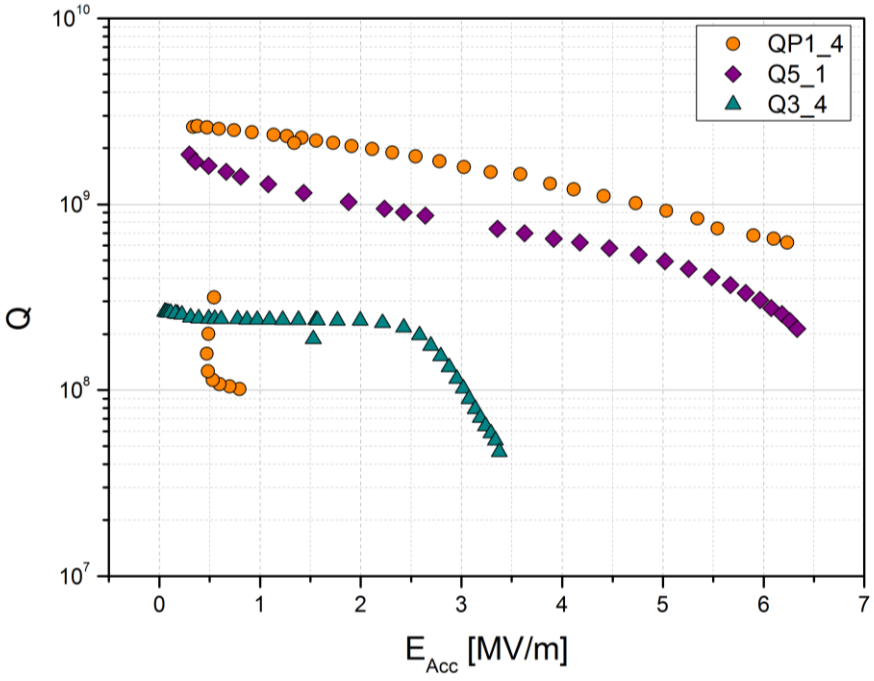

FIGURE 5.1 - FINAL Q(E) CURVES OBTAINED FROM THE RF MEASUREMENTS OF QP1_4, Q3_4, Q5_1 QUARTER WAVE RESONATOR.

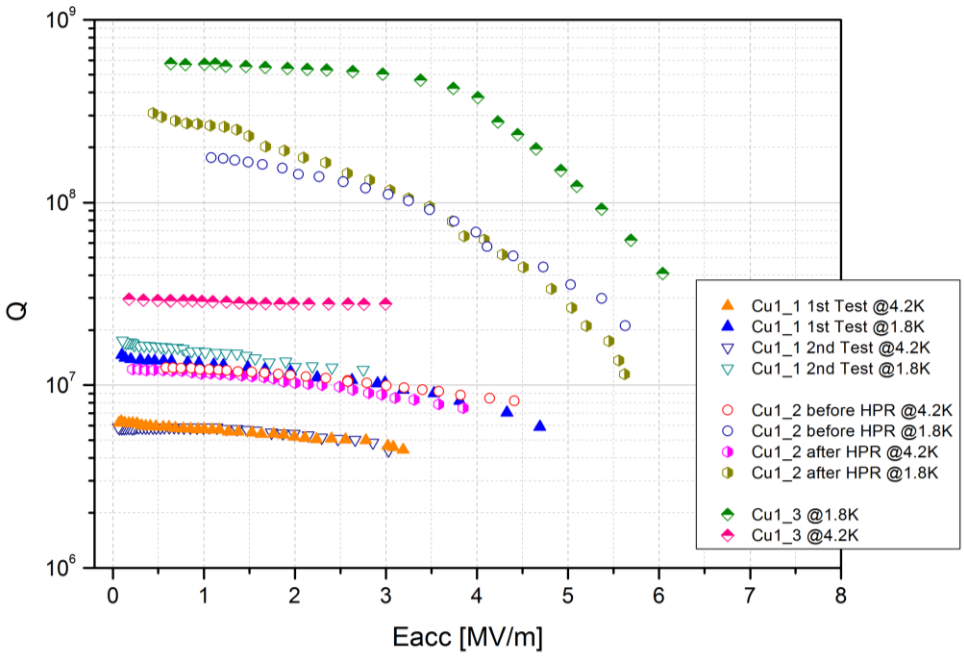

FIGURE 5.2 - FINAL Q(E) CURVES OBTAINED FROM THE RF MEASUREMENTS OF CU1_1, CU1_2, CU1_3 6GHZ CAVITIES.

Three Niobium on Copper sputtered cavities were measured. The Niobium deposition was made by a post-magnetron system in which an external coil provides the magnetic field. Moreover, the cavity was mounted on a linear feed-through, as explained in Chapter 3, which allows a linear cavity movement along the cathode length.

The elliptical cavities measured are the following:

- **Cu1_1**: The Niobium film was sputtered at room temperature. The cavity cell deposition was done with a cavity fixed in a central position respect the cathode length.
  - This cavity was measured two times. During the first measurement the thermometer was fixed at the upper flange of the RF stand, whereas the second time the thermometer was completely surrounded by the Helium bath.

- **Cu1_2**: The Niobium film was sputtered at room temperature. During the deposition the cavity was in motion: it accomplished linear movement up and down along the cathode length.

- The cavity was measured two times. The first one was just after the Niobium deposition, without doing any surface cleaning. After this test the inner cavity surface was cleaned with high pressure rinsing process and then the cavity was measured again.

- **Cu1_3**: The Niobium film was sputtered at 400°C.
  - The cavity was measured after the Niobium film deposition which was followed by HPR process.

As before, the name Cu1 is referred to the identification of the Copper substrate, the number which follows it indicates the Niobium film deposition. After the RF measurement, the Niobium film is stripped and the substrate is ready for another deposition.

In Figure 5.2 are reported the Q-factor versus accelerating field found for 6GHz cavities. The cavities will be individually analyzed further on.

5.2 QWR RF TEST

The QWRs measured, for the HIE-ISOLDE project, are the following: $Q3\_4$, $Q5\_1$ and $QP1\_4$.

The Niobium film of the cavity $Q3\_4$ was done with Biased Diode Sputtering technique. This is the fourth Niobium film deposited on the substrate $Q3$, in fact it is common, after the characterization of a Niobium film, if the property are not high as expected, to strip the film and re-sputter a new Niobium film on the same Copper substrate.

The data obtained are shown in Figure 3.2. One can recognize immediately the difference between the first measurement, did at Orsay, and the last ones, did at CERN; a further cavity inspection showed the cavity was not damaged during the transport from Orsay laboratories to CERN, so the decreasing of the performance should be attributed to the characteristics of the Niobium film. The curve of the 26/06/2013 displays a drop of the Q accompanied by a slight increase in the accelerating field, so the effect of the Q drop can be attributed to field emission. A proof of this is given by the increasing of the x-rays detected close to the cavity, that reached the value of $2,3mSV/hr$; also the temperature of the thermometer $TT845$, that is fixed at the bottom of the cavity, under the cavity plate, appeared higher than usual: $TT845 = 5.337K$.

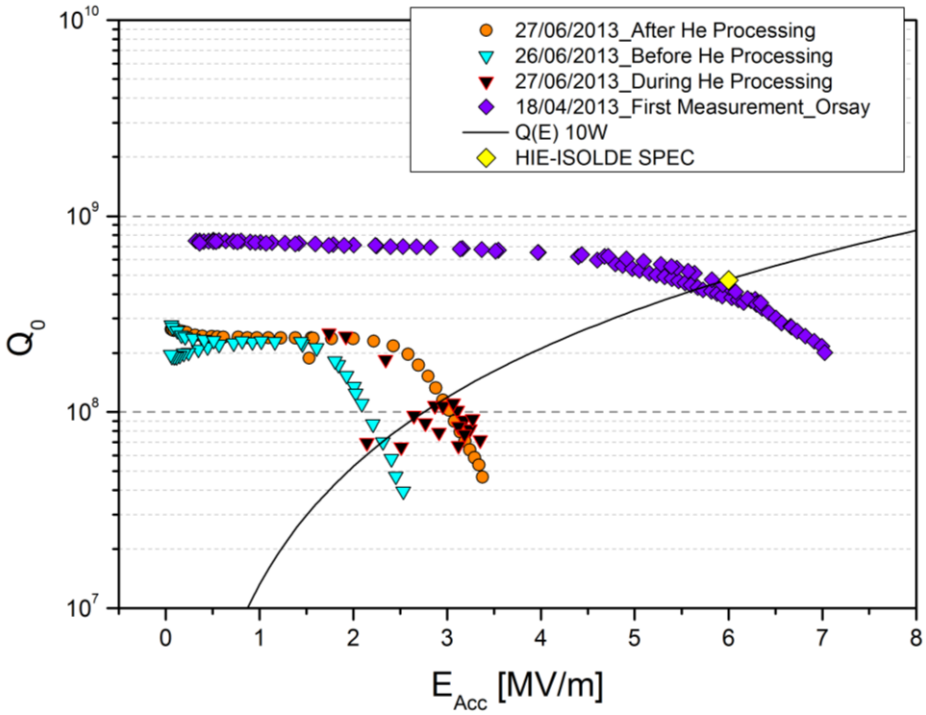

FIGURE 5.3 - RF MEASUREMENTS OF Q3_4 QUARTER WAVE RESONATOR. COURTESY OF W. VENTURINI.

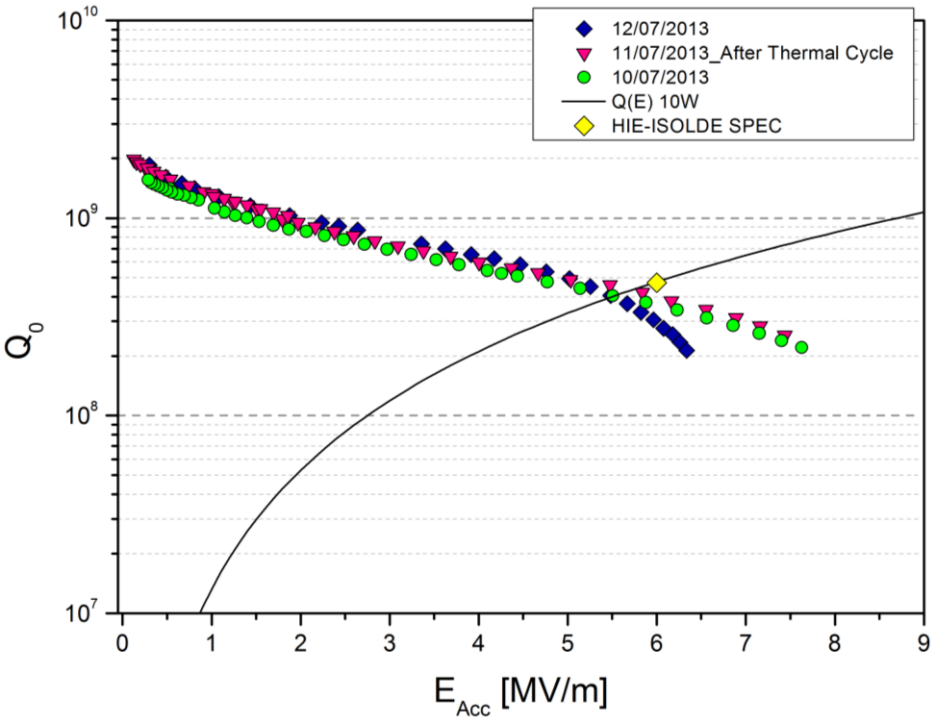

FIGURE 5.4 - RF MEASUREMENTS OF Q5_1 QUARTER WAVE RESONATOR. COURTESY OF W. VENTURINI.

Also the rising of the temperature on the plate is expected as a proof of field emission since the highest electric field zone is near to the inner conductor of the QWR, so the electrons ejected from the antenna have high probability to be accelerated to the bottom of the cavity and hitting the plate. After that the presence of field emission is recognized, the Helium processing is essential.

It can be seen that the points taken during the process start near the beginning of the Q slope seen before and, at the end of the processing higher field than the previous curve was reached. Indeed, considering the curve taken after the process, it is easy to notice that the drop starts at higher field, so the cavity can now reach higher field values. In any case, observing the measurements made at CERN the performances of the cavity are lower than expected: the field reached is less than $4MV/m$. So, in order to understand if the film degradation is a consequence of a sputtering process, it is necessary to study another cavity produced in the same manner, and to compare the results.

The Niobium film of the cavity $Q5\_1$ was done with Magnetron Sputtering, and this is the first Niobium film that has been deposited in the cavity $Q5$. The data obtained are shown in Figure 5.4. The fist measurement did on the 10/07/2013 exhibits high values of Q-factor, particularly at low field, and there is no field emission allowing to reach $8MV/m$. A thermal cycle was done in order to see whether the performance would increase or not; soon after the thermal cycle the Q factor was slightly higher than before but, the further measurements show field emission, unlike the previous ones: the Q decreases, the field increases slowly and a peak of $28mSV/hr$ of radiation was detected. At the end the cavity reached about $7MV/m$ as maximum accelerating field.

The coating method used for the cavity $QP1\_4$ is the Biased Diode Sputtering, that is done with very similar deposition parameters as the cavity $Q3\_4$. Unlike the previous cavities the $QP1\_4$ owns a *tuning plate* on the bottom, instead a normal plate. The substrate of the tuning plate is made in Copper Beryllium and the choice of the material was made considering that the tuning plate must have both a good thermal conducting and elastic proprieties. The tuning plate has the role of modifying the resonance frequency of the cavity; when it is deformed, the dimensions of the cavity change, inducing in this way a resonance frequency variation. The possibility to change the resonance frequency for a cavity working in an accelerator is extremely important in order to stabilize the frequency and counteract phenomena as *Lorentz force detuning*[1] and *microphonics*[2].

[1] Lorents force detuning: the Lorentz force is due to the interaction between the magnetic field and the RF wall current. Its radiation pressure causes a small deformation of the cavity shape resulting in a shift of the cavity resonant frequency.

[2] Microphonics: mechanical vibration phenomenon which changes the cavity resonant frequency.

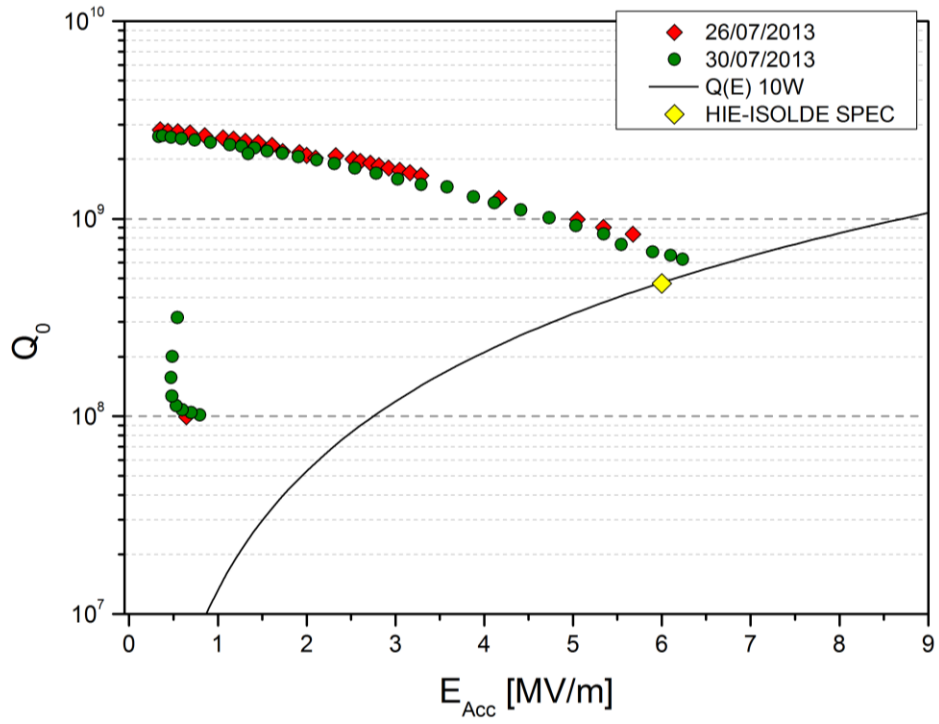

FIGURE 5.5 - RF MEASUREMENTS OF QP1_4 QUARTER WAVE RESONATOR. COURTESY OF W. VENTURINI.

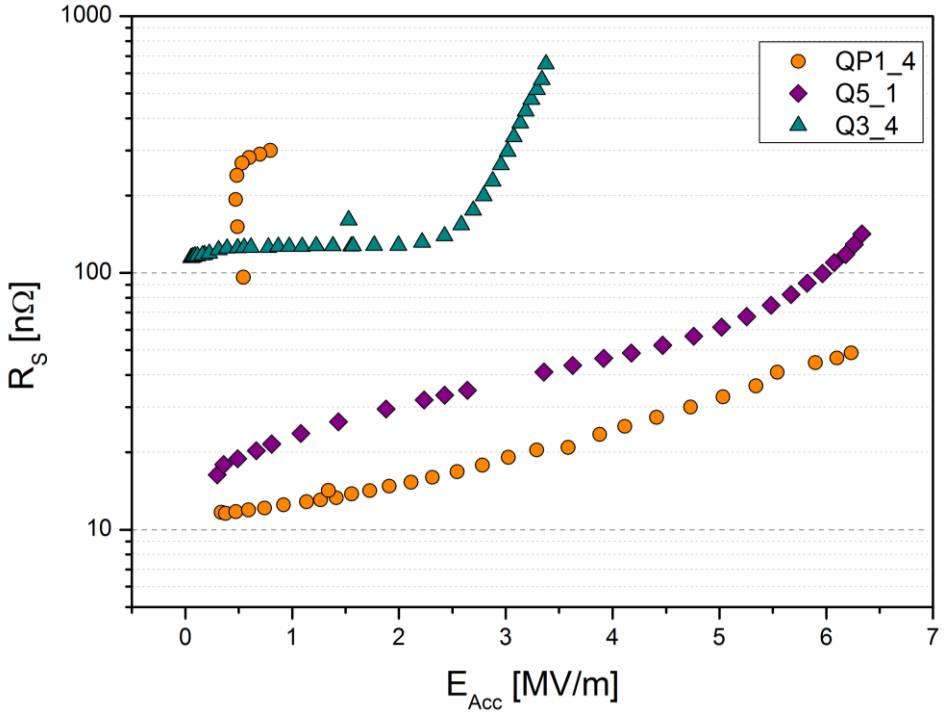

FIGURE 5.6 - RF MEASUREMENTS OF Q5_1 QUARTER WAVE RESONATOR

Observing the graph in Figure 5.5 it is clear that after thermal cycle the performance of the cavity improves significantly, both the Q factor and the accelerating field reach higher values after the treatment. Unfortunately in both cases a Q-switch appears, probably due to a presence of a tuning plate. In fact beyond a certain field the Q decreases of about one order of magnitude and the field decreases a value less than $1MV/m$. Moreover decreasing the RF power, the Q factor starts to increase while the accelerating field remains approximately constant. The Q-switch might be explained as a thermal breakdown due to a tuning plate, which might be not able to dissipate the heat as well as the Copper substrate. So, after a certain field, the temperature of the plate becomes higher than the critical temperature of Niobium and the power dissipation would start to increase considerably. In any case the cavity reaches high Q value and about $6MV/m$ as accelerating field before the Q-switch. Therefore an improvement of the tuning plate thermal conductivity should give to the cavity the performances required for the HIE-ISOLDE project.

The surface resistance of the cavity walls versus the accelerating field is displayed in Figure 5.6 for the cavities under study. From this graph it is clear the $QP1\_4$ cavity has the lower surface resistance value, that falls into the range between 10 and $100nW$. A slightly smaller value of surface resistance are shown by $Q5\_1$ cavity, instead the cavity $Q3\_4$ shows the worst value of surface resistance that falls into the range between 0.1 and $1m\Omega$.

5.3 Errors Analysis on QWR Test

The graph with the error bars obtained via **Propagation of Uncertainty** is shown in Figure 5.7. The standard deviation found for each point is rather small and the error bars increase, both in x and y axes, as the field increases. On the other hand the points measured after the Q-switch for the cavity $QP1\_4$ show the bigger error bars even thought they are at low field.

The graph with the error bars obtained via **Monte Carlo simulation** is shown in Figure 5.8. The standard deviation found for each point is again rather small and again the error bars increase as the field increases. This is due especially because the coupling get worse at high field since the reflection power increases. In accordance with the propagation of uncertainty result, the points measured after the Q-switch own a serious error, with many order of magnitude of size.

Comparing the results found with these two methods, the error bars found via propagation of uncertainty are slightly bigger than the ones found via Monte Carlo simulation, anyhow, these are comparable to each others, so this mean that both methods work well for the error bars estimation.

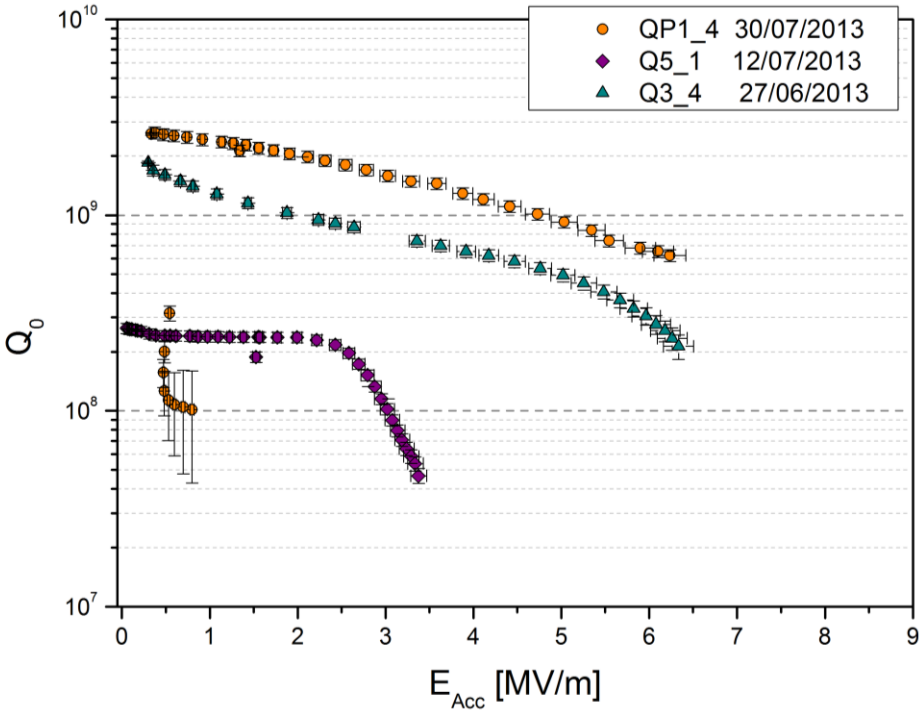

FIGURE 5.7 - QWR RF MEASUREMENTS WITH ERROR BARS FOUND VIA PROPAGATION OF UNCERTAINTY.

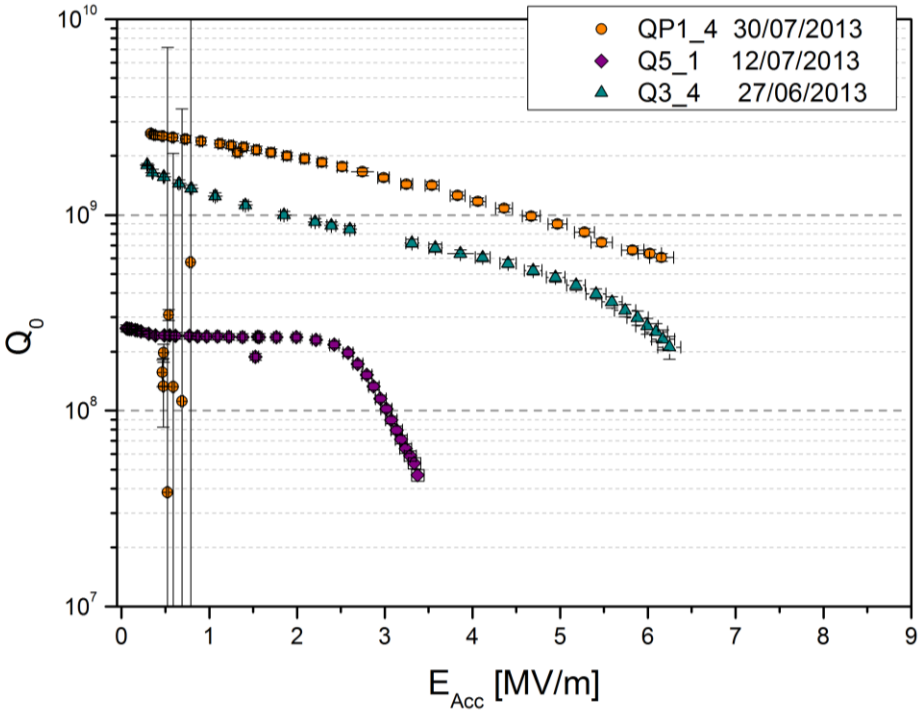

FIGURE 5.8 - QWR RF MEASUREMENTS WITH ERROR BARS FOUND VIA MONTE CARLO-LIKE METHOD.

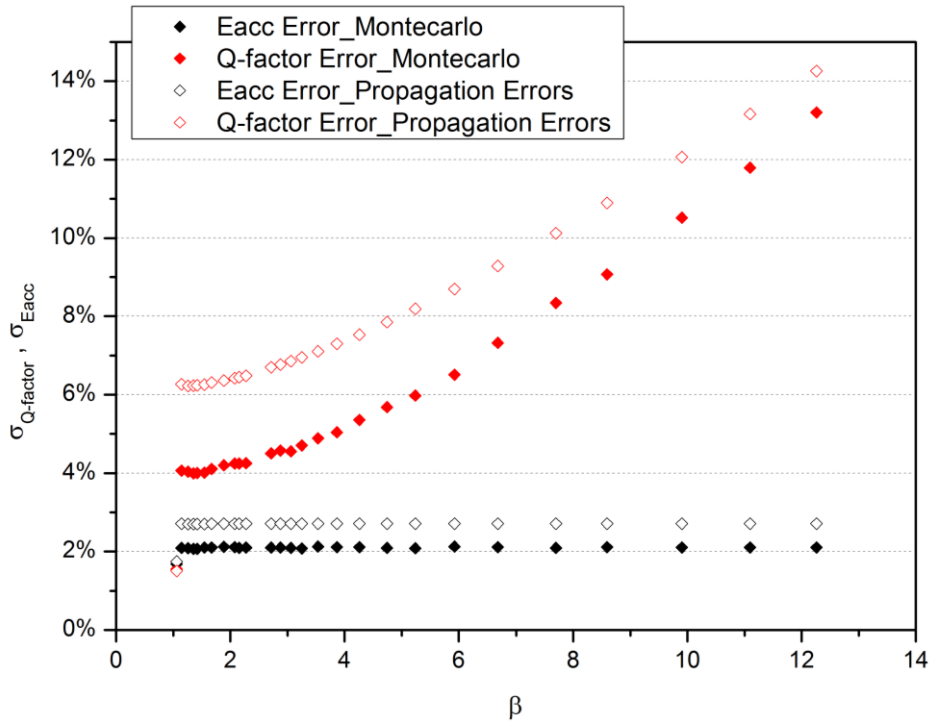

FIGURE 5.9 - Q-FACTOR AND ACCELERATING FIELD PERCENTAGE ERRORS AS A FUNCTION OF COUPLING STRENGTH β FOR Q5_1 CAVITY.

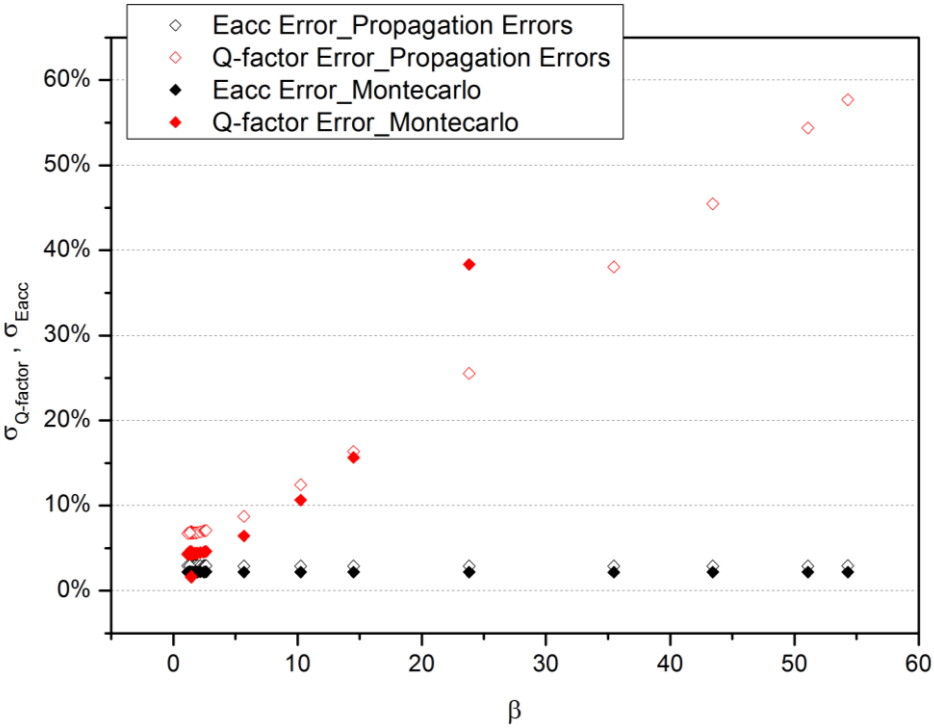

FIGURE 5.10 - Q-FACTOR AND ACCELERATING FIELD PERCENTAGE ERRORS AS A FUNCTION OF COUPLING STRENGTH β FOR QP1_4 CAVITY.

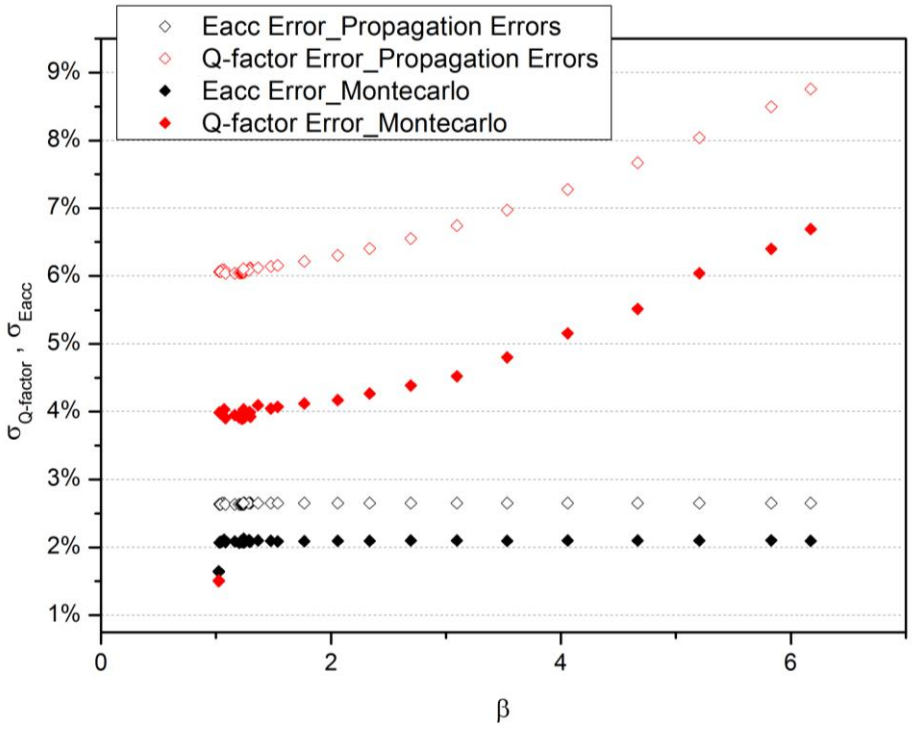

FIGURE 5.11 - Q-FACTOR AND ACCELERATING FIELD PERCENTAGE ERRORS AS A FUNCTION OF COUPLING STRENGTH β FOR Q3_4 CAVITY.

On the other hand, analyzing the points after the Q-switch, the errors found by propagation of uncertainty are smaller than the ones found by Monte Carlo simulation and in this case the propagation of errors became more trustworthy.

In order to explain the trend of the results found with these two methods it is necessary to take into account that the reflected power increases by increasing the field, so the coupling strength β gets worse, indeed as it was explained in Chapter 2, only for $\beta = 1$ the reflected power is equal to zero. As much as the reflected power increases, with the same forward power, the power dissipated from the cavity walls is less, and the uncertainty increases.

Let us analyze the percentage errors of Q-factor and accelerating field as a function of the coupling strength. The graphs in Figure 5.9, Figure 5.11, Figure 5.10, show that the percentage error of Q-factor values increments with β, whereas the percentage error of the accelerating field remains quite constant. So the Q-factor's errors depend on the coupling strength and it gets worse as much as β differs from 1.This result underlines that the best condition for doing RF measurements is in the critical coupling regime.

In Figure 5.10 the last four error points, that are the errors of the point acquired after the Q-switch, estimated with the Monte Carlo simulation were not plotted because these values exceeded the 100% of error. Indeed also the error bars in Figure 5.8 show a huge overestimation of these errors. This is also due to the worsening of the coupling regime, let us now understand why in the case of Monte Carlo simulation this effect is magnified.

In particular cases, such Q-switch case, the reflected power increases considerably and it can reach values very close to the forward power. Whether this situation occurs and the forward and the reflected power have the same value within its uncertainty, it can happen that some simulated values of the reflected power are higher than the forward one, leading to obtain negative value of the cavity dissipated power: $P_c = P_{FWD} - P_{RFL} - P_{TXM}$. These negative values cause a broadening of the Q-value: $Q_0 = \omega\tau_{pk}P_{TXM}/P_C$ and, as a consequence, the standard deviation of the generated Q-value is very high. The accelerating field is not affected by the coupling because it does not depend on the cavity dissipated power P_c: $E_{acc} = \sqrt{P_{txm}\tau_{pk}/k}$.

5.4 Resonance Frequency Shift Measurements near Critical Temperature

The real and the imaginary part of the surface impedance are related to the attenuation and to the phase shift of the reflected wave from a metal surface that is exposed to an electromagnetic field. In the case of accelerating cavities the surface impedance depends on the Q-factor and the resonance frequency of a cavity, in accordance with the Slater theorem [27,28]:

$$\frac{1}{Q} - 2i\frac{\Delta\omega}{\omega_0} = \frac{c^2 Z_S}{4\pi\omega_0}\int_S H_a^2 da^2 \tag{5.1}$$

where $\Delta\omega$ is the *frequency shift* due to the finite surface reactance, ω_0 is the unperturbed frequency, H_a is the magnetic field with volume integral over the cavity normalized to unity and Z_S is the surface impedance. In this case, the non perfect conductivity of the cavity walls perturbs the system involving the resonant frequency shift. The integral coincides with the geometrical factor of the cavity G:

$$\int_S H_a^2 da^2 = G \tag{5.2}$$

So the Equation 7.1 can be written as:

$$\frac{1}{Q} - 2i\frac{\Delta\omega}{\omega_0} = \frac{c^2(R_S + iX_S)}{4\pi\omega_0}G \tag{5.3}$$

After some algebra one finds that the surface reactance X_S is equal to:

$$X_S = -2G\frac{\Delta\omega}{\omega_0} \tag{5.4}$$

and, remembering that the surface impedance for the two fluid model is defined as: $X_S = \omega_0\mu_0\lambda$, it is clear that the resonance frequency depends on the penetration depth λ.

The relationship between the resonance frequency and the temperature is now easily due to the dependence between the penetration depth and the temperature, which, as it is explained in Chapter 1, for $T/T_C > 0.8$ it can be defined as:

$$\frac{1}{\lambda^2(T)} = \frac{1}{{\lambda_0}^2}\left[1 - \left(\frac{T}{T_C}\right)^4\right] \tag{5.5}$$

where λ_0 is the penetration depth at $T = 0K$:

$$\lambda_0 = \lambda_L\left(1 + \frac{\xi_0}{l}\right)^{1/2} \tag{5.6}$$

where ξ_0 is the *length of coherence* and l is the *electronic mean free path*. Therefore the resonance frequency as a function of temperature is given by:

$$\frac{\Delta\omega(T)}{\omega_0} = -\frac{\omega_0\mu_0}{2G}\lambda(T) \tag{5.7}$$

and the resonance frequency defined at fixed temperature $T_0 < T$ is:

$$\frac{\Delta\omega(T_{in})}{\omega_0} = -\frac{\omega_0\mu_0}{2G}\lambda(T_{in}) \tag{5.8}$$

where $\Delta\omega(T) = \omega(T) - \omega_0$ and $\Delta\omega(T_{in}) = \omega(T_{in}) - \omega_0$. Then it is possible to find the resonance frequency shift due to the temperature change, near T_C, from T_0 to T:

$$f(T) = f(T_{in}) + \frac{\pi\mu_0 f_{in}^2}{G - \pi\mu_0 f_{in}[\lambda(T_{in}) - \lambda(T)]}[\lambda(T_{in}) - \lambda(T)] \tag{5.9}$$

where $f(T_{in})$ and $\lambda(T_{in})$ are respectively the cavity resonance frequency and the penetration depth at the initial temperature of the resonance frequency shift measurement. This dissertation is explained in [29].

The resonance frequency data acquired as a function of temperature were then fitted using Equation 5.5 and Equation 5.9, and fixing the following parameters: T_{in}, which depends on the data, $G = 30.32$, $\xi_0 = 64nm$, $\lambda_L = 36nm$ [3]. The parameters T_C, f_{in} and l are instead extrapolated from the fit.

The data acquired fitted by the model explained above are shown in Figure 5.12 for cavity $Q3\_4$ and in Figure 5.13 for cavity $QP1\_4$. It was not possible to make such a measurements for the cavity $Q5\_1$ for some technical problems.

The results obtained for the Q3_4 cavity are shown in Table 5.1. From the graph it can be seen that the curves acquired with two different thermometers show some dissimilarity. Indeed, also the fit results are quite different. This is because the radiofrequency measurements show a global behaviour of the cavity and the frequency shift is also due to a global change which appear in the cavity. On the other hand, the heating of the cavity is not uniform along the entire surface, so, the thermometers are at different temperature during the entire acquisition. For this reason the results found are not very accurate, however they allow to understand the order of magnitude of the analyzed quantity and to compare qualitatively the proprieties of different cavities.

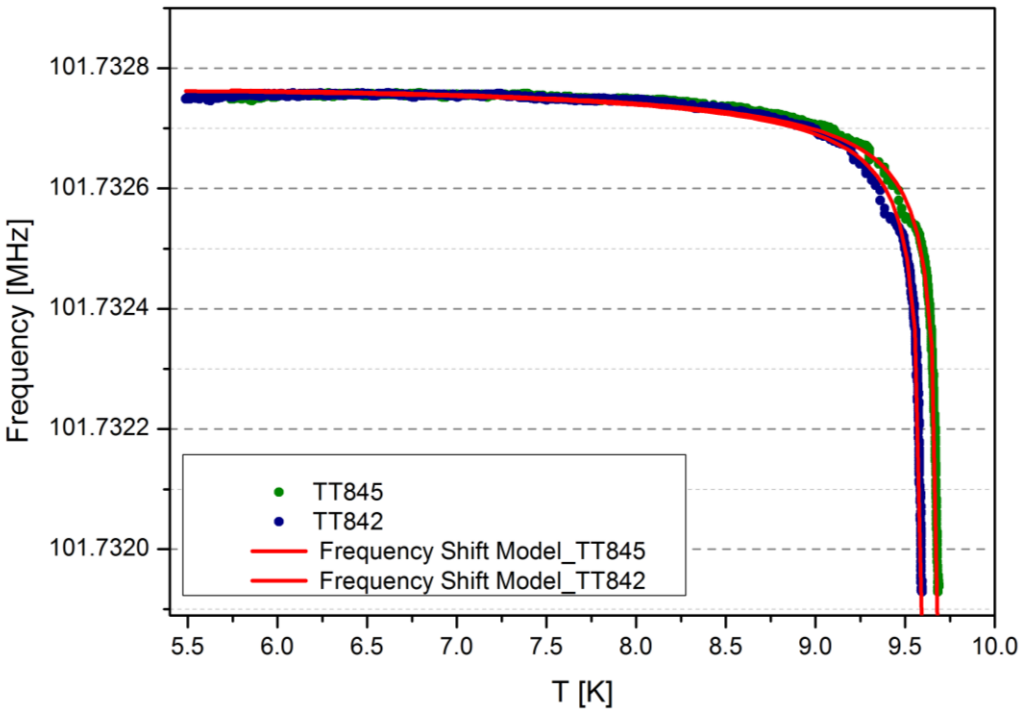

FIGURE 5.12 - FITTED DATA OF FREQUENCY SHIFT NEAR T_C MEASUREMENTS FOR Q3_4 CAVITY.

TABLE 5.1 - VALUE OF INITIAL FREQUENCY, CRITICAL TEMPERATURE AND MEAN FREE PATH GIVEN BY THE FIT AND THE CALCULATED VALUE OF RESIDUAL RESISTIVITY AND RRR FOR Q3_4 CAVITY.

	Q3_4 TT845	**Q3_4 TT842**
$\boldsymbol{f_{in}}$ $[\boldsymbol{Hz}]$	101733000.0 ± 0.2	101733000.0 ± 0.2
$\boldsymbol{T_C}$ $[\boldsymbol{K}]$	9.6989 ± 0.0006	9.6067 ± 0.0006
$\boldsymbol{l}$ $[\boldsymbol{nm}]$	52.9 ± 1.1	59.2 ± 1.2
$\boldsymbol{\rho_{imp}}[\boldsymbol{\mu\Omega \cdot cm}]$	0.69 ± 0.014	0.625 ± 0.12
RRR	$\mathbf{21.7 \pm 0.4}$	$\mathbf{24.2 \pm 0.5}$

The values found for the critical temperature are rather high compared to the value of Niobium bulk, $9.25K$. As already mentioned the critical temperature depends on the crystallographic propriety by the following equation:

$$T_C \approx 1.13\hbar\theta_D e^{-1/(N(0)V-\mu)} \tag{5.10}$$

So, high value of critical temperature means that the lattice constant decreases causing a higher electron-phonon interaction V. The Niobium films is then grown with tensile stresses. By the way the values found for critical temperature are related to tensile stresses too much higher for a Niobium sputtered film [30]. This fact suggests that the thermometers used for such analysis might be not well calibrated, leading to an overestimation of the critical temperature.

Once the mean free path l is extrapolated from the fit, the impurity contribution of the resistivity ρ_{imp} was calculated as follow:

$$\rho_{imp} = \frac{1}{l}\frac{m_e v_F}{ne^2} = \frac{1}{l}0.37 \cdot 10^{-11}\Omega \cdot cm^2 \tag{5.11}$$

Then the Residual Resistivity Ratio, RRR, was calculated as:

$$RRR = \frac{\rho(300K)}{\rho_{imp}} = \frac{\rho_{Ph}(300K)}{\rho_{imp}} + 1 \tag{5.12}$$

where $\rho_{Ph}(300K)$ is a constant value which depends on the materials, in the case of Niobium is $\rho_{Ph}(300K) = 15\mu\Omega \cdot cm$.

With a mean free path of about $60nm$, a RRR of about 23 is estimated, so this model reveals that the Niobium thin film analyzed has a good propriety.

Looking at the Figure 5.13, it is evident that something unusual happened during the data acquisition, indeed the graphs acquired for all three thermometers show a step, a sudden decreasing of the resonance frequency before the transition. This anomalous behaviour could be due to the presence of different superconducting phases that have the transition at lower temperatures compared to the others cavity zones. Moreover, taking into account the curve acquired with the thermometer TT831, it shows the transition at temperature well above the other two curves.

The fit results, about the impurity contribution on the resistivity ρ_{imp}, and the RRR, are shown in Table 5.2. Because of the large difference in temperature between TT831 thermometer and the other two, also the results found are very different.

With the thermometers TT844 and TT842 the critical temperature is about $9.5K$, whereas with the temperature TT831 is about $9.1K$. By the way the thermometer TT831 is fixed at the inner conductor of the Quarter Wave Resonator, that is the only area of the cavity directly in contact with the liquid Helium. For this reason the results found with the other two thermometers can be considered more trustworthy.

Considering a critical temperature near $9.5K$, and taking into account the Equation 5.10, it is possible to conclude that, also in this case, the Niobium film is grown with tensile stresses. A mean free path of about $30nm$ leads to an estimation of the RRR of about 13, hence, this model reveals that the Niobium thin film analyzed has low purity level than the film of the cavity $Q3\_4$.

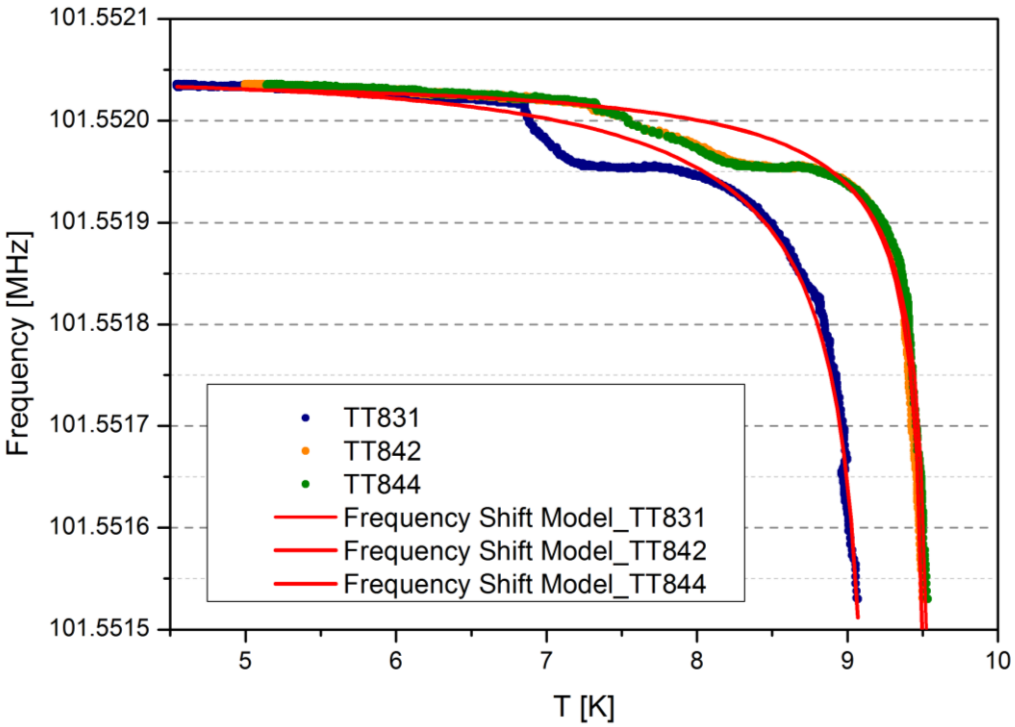

FIGURE 5.13 - FITTED DATA OF FREQUENCY SHIFT NEAR T_C MEASUREMENTS FOR QP1_4 CAVITY.

TABLE 5.2 - VALUE OF INITIAL FREQUENCY, CRITICAL TEMPERATURE AND MEAN FREE PATH GIVEN BY THE FIT AND THE CALCULATED VALUE OF RESIDUAL RESISTIVITY AND RRR FOR QP1_4 CAVITY.

	QP1_4 TT844	**QP1_4 TT842**	**QP1_4 TT831**
$f_{in}\ [Hz]$	101552000.0 ± 0.3	101552000.0 ± 0.3	101552000.0 ± 0.3
$T_C\ [K]$	9.573 ± 0.002	9.541 ± 0.001	9.195 ± 0.004
$l\ [nm]$	30.6 ± 0.7	34.7 ± 0.8	6.5 ± 0.13
$\rho_{imp}[\mu\Omega \cdot cm]$	1.21 ± 0.03	1.067 ± 0.02	5.7 ± 0.12
RRR	**13.0 ± 0.3**	**14.6 ± 0.3**	**3.5 ± 0.1**

However, the QP1_4 cavity showed a better Q-factor versus accelerating field curve and so one expects higher value of RRR. Maybe the fit does not work well because of the strange shape of the curve.

Considering again the cavity $Q3\_4$ and using the critical temperature and the mean free path already estimated, it is also possible to find the trend of the BCS contribution of the surface resistivity, in approximation of two fluid model:

$$R_{BCS}(\omega,T) = \frac{\omega^2\mu_0^2\lambda(T)^3}{2\rho_{imp}} = \frac{\omega^2\mu_0^2}{2\rho_{imp}} \cdot \left\{ \frac{1}{{\lambda_0}^2} \left[1 - \left(\frac{T}{T_C} \right)^4 \right] \right\}^{-3/2} \tag{5.13}$$

The trends found for the $R_{BCS}(T)$ are shown in Figure 5.14 and Figure 5.15. The BCS resistance changes as a function of frequency and as a function of temperature. At $5.5K$ the BCS resistance of about $8n\Omega$ is estimated, and this means that the surface resistance for a Quarter Wave Resonator at $4.2K$ is governed by the residual resistivity. Indeed, the surface resistance at low field for the cavity Q3_4 is about $100n\Omega$, Figure 5.6, and then: $R_S = R_{BCS} + R_0 \approx R_0$.

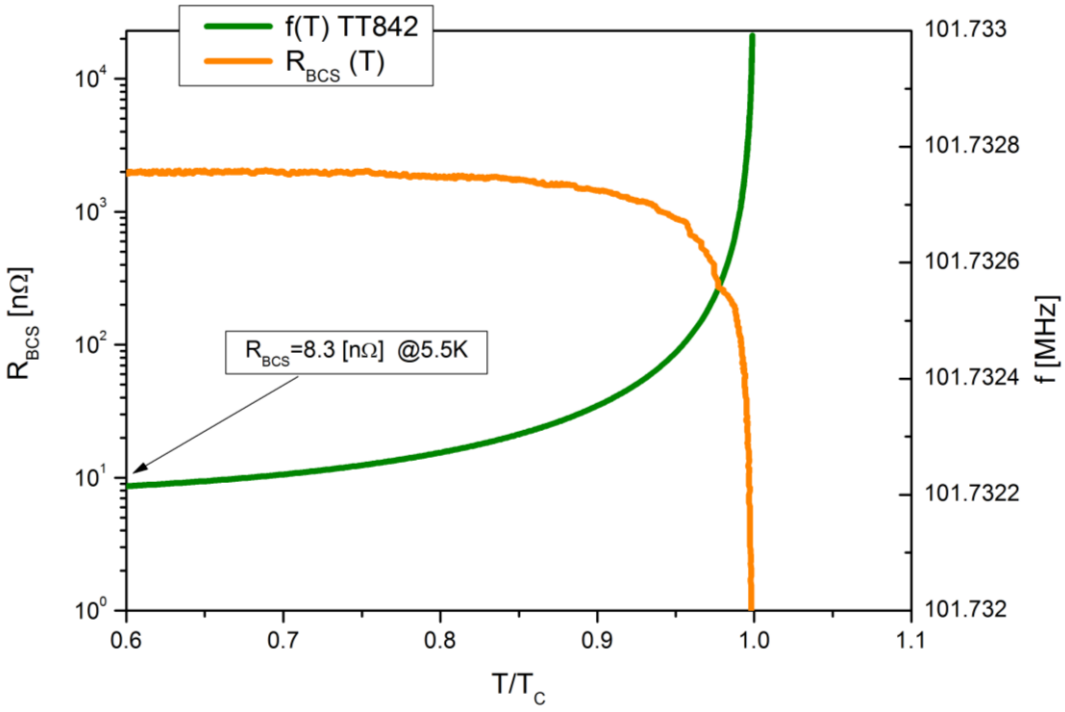

FIGURE 5.14 - R_{BCS} AND RESONANCE FREQUENCY VERSUS T/T_C FOR CAVITY Q3_4 AND THERMOMETER TT842.

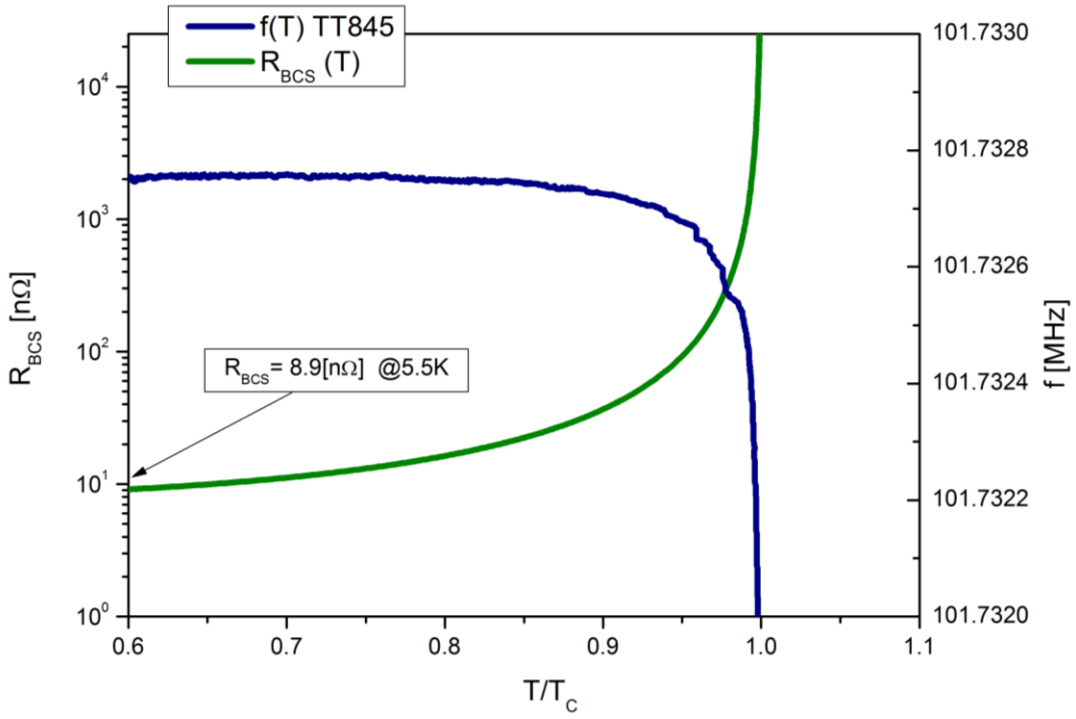

FIGURE 5.15 - R_{BCS} AND RESONANCE FREQUENCY VERSUS T/T_C FOR CAVITY Q3_4 AND THERMOMETER TT845.

5.5 ROOM TEMPERATURE RF TEST

The warm measurements were made for Niobium thin film cavity, $QP1\_4$, and for a Copper cavity. The results obtained are shown in Table 5.3.

From the Q-factor value at room temperature it is possible to obtain some information about the material, like: the surface resistance, the skin depth, the resistivity, the conductivity which are all linked together. Indeed these quantity are calculated as follows:

$$R_S = \frac{G}{Q_0}\,, \qquad \sigma = \frac{\pi \nu \mu_0}{{R_S}^2}\,, \qquad \delta = \frac{1}{\sigma R_S} \tag{5.14}$$

The results are shown in Table 5.4 where are also shown the literature values for a bulk Niobium cavity.

In the Niobium sputtered cavity the effective skin depth results: $\delta_{eff} = 9.42\mu m$, this value of skin depth is called "effective" because it is due to a global cavity behaviour, which depends on both the Niobium and the Copper regions.

Indeed, whether the Niobium layer is less thick than the effective skin depth, the field will pass through the entire film and it will decay into the Copper region. The surface resistance and the resistivity of the Nb/Cu cavity, calculated from the room temperature measurement, are higher than a Copper cavity but lower than a Niobium one. This fact is a proof that the field feels both the Niobium and the Copper materials. A useful model which allows to estimate the Niobium film thickness from the Q-factor warm measurements was made.

TABLE 5.3- LOADED Q-FACTOR, COUPLER AND PICK-UP SWR MEASURED AT ROOM TEMPERATURE AND UNLOADED Q-FACTOR CALCULATED FROM THESE VALUES.

Quantity	Nb/Cu cavity	Cu cavity
$\mathbf{Q_L}$	6315	8190
SWR coupler	3.58	2.76
SWR pick − up	/	13.65
$\mathbf{Q_0}$	8075	11770

TABLE 5.4- AC PROPRIETIES RESULTS FOR NIOBIUM THIN FILM CAVITY AND FOR COPPER CAVITY. THERE ARE ALSO THE AC PROPRIETIES FOUND IN LITERATURE FOR A CASE OF BULK NIOBIUM CAVITY.

Quantity	Nb/Cu cavity	Cu cavity	Nb cavity
Q	8075	1170	3990
$\mathbf{R_S}$ **[Ω]**	0.00375	0.00258	0.0076
σ [S/m]	$2.83 \cdot 10^7$	$6.00 \cdot 10^7$	$6.90 \cdot 10^7$
ρ[Ω · m]	$3.54 \cdot 10^{-8}$	$1.67 \cdot 10^{-8}$	$1.45 \cdot 10^{-8}$
δ [m]	$9.42 \cdot 10^{-6}$	$6.46 \cdot 10^{-6}$	$1.91 \cdot 10^{-5}$

Let us consider the surface impedance of a thin film cavity, as it is reported in [31]. The current density along the z direction $J(z)$ has to be divided into two components, Figure 5.16, one inside the Niobium layer, $\sigma^{Nb}E(z)^{Nb}$, and one inside the Copper region, $\sigma^{Cu}E(z)^{Cu}$:

$$\frac{1}{Z} = \frac{\int_0^{+\infty} J(z)dz}{E_y(0)} = \frac{\int_0^{a} \sigma^{Nb}E(z)^{Nb}dz + \int_0^{+\infty} \sigma^{Cu}E(z)^{Cu}dz}{E_y(0)} \tag{5.15}$$

where the electric field into the Niobium layer is given by:

$$E(z)^{Nb} = E_0 e^{-x/\delta^{Nb}} \tag{5.16}$$

and the electric field into the Copper substrate is instead given by:

$$E(z)^{Cu} = E_1 e^{-x/\delta^{Cu}} \quad , \quad E_1 = E_0 e^{-a/\delta^{Nb}} \tag{5.17}$$

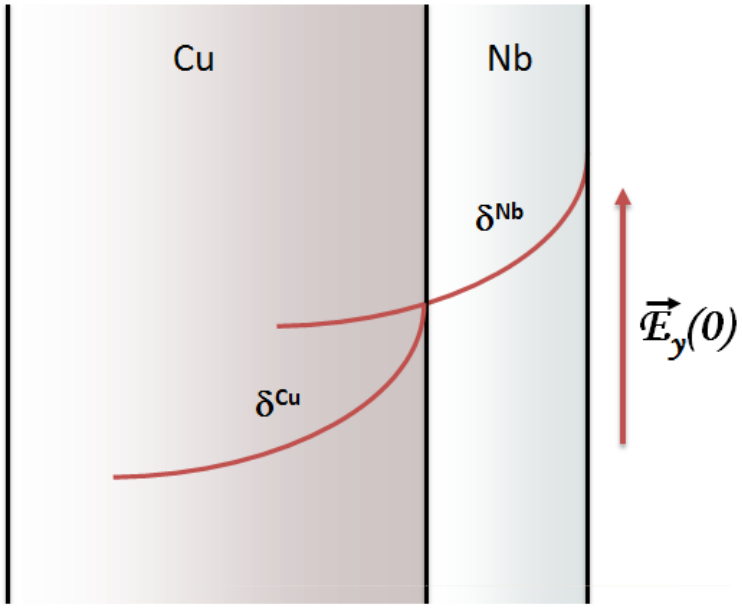

FIGURE 5.16 - SCHEMATIC REPRESENTATION OF THE PENETRATION SKIN DEPTH ON NIOBIUM THIN FILM ON COPPER SUBSTRATE.

Indeed the amplitude of the electric field at the interface Niobium/Copper depends on the ratio between the Niobium skin penetration depth and the layer thickness. The two integrals give the following results:

$$\int_0^a \sigma^{Nb} E(z)^{Nb} dz = \sigma^{Nb} \delta^{Nb} E_0 (1 - e^{-a/\delta^{Nb}}) \tag{5.18}$$

$$\int_0^{+\infty} \sigma^{Cu} E(z)^{Cu} dz = \sigma^{Cu} \delta^{Cu} E_0 e^{-a/\delta^{Nb}} \tag{5.19}$$

So the surface impedance becomes:

$$\frac{1}{Z} = \frac{\sigma^{Nb} \delta^{Nb} E_0 (1 - e^{-a/\delta^{Nb}}) + \sigma^{Cu} \delta^{Cu} E_0 e^{-a/\delta^{Nb}}}{E_y(0)} \tag{5.20}$$

Now the surface impedances of Copper and of Niobium, when the thickness is large than the skin depth, are defined as:

$$\frac{1}{Z^{Cu}} = \frac{\sigma^{Cu} \delta^{Cu} E_0}{E_y(0)} \quad , \quad \frac{1}{Z^{Nb}} = \frac{\sigma^{Nb} \delta^{Nb} E_0}{E_y(0)} \tag{5.21}$$

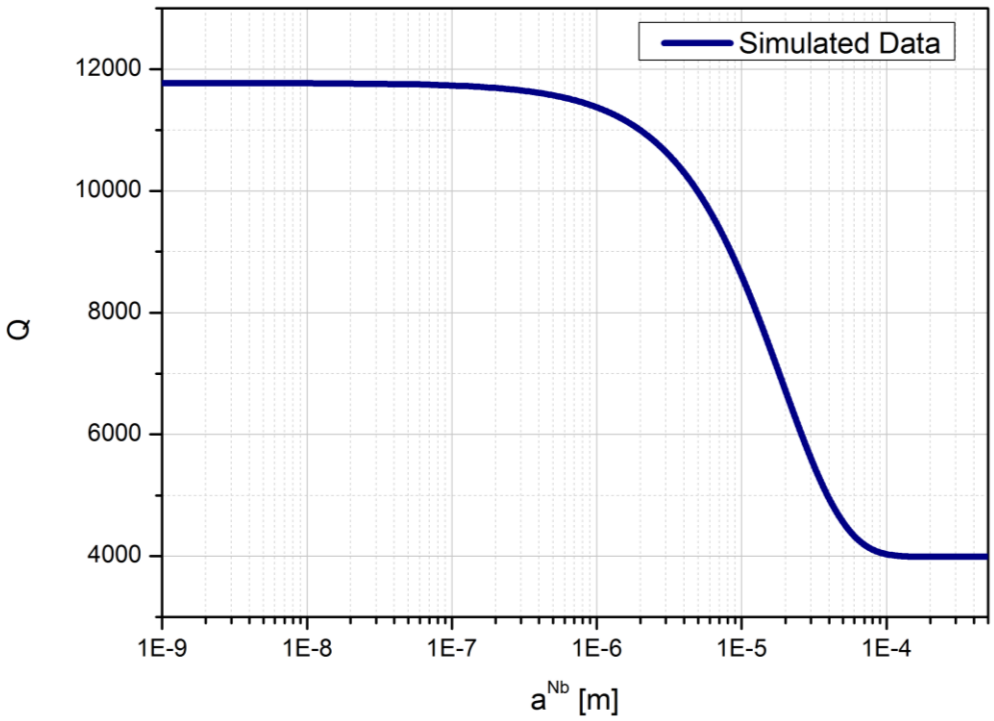

FIGURE 5.17 - SIMULATION OF Q-FACTOR AT WARM TEMPERATURE AS A FUNCTION ON NIOBIUM FILM THICKNESS .

So:

$$\frac{1}{Z} = \frac{1}{Z^{Nb}} E_0 (1 - e^{-a/\delta^{Nb}}) + \frac{1}{Z^{Cu}} e^{-a/\delta^{Nb}} \tag{5.22}$$

Since the surface resistance is the real part of the surface impedance and the Q-factor is defined as $Q = G/R_S$, hence the Q-factor of a Niobium on Copper cavity at warm temperature can be defined as:

$$Q = Q^{Nb}(1 - e^{-a/\delta^{Nb}}) + Q^{Cu} e^{-a/\delta^{Nb}} \tag{5.23}$$

Which is equal to:

$$Q = Q^{Nb} + (Q^{Cu} - Q^{Nb}) e^{-a/\delta^{Nb}} \tag{5.24}$$

It was so found a relation between the Q-factor at warm temperature and the thickness of the Niobium film. The simulated trend is shown in Figure 5.17, when the film thickness is about some nanometers the RF behaviour is completely governed by the Copper substrate, indeed the Q-factor is equal to the Copper cavity value. As much the film thickness increases the Q-factor decreases, as long as it approaches at the Niobium cavity value when the field remains completely inside the Niobium layer.

A Niobium film thickness of about $12\mu m$ is found for a Q-factor of 8075.This value seems overestimated because the thickness of the film should be of about few *micrometers*. This discrepancy could be due to the non uniformity of the sputtered Niobium layer, while the RF measurement gives as result a global behaviour of the cavity. By the way such indirect method used for the thickness calculation is not very accurate, because the Q-factor measurement at room temperature cannot be estimated accurately by using a network analyzer [32].

5.6 RF TEST OF NIOBIUM ON COPPER 6GHZ CAVITIES

At the Legnaro National Laboratories (LNL, INFN) three Niobium on Copper 6GHz elliptical cavities were measured. Let us now analyze the results obtained.

5.6.1 CU1_1: FIRST NIOBIUM DEPOSITION

The RF measurement of the first Niobium sputtered cavity, Cu1_1, gives as result the graph shown in Figure 5.18. Two curves Q-factor versus accelerating field were measured, at $4.2K$ and at $1.8K$, and during the cool-down of the cavity some points were measured at fixed power values: $100mW$, $300mW$, $600mW$, $1W$. This cavity was sputtered at room temperature, but after the HPR process part of the film went away, in particular at the cut-off region.

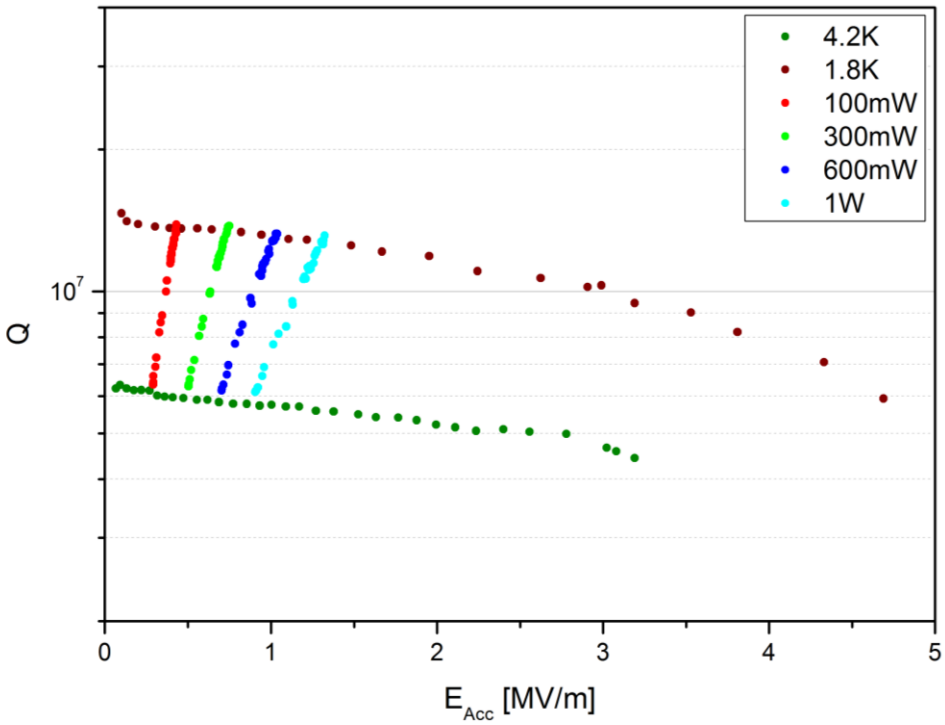

FIGURE 5.18 - RF MEASUREMENTS ON CU1_1 SPUTTERED NIOBIUM CAVITY .

The performances of this cavity are rather low, the Q-factor starts from $6 \cdot 10^6$ at $4.2K$ and from $1 \cdot 10^7$ at $1.8K$ and the maximum accelerating field reached is about $3MV/m$ at $4.2K$ and $5MV/m$ at $1.8K$. Because of the low Q-factor, the power dissipated by this cavity is very high and it does not allow to reach high accelerating field.

The low cavity performances might be due to the normal-conducting zones which increments considerably the global surface resistance of the cavity. The dissipated power also increases because it depends on the surface resistance and on the applied magnetic field $\bar{H}$:

$$P_C = \frac{1}{2} R_S \int_S |\bar{H}|^2 ds \tag{5.25}$$

Under such condition the accelerating field obtained is very low because of the RF power losses.

The points taken at constant power as a function of temperature are useful in order to study the superconducting properties of the cavity surface. Indeed, remembering that $Q = G/R_S$, it is possible to graph the surface resistance R_S as a function of $1/T$.

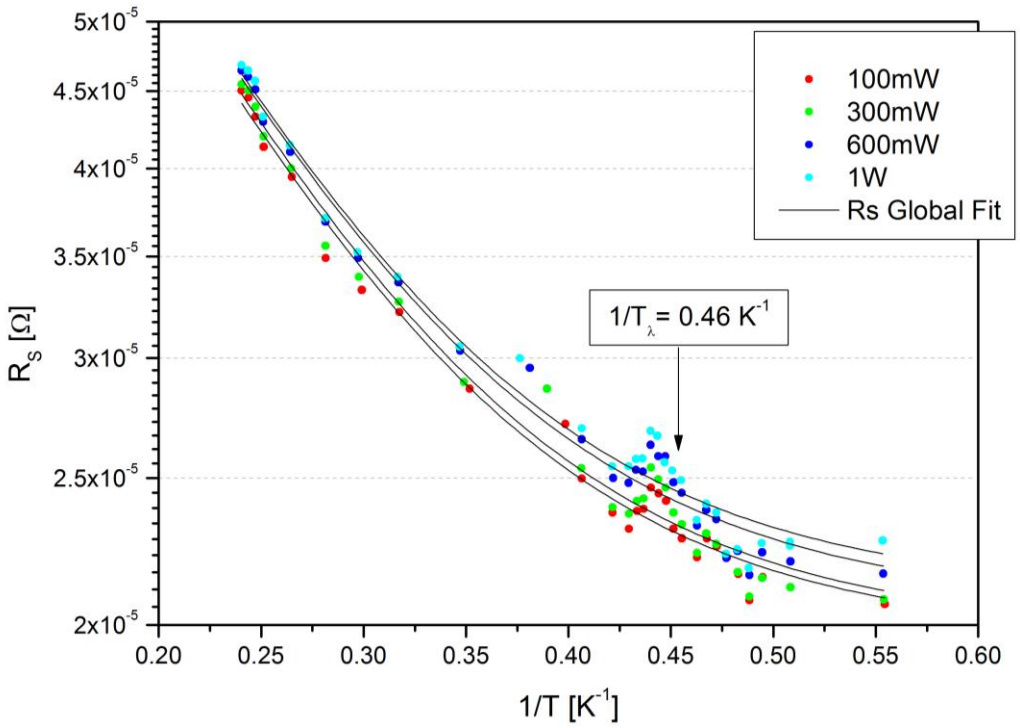

FIGURE 5.19 - SURFACE RESISTANCE VERSUS 1/T FOR CU1_1 SPUTTERED NIOBIUM CAVITY .

The graph obtained is shown in Figure 5.19. It displayes that the surface resistance decreases with the temperature as long as it approaches at a quite constant value. This behavior is expected from the theory in which the surface resistance is given by the sum of the BCS resistance, $R_{BCS}(T)$, which decreases with temperatures, and the residual resistance, R_0, which does not change with temperature:

$$R_S = A\rho_n^{\frac{1}{2}}\omega^2 ln\left(\frac{\Delta}{\hbar\omega}\right)\frac{e^{-\frac{\Delta}{k_BT}}}{T\sqrt{sT_c}\left(1+e^{-\frac{\Delta}{k_BT}}\right)^2} + R_0 \cong \frac{A'\omega^2}{T}e^{-\Delta/k_BT} + R_0 \qquad (5.26)$$

Therefore, the curves of the surface resistance versus $1/T$ were fitted by using Equation 5.26 with $\omega = 2\pi f$ and $\Delta = \frac{s}{2}k_BT_C$. The critical temperature and the resonance frequency were used as fixed parameters equal for all curves (global fit): $T_C = 9.25K$, $f = 6 \cdot 10^9 GHz$. Fitting the data using the surface resistance and the strength coupling s as free fit parameters, an estimation of these values is realized. Thanks to the global fit approach, the parameter A was also set as free parameter, but it was set as shared between all the data sets. Then the fitting program calculate A as the best fit parameters between them. The critical temperature was fixed at $T_C = 9.25K$ which the value found in literature because we do not have an experimental estimation of this value. The results of the surface resistance global fit are shown in Table 5.5.

TABLE 5.5 - SURFACE RESISTANCE FIT RESULTS FOR CU1_1 CAVITY.

Parameter	**100mW**	**300mW**	**600mW**	**1W**
$\boldsymbol{A\ [\Omega K s^{-2}]}$	$(1.4 \pm 0.13) \cdot 10^{-24}$	$(1.4 \pm 0.13) \cdot 10^{-24}$	$(1.4 \pm 0.13) \cdot 10^{-24}$	$(1.4 \pm 0.13) \cdot 10^{-24}$
$\boldsymbol{R_0\ [\Omega]}$	$(1.97 \pm 0.04) \cdot 10^{-5}$	$(1.99 \pm 0.04) \cdot 10^{-5}$	$(2.06 \pm 0.04) \cdot 10^{-5}$	$(2.11 \pm 0.04) \cdot 10^{-5}$
$\boldsymbol{s}$	2.68 ± 0.09	2.67 ± 0.09	2.66 ± 0.09	2.67 ± 0.09

The residual resistance R_0 estimated, as expected, is very high, the mean value is $R_0 = 20.3\ \mu\Omega$. Looking carefully at the graph it can be noticed that the surface resistance seems to have a small peak just before the lambda point T_λ, i.e. at slightly higher temperature.

This set of measurements was done with a thermometer fixed on the upper flange of the RF stand, as it is shown in Figure 5.20 (a). The thermometer was thermalized by the flange, made of stainless steel, hence the measured temperature might differ from the Helium bath one. For this reason a second RF test of the same cavity was made changing the thermometer position, Figure 5.20 (b), in order to be sure that the Helium bath temperature was monitored.

The results of this test are shown in Figure 5.21, whereas in Figure 5.22 is shown the graph of the surface resistance curves as a function of $1/T$ taken at different level of dissipated power.

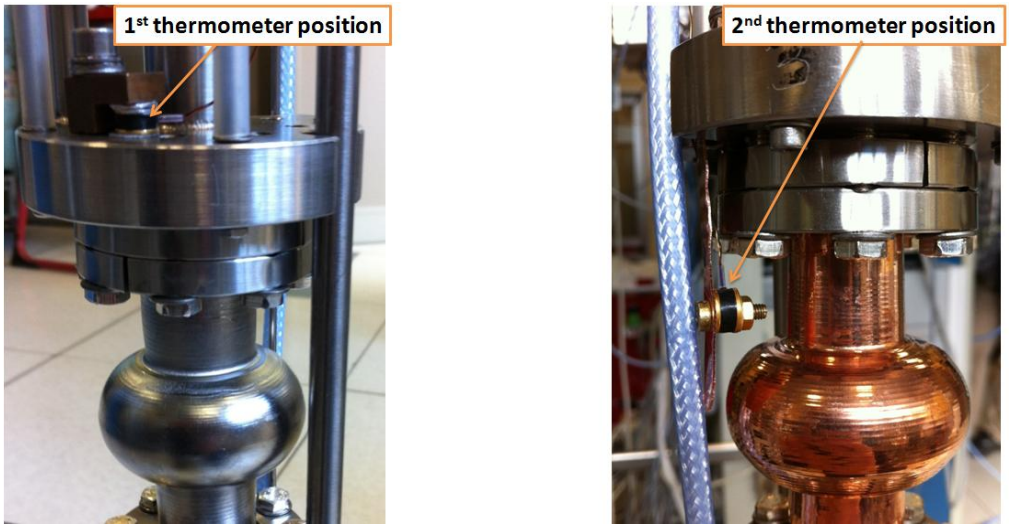

(A) (B)

FIGURE 5.20 - (A) FIRST RF TEST THERMOMETER POSITION (B) SECOND RF TEST THERMOMETER POSITION.

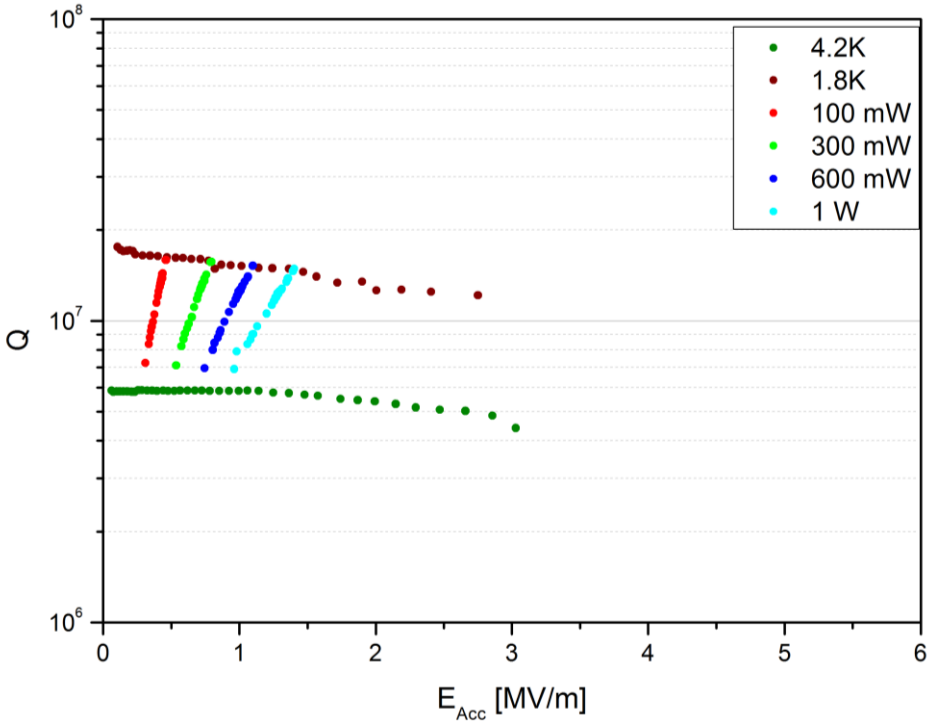

FIGURE 5.21 - RF MEASUREMENTS ON CU1_1 NIOBIUM SPUTTERED CAVITY WITH THERMOMETER IN SECOND POSITION.

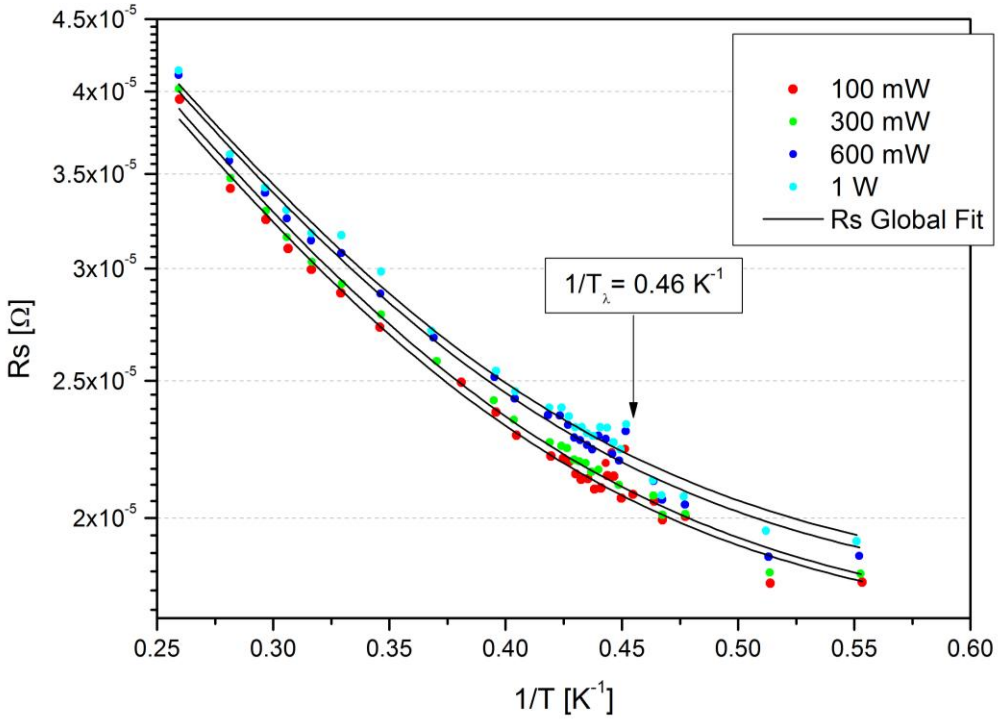

FIGURE 5.22 - SURFACE RESISTANCE VERSUS 1/T FOR CU1_1 NIOBIUM SPUTTERED CAVITY USING THE SECOND THERMOMETER POSITION.

TABLE 5.6 - SURFACE RESISTANCE FIT RESULTS FOR CU1_1 CAVITY USING THE SECOND THERMOMETER POSITION.

Parameter	100mW	300mW	600mW	1W
$\boldsymbol{A}\ [\boldsymbol{\Omega K s^{-2}}]$	$(1.13 \pm 0.07) \cdot 10^{-24}$	$(1.13 \pm 0.12) \cdot 10^{-24}$	$(1.13 \pm 0.12) \cdot 10^{-24}$	$(1.13 \pm 0.12) \cdot 10^{-24}$
$\boldsymbol{R_0}\ [\boldsymbol{\Omega}]$	$(1.64 \pm 0.03) \cdot 10^{-5}$	$(1.65 \pm 0.04) \cdot 10^{-5}$	$(1.72 \pm 0.04) \cdot 10^{-5}$	$(1.76 \pm 0.04) \cdot 10^{-5}$
$\boldsymbol{s}$	2.45 ± 0.06	2.44 ± 0.06	2.42 ± 0.06	2.42 ± 0.06

The curves at 4.2K and 1.8K for the Q-factor versus the accelerating field do not differ considerably from the previous measurement, whereas the graph of the surface resistance versus $1/T$ displays quite different results.

These measurements also show higher value of surface resistance close to the lambda point. The data points were, in any case, interpolated with the previous fitting function, giving the data listed in Table 5.6.

The mean value obtained for the residual resistance is $R_S = 16.9\ \Omega$, which is smaller than the one found with the first RF test. Maybe the surface properties was condictioning during the first RF test. Indeed it sometimes happens that the surface is conditioned by the RF field, i.e. some defects or dust particles may be modified by the electric field.

By the way, looking at the values of the residual resistance, they seem to depend on the dissipated power. Plotting this value for both the measurements, Figure 5.23, a clear trends appear: the residual resistance increases with the dissipated power.

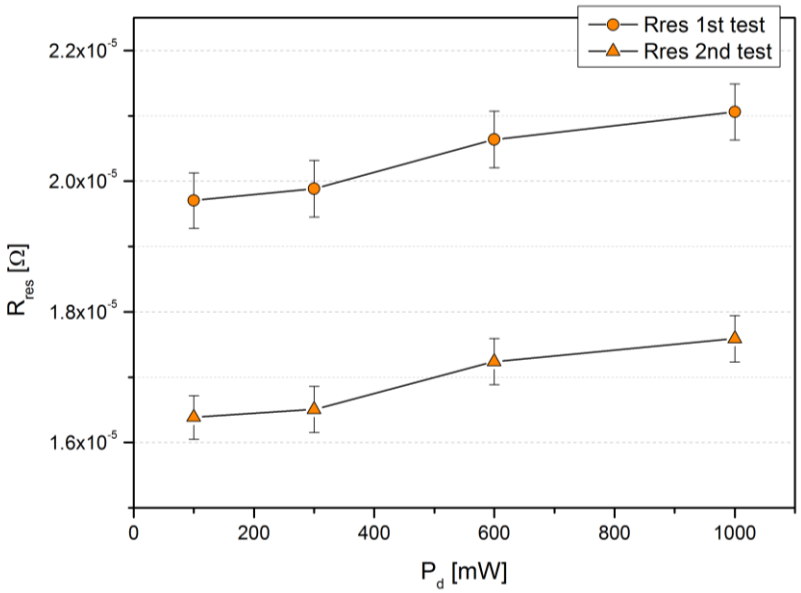

FIGURE 5.23 - RESIDUAL RESISTANCE AS A FUNCTION OF THE DISSIPATED POWER FOR THE CU1_1 CAVITY.

The BCS theory does not consider the dependence between the surface resistance and the dissipated power, therefore it is important to verify if the same trend will be found in other data, in order to understand what kind of effect might be the cause. In addition, remembering that the cavity analyzed does not have good superconducting proprieties, it is not possible to obtain any reliable conclusion from this analysis.

5.6.2 CU1_2: SECOND NIOBIUM DEPOSITION

The cavity Cu1_2 was also sputtered at room temperature and, because of the adhesion problem encountered with Cu1_1 cavity, the cavity Cu1_2 was measured before and after the High Pressure Rinsing; the results of the RF measurements are shown is Figure 5.24. The curves of Q-factor versus accelerating field were measured at $4.2K$ and at $1.8K$, and at fixed power values ($50mW$ and $1W$ for the measurement before the HPR, only at $50mW$ for the measurement after the HPR) as a function of temperature.

Both the measurements done before and after the HPR, for the Cu1_2 cavity, show better superconducting proprieties compared to the first cavity measured. Indeed, in this case the Niobium film is more adherent to the Copper substrate given that it was not removed during the high pressure rinsing process. At $4.2K$ the curve starts from $Q{\sim}10^7$ and at 1.8K from $Q{\sim}2\cdot10^8$.

Unluckily the Q-slope of the curve at $1.8K$ is conspicuous, the dissipated power gets bigger and bigger as the accelerating field increases. The slope is so large than the Q-factor approaches at the values found at $4.2K$ at about $5.5MV/m$ as accelerating field. After the HPR, the curve $Q(E_{acc})$, at $4.2K$, decreases just a little compared to the previous measurements, whereas the curve at $1.8K$ changes more considerably: for low field the Q values are higher after the HPR, whereas for high field the Q-factor values become smaller than without HPR. Around $1W$ of dissipated power the two curves approach the same values. This cavity did not present field emission, by the way the HPR process is important to remove the dust particles from the surface so the RF measurement is more precise and it is not affected by foreign particles on the surface.

The RF measurement was performed using two thermometers which monitor the Helium bath temperature, as it is shown in Figure 5.25. The curves of the surface resistance as a function of $1/T$ are shown in Figure 5.26 for the measurement done with the thermometer 1 ($Cernox\ X62101$), and in Figure 5.27 for the measurement done with the thermometer 2 ($Cernox\ X63398$). Also in this case the curves were fitted using the surface resistance formula given by the BCS theory

A global fit was done for the two curves measured before the HPR fixing the critical temperature and the resonance frequency: $T_C = 9.25\ K$, $f = 6\cdot10^9\ GHz$ and using the surface resistance and the strength coupling s as free fit parameters. Also the parameter A was left as a free parameter but it was restricted to have the same value for both curves. A single fit of the curve measured after the HPR was performed in the same manner. The results are displayed in Table 5.7.

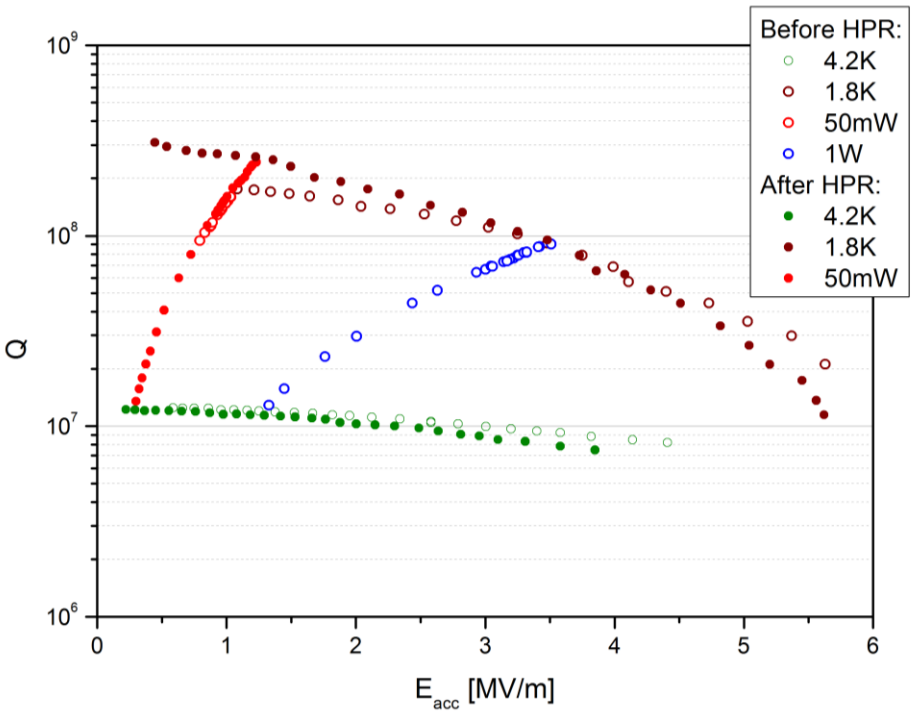

FIGURE 5.24 - RF MEASUREMENTS OF CU1_2 SPUTTERED NIOBIUM CAVITY, BEFORE AND AFTER THE HPR.

.

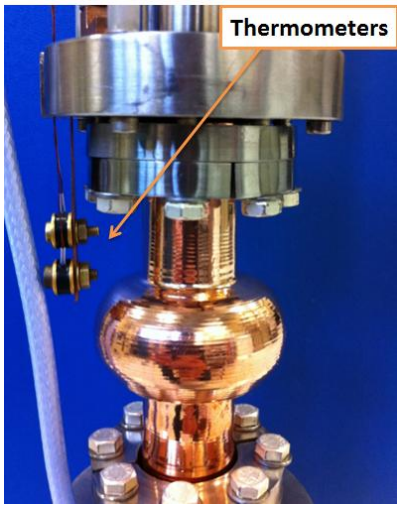

FIGURE 5.25 - CU1_2 RF TEST THERMOMETER POSITION.

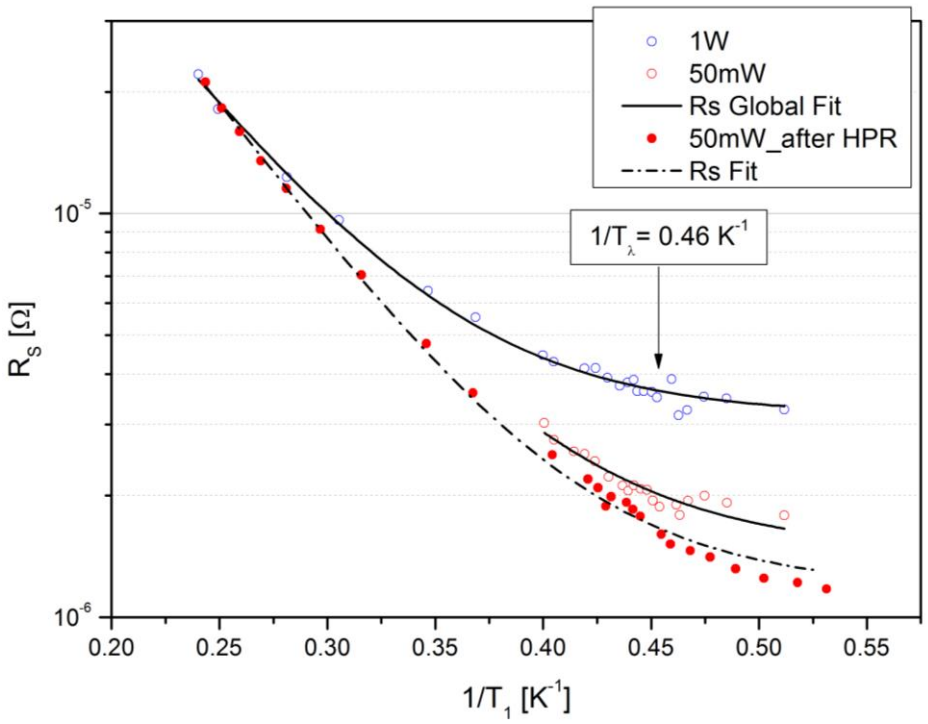

FIGURE 5.26 - SURFACE RESISTANCE VERSUS 1/T FOR CU1_2 NIOBIUM SPUTTERED CAVITY USING THE THERMOMETER1.

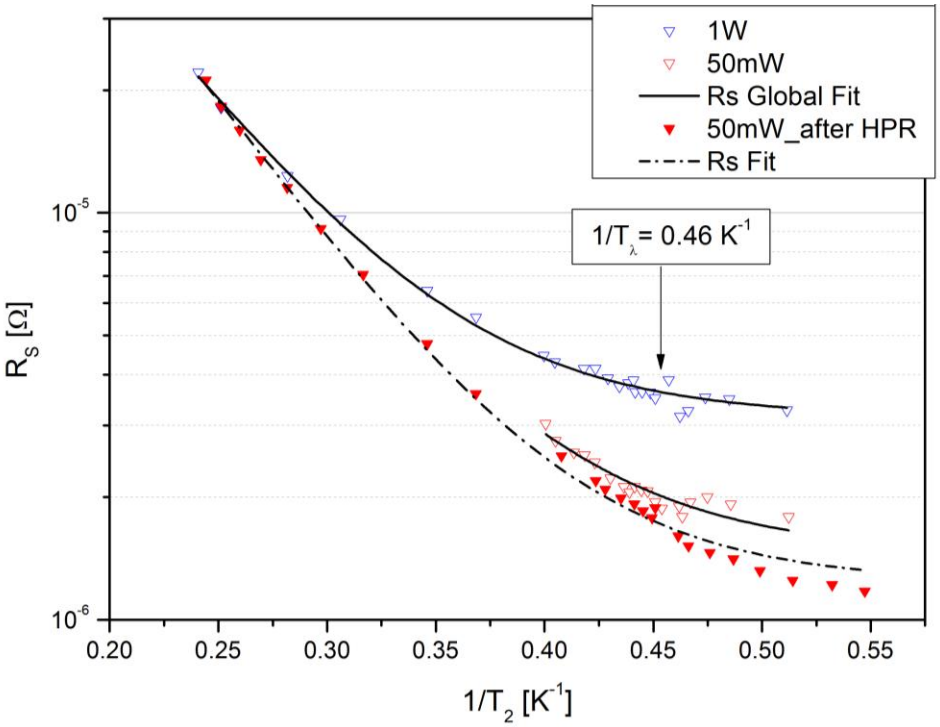

FIGURE 5.27 - SURFACE RESISTANCE VERSUS 1/T FOR CU1_2 NIOBIUM SPUTTERED CAVITY USING THE THERMOMETER2.

TABLE 5.7 - SURFACE RESISTANCE FIT RESULTS FOR CU1_2 CAVITY.

	Parameter	50mW	50mW after HPR	1W
T1	$\boldsymbol{A\ [\Omega K s^{-2}]}$	$(6.8 \pm 0.8) \cdot 10^{-24}$	$(8.5 \pm 0.7) \cdot 10^{-24}$	$(6.8 \pm 0.8) \cdot 10^{-24}$
	$\boldsymbol{R_0\ [\Omega]}$	$(1.5 \pm 0.14) \cdot 10^{-6}$	$(1.18 \pm 0.06) \cdot 10^{-6}$	$(3.16 \pm 0.08) \cdot 10^{-6}$
	$\boldsymbol{s}$	4.3 ± 0.11	4.45 ± 0.07	4.35 ± 0.1
T2	$\boldsymbol{A\ [\Omega K s^{-2}]}$	$(7.1 \pm 0.7) \cdot 10^{-24}$	$(8.7 \pm 0.7) \cdot 10^{-24}$	$(7.1 \pm 0.7) \cdot 10^{-24}$
	$\boldsymbol{R_0\ [\Omega]}$	$(1.5 \pm 0.12) \cdot 10^{-6}$	$(1.24 \pm 0.06) \cdot 10^{-6}$	$(3.16 \pm 0.07) \cdot 10^{-6}$
	$\boldsymbol{s}$	4.3 ± 0.1	4.47 ± 0.08	4.4 ± 0.1

Taking into account the curve taken at $50mW$, after the HPR the surface resistance found is lower than the one found before the HPR. The data points seem to be also less scattered. Unfortunately, it was not possible to take other curves at constant power during this test. By the way, both the values of surface resistance at $50mW$ are smaller than the value for $1W$ of dissipated power. This means that we have found again that the surface resistance increases with the power. Watching accurately at the curve taken at 50mW before the HPR, it is easy to note that the fitting curve starts to differ from the experimental data at the lambda point.

5.6.3 CU1_3: HIGH TEMPERATURE NIOBIUM DEPOSITION

The Niobium film of the third cavity analyzed was sputtered at high temperature for improving the superconducting properties of the film. The process was done at 400°C, so the Niobium layer should have better crystallographic properties than the previous cavity which were sputtered at room temperature instead. The RF behavior of a cavity is largely influenced by the surface properties and, incrementing the grain boundaries size, one can expect to decrease both the BCS and the residual resistance.

The results of the RF measurements are shown in Figure 5.28. The Q-factor versus accelerating field curves were measured at $4.2K$ and at $1.8K$, and at fixed power values ($50mW$, $100mW$, $200mW$) as a function of temperature.

The cavity performances are higher than the previous analyzed cavities. At $4.2K$ the Q-factor remains quite constant with the accelerating field, maintaining values around $Q{\sim}3 \cdot 10^7$. At $1.8K$ the curve starts from high value of Q-factor, about $Q{\sim}6 \cdot 10^8$, and the slope remains low until the accelerating field reaches about $3.5MV/m$. From this point the slope becomes important and near $6MV/m$ the Q-value approaches at the value measured at 4.2K. Then, the peculiarity of this curve is that it is characterized by own two different slope. The large slope, which really lowered the performances starts from about $3.5MV/m$.

The RF measurement was performed using two thermometers for monitoring the Helium bath temperature. As it is shown in Figure 5.29 only one thermometer was positioned close to the Cu1_3 cavity, the other one was fixed to another cavity inserted into the cryostat during the same measurement. The curves of the surface resistance as a function of $1/T$ acquired with the thermometer 1 ($Cernox\ X62101$) are shown in Figure 5.30 and with the thermometer 2 ($Cernox\ X63398$) in Figure 5.31 .

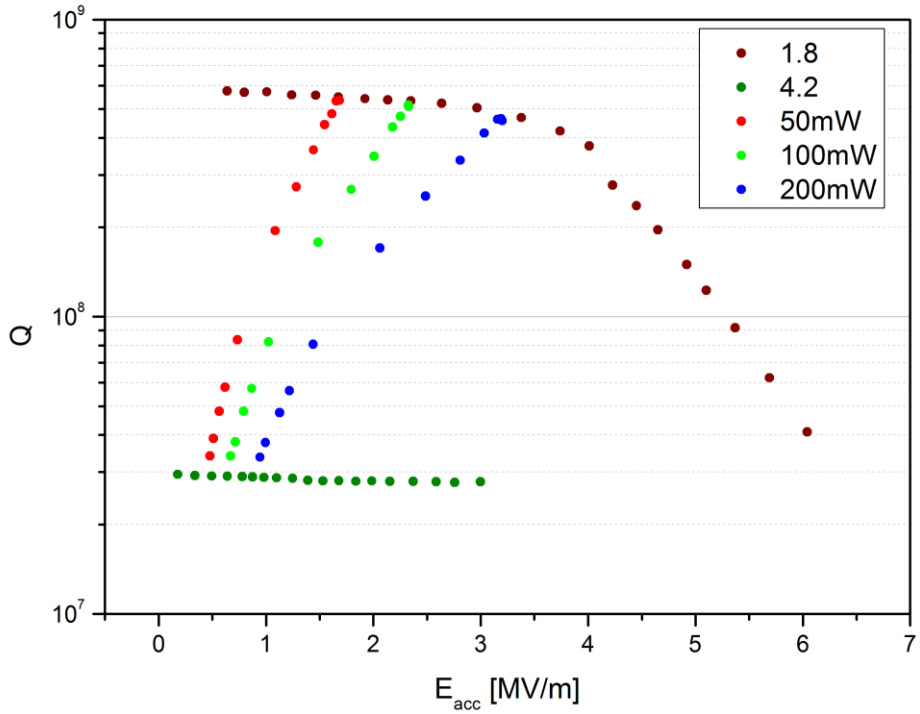

FIGURE 5.28 - RF MEASUREMENTS OF CU1_3 NIOBIUM SPUTTERED CAVITY.

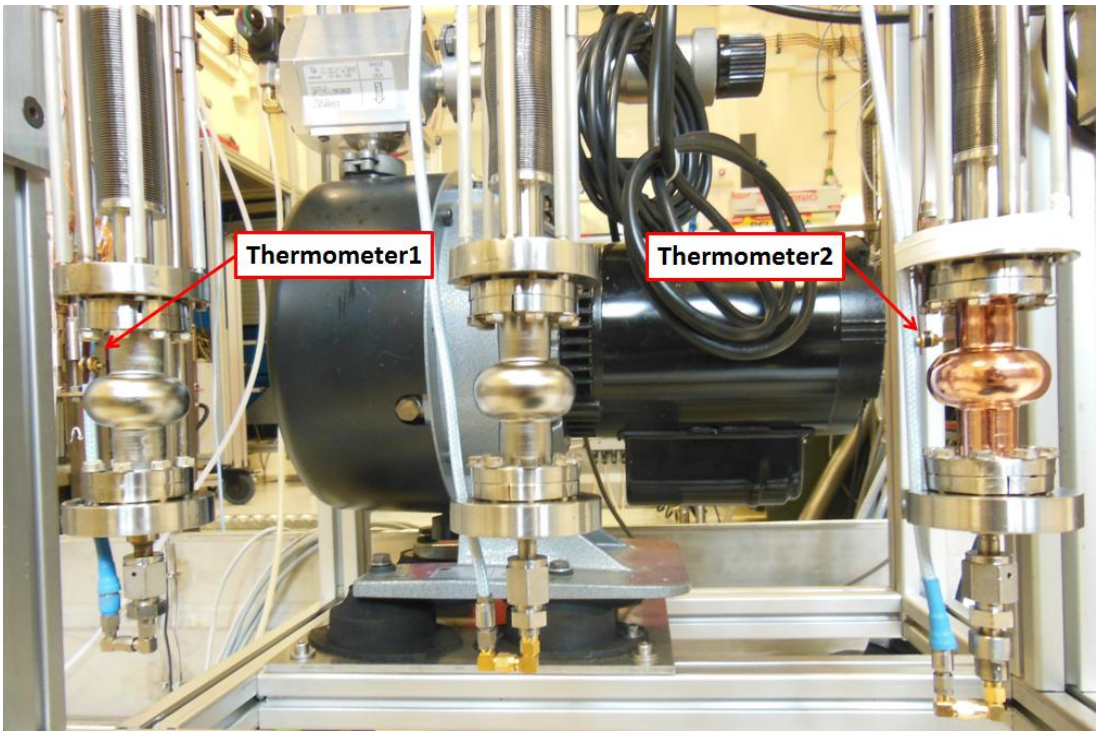

FIGURE 5.29 - PHOTO OF THE THERMOMETERS POSITION DURING THE RF MEASUREMENT.

The surface resistance was fitted by doing a global fit in which the parameter A, the critical temperature and the resonance frequency must remain the same for all curves, and while $T_C = 9.25K$, $f = 6 \cdot 10^9 GHz$ were fixed parameters, the constant A was left as free parameter. Whereas the residual resistance and the strong coupling s were free fit parameters that can be different for each curve. The results are displayed in Table 7.5.

TABLE 5.8 - SURFACE RESISTANCE FIT RESULTS FOR CU1_3 CAVITY.

	Parameter	50mW	100mW	200mW
T1	$A\ [\Omega K s^{-2}]$	$(3.3 \pm 0.2) \cdot 10^{-24}$	$(3.3 \pm 0.2) \cdot 10^{-24}$	$(3.3 \pm 0.2) \cdot 10^{-24}$
	$R_0\ [\Omega]$	$(4.5 \pm 0.4) \cdot 10^{-7}$	$(4.60 \pm 0.04) \cdot 10^{-7}$	$(4.75 \pm 0.03) \cdot 10^{-7}$
	s	4.36 ± 0.06	4.36 ± 0.06	4.36 ± 0.06
T2	$A\ [\Omega K s^{-2}]$	$(3.4 \pm 0.2) \cdot 10^{-25}$	$(3.4 \pm 0.2) \cdot 10^{-25}$	$(3.4 \pm 0.2) \cdot 10^{-25}$
	$R_0\ [\Omega]$	$(4.7 \pm 0.4) \cdot 10^{-7}$	$(4.9 \pm 0.4) \cdot 10^{-7}$	$(5.3 \pm 0.4) \cdot 10^{-7}$
	s	4.34 ± 0.05	4.34 ± 0.05	4.33 ± 0.05

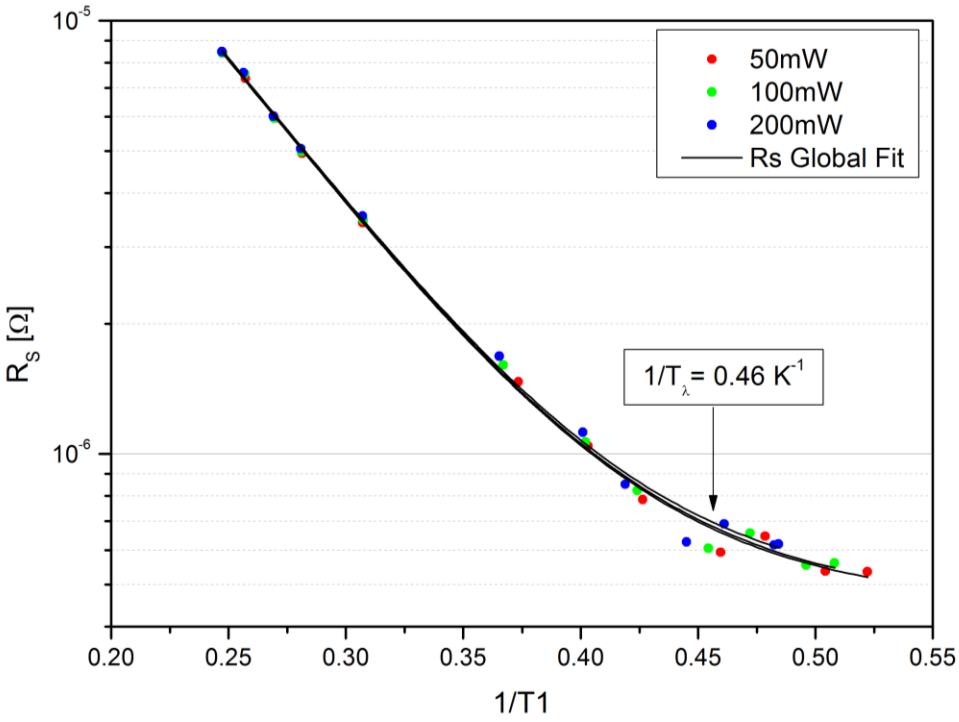

FIGURE 5.30 - SURFACE RESISTANCE VERSUS 1/T FOR CU1_3 NIOBIUM SPUTTERED CAVITY USING THE THERMOMETER1.

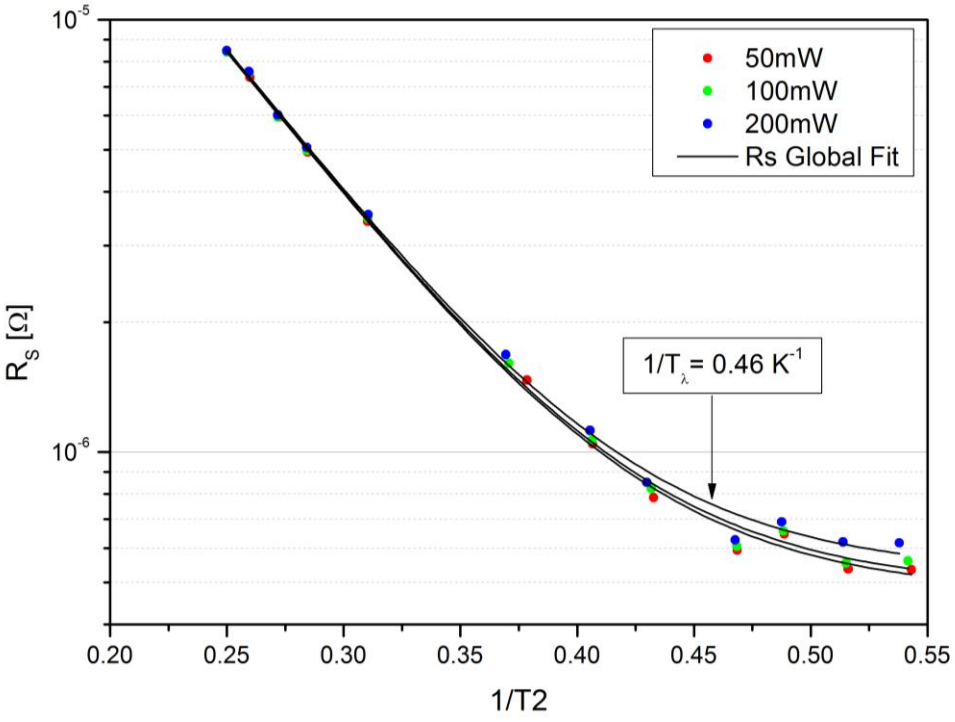

FIGURE 5.31 - SURFACE RESISTANCE VERSUS 1/T FOR CU1_3 NIOBIUM SPUTTERED CAVITY USING THE THERMOMETER2.

The trend of the residual resistance as a function of the dissipated power is plotted in Figure 5.32. This graph shows that R_0 increases with the dissipated power, such trend was found for all RF tests done. The data are, so, not completely in agreement with the BCS theory, inasmuch it does not take into account any dependence of the residual resistance from the dissipated power. Furthermore, from Figure 5.32 one notices that the values of the residual resistance are underestimated for the measurements with thermometer1 compared to the ones with the thermometer2. As mentioned before, the two thermometers were fixed closed to two different cavities, the thermometer2 (fixed on another cavity) measured smaller temperature than the termometer1 (fixed on Cu1_3 cavity) for the same value of Q-factor, and therefore of surface and residual resistances.

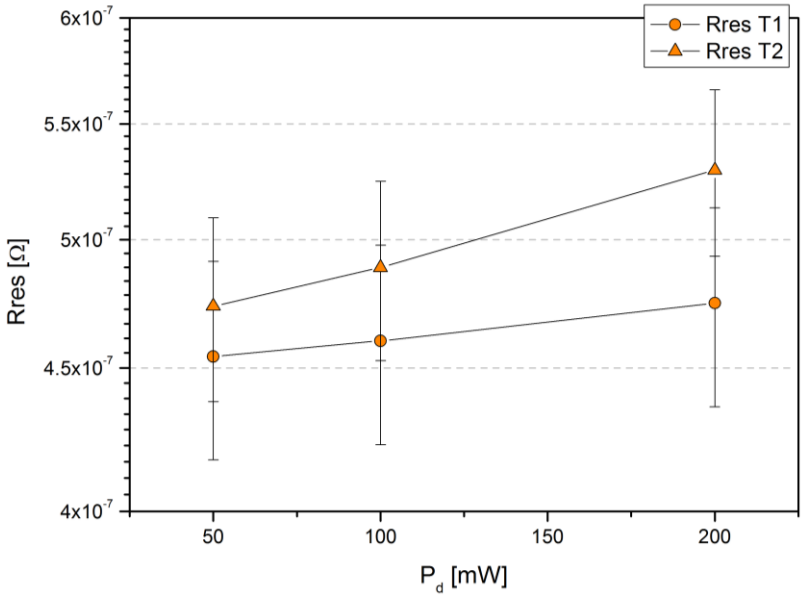

FIGURE 5.32 - RESIDUAL RESISTANCE AS A FUNCTION OF THE DISSIPATED POWER FOR THE CU1_3 CAVITY.

In addition, considering the Figure 5.30 (measurements done with thermometer1) it can be notice that there is a strange behavior for the data near the lambda point. For temperature just after the super-fluid Helium transition $T_\lambda = 2.1768K$ the surface resistance increases and then it remains quite constant for lower temperatures. The fitting curves have indeed a different behavior respect to the data analyzed, and the trend of the fit differs particularly after the lambda point, in which the experimental values show lower surface resistance value.

The experimental observations suggest that close to the external cavity surface the temperature increases considerably, the thermometer near the cavity surface showed higher value than the other thermometer during the curve at 1.8K. Furthermore, as the previous results, the residual resistance increases with the dissipate power.

5.6.4 NIOBIUM SPUTTERED 6GHZ CAVITY: SUMMARY OF RESULTS

In Figure 5.33 the surface resistance versus accelerating field curves, of all 6GHz Niobium on Copper cavities, are displayed.

The higher surface resistance values are found for the cavity Cu1_1 either at $4.2K$ and $1.8K$, but the particularly lower performances of this cavity are highlighted with the curve at $1.8K$ which shows values so low that the curve at $4.2K$ for the cavity Cu1_3 has a lower surface resistance. Better results are instead obtained for the cavity Cu1_2, which was sputtered at room temperature as the previous one.

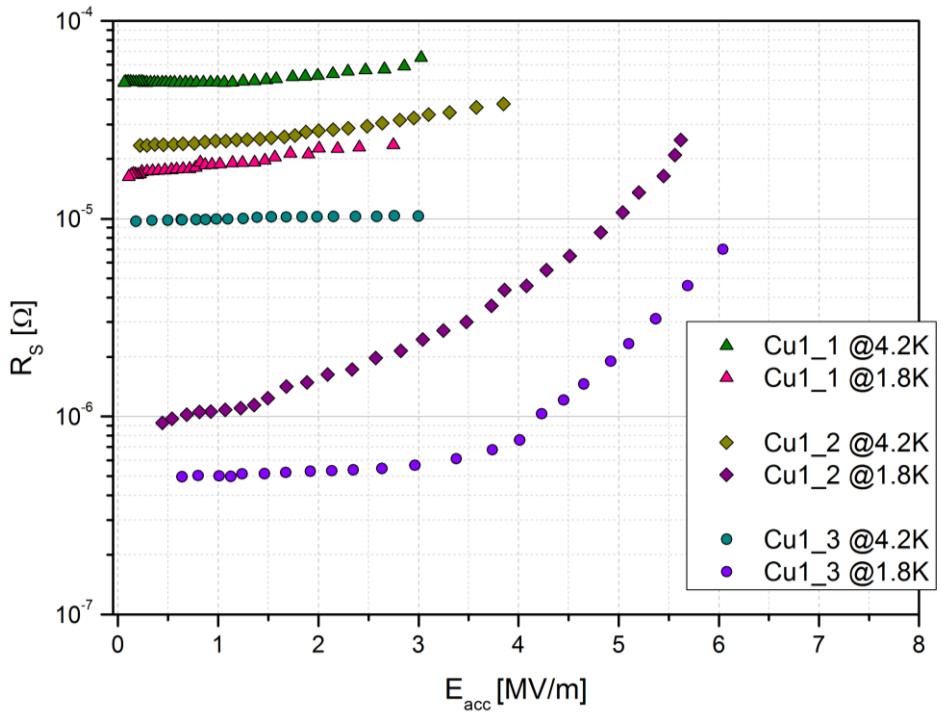

FIGURE 5.33 - RESIDUAL RESISTANCE AS A FUNCTION OF ACCELERATING FIELD FOR THE 6GHZ NB/CU CAVITIES.

The difference between the two processes was in the continuous movement of the cavity during the deposition which probably involves a more film uniformity. However, the very high values of surface resistance of the cavity Cu1_1 are due to the presence of many normal-conducting zones.

In any case the best performances were obtained by the cavity Cu1_3 which was sputtered at 400°C. As expected the crystallographic proprieties of the Niobium film were improved in this manner. Also the slope of the curve at $4.2K$ for this cavity is decreased compared to the other two cavities, but unfortunately the slope at $1.8K$ at high field is similar to cavity Cu1_2 and well pronounced.

Also the values of residual resistance summarized in Table 5.9 are in agreement with these assertion. It is also clear that the strong coupling factor s is underestimated for cavity Cu1_1 and overestimate for Cu1_2 and Cu1_3 cavities compared to the literature values ($s = 3.8$). A not optimized estimation of this parameter might be due to the value of critical temperature, that was fixed using the value reported in literature. Also the data discontinuity found at lambda point, which is not expected by the BCS theory, might play a role in this discrepancy.

TABLE 5.9 - SUMMARY RESULTS FOUND WITH BCS THEORY FOR THE 6GHZ CAVITY ANALYZED.

Parameter	**Cu1_1**	**Cu1_2**	**Cu1_3**
$\boldsymbol{A\ [\Omega K s^{-2}]}$	$1.13 \cdot 10^{-24}$	$7.5 \cdot 10^{-24}$	$3.4 \cdot 10^{-24}$
$\boldsymbol{R_0\ [\Omega]}$	$1.69 \cdot 10^{-5}$	$1.96 \cdot 10^{-6}$	$4.79 \cdot 10^{-7}$
$\boldsymbol{s}$	2.43	4.38	4.35

5.7 THIN FILM CAVITY Q-SLOPE AS A THERMAL PROBLEM

Let us recall the surface resistance defined by the BCS theory, used for the previous fit:

$$R_S \cong \frac{A'\omega^2}{T} e^{-\Delta/k_B T} + R_0 \tag{5.27}$$

where T is the temperature of the superconducting Niobium film. Until now we have considered T as the temperature measured in the Helium bath making the strong approximation that this is equal to the Niobium film temperature. However, what really happens is that the heating, due to the RF losses on the cavity walls, flows from the Niobium film surface to the Helium bath, where the temperature is really measured. So we have:

$$T_0 = T_{surface} - \Delta T \tag{5.28}$$

where T_0 is the Helium bath temperature and, $T_{surface}$ is the Niobium film surface temperature and ΔT is the temperature difference between them.

Let us now resort to a *thermal feed-back model* [33] in which the superconductor surface resistance dependence on temperature is described by the derivative of the resistance respect to the temperature itself. Then the surface resistance can be expressed as:

$$R_S(T) = R_S(T_0) + \left(\frac{\partial R_S}{\partial T}\right)_{T=T_0} \Delta T \tag{5.29}$$

where:

$$\Delta T = \frac{R_{thermal} \cdot P_d}{\Sigma} \tag{5.30}$$

ΔT is the temperature rising due to the thermal feedback, $R_{thermal}$ is the thermal resistance which is responsible to the feed-back loop, P_d is the dissipated power, Σ is the surface in which the power is dissipated. Therefore the thermal feed-back is due to the dissipated power which increases the temperature, because of the thermal resistance. Such rising causes also the global surface resistance increasing and, again, higher temperature. Then the RF field is increased giving a new temperature rising and so on.

Deriving the surface resistance for the temperature, the following equation is found:

$$\left(\frac{\partial R_S}{\partial T}\right)_{T=T_0} = \frac{A\omega^2}{T_0} e^{-\Delta/k_B T} \left(\frac{\Delta}{k_B {T_0}^2} - \frac{1}{T_0}\right) \tag{5.31}$$

It is so necessary to correct the Equation 7.27 as:

$$\begin{aligned} R_S(T_0, P_d) &= R_S(T_0) + \frac{A\omega^2}{T_0} e^{-\frac{\Delta}{k_B T_0}} \left(\frac{\Delta}{k_B {T_0}^2} - \frac{1}{T_0}\right) \Delta T \\ &= \frac{A\omega^2}{T_0} e^{-\frac{\Delta}{k_B T_0}} + R_0 + \frac{A\omega^2}{T_0} e^{-\frac{\Delta}{k_B T_0}} \left(\frac{\Delta}{k_B {T_0}^2} - \frac{1}{T_0}\right) \frac{R_{thermal} \cdot P_d}{\Sigma} \\ &= \frac{A\omega^2}{T_0} e^{-\frac{\Delta}{k_B T_0}} \left[1 + \left(\frac{\Delta}{k_B {T_0}^2} - \frac{1}{T_0}\right) \frac{R_{thermal} \cdot P_d}{\Sigma}\right] + R_0 \end{aligned} \tag{5.32}$$

The thermal feed-back model asserts that the BCS resistance has to be modified, indeed in Equation 5.27 it must be considered an additional term, which takes into account the temperature rising. The Equation 5.32 cannot be used, however, for fitting the data R_S versus $1/T$ at constant power, because the additional term $R_{thermal}$ will be defined further on as dependent on temperature.

TABLE 5.10 - FIXED PARAMETERS SET FOR THE THERMAL MODEL FIT .

Critical Temperature T_C	$9.25K$
Bath temperature T_0	$1.8K$
Resonance frequency f	$6 \cdot 10^9\ Hz$
Residual Resistance R_0	$1 \cdot 10^{-7}\Omega$
Surface Σ	$42.86\ cm^2$
Strong coupling factor s	3.8

The surface resistance versus dissipated power curve found at $1.8K$ was fitted using the Equation 5.32, and defining the energy gap as $\Delta = \frac{s}{2} k_B T_C$. From the thermal model one can expect that the surface resistance increases with the dissipated power, which is in accordance with the results found in the previous section.

The fixed fit parameters are listed in

Table 5.10, whereas the constant A and the thermal resistance $R_{thermal}$ are free parameters. The residual resistance was fixed by choosing the values as close as possible to the ones found with the previous fit, and that allow to interpolate well the data. For this purpose the residual resistance had to be chosen lower than the value of the previous result ($1 \cdot 10^{-7}$ instead of $4 \cdot 10^{-7}$).

In Figure 5.34 the graph surface resistance versus dissipated power for the measurements done at $4.2K$ and $1.8K$, is displayed. At $4.2K$ the surface resistance is quite constant with the power, whereas at 1.8K it increases rapidly as the dissipated power increases. The graph displays also the fit done, for the curve at $1.8K$, with the thermal model, and the results are shown in Table 5.11.

TABLE 5.11 - THERMAL MODEL FIT RESULTS.

Constant A	$(3.2 \pm 0.2) \cdot 10^{-23}$
Thermal Resistance $R_{thermal}$	$(18.8 \pm 1.5)\ cm^2 K \Omega^{-1}$

The increasing of the dissipated power causes the heating of the system (Niobium thin film and Copper substrate) leading to a thermal feedback loop governed by a thermal resistance of about 19 $cm^2 K \Omega^{-1}$.

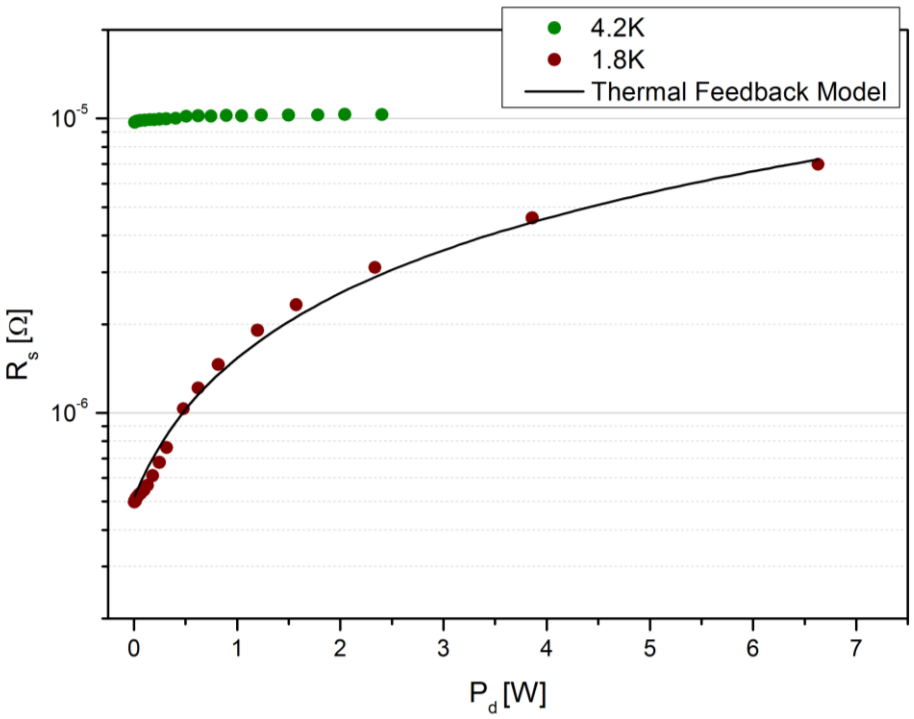

FIGURE 5.34 - SURFACE RESISTANCE VERSUS DISSIPATED POWER FOR CAVITY CU1_3. THE DATA AT 1.8K WAS FITTED USING THE THERMAL FEED-BACK MODEL.

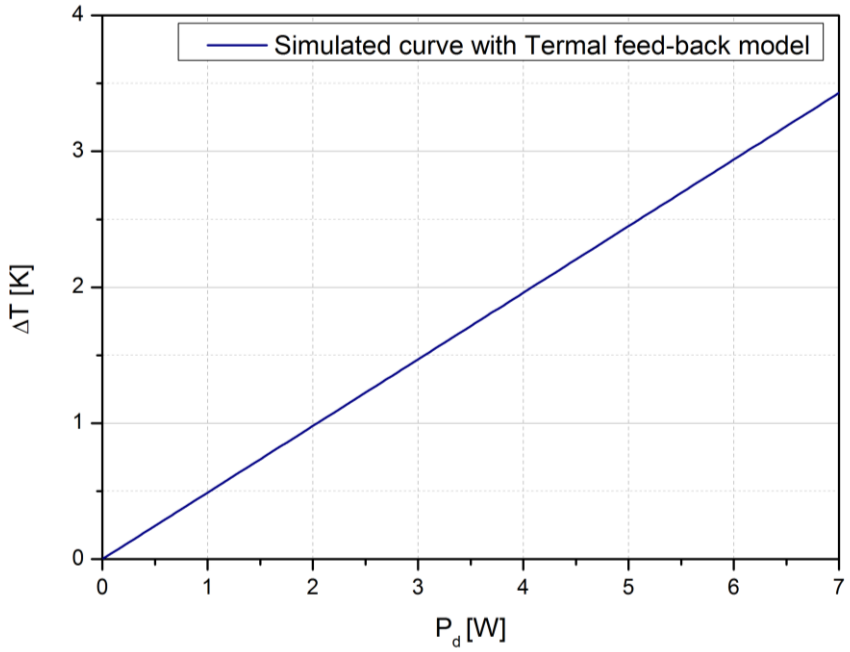

FIGURE 5.35 - TEMPERATURE GRADIENT BETWEEN THE INNER AND OUTER CAVITY SURFACES AS A FUNCTION OF DISSIPATED POWER.

Now the total temperature difference as a function of dissipated power can be simulated using these results, indeed: $\Delta T_{\mathrm{tot}} = \frac{R_{thermal} P_d}{\Sigma}$. The simulation is shown in Figure 5.35. The increasing of the temperature with the power is rather fast, a temperature difference of some Kelvin is found between the inner and the external cavity surface considering some Watt of dissipated power. The experimental curve was measured until the dissipated power was $6.6W$, from this model the film heating during its measurement reached about $3.5K$. The model suggests that the Q-slope found for the curve at $1.8K$ for the cavity Cu1_3 might be due to the heating of the Niobium surface which reaches a temperature of about $5.3K$.

The thermal resistance which determines the value of ΔT depends on the heat exchange from the inner cavity surface to the external one. In sputtered cavities the heat exchange takes place through the Niobium film, the Niobium/Copper interface, the Copper substrate and the Copper/Helium interface, as it is sketched in Figure 5.36. The heat transport occurs for conduction both into the Niobium layer and into the Copper layer, therefore the exchanged heat $\dot{Q}$ can be defined as:

$$\dot{Q}^{Nb} = \frac{\Sigma K^{Nb}}{s^{Nb}}(T_4 - T_3) = \frac{\Sigma K^{Nb}}{s^{Nb}} \Delta T_1 \tag{5.33}$$

$$\dot{Q}^{Cu} = \frac{\Sigma K^{Cu}}{s^{Cu}}(T_2 - T_1) = \frac{\Sigma K^{Cu}}{s^{Cu}} \Delta T_3 \tag{5.34}$$

where Σ is the surface involved in the heat exchange, K^{Nb} and K^{Cu} are the thermal conductibility, s^{Nb} and s^{Cu} are the thicknesses of Niobium and Copper respectively.

Whereas at the interface between two materials, as in the case of both Niobium/Copper interface and Copper/Helium interface, the heat transport is defined as:

$$\dot{Q}^{Nb/Cu} = \Sigma h_{Nb/Cu}(T_3 - T_2) = \Sigma h_{Nb/Cu} \Delta T_2 \tag{5.35}$$

$$\dot{Q}^{Cu/He} = \Sigma h_{Cu/He}(T_1 - T_0) = \Sigma h_{Cu/He} \Delta T_4 \tag{5.36}$$

where $\mathrm{h_{Nb/Cu}}$ is the thermal boundary resistance between Niobium and Copper and $h_{Cu/He}$ is the thermal boundary resistance between Copper and liquid Helium [34]. Indeed, when the heat flux passes through the boundary between two media, a temperature jump ΔT will occur at the boundary and a thermal boundary resistance can be defined. This effect was detected by Kapitza at the boundaries between metals and He II and further experiments found the thermal boundary resistance also between two solids. By the way this resistance can be observed between two metals only if at least one of these is superconducting. Indeed the thermal boundary resistance is a

consequence of acoustic mismatch, i.e. the phonon reflection at the boundary, and for metal in the normal state the heat conduction by electrons by far dominates [35].

The Kapitza conductance is defined by an empirical definition as the heat flux q over the temperature difference between two materials ΔT, when this variation tends to zero:

$$h_k = \lim_{\Delta T \to 0} \frac{q}{\Delta T} \tag{5.37}$$

This term is characterized by a temperature dependence T^n with n between 2 and 4, so the importance of Kapitza resistance to heat transfer problems increases with decreasing the temperature.

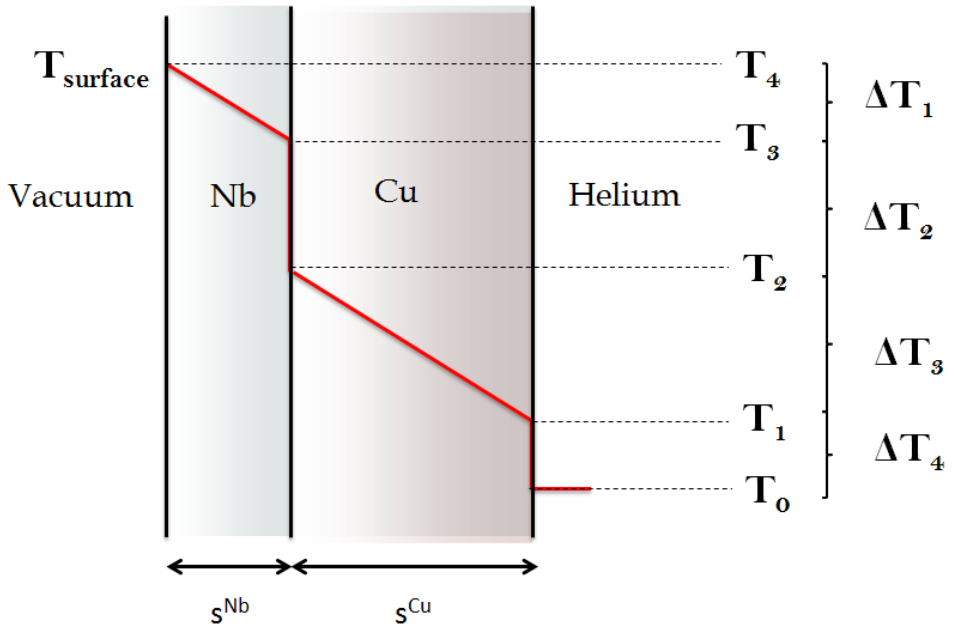

FIGURE 5.36 - SCHEMATIC REPRESENTATION OF THE HEAT FLUX EXCHANGE FROM THE INNER SURFACE TO THE EXTERNAL SURFACE OF THE NB/CU CAVITY.

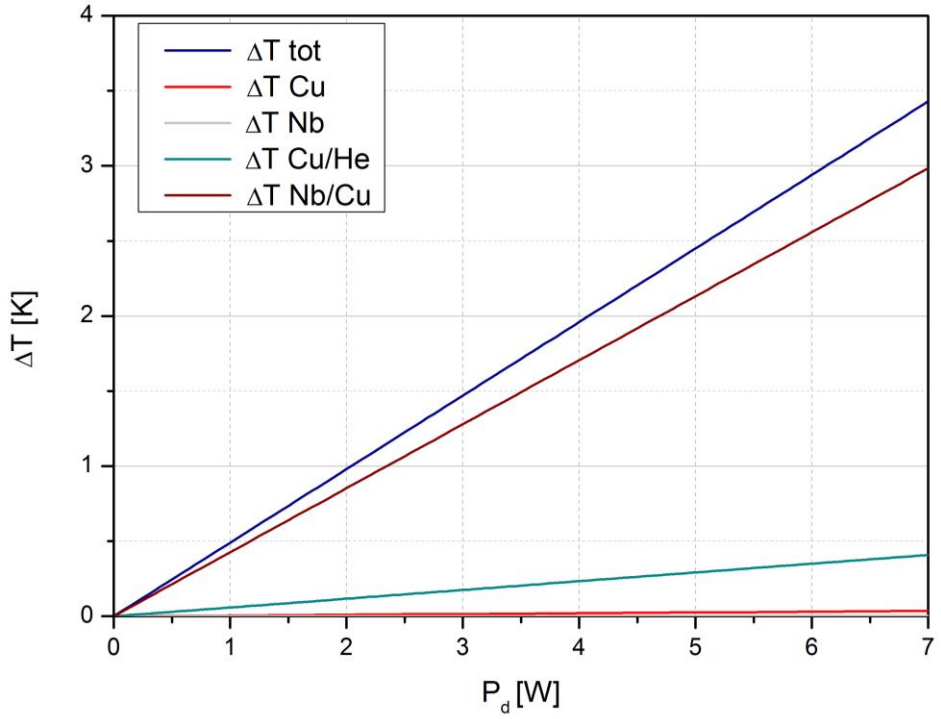

FIGURE 5.37 - THE TOTAL TEMPERATURE DIFFERENCE BETWEEN THE INNER AND THE OUTER CAVITY SURFACE(BLUE LINE) IS COMPARED WITH THE SIMULATED CURVES FOR THE DIFFERENT CONTRIBUTIONS AT THE HEAT EXCHANGE.

Therefore such conductance contributes to the heat transfer process between the metal surface and both Helium-I and Helium-II. By the way, in Helium-I the thermal exchange is dominated by the thermal boundary resistance and the Kapitza term becomes negligible. Indeed in Helium-I three heat exchange regime can be defined, as it will be explained further on, and the thermal properties of such regimes dominates on the Kapitza resistance. For this reason the thermal model is here implemented considering only the curve $Q(E)$ at 1.8K.

The total temperature gradient between the inner and the outer cavity surface is the sum of the thermal resistance contributions discussed above:

$$\Delta T_{tot} = \Delta T_1 + \Delta T_2 + \Delta T_3 + \Delta T_4 = \frac{\dot{Q}}{\Sigma}\left(\frac{s^{Nb}}{K^{Nb}} + h_{Nb/Cu} + \frac{s^{Cu}}{K^{Cu}} + h_{Cu/He}\right) \qquad (5.38)$$

In order to understand what is the rule of the thermal boundary resistance between the Copper layer and the Niobium layer, the data of the different contributions ΔT_1, ΔT_2, ΔT_3, ΔT_4 were simulated using the literature values for K^{Cu}, K^{Nb} and $h_{Cu/He}$. For Niobium/Copper interface the following relation was instead taken into account:

$$\Delta T_{tot} = \frac{R_{thermal} P_d}{\Sigma} = \frac{P_d}{\Sigma}\left(\frac{s^{Nb}}{K^{Nb}} + \frac{1}{h_{Nb/Cu}} + \frac{s^{Cu}}{K^{Cu}} + \frac{1}{h_{Cu/He}}\right) \quad (5.39)$$

Which leads to:

$$\frac{1}{h_{Nb/Cu}} = R_{thermal} - \frac{s^{Nb}}{K^{Nb}} - \frac{s^{Cu}}{K^{Cu}} - \frac{1}{h_{Cu/He}} \quad (5.40)$$

The simulated curves are shown in Figure 5.37, whereas the values used for the simulation are listed in Table 5.12.

From the graph in Figure 5.35 one notices that the main contribution to the thermal resistance is due to the thermal boundary resistance at the Niobium/Copper interface, the other important contribution is the thermal boundary resistance between Copper and Helium, i.e. the Kapitza resistance. The contribution of the Niobium and the Copper layers are instead very small compared to these. The most part of the heating is so due to the interface between the two metals, which causes the heat entrapment.

TABLE 5.12 - PARAMETERS USED FOR THE THERMAL MODEL ΔT SIMULATION [36,37].

Niobium Thermal Conductivity, K^{Nb}	0.018 $Wcm^{-1}K^{-1}$
Niobium film thickness, s^{Nb}	2μm
Copper Thermal Conductivity, K^{Cu}	0.92 $Wcm^{-1}K^{-1}$
Copper thickness, s^{Cu}	2mm
Cavity Surface, Σ	42.86 cm^2
Cu/He Thermal Boundary Conductivity, $h_{Cu/He}$	0.4 $Wcm^{-2}K^{-1}$
Cu/Nb Thermal Boundary Conductivity, $h_{Nb/Cu}$	0.055 $Wcm^{-2}K^{-1}$

It is well known that a poor thermal contact at the interface can significantly decrease the efficiency of a thermal link in a conduction cooled system. We have found that the Q-slope of the Copper sputtered cavity can be due just to a bad interface between the sputtered film and the substrate, which causes an increasing of the film temperature and, as a consequence, the worsening of the BCS resistance. Indeed, we have already encountered that one of the main problems of thin film cavities is that often the high pressure rinsing causes a the partial removal of the Niobium film, highlighting that the film adhesion is rather poor. It is also true that this measurement was done using a cavity in which the Niobium film remained adherent at the substrate after the HPR, however, the contact between Niobium and Copper could be not

optimized to heat transfer. Indeed, Copper and Niobium atoms usually cannot form a solid solution because they do not have the tendency to form together a thermodynamically stable phase. Furthermore, also the film porosity can lead to a bad interface with the substrate, decreasing the contact area between the two materials.

The value found for the thermal boundary resistance between Copper and Niobium is: $R_{Nb/Cu} = 18.3\ cm^2KW^{-1}$, which is higher of about one order of magnitude compared to experimental results in [35]. By the way in [35] the interface between Niobium and Copper was prepared at 850°C and $10^{-6}Torr$ pressing the two materials toghether for a few minutes at a pressure of $5atm$ leading to a good interface between them. So working in order to improve the contact between the Niobium film and the cavity substrate, one could obtain the cure of the Niobium sputtered Copper cavity Q-slope. Let us evaluate the value of Q-factor simulated using the thermal feed-back model, with and without this thermal boundary resistance. The formulas used for the simulations are the following:

$$Q_{simulation}(T_0, P_d) = \frac{G}{\frac{A\omega^2}{T_0} e^{-\frac{\Delta}{k_B T_0}} \left[1 + \left(\frac{\Delta}{k_B {T_0}^2} - \frac{1}{T_0}\right) \Delta T_{tot}\right] + R_0} \tag{5.41}$$

$$Q_{no\ interface\ Nb/Cu}(T_0, P_d) = \frac{G}{\frac{A\omega^2}{T_0} e^{-\frac{\Delta}{k_B T_0}} \left[1 + \left(\frac{\Delta}{k_B {T_0}^2} - \frac{1}{T_0}\right) \left(\Delta T_{tot} - \Delta T_{Nb/Cu}\right)\right] + R_0} \tag{5.42}$$

and the parameters used were the same listed in Table 5.12. The results are displayed in Figure 5.38, in which the real measured value and the two simulated curves are plotted. A great difference appears in terms of Q-factor whether the thermal boundary resistance between Copper and Niobium is neglected, the Q-factor increases of about one order of magnitude. Without this contribution the curve Q-factor versus accelerating field should not be affected by Q-slope.

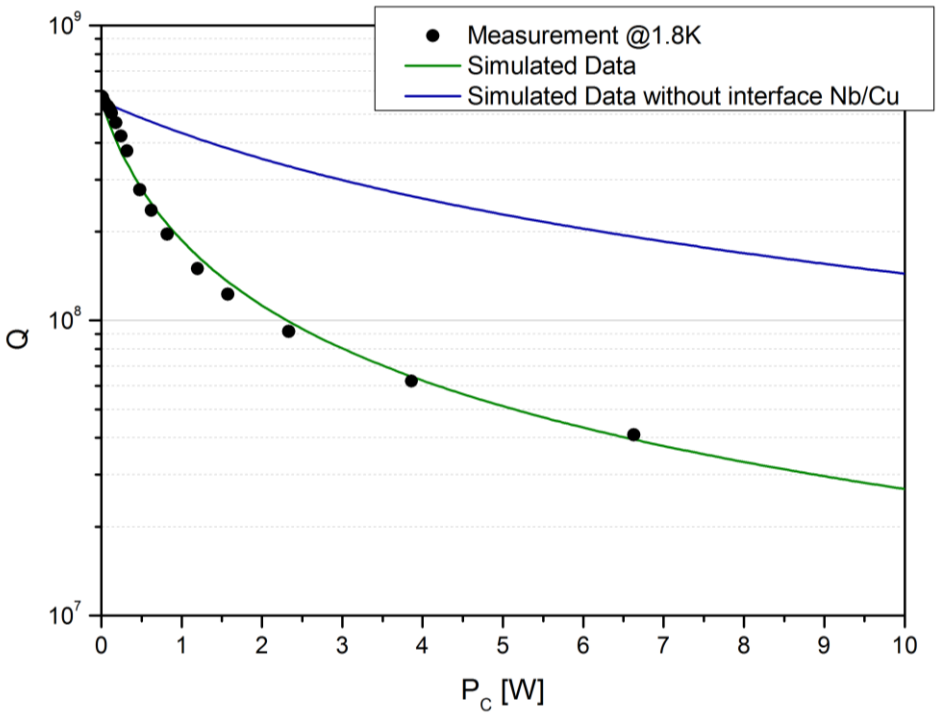

FIGURE 5.38 - Q-FACTOR VERSUS DISSIPATED POWER, THE BLACK DOTS ARE THE REAL DATA MEASURED, THE GREEN CURVE WAS SIMULATING USING THE THERMAL MODEL, AND THE BLUE IS SIMULATED USING THE SAME MODEL BUT WITHOUT CONSIDERING THE THERMAL BOUNDARY CONTRIBUTION BETWEEN COPPER AND NIOBIUM.

5.8 HELIUM BOILING CONSEQUENCES ON NIOBIUM ON COPPER CAVITIES BEHAVIOR

Whether a significant heating of the cavity occurs, this lead to another effect which can also play a role in the Q-slope of Niobium thin film cavities. If during the measurement at $1.8K$ the temperature increases over T_λ, the transition Helium-II to Helium-I appears and it causes the change of the heat transfer regimes, which are less efficient in Heium-I than in Helium-II.

Let us analyze the trend of the temperature during the measurement of the cavity Cu1_3 and of the two cavities in Niobium bulk at 1.8K, this is shown in Figure 5.39. The thermometer T1 was fixed close to the Cu1_3 cavity's cell, whereas the thermometer T2 was fixed close to one of the other two Niobium bulk cavities that were inserted together into the cryostat and measured just after the Copper cavity. It is clear from the graph that during the RF test of the Niobium on Copper cavity there is a significant rising of the temperature. Such rising is more pronounced near the Copper cavity but it is also visible far away, since even the thermometer T2 reveals a temperature increasing.

However, the surprising fact is that the increasing of the Helium bath temperature was measured only during the measurement of the sputtered Copper cavity, indeed looking at the zone of the graph concerning the Niobium bulk cavities measurements, the temperature acquired from both thermometers remains quite constant.

The heating of the cavity is, generally speaking, dependent on the cavity performances, high Q-values mean low dissipated power and then low surface heating. However, in this case one of the two Niobium bulk cavities measured after the Cu1_3 one shows higher Q-factor values, whereas the other one shows lower Q-factor values. Therefore such temperature rising does not depends on the Q-factor but it seems to be intrinsically due to the Copper, or as seen before, to the Niobium/Copper interface.

The super-fluid Helium transition occurs at $T_\lambda = 2.1768K$, the graph shows that during the measurement, the temperature becomes higher than T_λ, so from a certain point the Helium around the cavity is not super-fluid anymore, i.e. the transition He-II to He-I appears. In Figure 5.40 it is shown the trend of the temperature as a function of the accelerating field, during the RF test. The super-fluid to normal-fluid Helium transition appears around $3.5 MV/m$ of accelerating field, which corresponds to about $0.2W$ of cavity dissipated power and about $0.005\ Wcm^{-2}$ of heat flux. After this point the cavity is surrounded by a layer of He-I, this is a macroscopic layer thick enough to surround also the thermometer T1 (Figure 5.29).

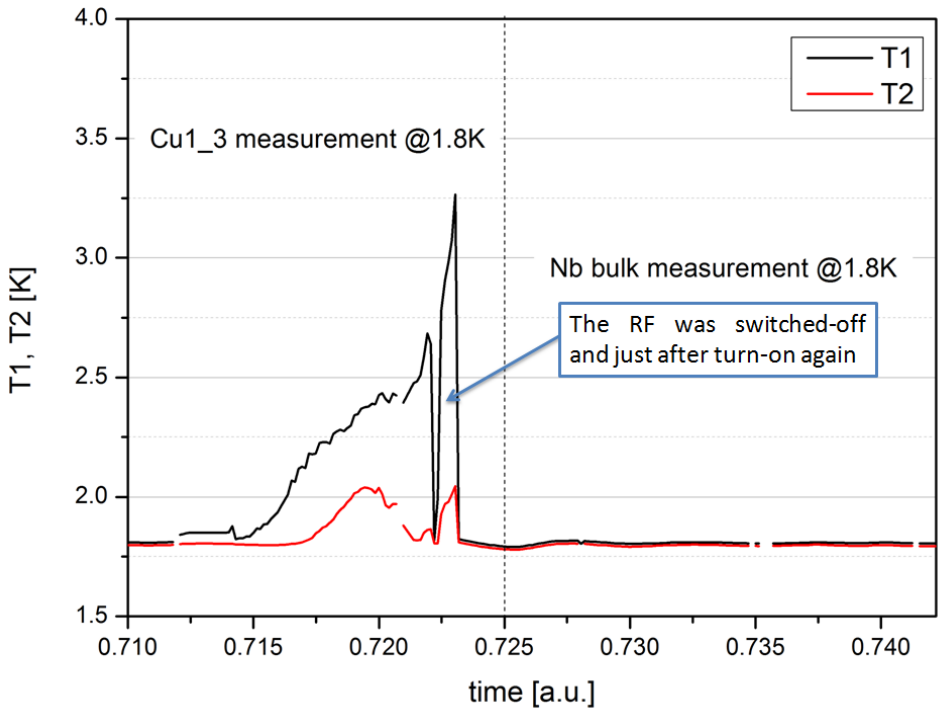

FIGURE 5.39 - TEMPERATURE DATA MEASURED FROM THERMOMETERS 1 AND 2 DURING THE RF MEASUREMENT AT 1.8K OF THE CU1_3 CAVITY AND TWO NIOBIUM BULK CAVITIES .

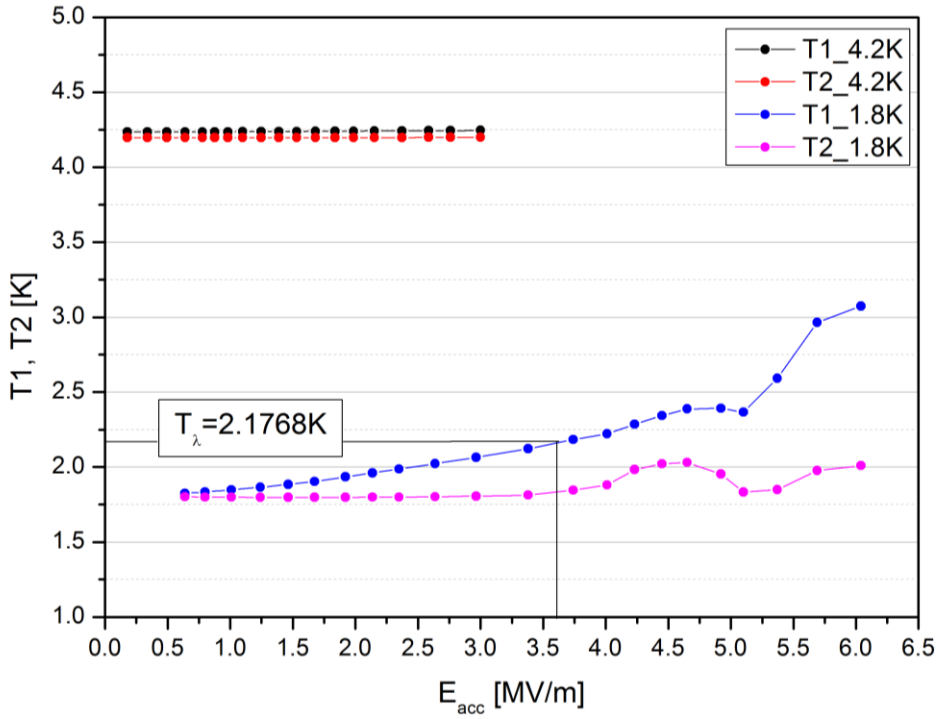

FIGURE 5.40 - TEMPERATURE DATA MEASURED FROM THERMOMETERS 1 AND 2 AS A FUNCTION OF ACCELERATING FIELD, THE DATA ARE DISPLAYED FOR THE CURVES AT 4.2K AND 1.8K..

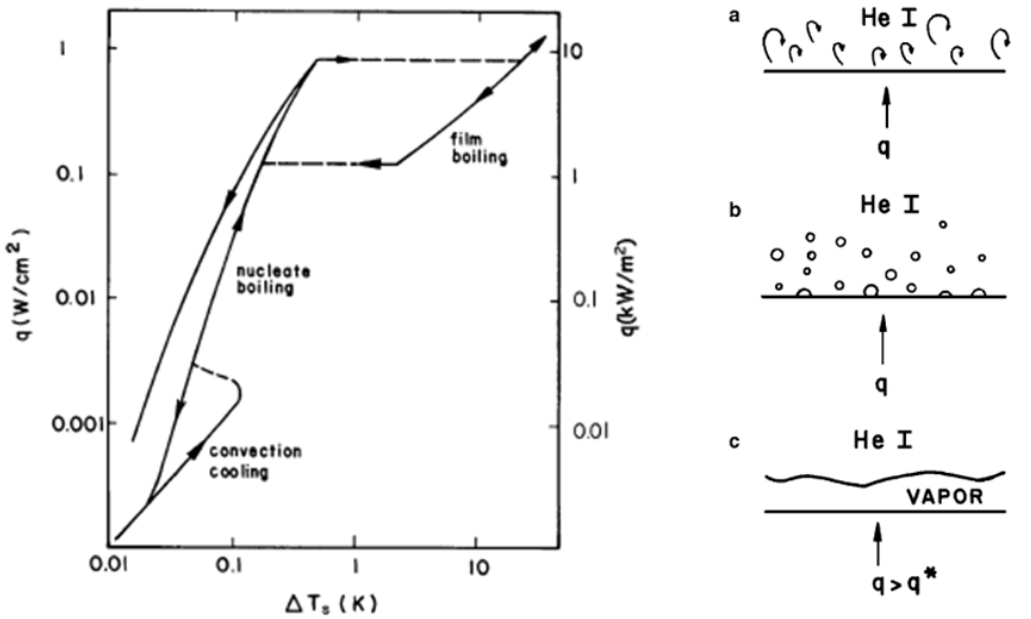

(A) (B)

FIGURE 5.41 - RF MEASUREMENTS OF CU1_3 SPUTTERED NIOBIUM CAVITY.

Surprisingly, $3.5MV/m$ corresponds also at the accelerating field in which the curve $Q(E_{Acc})$, for the cavity Cu1_3 at $1.8K$, increases its slope entails the conspicuous lowering of the performances (see Figure 5.28). In addition, from the Figure 5.40 it can be seen that after $3.5MV/m$ the temperature rising seems to be more and more conspicuous.

When the cavity is surround by Helium-I, there are principally three regimes of heat transfer: natural convection, nucleate boiling, and film boiling, as is shown in Figure 5.41. During the natural convection, with few W/m^2 of heat flux, a density driven convection currents are established near the heated surface. Increasing the heat flux the nucleate boiling regime is encountered, in which bubbles of Helium vapor start to nucleate at the surface defects and as the flux is increased the bubbles growth and detach. In order to obtain such regime it is necessary to satisfy two conditions, a boundary superheated layer must create adjacent to the surface, and a local surface imperfection must exist. The heat transfer is now governed to the hydrodynamics of bubble growth and detachment.

The bubbles continue to grow and to coalesce until the heat flux is so high that both the growth and the detachment mechanisms become unstable and the system tends to create a continuous vapor film which minimize the system energy. This regime is called film boiling and it occurs at the peak nucleate boiling heat flux q^*. Once such regime is established, the Helium forms two stable phases near the heat transfer boundary, a thin vapor layer interfaced with the liquid Helium-I phase [37].

Therefore, during the Cu1_3 cavity measurement at $1.8K$, the cavity is at first surrounded from Helium-I, and then to Helium-II, so as the dissipated power increases, the heat transfer might reach the film boiling regime. When this happens, the vapor Helium surrounded the cavity, and it is not thermalized efficiently anymore.

We can conclude that, the change of the Q-slope, analyzed for the cavity Cu1_3 measured at $1.8K$, might be really due to the less efficient heat transfer which takes place with the vapor Helium than with the super-fluid Helium.

Let us now take into account the graph of the surface resistance versus $1/T$ for the Nb/Cu 6GHz cavities, and compare that curves with the ones acquired for a 6GHz bulk Niobium cavity (Nb123), Figure 5.42 (a) and (b).

The bulk measurements, Figure 5.42 (a), show that for $T > T_\lambda$ the surface resistance has a strong dissipated power dependence, as the Niobium sputtered cavities. Whereas for $T < T_\lambda$ after the sudden decreasing of the surface resistance at the λ -point, the dissipated power dependence seems to disappear. The better properties in terms of the heat exchange of Helium-II compared to Helium-I might explain this beneficial behavior [38].

This fact might mean that the super-fluid properties of Helium-II do not appear in the case of Niobium on Copper cavities, in agreement with the conclusion done before.

Putting together these experimental facts it is possible to assert that with high probability the heat exchange between cavity and Helium, plays an essential role regarding the cavity performances. The Niobium bulk cavities benefits from the heat exchange with super-fluid Helium, on the contrary for the Copper cavities this benefits do not appear, the surface resistance still remain considerably higher with higher dissipate powers, than with lower ones.

With low dissipated power values the super-fluid Helium increases its temperature, but the heat exchange still occurs efficiently, only when T_λ is exceeded the cavity temperature increasing is even less counterbalanced by the Helium environment and, increasing the field, the Q-factor slope becomes even more pronounced . The thermal model analyzed before would be well-improved taking into account this effect which probably dominates over the Kapitza Copper/Helium resistance. In other word, the heating found at the interface Copper/Niobium, with the thermal feed-back model, might be erroneous because only the literature value of the Kapitza resistance was taken into account as thermal resistance in Helium-I. On the other hand, the implementation of the film boiling and the other heat transfer regime is of particularly difficult implementation.

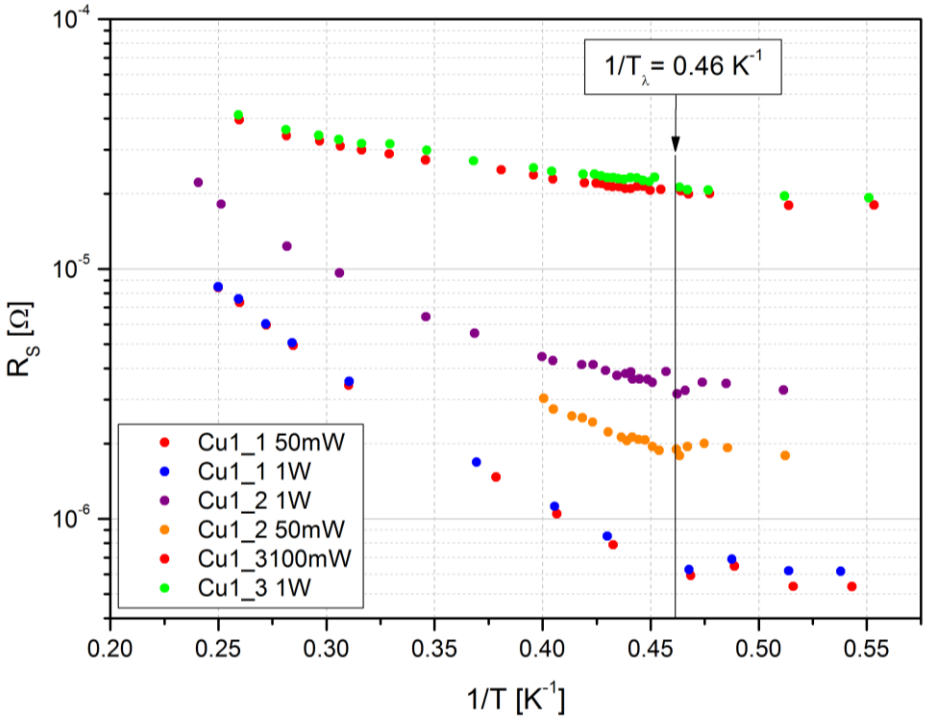

(A)

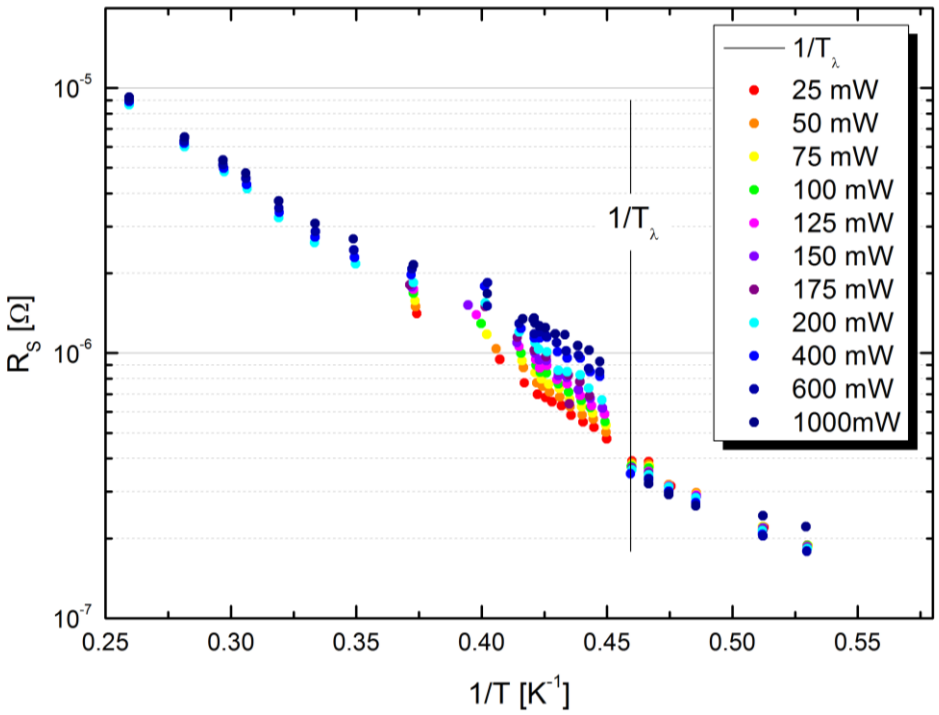

(B)

FIGURE 5.42 - (A) SURFACE RESISTANCE AS A FUNCTION OF 1/T OF A CU1_3 NB/CU SPUTTERED CAVITY. (B) SURFACE RESISTANCE AS A FUNCTION OF 1/T OF A NB123 BULK CAVITY (COURTESY OF M. CHECCHIN)

Chapter 6

CONCLUSIONS

During the work at CERN, Quarter Wave Resonators were characterized by means the RF measurements. The cavities analyzed were made with Biased Diode Sputtering or with Magnetron Sputtering deposition techniques. The discovery of the best implementable and reproducible technology, between biased diode sputtering and magnetron sputtering, is particularly important in the case of HIE-ISOLDE project in which a large number of resonators must be done for the imployment in the REX-ISOLDE LINAC.

Let us consider the performances of the three cavities analyzed at CERN. The cavity with the higher performances, in terms of Q-factor, is the QP1_4 cavity. This cavity was sputtered by Biased Diode Sputtering technique and its surface resistance shows the lowest values, compared to the other two measured QWRs. The performances of this cavity exceed the HIE-ISOLDE specification, and it can be utilized in the superconducting LINAC.

The cavity Q5_1 was sputtered with Magnetron Sputtering technique and it shows performances sligtly lower than the QP1_4 cavity in terms of Q-factor, regarding the accelerating field it reached a little bit larger values than the QP1_4 cavity. Its surface resistance shows value sligthly higher than the previous cavity but the performance of this cavity does not achieve the expected values. The worst cavity was the Q3_4, made with Biased Diode Sputtering technique. This cavity was initially measured at Orsey laboratories, where it showed high performance, comparable with QP1_4 cavity one. Unfortunately the further measurements done at CERN show bad results, highlighte the degradation of the Niobium film properties.

Taking into account the values estimated for the Niobium films RRR, these results are in discepancy with the previous conclusion. Indeed high value of RRR was found for the Q3_4 cavity and low value was found for the cavity QP1_4 instead. The cavity Q5_1 was not analyzed in such way becouse of some technical problem. By the way, it is important to underline that the frequency shift agains temperature acquired curves, for the cavity QP1_4, show a strange trend which may not allowe the fit to find the best parameters. Such strange behaviour can be due to a presence of many superconducting phases which have the superconducting transition at different temperatures.

The simulation done for the BCS resistance as a function of temperature, using the two fluid model approximation and the results from the resonance frequency shift model, show that the superconducting behaviour of the QWRs, measured at 4.5K, is almost completely governed by the residual resistance term and the BCS resistance contribution is instead eclipsed. Therefore the behaviour of such cavities can be improved working on the minimization of the residual term, for example, decreasing the superficial defects, the Hydrogen content, and so on.

During the thesis work at the LNL, the Niobium sputtering on 6GHz Copper cavities was performed using a magnetron sputtering system. The Niobium deposition of such substrate encounters some problems. The main problems were the poor film adhesion and the cavity-cathode aligment. Indeed, after two different depositions, some parts of the Niobium film deposited went away during the high pressure rinsing process, in which ultra pure water at $100bar$ strikes the inner cavity surface. Several reason could be the cause of the poor film adhesion. For examples the particularly smooth Copper surface substrate brings several benefit for this application, but, on the contrary, a smooth surface is not the optimum choice for the sputtering deposition just because it does not allow a well attachment between sputtered atoms and substrate atoms. The poor adhesion can be also because the sputtered atoms arrive at the substrate with oblique incidence which can causes shadowing effects, involving, for example, a deposition of a high porosity film. Further studies should be done in order to understand, however, if also the manner in which the HPR is done might affect the unexpected stripping of the Niobium film.

Another problem encountered during the depositions, was the aligment between the cathode and the cavity, indeed sometimes happend that, during its movement, the cavity touched the cathode. This was an important problem becouse whether it happened during the deposition, a short-circuit would appear, compromizing the sputtering process. For the high temperature deposition un upgrading of the sputtering system lead to overcome this problem by using a flexible bellow provided with three adjustable screws.

Three different Niobium sputtered 6GHz cavities were measured during the thesis work. The better performances, in terms of both Q-factor and accelerating field, were found, as expected, for the Cu1_3 cavity which was made with a high temperature deposition. The Copper substrate temperature was fixed at 400°C. Sligthly lower performances are shown from the Cu1_2 cavity, which was sputtered at room temperature instead. The worst Q-factor and accelerating field values belongs the cavity Cu1_1, but also this result was expected since this cavity is not completely superconducting. Indeed part of the Niobium film went away during the HPR, it remained almolst intact in the cell region, allowing the RF measurement.

Fitting the data of the surface resistance versus one over the temperature, using the BCS theory, a residual resistance values were estimated. These results are in agreement with the previous conclusion, i.e. the cavity Cu1_3 has the better RF superconducting performances.

During this analysis an unexpected trend appears: the residual resistance increases with the dissipated power. This behaviour is not explained with the BCS theory, the experimental observations can be instead explained with the thermal feed-back model. Using this model it is possible to take into account that the inner cavity surface, i.e. the superconducting layer subjected to RF field, has not the same temperature of the Helium bath. Indeed the dissipated power causes an increasing of the temperature which in turn causes the increasing of the surface resistance. From this model a temperature difference of about $3K$ was calculated between the inner and the outer cavity surfaces, analyzing the surface resistance versus dissipated power curve taken at $1.8K$ for the cavity Cu1_3.

The thermal resistance, which causes these effects, may be scomposed in four terms: the Kapitza resistances between the two interfaces, Copper/Niobium and Copper/Helium, and the thermal resistances due to the Niobium and the Copper layers. It was found that the main contribution to the thermal resistance is due to the Copper/Niobium interface.

Therefore the Q-slope problem which affects the Niobium sputtered cavities may be due to a bad interface between Copper and Niobium, which causes a substancial temperature rising, lowering the superconducting proprieties of the Niobium film. The bad interface is caused by the sputtered Niobium atoms which do not form strong bound with the substrate, because of the low tendency of these two elements to form any stable alloy. An interesting future work would be the study of how the cavity performances change after modifications of the film/substate interface. The deposition of a layer, between Copper and Niobium, which increases their bound, should increase the RF perfomances of the cavity. As, for example, the deposition of an Alluminum layer should be a good solution becouse of the good tendency of this metal to bound with both metals, Niobium and Copper.

Another unexpected conclusion was done analyzing the different behaviour of the surface resistance between a thin film Copper cavity and a bulk Niobium one, before and after the lambda point, i.e. the critical temperature of the superfluid transition from Helium-I to Helium-II. A bulk Niobium cavity shows a jump of the surface resistance at T_λ, which deacrese it noticeably, and for $T < T_\lambda$ the surface resistance do not show correlation with the dissipated power. On the contrary, the sputtered cavities does not show any particular benefits for $T < T_\lambda$, i.e. when the cavities are sourrounded by superfluid Helium instead of liquid Helium. From this comparison appears that the Copper cavities seem to be not thermalized by the superfluid Helium.

The cavity Cu1_3 was measured at $1.8K$ just before other two Niobium bulk cavities, giving the possibility to observe a Helium bath temperature increasing of some Kelvins, near the

Nb/Cu cavity during its measurements. The temperature rising was not revealed during the measurements of the bulk cavities. A possible explanation of that could be the formation of a vapour Helium layer which surrounds the external cavity surface, instead of the superfluid Helium. This regime of heat exchange is called film boiling and it is less efficient compared to the case of superfluid Helium. Also the thermal boundary resistance increases, so much that the Kapitza resistance becomes negligible.

We have found two possible explanations of the lower RF performance of the Niobium sputtered cavities. In one case the inner cavity interface, Niobium/Copper, causes the lowering of the performance because of an extra-increasing of the temperature. In the second case a temperature rising around the Copper surface causes the formation of a vapour Helium layer around the cavity when the bath is cooled below the λ-point.

Important food for thought were found out during this thesis work. The Q-slope problem was analyzed from a new point of view in which a thermal feed-back approach was combined with the effects of the heat exchange. The first innovative idea consists of to blame the Copper/Niobium interface as a responsible of the Q-slope problem. In addition the temperature rising causes the cavity to be thermilized by a valour Helium layer instead of superfluid Helium. Further studies should be carried out in order to understand deeply how these thermal problem operate, how of those has the main role in the Q-slope, and whether they are correlated each other.

APPENDIX I

PROPAGATION OF UNCERTAINTY EQUATIONS

- CALIBRATION POINT:

$$P_{inc}[dBm] = P_{inc}^{meas} + P_{inc}^{cal}$$

$$\sigma_{P_{inc}[dBm]} = \sqrt{\sigma_{P_{inc}^{meas}}{}^2 + \sigma_{P_{inc}^{cal}}{}^2}$$

$$P_{ref}[dBm] = P_{ref}^{meas} + P_{ref}^{cal}$$

$$\sigma_{P_{ref}[dBm]} = \sqrt{\sigma_{P_{ref}^{meas}}{}^2 + \sigma_{P_{ref}^{cal}}{}^2}$$

$$P_{txm}[dBm] = P_{txm}^{meas} + P_{txm}^{cal}$$

$$\sigma_{P_{txm}[dBm]} = \sqrt{\sigma_{P_{txm}^{meas}}{}^2 + \sigma_{P_{txm}^{cal}}{}^2}$$

$$P_{inc}[W] = \frac{10^{P_{inc}[dBm]}}{1000}$$

$$\sigma_{P_{inc}} = 10^{(P_{inc}[dBm]-40)/10} ln(10) \sigma_{P_{inc}[dBm]}$$

$$P_{ref}[W] = \frac{10^{P_{ref}[dBm]}}{1000}$$

$$\sigma_{P_{ref}} = 10^{(P_{ref}[dBm]-40)/10} ln(10) \sigma_{P_{ref}[dBm]}$$

$$P_{txm}[W] = \frac{10^{P_{txm}[dBm]}}{1000}$$

$$\sigma_{P_{txm}} = 10^{(P_{txm}[dBm]-40)/10} ln(10) \sigma_{P_{txm}[dBm]}$$

$$P_c = P_{inc} - P_{ref} - P_{txm}$$

$$\sigma_{P_c} = \sqrt{{\sigma_{P_{inc}}}^2 + {\sigma_{P_{ref}}}^2 + {\sigma_{P_{txm}}}^2}$$

$$\beta_{pk} = \frac{P_{txm}}{P_c}$$

$$\sigma_{\beta_{pk}} = \beta_{pk} \sqrt{\left(\frac{\sigma_{P_{txm}}}{P_{txm}}\right)^2 + \left(\frac{\sigma_{P_c}}{P_c}\right)^2}$$

$$\beta_{cpl} = \frac{1 + \sqrt{P_{ref}/P_{inc}}}{1 - \sqrt{P_{ref}/P_{inc}}}$$

$$\sigma_{\beta_{cpl}} = \sqrt{\frac{P_{ref}/P_{inc}}{P_{inc}\left(\sqrt{P_{ref}/P_{inc}} - 1\right)^4} {\sigma_{P_{inc}}}^2 + \frac{P_{ref}/P_{inc}}{{P_{ref}}^2\left(\sqrt{P_{ref}/P_{inc}} - 1\right)^4} {\sigma_{P_{ref}}}^2}$$

$$\beta_{cpl} = \frac{1 - \sqrt{P_{ref}/P_{inc}}}{1 + \sqrt{P_{ref}/P_{inc}}}$$

$$\sigma_{\beta_{cpl}} = \sqrt{\frac{P_{ref}/P_{inc}}{P_{inc}\left(\sqrt{P_{ref}/P_{inc}} + 1\right)^4} {\sigma_{P_{inc}}}^2 + \frac{P_{ref}/P_{inc}}{{P_{ref}}^2\left(\sqrt{P_{ref}/P_{inc}} + 1\right)^4} {\sigma_{P_{ref}}}^2}$$

$$Q_0 = \frac{2\pi f\, t/2 \left(1 + \beta_{pk} + \beta_{cpl}\right)}{ln2}$$

$$\sigma_{Q_0} = Q_0 \sqrt{\left(\frac{\sigma_{\beta_{cpl}}}{(1+\beta_{pk}+\beta_{cpl})}\right)^2 + \left(\frac{\sigma_{\beta_{pk}}}{(1+\beta_{pk}+\beta_{cpl})}\right)^2 + \left(\frac{\sigma_{t/2}}{t/2}\right)^2 + \left(\frac{\sigma_f}{f}\right)^2}$$

$$E_{acc} = \sqrt{\frac{U}{k}}$$

$$\sigma_{E_{acc}} = \frac{E_{acc}}{2U}\sigma_U$$

$$U = \frac{Q_0 P_c}{2\pi f}$$

$$\sigma_U = U\sqrt{\left(\frac{\sigma_{Q_0}}{Q_0}\right)^2 + \left(\frac{\sigma_{P_c}}{P_c}\right)^2 + \left(\frac{\sigma_f}{f}\right)^2}$$

$$\tau_{pk} = \frac{U}{P_{txm}}$$

$$\sigma_{\tau_{pk}} = \tau_{pk}\sqrt{\left(\frac{\sigma_U}{U}\right)^2 + \left(\frac{\sigma_{P_{txm}}}{P_{txm}}\right)^2}$$

- CW MEASUREMENTS:

$$P_{inc}[dBm] = P_{inc}^{meas} + P_{inc}^{cal}$$

$$\sigma_{P_{inc}[dBm]} = \sqrt{\sigma_{P_{inc}^{meas}}{}^2 + \sigma_{P_{inc}^{cal}}{}^2}$$

$$P_{ref}[dBm] = P_{ref}^{meas} + P_{ref}^{cal}$$

$$\sigma_{P_{ref}[dBm]} = \sqrt{\sigma_{P_{ref}^{meas}}{}^2 + \sigma_{P_{ref}^{cal}}{}^2}$$

$$P_{txm}[dBm] = P_{txm}^{meas} + P_{txm}^{cal}$$

$$\sigma_{P_{txm}[dBm]} = \sqrt{\sigma_{P_{txm}^{meas}}{}^2 + \sigma_{P_{txm}^{cal}}{}^2}$$

$$P_{inc}[W] = \frac{10^{P_{inc}[dBm]}}{1000}$$

$$\sigma_{P_{inc}} = 10^{(P_{inc}[dBm]-40)/10} ln(10) \sigma_{P_{inc}[dBm]}$$

$$P_{ref}[W] = \frac{10^{P_{ref}[dBm]}}{1000}$$

$$\sigma_{P_{ref}} = 10^{(P_{ref}[dBm]-40)/10} ln(10) \sigma_{P_{ref}[dBm]}$$

$$P_{txm}[W] = \frac{10^{P_{txm}[dBm]}}{1000}$$

$$\sigma_{P_{txm}} = 10^{(P_{txm}[dBm]-40)/10} ln(10) \sigma_{P_{txm}[dBm]}$$

$$P_c = P_{inc} - P_{ref} - P_{txm}$$

$$\sigma_{P_c} = \sqrt{\sigma_{P_{inc}}{}^2 + \sigma_{P_{ref}}{}^2 + \sigma_{P_{txm}}{}^2}$$

$$E_{acc} = \sqrt{\frac{P_{txm}\tau_{pk}}{k}}$$

$$\sigma_{E_{acc}} = \frac{E_{acc}}{2} \sqrt{\left(\frac{\sigma_{P_{txm}}}{P_{txm}}\right)^2 + \left(\frac{\sigma_{\tau_{pk}}}{\tau_{pk}}\right)^2}$$

$$Q_0 = \frac{2\pi f \tau_{pk} P_{txm}}{P_C}$$

$$\sigma_{Q_0} = Q_0 \sqrt{\left(\frac{\sigma_{\tau_{pk}}}{\tau_{pk}}\right)^2 + \left(\frac{\sigma_{P_{txm}}}{P_{txm}}\right)^2 + \left(\frac{\sigma_{P_C}}{P_C}\right)^2 + \left(\frac{\sigma_f}{f}\right)^2}$$

LIST OF FIGURES

LIST OF TABLES

BIBLIOGRAPHY

[1] C. Kittel, *Introduction to Solid State Physics*, Wiley-VHC (2005)

[2] A. A. Abrikosov, *Fundamentals of the Theory of Metals*, North-Holland (1988)

[3] H. Padamsee, J. Knobloch, T. Hays, RF *Superconductivity for Accelerators*, Wiley-VCH (2008)

[4] V. Palmieri *The classical superconductivity: phenomenology of low temperature superconductors*, European Training on Technologies and Industrial applications of superconductivity 1-34 (1992)

[5] V. V. Schmidt *The Physics of Superconductors*, Springer-Verlag (1997)

[6] J. Turneaure, J. Halbritter, H. A. Schwettman *J. Supercond.* 4 (1991) 341

[7] M. Tinkham *Introduction to Superconductivity*, McGraw-Hill (1976)

[8] S. B. Nam *Phys. Rev.* 156 (1967) 487

[9] H. Padamsee Supercond. Sci. Technol. 14 (2011) R28-R51

[10] T. P. Wangler *RF Linear Accelerators*, Wiley-VHC (2008)

[11] H. Padamsee *RF Superconductivity - Science, Technology and Applications*, Wiley-VHC (2009)

[12] A. M. Porcellato, S. Stark, V. Palmieri *Nb sputtered Cu QWR: a 20 years of experience from an idea to the routhine beam acceleration*, Proceedings of The International Workshop on Thin Films and new ideas for pushing the limits of RF superconductivity, Legnaro, October 2006

[13] C. Benvenuti, S. Calatroni, I. E. Campisi, P. Darriulat *Phisica C* 316 (1999) 153-188

[14] C. Benvenuti, S. Calatroni, M. Hakovirta, A.-M. Valente *Proceedings of The 10th Workshop on RF Superconductivity* MA002, Tsukuba, Japan 2001

[15] G. Lanza, PhD Thesis, *New Magnetron Configurations For Sputtering Niobium Thin Film Onto Copper Tesla-Type Superconducting Cavities* (2008)

[16] V. Palmieri *Proceedings of the 8th Workshop on RF Superconductivity* SRF97C18, Abano Terme, Italy 1997

[17] R. Losito *Design of a β=0.66 Monocell Cavity* CERN SL-Note-98-008, February 1998

[18] D. Tonini, C. Greggio, V. Palmieri *Proceedings of The 11th Workshop on RF Superconductivity* THP11, Lubek, Germany 2003

[19] A. M. Valente-Feliciano *Proceedings of the 11th International Conference on RF Superconductivity* TUIOB06, Chicago, IL USA 2011

[20] I. Petrov *J. Vac. Sci. Technol., A* 21-5 (2003) S117-S128

[21] www.engineeringtoolbox.com

[22] www.wikipedia.com

[23] O. Capatina, J.-P. Brachet *Proceedings of the 2nd International Particle Accelerator Conference* MOPC103**,** San Sebastián, Spain (2011)

[24] I. Mondino *HIE-ISOLDE Cavity Q2_4 Report,* CERN HIE-ISOLDE-PROJECT, November 2011

[25] G. Vogt *Phys. Rev. Spec. Top.--Accel. Beams* 16 (2013) 102002

[26] C. E. Papadopolous *Flow Meas. Instrum*. 12 (2001) 291-298

[27] J. C. Slater *Rev. Mod. Phys.* 18-4 (1946) 441-512

[28] J. C. Slater *Phys. Rev.* 76-9 (1949) 1332-1347

[29] A. D'Elia *CERN HIE-ISOLDE-PROJECT-Note-0014*, September 2012

[30] Private talk with V. Palmieri

[31] V. Palmieri *Proceedings of the 12th International Workshop on RF Superconductivity* TUA02, Cornell University, Ithaca 2005

[32] M. Martinello, Characterization of Superconducting Cavities for HIE-ISOLDE, CERN-STUDENTS-Note-2013-242

[33] E. Haebel *R&D Issues in the Field of Superconducting Cavities*, TESLA 98-05 in TTF Meeting 60, Desy, 1998

[34] B. Baudouy *Proceeding of the CERN Accelerator School - Superconductivity for Accelerators*, Erice 2013 (on press)

[35] C. Schmidt *J. Appl. Phys.* 46-3 (1975) 1372-1375

[36] P. Duthil *Proceeding of the CERN Accelerator School - Superconductivity for Accelerators*, Erice 2013 (on press)

[37] S. W. Van Sciver *Helium Cryogenics*, Springer-New York (2012)

[38] M. Checchin, M. Martinello, A. A. Rossi, S. Stark, F. Stivanello, R. M. Thakur, G. L. Yu and V. Palmieri, R. Vaglio *Proceedings of the 16th International Conference on RF Superconductivity* MOIOC01, Paris 2013 (on press)